The University Of Sheffield.

Study of cross flows and large flow structures in nuclear reactors

Yu Duan

Supervised by Professor Shuisheng He

This thesis is submitted to in partial fulfilment of the requirements for the degree of *Doctor of Philosophy*

The University of Sheffield

Faculty of Engineering

Department of Mechanical engineering

June 2015

To my parents, my girlfriend and all my families

Acknowledgements

First and foremost, I would like to express my sincere gratitude to Professor Shuisheng He, for not just offering me such a good opportunity to join in the PhD program, but also for his advice, support and invaluable guidance during the past 40 months. I have also benefited a lot from his valuable knowledge and experience on CFD as well as the thermal hydraulic problems in the nuclear reactor.

I also would like to thank Jim Gotts and Dr. Poo Balan Ganesan for their guidance and cooperation in the study of the cooling effect of cross flow in the AGRs. I especially received a lot of help from Dr. Poo Balan Ganesan on using the Ansys software package, which plays an important role in my PhD study. I would like to appreciate the discussions with Dr. Kristin Newlands, Charles Moulinec and Yvan Fournier on the usage of Code_Saturne. To all my fellow research in 'Heat, Flow and Turbulence Research Group', thank you for listening and offering me advice throughout this entire project. A special thanks to Akshat Mathur for his great help with my English.

I also acknowledge the financial support provided by EDF Energy as well as the support of the EPSRC UK Turbulence Consortium, which supports the use of the facilities of the UK national supercomputer ARCHER. I appreciate the computing resources, Iceberg and ARCHER, and their corresponding support teams.

Last but not the least, I wish to devote my greatest gratitude to my parents, other family members and friends for their enthusiastic support over the years. Finally I owe much to my girlfriend Xinyuan Ke, without whose love and understanding I would not have completed this work.

Abstract

The aim of the present PhD project is to develop a better understanding of the complex thermal hydraulic phenomenon of nuclear reactors using advanced computational fluids dynamics (CFD). In particular, this PhD project investigates the horizontal flows in the AGRs, and the large flow structure and flow instability in tightly packed fuel assemblies.

The horizontal flows in Hartlepool/Heysham 2 advanced gas-cooled reactors are investigated by solving RANS/URANS equations with RNG k-ε model. Even though it has been known for some time that there are some horizontal flows in these reactors, but their effects on the cooling of graphite bricks have not been previously assessed. The study reveals that the horizontal cross flow helps to improve the cooling of the moderator brick, while the HIBL flow can result in local hot spots in some narrow gap regions. The axial variation of the brick geometry has also been found to significantly influence the distribution of the temperature within the brick. It is also found that there may be flow instabilities in the flows in the lower level of the AGR fuel channels.

Large-eddy simulation (LES) with WALE subgrid scale model is applied to study the buoyancy effect on the behaviour of the ascending flow in the tightly-packed-rod-bundle geometry. The buoyancy effect is modelled using the Boussinesq approximation. The existence and behaviours of large flow structures in the gaps of the flow passage are demonstrated using instantaneous flow fields, spectrum analysis and correlation analysis. The relationship between the Strouhal number of flow structures and the buoyancy parameter Bo^* is established. The study also demonstrates that the local buoyancy effect on the turbulence in the non-uniform flow passage is non-uniform as well. It has been shown that buoyancy-induced heat

transfer deterioration in the non-uniform sub-channel considered herein is much weaker than that in a circular pipe under similar conditions.

LES and WALE SGS model is again utilized to investigate the effect of strong variations of fluid properties on the flow in the tightly-packed-rod-bundles geometry addressed earlier under supercritical pressure. Even through the flow has been significantly influenced by the variation of fluid properties, especially, thermal expansion, the large unsteady coherent flow structures remain similar. The swinging flow in the narrow gap is still an important feature. It has been found that the r.m.s of the horizontal fluctuating velocity is always increased by the heating due to the variation of fluids properties. In contrast, the r.m.s of the vertical fluctuating velocity is first suppressed when the heating is weak to medium, but is enhanced when the heating is very strong.

Contents

List of Figures

List of Tables

Nomenclature

Roman Symbols

A	event
a, b	Constant values
Bo^*	Buoyancy Parameter
Bo_0^*	Critical Buoyancy Parameter
$cov(\cdot)$	covariance
$corr(\cdot)$	correlation coefficient
CO_2	Carbon dioxide
Cp	Thermal Capacity
D	Diameter
d	distance to the closest wall
D_h	Hydraulic Diameter
$E(f)$	power spectral density/energy spectrum of $U(t)$
$\bar{E}(f_n)$	estimated spectrum by Welch's methodology
E	sum of internal energy and kinetic energy
Gr^*	Grashof Number
$F(V)$	Cumulative distribution function
$f(V)$	probability density function
f	Frequency
$I_k(\cdot)$	periodograms of the k_{th} segments of the time signal U

I	the ration of strength of fluctuation over the mean velocity (turbulence intensity)
k	Turbulence kinetic energy
L	Characteristic Length Scale of Flow
L_s	mixing length fro subgrid scales
l	Length Scale of Eddies
l_0	length scale of largest eddies
l_{DI}	Demarcation length scale between the Dissipation Range ($l<l_{DI}$) and the Inertial Subrange ($l<l_{DI}$)
l_{EI}	demarcation length scale between the energy containing range of eddies ($l>l_{EI}$) and the small eddies ($l<l_{EI}$)
Nu	Nusselt Number
Nu_f	Nusselt Number at Forced Convection Conditions
P	Pitch, Pressure or Possibility of event A
p', T' and ρ'	fluctuating component of pressure, temperature and density.
P/D	Pitch to Diameter Ratio
Pr	Prandtl Number
$R(\cdot)$	autocorrelation
$R_{ij}(\cdot)$	cross correlation function
Re	Reynolds Number
S	strain rate
$\overline{S}$	filtered strain rate
S_M	Sources terms in momentum equations
S_E	Sources terms in energy equation
$St = fD_h/u$	Strouhal Number
$St_\tau = fD_h/u_\tau$	Strouhal Number based on u_τ
T	temperature or duration of the signal
T_b	Bulk Temperature

t time

u Characteristics Velocity

u_τ Friction Velocity

u_η Kolmogorov velocity

$\vec{U}(\vec{x}, t)$ velocity field

$U(t)$ random process

$\widetilde{U}(f)$ Fourier transform of $U(t)$

U Characteristic Velocity or the set of random variable

U_c Convection Velocity of the Flow Structures in the Narrow Gap

U_b Bulk Velocity

U_i $=(U, V, W)^T$, $(i = 1, 2, 3)$, instantaneous velocity components in Cartesian coordinates or the component of set U

u_l Characteristic Velocity of Eddies with Length Scale as l

u_i/u_i' $=(u, v, w)^T$ or $(u', v', w')^T$ $(i = 1, 2, 3)$, fluctuating velocity component or the residual part of the velocity in the large eddy simulation

$\overline{u_i}$ filtered velocity

u_0 Characteristic Velocity of Eddies with Length Scale as l_0

UO_2 Uranium dioxide

V_a a certain velocity value in the event $A = \{U < V_a\}$

V_b a certain velocity value in the event $A = \{U < V_b\}$

$var(\cdot)$ variance function

W Streamwise Velocity or Sum of Gap Width and Diameter of Rod

W_b Bulk Velocity

x_i $=(x, y, z)^T$, $(i = 1, 2, 3)$, Cartesian coordinates

Greek Symbols

δ_{ij} Kronecker delta

Δ local grid scale

ε Turbulence Dissipation Rate

θ scalar

$\overline{\theta}$ filtered scalar

ζ random velocity values

η Kolmogorov length scale

κ von Karman constant or thermal conductivity

κ_{eff} $=(Cp\ \mu_{eff}/Pr)$ effective thermal conductivity

λ wave length of the flow structures in the narrow gap or thermal conductivity

μ dynamic viscosity

μ_{eff} $=(\mu+\mu_t)$ effective viscosity

μ_{eff} sub-grid scale viscosity

μ_t eddy/turbulent viscosity

ν kinetic viscosity

ρ density

τ time scale

τ_{ij} stress tensor

τ_0 time scale of large Scales Eddies with Length Scale l_0.

Ω the set of all possible value of random velocity U

ω vorticity

Other Symbols

$\langle\cdot\rangle$ mean or Reynolds average

$\sim$ Favre-average

Acronyms

2D Two Dimensional

3D Three Dimensional

AGR Advanced Gas-Cooled Reactor

BWR Boiling Water Reactor

CF Cross Flow

CFD Computational Fluid Dynamics

CFL Courant-Friedrichs-Lewy condition or number

DNS Direct Numerical Simulations

HF Heat flux

HF_{loc} local heat flux

HF_{avg} Averaged heat flux

HIBL Horizontal Inter-Brick Leakage

HPLWR High Performance Light Water Reactor

HTC Heat Transfer Coefficient

HTD Heat Transfer Deterioration

GIF Generation IV Forum

LES Large Eddy Simulation

NS Navier-Stokes

PDF probability density function

POD principal orthogonal decomposition

PWR Pressurized Water Reactor

PHWR/CANDU Pressurized Heavy Water Reactor/Canada Deuterium Uranium Reactor

PSD Power spectral density

PSDX Power spectral density of u'

PSDZ Power spectral density of w'

RANS Reynolds-Averaged Navier-Stokes

RSM Reynolds Stresses Model

SCWR Supercritical Water-Cooled Reactor

SEM synthetic eddy method

SST Shear Stress Transport Model

TKE Turbulence kinetic energy

URANS Unsteady Reynolds-Averaged Navier-Stokes

VVER Water-Water Energetic Reactor

WALE Wall Adaptive Local-Eddy Viscosity Sub-Scale Model

Chapter 1

Introduction

1.1 Inspiration of the PhD project.

The huge amount of energy released from the nuclear fission was first visualized in a violent way --- the nuclear bomb. Inspired by providing human beings with cheap and inexhaustible energy, the first generation of the nuclear power plants was connected to the electricity grid in 1950s. Since then, the nuclear industry experiences its ups and downs.

During 1960s, nuclear power generation had been proved to be commercially viable. The boom of the nuclear industry started in early 1970s, due to the surge of oil prices after the oil crisis. By 1980, there were 253 operating nuclear power plants with 1,350,000MWe total capacity in 22 countries while additional 230 units were under construction at that time. However, this enthusiasm ended by major disasters occurred at Three Mile Island in USA in 1979, and then Chernobyl in Ukraine in 1986. The growth of the nuclear power had been hugely slowed down until we turned into the 21th century. Due to high demand of energy and the public concerns on the global warming and air pollution, the enthusiasm on the nuclear energy has been led by two fast developing countries, China and India. Many new building programs have been planed; some new builds are already in operation in these two countries. The recent disaster at Fukushima in Japan has made the policy makers in these two countries more conservative, but the tide does not change much.

After more than five decades of development, several types of the reactors have been developed. The primary function of a nuclear power plant is to transfer energy from

the nuclear fission to steam which drives the turbine. Although the designs of different types of reactors are different, they all share some common components, such as fuel, moderator, coolant, control rods, steam generator, pressure vessel and containment. There are 4 main types of the nuclear reactors are in service nowadays. They are pressurized water reactors (PWR), boiling water reactors (BWR), pressurized heavy water reactors (PHWR or CANDU) and advanced gas-cooled reactors (AGR).

In 2002, the members of the Generation IV Forum (GIF) announced six types of the new nuclear reactor concepts. They are supercritical water-cooled reactors (SCW) or High performance light water reactors (HPLWR); very high temperature gas reactors; gas-cooled fast reactors; lead-cooled fast reactors; sodium cooled fast reactors and molten salt reactors. The operating temperature of these six design are higher than most of the reactors today. So they are more thermally efficient.

After tracing back the history of the nuclear industry, it is clear that nuclear power plays a crucial part in the whole world power generation. Although, the nuclear disasters incite public concerns on the safety of operating nuclear power plant, the nuclear power is much cleaner and greener than the fossil fuel power plant. To fit the energy demands of the human society, we do not have too many choices. To enjoy the benefits brought by the nuclear energy, it is essential to make sure it is safe. In order to control the risk in the nuclear industry, a good understanding of the thermal hydraulics of the nuclear reactor is very important, especially in the aging reactors and newly proposed designs.

The design of AGR and the different fuel assemblies will be described briefly in section 1.2 to provide a full picture of the background of the study.

1.2 Advanced gas-cooled reactor (AGR) and fuel assemblies

Advanced gas-cooled reactor (AGR)

Advanced gas-cooled reactors (AGR) is the main design of reactor currently operating in the UK. Unlike other types of reactors, graphite is used as the moderator, while pressurized $CO_2$is used as the coolant (Headand Kinkead, 1972; O'Connor, 2009; Ganesan et al., 2013; He and Gotts, 2005). Eight fuel elements, each of which host a cluster of 36 fuel pins and covered by the graphite sleeves, are connected axially to form a fuel assembly. It sits in axially connected cylindrical graphite moderator bricks. Square interstitial bricks are used to connect a group of 4 cylindrical bricks, see Fig. 1.1.The main moderator bricks and interstitial bricks together with fuel elements form the fuel channels in the reactors. Normally, the reactor core contains over 300 fuel channels. The moderator bricks are connected to each other through a radial key/keyway system on the outer surface of the graphite moderator bricks.

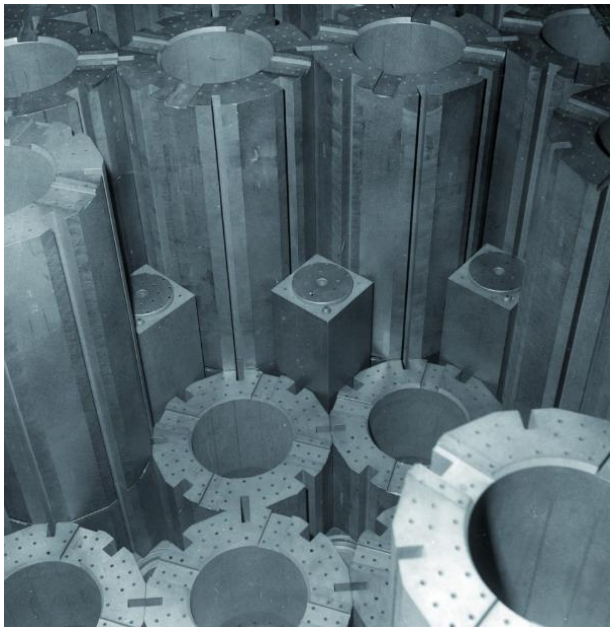

Fig.1.1 The graphite core of the Advanced Gas-Cooled Reactor (credit to the website of *Nuclear Engineering International*)

There are two types of vertical passages for cooling each moderator brick. One is the passage between the graphite sleeve and moderator brick; and the other on the outer surface of the moderator brick, bounded by the moderator bricks and connected interstitial bricks. The main cooling flow is vertically downwards through the annulus and arrowhead passages, mixed with the coolant flowing through the bottom

of the reactor core, and then, vertically up through the fuel pins. However, due to the horizontal pressure gradient in the reactor, there is a horizontal cross flow (CF) from peripheral fuel channels to inner fuel channels through the narrow gap between the outer surfaces of the moderator bricks. In addition, there is horizontal inter-brick leakage (HIBL) flow from the arrowhead passage to the annular passage, through the gaps between the vertically stacked bricks.

There are several thermal hydraulic performance issues in the reactors' operation. For instance, carbon deposition on fuel pins, stringer/brick eccentricity, and thermal radiation pessimisms and brick temperature over-prediction could occur in the advanced gas-cooled reactors (AGR), especially as they age.

Design of fuel assemblies

Usually, pellets of the uranium oxide (UO_2) are stacked in the fuel cladding tubes to form fuel rods. These rods are arranged into fuel assemblies in specific geometry configurations according to the reactor designs. Variations among fuel assembly designs for different types of reactor are considerable. In the following description, they are characterized by their geometric layout and the typical spacing among rods, which is defined by pitch-to-diameter ratio (P/D).

Square lattice arrangement of the fuel assembly is a typical design in both PWRs and BWRs, which makes it the most popular design. The standard PWR nuclear fuel assembly contains 17×17 fuel rods, while it only contains 6×6 or 10×10 fuel rods in the BWRs. The pitch diameter ratio of the fuel assembly in both types of reactor is the same (P/D=1.3). The fuel assemblies used in the Russian type of PWRs (VVER) are characterized by its hexagonal arrangement. The fuel rods in PHWRs (CANDU) and AGRs are assembled into bundles. The pitch to diameter ratio of fuel assemblies in CANDU is ~1.2, which is much smaller compared to the design of AGRs (P/D=1.7). To fit the high thermal efficiency requirement in the Generation IV nuclear reactors, the suggested fuel assembly designs are more packed in some designs. The pitch to diameter ratio of the fuel assembly in the high performance light water reactor, the European version of the SCWR, is 1.20 (Schulenberg & Starflinger,2007 & 2012). P/D in the fuel assembly design proposed by Yamaji et al.

(2005) for SCWR is 1.10. The cross section of these two concepts can be seen in Fig. 1.1.

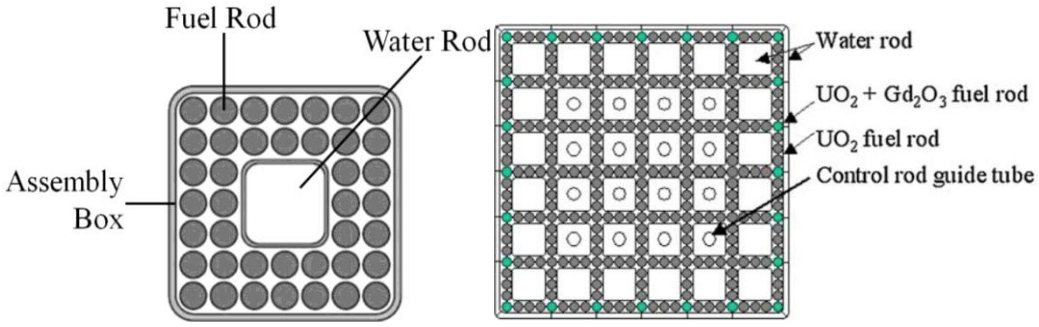

(a) (b)

Fig.1.2 Cross section of proposed fuel assemblies (a) for HPLWR by Schulenberg & Starflinger, 2012; (b) for SWR by Yamaji et al., 2005 (Credited to Yamaji et al., 2005).

The coolant flows through the subchannel formed between the rods. The adjacent subchannels are connected to each other by narrow gaps of various sizes. The existence of large flow structures in the gap between rods was experimentally detected from 1960s.The strong turbulence in the vicinity of the gap is a typical consequence. A detailed literature review is presented in Chapter 2. According to the present author's knowledge, the performance of such structures under mixed convection condition has not been investigated in the literature. It is reasonable to predict that the buoyancy effect on the large flow structures is non-negligible when the buoyancy force is strong enough. Due to non-uniform distribution of the buoyancy force in the non-uniform geometry, the flow distribution is expected to be changed.

1.3 Objective of the study

There are three main objectives of the present PhD project. The first is to investigate and further understand the cooling effect of the horizontal flow on the moderator brick in the AGRs. This research was financially supported by EDF Energy. Their subchannel code PANTHER AE does not consider the horizontal flow and it is expected that this may be an important contributing factor for the over-prediction of

brick temperature compared to the measurement in some AGR power plant by thermocouples. With the AGRs aging, a full understanding of this problem becomes important. Meanwhile, the effects of the axial variation of graphite moderator brick and the horizontal inter-brick leakage (HIBL) flow on the cooling of the moderator brick are also investigated.

The second objective is to investigate the buoyancy effect on flow instability in the gaps between the rod-bundles in the mixed convection by using large eddy simulation (LES). Instead of considering a real fuel bundle design, a simple geometry configuration had been chosen. It is a trapezoid channel enclosing a circular rod in it, which forms a flow passage with relatively narrow gaps in it. This geometry can be used to simulate the triangular arrangement of the fuel assembly. The buoyancy-aided condition is considered. The effect of the buoyancy on the heat transfer of flow in the heated non-uniform geometry is also investigated

The last objective is to investigate the flow of fluids at supercritical pressure in a tight packed rod bundle. Again the same simplified geometry configuration as mentioned above is chosen in this study. The main target is to understand the effect of the strong variation of thermal properties on the flow structures in the non-uniform (rod-bundle like)flow passage.

1.4 Outline of the thesis

This thesis is divided into two parts. The first part is dedicated to the review of relevant literature and theories (Chapter 2& 3), while the second part focuses on the presentation and discussion of the results and conclusions of the investigations (Chapter 4, 5, 6& 7). The detailed over views are listed below.

A review of the background of the studies is documented in the Chapter2, which contains the literature review on the heat transfer of rod bundles in the horizontal cross flows, followed by a review on the studies of the flow structures in tightly packed rod bundles, and ends with a brief review of the mixed convection and heat transfer to the supercritical fluid flow. A brief introduction on turbulence theory,

turbulence modelling and the software packages applied in the research is presented in Chapter 3. The results of the cooling effect of the horizontal flow study in the AGRs are reported in Chapter 4. Chapter 5 documents the results of the investigation of the flow instability in the narrow gap under the buoyancy aided convection condition. Chapter 6 presents the results of the simulation of the supercritical fluid flow in a heated rod bundle like geometry. Conclusions and some suggestions on future work are included in Chapter 7.

Chapter 2

Literature Review

This chapter begins with a review of the heat transfer in flows across a cylinder or tube banks, followed by a review on the understanding of the gap flow instability in the narrow gap of the non-uniform geometry. The theory and numerical simulation of mixed convection will be briefly summarized in the third section of this chapter which ends with a brief review on the heat transfer of supercritical fluids flow in heated channels.

2.1 Cross flows in the AGRs

The graphite brick used as the moderator in the Advanced Gas Cooled Reactors (AGR) is cylindrical in geometry as mentioned in Chapter 1. Heat is generated in the graphite brick due to neutron absorption and thermal radiation from the sleeve. The CO_2coolant which is circulated in the reactor cools not only the fuel assembly but also the moderator brick. The sub-channel code PANTHER AE is currently used to carry out thermal hydraulic analysis of AGRs by EDF Energy (Hutt, 1991).However, PANTHER AE over-predicts the brick temperature in comparison to that measured by thermocouples in some reactors. A potential reason for such discrepancies is the simplified treatment of the cross flows in the subchannel code, in which only the mass and energy imbalance due to the cross flow is considered at discrete regions of the channel, while the momentum imbalance of the cross flow is ignored. The cooling effect of the cross flow is potentially higher than the original consideration of PANTHER AE. Due to the unique design of the AGRs, the literature on the cross flow between the different moderator brick is very limited. According to the present author's best knowledge, the first work on the topic is done by Ganesan et al. (2013),

in which the AGR design of 'Torness/Heysham 2' was considered. As demonstrated in the paper, the cooling effect of the cross flow is very significant due to the strong cross flow in the key/keyway clearance and the redistributed vertical velocity.

In addition to the limited knowledge of cross flow cooling effect in the AGR reactor, much attention has been paid to the understanding of flow passing a cylinder or a tube bundle. In general, there are three types of geometries considered by the researchers: single cylinders, staggered tube bundles or inline tube bundles. Most of them devoted their efforts to investigate the cross flow induced vibration. The review of early work on this topic can be found in Weaver and Fitzpatrick (1988), while recent works can be found in Shahab Khushnood et al. (2012). Some authors studied the benefit of the cross flows on heat transfer problems. A summary of several papers on the cooling effect of cross flow is provided below.

Perkins and Leppert (1964) studied the effect of the blockage ratio on the local heat transfer of a heated cylinder to cross flow in a channel. The blockage ratio varies from 0.208 to 0.415, and the Reynolds number is from 2000 to 120000. It was shown that the heat transfer rate was enhanced with decreasing the blockage ratio, which is mainly due to the increased velocity around the cylinder. The blockage ratio mentioned here is the ratio of the rod diameter over the channel width. It was also shown that the free stream turbulence intensity had significant effect on heat transfer once its value is above 1%. A positive correlation between Reynolds number and heat transfer rate was also observed.

Lowery and Vachon (1975) experimentally investigated the effect of the free stream turbulence intensity on heat transfer to a cylinder in a cross flow. It was shown that increased turbulence intensity can either have a positive or negative effect on the overall heat transfer. The impairment of heat transfer is mainly related to the existence of the flow separation and transition. The results also revealed that even a small increase in the turbulence in the laminar boundary layer, formed at the front of the cylinder, remarkably increases the local heat transfer rate.

Aiba et al. (1982) carried out an experimental investigation to study the general effects of gap sizes on the heat transfer of heated staggered tube banks in the cross

flow. The gap size is determined by using the pitch-to-diameter ratio, which were 1.2 and 1.6. Owing to the vortex generated from the front rods, a large enhancement of heat transfer from the heated rod behind the first row was observed in the experiment. The heat transfer was improved as the Reynolds number increased. Aiba et al. (1985) studied the heat transfer around a rod close to a plane. The effects of the Reynolds number and gap size were discussed. At a high Reynolds numbers, there is a critical value for the gaps size. Before the critical point the averaged Nusselt number increases significantly as the gaps become wider. Beyond the peak, the heat transfer coefficient (HTC) of the pipe decreases quickly as gaps become bigger. The HTC remained more or less the same later on. Aiba (1990) reported an experimental study on the heat transfer of in-line tube banks near a plane. Only the heat transfer at the fourth rod was presented in the paper. The effect of the gap sizes on the overall heat transfer was found to be similar to that found in Aiba et al. (1985)

Achenbach (1989) considered the heat transfer from the staggered tube bundles in the cross flow with Reynolds number varying from 5×10^4 to 7×10^6. It was concluded that the flow and heat transfer phenomena observed for a staggered tube bundle is similar to those in a single cylinder in a cross-flow. The laminar boundary will change to turbulence once the Reynolds number is beyond a critical value, which is dependent on the roughness of the rod surface. As a result, heat transfer is improved if the Reynolds number of the flow is larger than the critical value. In the article by Achenbach (1991), an experimental study of a heated in-line tube bank in a high Reynolds number cross flow was reported. The paper focused on the flow and heat transfer mechanism around the critical Reynolds number and the effect of the roughness. It was suggested that the in-line design does not decrease the shape resistance but also increased the efficiencies of the heat transfer by reducing the entrance effect, which affect several rows in the staggered tube bundle. The better heat transfer performance of the in-line design is also demonstrated by Murray (1993).

Zdravistch et al. (1995) used the *k-ε* turbulence model to investigate the laminar/turbulent flow and heat transfer in an in-line/staggered tube bank. Only a section of the geometry was considered in the CFD model. The results show a good agreement with the experiment data, especially the Nusselt numbers. It was also

demonstrated in the paper that both standard wall function and two-layer wall function can accurately predict the trend of the heat transfer coefficient on the outer surface of the cylinder.

Wilson and Basiouny (2000) applied RANS method with the *k*-*ε* model modified by Launder and Spalding (1974) to study heat transfer of two heated in-lined/staggered rods. The effect of the pitch to diameter ratio was investigated. The overall Nusselt number of the rod decreases as the pitch to diameter ratio decreases until it reaches the value 3. The difference between the values of Nu in the tightly and loose packed bundles reduces as the Reynolds number increases.

Bouhairie and Chu (2007) numerically investigated the heat transfer of a single cylinder in a cross flow by using a two-dimensional model. They pointed out that heat transfer from a cylinder to the cross flow starts in the viscous layer, then the eddies detach from the cylinder transporting heat to the flow. As a result, the heat transfer on the back surface of the cylinder could be better than at the front stagnation point. Further, the non-uniformity of the temperature distribution was greatly increased as Reynolds number of flow was increased.

Paul et al.(2008) compared the suitability of four turbulence models (*k*-*ε* model, LRR-IP model, *k*-*ω* model & SST model) on predicting the flow cross a staggered tube bundle. All of the models were found to predict the mean velocity profile reasonably well, but the k-based models can produce a more accurate prediction on the Reynolds normal stress. It is also pointed out that k-ε model is less sensitive to the changes of the mesh compared to the *k*-*ω* model and SST model.

Bhutta et al. (2012) carried out a literature review on the utilization of CFD code on predicting flow and heat transfer in the heat exchangers. After a comparison of numerous articles, they pointed out that the *k*-*ε* type turbulence model is the most widely adopted, although its accuracy is dependent on the different cases.

Li et al. (2014) reported a numerical simulation of heat transfer from a heated tube bundle in the cross flow by using unsteady Reynolds Average method. They compared the performance of three different turbulent models: standard *k*-*ε* model,

SST k-ω model and Reynolds stress model. The results of the k-ε and RSM models agreed well on the velocity distribution and turbulent intensity with experimental work.

Summary:

Cross flow can cause non-uniformly heat transfer on the surface of a cylinder. Due to the turbulence generated by the front tubes due to flow separation, heat transfer of the rods/tubes located at the downstream of the incoming cross flow improves significantly. Also, the increased cross flow velocity around the rod/tube can enhance heat transfer, which is the main mechanism of the cross flow on cooling the graphite moderator brick as demonstrated by Ganesan et al. (2013). In addition, the RANS method is a good tool to study the heat transfer of the heat rod bundle in the cross flow, while the k-ε type model is the most widely famous turbulence model in such research.

2.2 Flow instability in the fuel bundles

The experimental studies

As the first generation of nuclear power plant was integrated in to the electricity grid in 1950s, the flow, heat and mass transfer in the rod bundles attracted scientists' attentions. People soon detected the unusual turbulent intensity distribution and high inter-channel mixing rate in the narrow gap which connects the subchannels at both sides. A strong anisotropic turbulence transport in the rod bundle was recorded. Reynolds stresses are high in the narrow gaps, and their magnitude can be enhanced by decreasing the rod-to-wall gap size. Most authors agreed that this phenomenon is related to the secondary flow before 1990s (refers to Ouma and Tavoularis,1991; Guellouz and Tavoularis, 1992).

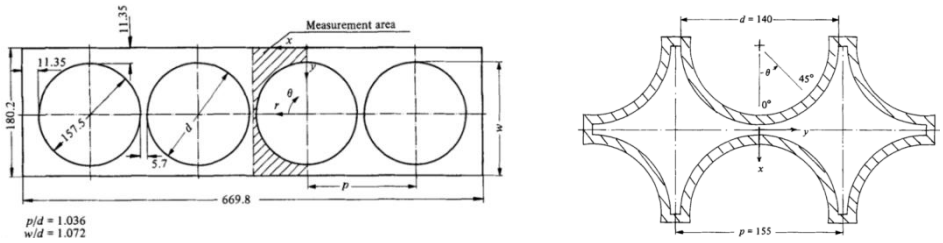

(a) (b)

Fig.2.1 The geometry scheme (credit to Hooper and Rehme, 1984) (a) four rad arrays; (b) six rods clusters.

Hooper and Rehme (1984) first linked the high axial and azimuthal turbulence intensity to the existence of the energetic and almost periodic flow structures in the vicinity of gaps formed by the rods, see Fig. 2.1. They also pointed out that the size of the flow structure is correlated to the gap width. Möller (1991 & 1992) continued to investigate the flow structures in the same channel. The flow Reynolds number ranged from $2 \times 10^4$to 1.5×10^5. A very pronounced peak was found in the power spectra density (PSD) of azimuthal turbulent velocity at the centre of the gap at a location away from the centre. However, there was no obvious peak existing in the PSD of axial turbulent velocity at the centre of gap but the peak appears at the location away from the centre. The friction velocity was chosen to evaluate the non-dimensional frequency $St = fD_h/u$ (Strouhal number), where f is the dominant frequency of the flow structures, D_h and u are the hydraulic diameter and characteristic velocity. The Strouhal number based friction velocity is nominated as St_τ in the following discussion. Möller (1991 & 1992) pointed out that this number was just related to the gap size. And, a correlation between St_τ^{-1} and *S/D* was proposed:

$$St_\tau^{-1} = \frac{0.808S}{D} + 0.056 \tag{2.1}$$

where *S* is the gap size and *D* is the diameter of the rod. He also pointed out that the structures in the narrow gap are a von Karman vortex street like structures. The scheme of the flow structures suggested by Möller (1991 & 1992) can be seen in Fig. 2.2.

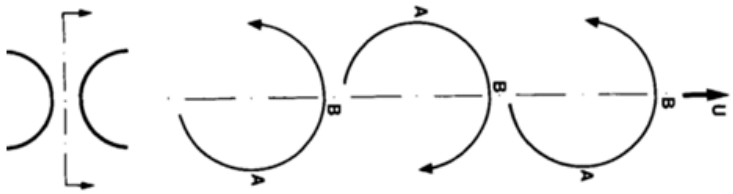

Fig.2.2 The large eddies in the gap proposed by Möller (1991).

Meyer (1994) and Krauss and Meyer (1996, 1998) reported a series of experimental investigations of fully developed flow in a heated 37-rod bundle, see Fig. 2.3, with pitch-to-diameter ratio (P/D) varying from 1.12 to 1.06 and a fixed *W/D* of 1.06. 'W' mentioned here is the sum of gap width between rod and wall and rod diameter. The existence of large structures in the gaps was determined by using the power spectra density of the turbulent velocities and the temperature fluctuation. They also suggested that the large flow structures would contribute to enhancement of the inter subchannel mass and heat exchange. A new flow model was mentioned in the article by Krauss and Meyer (1998), which is shown in Fig. 2.4. Two vortices are driven by the higher velocity outside the gap. These rotate in opposite directions, with their axes being on both sides of the gap centre. Furthermore, they found that such flow structures in the adjacent gaps were correlated with each other, which was agreed by the finding of Baratto, et al.(2006).

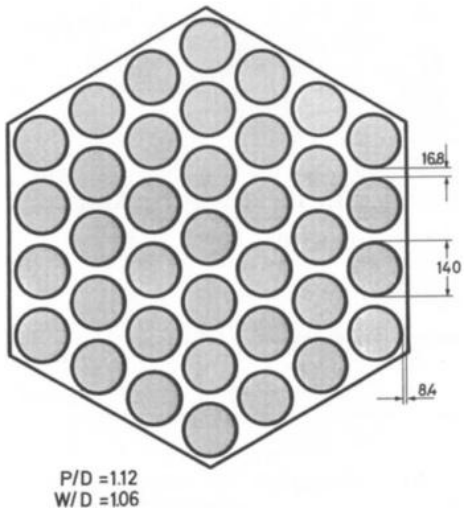

Fig.2.3 cross section of the 37 rod-bundles (credit to Meyer, 1994).

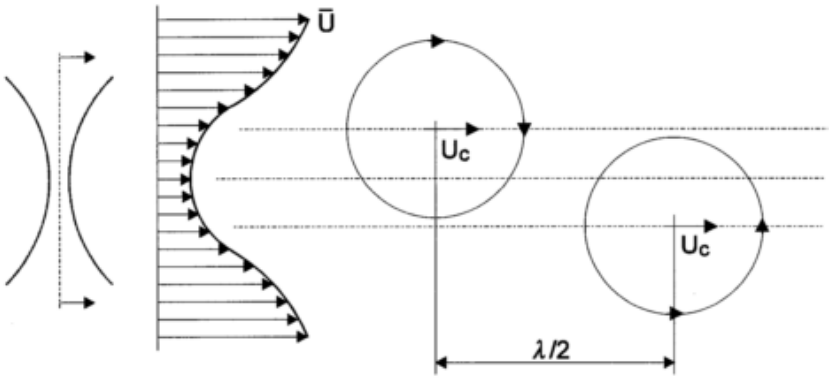

Fig.2.4 Flow model for the gap region, proposed by Krauss and Meyer (1998).

The flow instability mentioned above does not just exist in the rod bundles but also in other non-uniform geometries. Wu and Trupp (1993) experimentally proved the existence of the flow structures in a trapezoid duct with a rod irregularly mounted in it, see Fig. 2.5. St_τ that they obtained lied within 30% of the value predicted by using equation (2.1) proposed by Möller (1991 & 1992). Meyer and Rehme (1994 & 1995) looked at the flow in the channels which contains a narrow flow passage, see Fig. 2.6. The studies also show the existence of large flow structures and anisotropic performance of mass transfer in the narrow part of these simplified geometries. The size of these structures was only dependent on the size of the narrow flow passages in the channel, when the Re of flow was fixed. Furthermore, they found that the structures can be presented in the flow within a wide range of Re. Large structures existed in the geometry even in a flow with Re =2300.

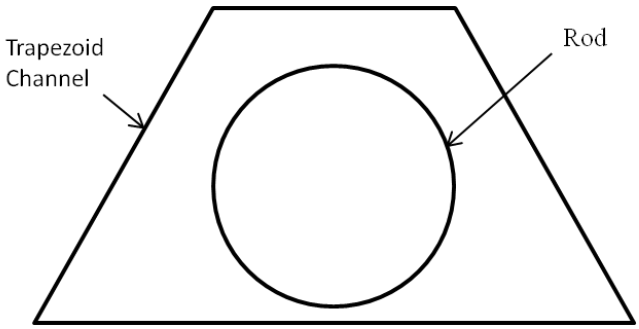

Fig.2.5 The out schematic of the channel considered in the experiments by Wu and Trupp (1993).

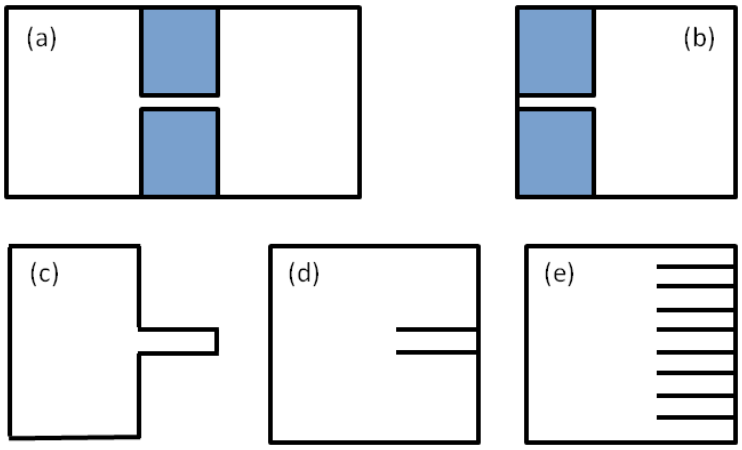

Fig.2.6 The schematic of the compound rectangular channels considered in the experiments by Meyer and Rehme (1994 & 1995), (a) two rectangular connected by a narrow gap, (b)large rectangular with a small gap (Meyer and Rehme,1994); (c)slots, (d)fins, (e)multi-fins(Meyer and Rehme, 1995).

To further understand such flow structures, Guellouz and Tavoularis (2000a & 2000b) documented their experimental results on the flow in a channel with a cylinder mounted in it, see Fig. 2.7. The ratio *W/D* varied from 1.025 to 1.35. It was mentioned in the articles that flow structures existing in the narrow gap were a kind of coherent flow structure. They claimed that mixing layer conception can be used to explain the two vortices located at both sides of narrow gap, while the von Kármán vortex theory can explain the cross-channel mixing induced by the coherent structure. They also proposed two equations (2.2) & (2.3) to evaluate the convection speed and wavelength of the structures just by using *W/D*. It should be noted that these two correlations are based on flows with very similar Reynolds numbers.

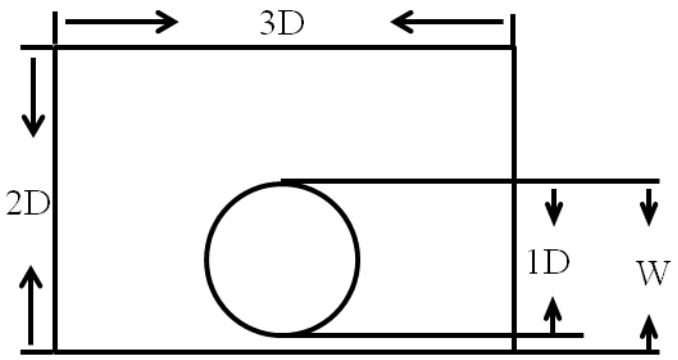

Fig.2.7 The scheme of the flow channel studied by Guellouz and Tavoularis (2000).

$$\frac{U_c}{U_b} = 1.04\left(1 - e^{-10.9\frac{W}{D}+10.6}\right)6 \tag{2.2}$$

$$\frac{\lambda}{D} = 18.7\frac{W}{D} - 16.3 \tag{2.3}$$

To investigate the valid range of Reynolds number for the existence of the flow structures, Gosset and Tavoularis (2006) experimentally explored the laminar flow with various Re in the same geometry, refer to Fig. 2.7. They found that there is a critical Reynolds number Re_c for the existence of the flow structures. As the Reynolds number increases beyond Re_c, the basic, laminar, parallel flow becomes unstable and pulsates transversely across the narrow rod-wall gap, The Strouhal number at this initial stage is named as St_c. With *Re* is further increased, *St* deceases until *Re* reaches a certain level. And, the St_c increases as the gap is widened. When the *Re* is sufficiently high, the ratio of wavelength over wave width only depends on the geometry configuration.

Poit and Tavoularis (2011) experimentally studied the fully developed laminar flow in eccentric annular channels with the similar idea of the work as Gosset and Tavoularis (2006). The diameter ratio of the eccentric annulus was 0.28 and the eccentricity *e* ranged from 0 to 0.8. They found Re_c is sensitive to the eccentricity when$0.5<e<0.8$, but insensitive to it as *e* varies from 0 to 0.5. Choueiri and Tavoularis (2014) presented their experimental investigation of development of flow structures in the eccentric annular channel with diameter ratio of 0.5 and eccentricity of 0.8, while the flow Reynolds number was 7300. Three regions (entrance region, fluctuation-growth region and rapid mixing region) were defined to describe the different stages of the development of coherent flow structure in the narrow gap. They also agreed with Krauss and Meyer (1998) on the flow model that they had proposed.

Computational fluid dynamics (CFD) studies

Thanks to the fast development of the computer power, increasingly more researchers adopt CFD method as their study tool. The first attempt to use the CFD

method to study the flow structure in the non-uniformly geometry is dated back to the early 1990s. Most of the works were done by using the RANS/URANS method. Several authors used the large eddy simulation to study the flow structures.

Initially, studies were conducted using steady RANS with various turbulence models to simulate the flow in the non-uniformly geometry. Although steady RANS with anisotropic model can predict the wall shear stress with reasonable accuracy, when pitch-to-diameter ratio (P/D) is smaller than 1.1, it cannot successfully predict the high turbulence intensity in the vicinity of narrow gap as demonstrated by In, et al. (2004), Baglietto, et al. (2005, 2006) and Chang & Tavoularis (2012). This is simply because that the steady RANS model cannot capture the large flow structures in the narrow gap.

The team led by Tavoularis, in the University of Ottawa not only used the experimental facility to investigate the coherent flow structure in the gap region, but also devoted a large amount of efforts to study the flow structures numerically. Chang and Tavoularis (2005, 2006, 2008 and 2012) conducted a series of numerical studies on the fully developed flow in the geometry similar to the channel adopted in Guellouz and Tavoularis (2000), see Fig. 2.7. It was shown in their first paper that unsteady RANS method can capture the large flow structures in the narrow gap, although, the obtained *St* was higher than the experiment measurement (refer to the value of the experiment by Guellouz and Tavoularis, 2000). Heat flux was introduced into the system in the work done in 2006. Strong oscillations in the instantaneous temperature and local Nusselt number were found in the centre of narrow gap. They also reported that the *St* of the instantaneous temperature in the centre of the narrow gap was almost double that of the spanwise instantaneous velocity. Following this work, they applied the same methodology to explore the effect of the demolishing gap size on the existing flow structures. They found that the so called coherent part of the turbulent kinetic energy and the temperature fluctuation was dramatically increased as the gap size was decreased from *0.1D* to *0.03D*, and the coherent fluctuations essentially disappeared when the gap was decreased to *0.01D*. In the meantime, the decreasing rate of Nusselt number between *0.1D* case and *0.03D* case is smaller than that between *0.03D* and *0.01D*. In their article published in 2012, they documented their results on comparing the

performance of various turbulence models and the effect of the different types of boundary conditions (including uniform inlet boundary condition and periodic boundary condition) on the simulation of gap flow instability. They pointed out that URANS can capture the large flow structure in the narrow gap, no matter which turbulence model is chosen, which was supported by Home, et al. (2009) and Merzari and Ninokata (2009). However, more accurate prediction was obtained by using LES, which was supported by Biemüller et al. (1996) and Abbasian et al.(2010). Chang and Tavoularis (2012) also claimed that the periodic boundary condition was possibly responsible for the inconsistency of the Strouhal number in their previous studies. This is because the *St* at the developing region is larger than it is in the fully developed flow region. While the periodic boundary condition can make sure the flow is fully developed, the probe can be located in the developing region in the experimental rigs.

It is worth noting that Biemüller et al. (1996) applied LES to simulate flow in two channels connected with each other by a gap. A pair of counter-rotating vortices was captured in the gap region, which is in agreement with the flow structures proposed by Krauss and Meyer (1998).

Unsteady RANS with standard Reynolds stress turbulence model was used to simulate the fully developed flow in a 60^o sector of the 37-rod bundle by Chang and Tavoularis (2007). The *St* was about twice the experimental value obtained by Baratto et al. (2006). The existence of the side and bottom walls in the experimental rig was blamed for this inconsistency. They also demonstrated that the flow structures in the narrow gaps in the rod bundle were highly correlated with each other. So the dislocation of one rod had been shown to affect the performance of the flow structure in the other locations.

A research group in Tokyo Institute of Technology is also interested in this topic. In addition to the three papers mentioned above (Baglietto. et al., 2005 & 2006 and Merzari and Ninokata, 2009), several other papers were published by this group. Merzari et al.(2008) carried out large-eddy simulation with the Samgorinsky model of the flow (Re=2690) in a simple geometry, namely two rectangular ducts connected with each other by a narrow gap, which is similar to the geometry

considered by Biemüller et al. (1996). Furthermore, the URANS with anisotropic(quadratic)/isotropic k-epsilon model was used to simulate flow in the sub-channel between 4 rods. Merzari and Ninokata (2008) numerically investigated the flow in an eccentric annular channel with different Reynolds numbers and eccentricities by using LES with a dynamic Sub-Grid Scale(SGS) model. Ninokata, Merzari, and Khakim (2009) documented DNS, LES and unsteady RANS simulations of the flow in a part of a subchannel of fuel subassemblies and eccentric annulus. All of these works confirmed a reasonably good performance of the URANS method on predicting the coherent flow structures in the narrow gap in the channel. But the LES can produce more accurate results. In the rod bundles the flow becomes more anisotropic as the P/D decreases. Merzari and Ninokata (2008) found that the coherent structures (formed by two counter rotating vortices located at either side of the narrow gap) in the narrow gap becomes less dominant as the Reynolds number increases. They also found the existence of the structures dependent on the gap size. They agreed that the founding by Gosset and Tavoularis (2006) that the observed coherent flow structure origin from the initial perturbation in the laminar flown field in the same geometry.

Ikeno and Kajishima (2010) simulated turbulent flow in rod bundles of different pitch to diameter ratio (1.43, 1.25 and 1.11) by using large eddy simulation. They still insisted the flow pulsation in the narrow gap was due to the secondary flow. The relatively short domain in their study can be one reason why they did not capture the coherent structures in the study.

Liu and Ishiwatari (2011 & 2013) applied the URANS to study the flow in the simplified geometries, such the one used in the experimental study as adopted by Guellouz and Tavoularis (2000), two tubes connected by a thin channel, and tight lattice geometry. They results showed the great improvement of the interchannel mixing due to the existence of the flow pulsation. They also pointed out that there is a developing region for the flow structure as proposed by Choueiri and Tavoularis (2014).

Summary

Generally speaking, the large flow structures have been found to exist in the gaps formed by rods in tight lattice rod bundles and similar non-uniformly channels with a narrow gap. It has been shown that such flow structures not only exist in turbulent flows but also in laminar flows. There is no doubt that this will enhance the mixing rate in the narrow gap region.

Nowadays, most researchers agree that such pulsation flow structures are coherent flow structures. The most popular flow model was proposed by Krauss and Meyer (1998). There is a vortex street formed by counter rotating vortices located at both sides of the narrow gap. However, there is still disagreement on the origin of the coherent structures. The mixing layer theory was widely accepted to explain the generation of the vortices, while the von Kármán vortex street model was used to explain the cross gap mixing.

The existence of the large flow structures and the non dimensional frequency *St* (Strouhal number) are dependent on the size of the gap, when the Reynolds number is sufficiently high. Thanks to the existence of the cross channel flow structures, the mixing between the subchannels can be higher than expected.

2.3 Mixed Convection in vertical channels

The term ‘mixed convection’ is used to describe the heat transfer phenomenon which combines the forced and natural convections. The latter is due to buoyancy force in the flow domain. It is a well known heat transfer problem exiting in many engineering applications, such as nuclear reactors and electronic heat exchangers. Petukhov and Polyakov (1988) and Jackson et al.(1989) provide very good summary of the early works from 1960s to 1980s. The recent review can be seen in the article by Jackson (2006).

As observed in many experimental studies, the effect of buoyancy force can either improve or reduce the heat transfer rate. It is dependent on the flow direction, heat transfer boundary conditions and the characteristics of flow (laminar or turbulent). In general, the mixed convection in the vertical channels can be divided into two types,

buoyancy-aided or -opposite convection. In the buoyancy-aided convection, the body direction is in the same direction as the flow, while it is the opposite in the buoyancy-opposite convection.

If the flow is laminar, the heat transfer rate is enhanced in the buoyancy-aided convection. Here the accelerated velocity by the body force in the near wall region enhances the heat transfer due to advection. The heat transfer rate is impaired in the buoyancy-opposite convection. The velocity is decreased by the body force in the vicinity of the heated surface, which impairs heat transfer.

The situation is more complicated, when the flow is turbulent. Heat transfer is improved in the buoyancy-opposite convection, because the increased shear stresses due to the buoyancy force result in more turbulence in the near-wall region, which consequently enhances the heat transfer. The situation is more complex in the buoyancy-aided case. When the heat flux is small, the flow is being laminarized by the body force. The laminarization effect becomes more remarkable when the heat flux is increased. This continues until a certain body force strength, when flow is completely laminarized. Consequently, the heat transfer is most severely impaired. When the heat flux is further increased, turbulence will be regenerated in the flow, so heat transfer recovers. All in all, the flow in the buoyancy-aided case can be divided into laminarizing regime and recovery regime depending on the effect of body force on turbulence. Both the turbulence level and heat transfer coefficient decrease with increasing heat flux in the laminarizing region, but they increase as the heat flux is increased in the recovery regime.

According to the article by Petukhov and Polyakov (1988), the buoyancy force can modify the turbulent transport either by changing the velocity profile or the velocity fluctuations (namely turbulence quantities). The former is referred to as the ‘external’ effect, while the latter is named as ‘structural’ effect. These effects had been observed in the DNS study by Kasagi and Nishimura (1997). Similarly, in the article by Cotton and Jackson (1990), the effect of the buoyancy force on the shear production of the turbulence was named as 'indirect effect', and the buoyant generation as 'direct effect'. It is also pointed out that the direct effect is negligible in comparison with the indirect effect.

Several correlations for predicting the Nusselt number under the mixed convection were proposed by the research team in the University of Manchester. In the article by Jackson and Hall (1979), they suggested a semi-empirical function to evaluate the Nusselt number of a fully developed turbulent mixed convection in a uniformly heated vertical passage:

$$\frac{Nu}{Nu_f} = \left(\left| 1 \pm 2.5 \times 10^5 Bo^* \left(\frac{Nu}{Nu_f} \right)^{-2} \right| \right)^{0.46} \tag{2.4}$$

A refined version was introduced in the PhD thesis of Rouai (1987) and also mentioned by Jackson and Hall (1987)

$$\frac{Nu}{Nu_f} = \left(\left| 1 \pm 8 \times 10^4 Bo^* \left(\frac{Nu}{Nu_f} \right)^{-2} \right| \right)^{0.46} \tag{2.5}$$

The negative sign in equations (2.4) & (2.5) is for the buoyancy-aided convection, while the positive sign is for the buoyancy-opposite convection. $Nu$and$Nu_f$are the Nusselt numbers for the mixed convection and forced convection, respectively. $B_o^*$is the buoyancy parameter to quantify the strength of buoyancy force, which is defined as:

$$Bo^* = \frac{Gr^*}{Re^{3.425} Pr^{0.8}} \tag{2.6}$$

whereRe is the Reynolds number, Pr is the Prantl number of the fluid, and Gr^* is Grashof number based on the heat flux:

$$Gr^* = \frac{g\beta D_H^4 q}{\lambda \nu^2} \tag{2.7}$$

There is a discontinuity in the relationship between $Nu$and Bo^*, for the buoyancy-aided mixed convection case in the equation (2.5), which occurs as $Bo^* \sim 3 \times 10^{-6}$. The Nu decreases with the increase of Bo^* when $Bo^* < 3 \times 10^{-6}$. However it increases monotonically when $Bo^* > 3 \times 10^{-6}$.

CFD method has now become a very useful tool in the study of flow and heat transfer phenomena. According to the review by Jackson et al.(1989), the first

attempt to use CFD method to investigate the mixed convection can be dated back early 1960s. Hsu and Smith (1961) applied mixing length turbulence model with the turbulence viscosity function for flow in the near wall region proposed by Deissler (1950) to simulate mixed convection. No heat transfer deterioration was predicted for heated ascending flow in the tube, which is inconsistent with the observations in the experiments. About ten years later, Tanaka et al (1973) applied the Reichardt's eddy diffusivity model to study the turbulent mixed convection in the vertical tube. The heat transfer they obtained was inconsistent with the observation in the experiments. Heat transfer impairment was predicted for the buoyancy-opposite case, while heat transfer was enhanced in the buoyancy-aided flow. The simple assumption adopted by Reichardt's model was blamed. In the model, turbulence viscosity is just dependent on the distance to the wall.

Walklate (1976) compared predicted heat transfer results by using several mixing length models and k-ε models with experimental results by Carr et al. (1973) in his PhD thesis. A reasonable agreement with experimental results was achieved by using a low-Reynolds-number model (proposed by Jones and Launder, 1973). The same low-Reynolds number models and the modified version by Kawamura (1984) were utilized to simulate the heated upward pipe flow by Tanaka et al. (1987). The results also show the good capability of the models on predicting the distorted velocity profile and heat transfer impairment of the buoyancy-aided mixed convection in the vertical tube.

Cotton (1987) developed a code to use the Boussinesq approximation to simulate the effect of buoyancy force while the Launder-Sharma (1974) model was utilized to model the turbulence viscosity. The paper by Cotton and Jackson (1990) showed the code was very successful on simulating some earlier experiments on the mixed convection buoyancy-aided flow in the vertical tubes, such as the experimental works done by Carr et al. (1973), Steiner(1971) and Easby (1978). Good agreement was not just achieved on the heat transfer results, but also on the velocity profile and the Reynolds stress distributions. The good performance of the Launder-Sharma model on the prediction of the heat transfer impairment in buoyancy-aided convection was also demonstrated by Behzadmehr et al. (2003).

Several researchers have also assessed the performance of turbulence models for simulations of mixed convection. In Wang et al. (2004), they compared the simulated results by using Launder-Sharma (1974) model and Chien (1982) model with their experimental data on the turbulence mixed convection in a vertical tube. They demonstrated that both Lauder-Sharma model and Chien model can reproduce some of the flow features and heat transfer in the selected experiment. And Chien model is better than the Launder-Sharma model in terms of the turbulence regeneration due to buoyancy force as the heat flux is sufficiently high in the buoyancy-aided mixed convection or turbulence enhancement in the buoyancy-opposite case.

A systematic assessment of the performance of several turbulence models on predicting the buoyancy aided flow in the heated tube was carried out by Kim et al. (2008). The DNS data by You et al. (2003) was chosen as the reference. Turbulence models assessed are due to Launder-Sharma (1974), Chien (1982), Lam-Bremhorst (1981), Abe-Kondoh-Nagano (1994), Wilcox (1988), Yang-Shih (1993), Myoung-Kasagi (1990), Hwang-Lin (1998), *V2-F* by Behnia et al (1998) and Cotton-Kirwin (1995). The results revealed that the most accurate models to predict the general trend of the buoyancy effect in the heated ascending flow are still the early ones, like Launder-Sharma (1974).However, these models over-predict the reduction of turbulence kinetic energy due to buoyancy force which makes them unable to capture turbulence recovery when the heat flux is sufficiently high. The over prediction of the reduction of k^2/ε due to the influent of buoyancy was found to be the reason.

Overall, owing to the damping function, the RANS with low-Reynolds number models can reproduce certain flow phenomena of the turbulent mixed convection in a vertical channel. However, no model can predict results accurately for all cases. There are always some parameters either over-predicted or under-estimated. This will not happen in DNS. In the meantime, the DNS method can produce much more details on the flow field than the experiments. One of the earliest DNS studies was done by Kasagi and Nishimura (1997), which was mentioned above.

In You et al. (2003), DNS was used to simulate laminar/turbulent mixed convection in a vertical channel. It revealed the buoyancy effect on the velocity profile and the turbulence quantities. They pointed out that, in the case of upward turbulent mixed convection, the structure effect dominates the near wall region, whereas the external effect is dominant in the region away from the wall, when the heat flux is small enough. The external effect is dominant if the heat flux is sufficiently high. However in the downward case these two effects are of the same order.

Although the DNS is the most accurate, its requirement on computing resources is very high. LES can be alternative choice. It can achieve a reasonable accuracy while being less expensive than DNS as demonstrated in Lee et al. (2004) and Keshmiriet et al. (2012). The dynamic SGS model introduced by Germano et al. (1991) and the SGS model due to Smagorinsky and Lily (1966) were chosen to model the SGS viscosity in those two papers, respectively.

Compared with the enormous number of papers on the mixed convection in uniform geometries, such as tube, channel, and concentric annulus, much fewer papers focused on the non-uniformly geometry, like rod bundles or eccentric annulus. Even less attention was paid to the turbulent mixed convection in a heated non-uniform geometry. According to the best knowledge of the present author, only two papers discussed such phenomenon, namely Forooghi et al. (2015) and Chauhan, et al. (2014).

Chauhan, et al. (2014) adopted the *SST-ω* model to investigate the buoyancy-aided flow in an annulus with various radial ratios and eccentricities. The most interesting finding reported in the article is that Nu increases with Re in the narrow gap, but the opposite is true in the wider gap region.

In Forooghi et al. (2015), *V2-F*model was used to investigate the turbulent buoyancy-aided flow in the concentric and eccentric annulus. The eccentricities (*e*) of the annuli are 0, 0.25 and 0.5. It was revealed that heat transfer deterioration can be moderated when the eccentricity is high. The velocity profile in an annulus with a high eccentricity was hugely distorted when the heat flux was sufficiently high. For instance, the velocity in the narrow gap can be greater than it in the big gap if the

heat flux is sufficiently high. In addition, the reduction of the turbulent kinetic energy in the narrow gap due to buoyancy force is much weaker than it in the wider part of the channel.

Summary:

Mixed convection is a common phenomenon in everyday practice. After continuous efforts devoted to the topic in the past decades, the understanding of mixed convection in a circular tube has been reasonably well established. It has been demonstrated by previous studies that the RANS method with low Reynolds number models can reproduce turbulent mixed convection to some extent, but not all of the aspects. For instance, turbulence models can not accurately predict turbulence recovery in buoyancy-aided case or the increased turbulence level in buoyancy-opposite case. To gain a more accurate understanding of the flow field and heat transfer, DNS and LES are necessary. It is also demonstrated in the previous works that the Boussinesq approximation is a useful method to model the effect of buoyancy force in mixed convection. More details regarding this will be discussed in the following chapter.

But the understanding of mixed convection in the non-uniform geometries is still limited. A part of the present study is contributed to improve the understanding of the buoyancy effect on the heated ascending flow in the rod-bundle-like geometry.

2.4 Supercritical fluids flow

A so-called supercritical fluid is a fluid at the supercritical pressure; the phase change from liquid to gas does not exist as the temperature increases. Although the phase change does not happen, the thermal properties of the fluids vary greatly around the pseudo-critical point with both pressure and temperature. The property variations of supercritical water at different pressures (24.4 MPa, 25.4MPa & 26.4 MPa) are shown in Fig. 2.8.The dramatic change of the properties can be found around the pseudo-critical temperature at each pressure. Such severe changes of the properties can significantly affect turbulence behaviour in a heated tube and channel.

Consequently, the heat transfer rate can be hugely affected by such property changes, especially around the pseudo-critical point.

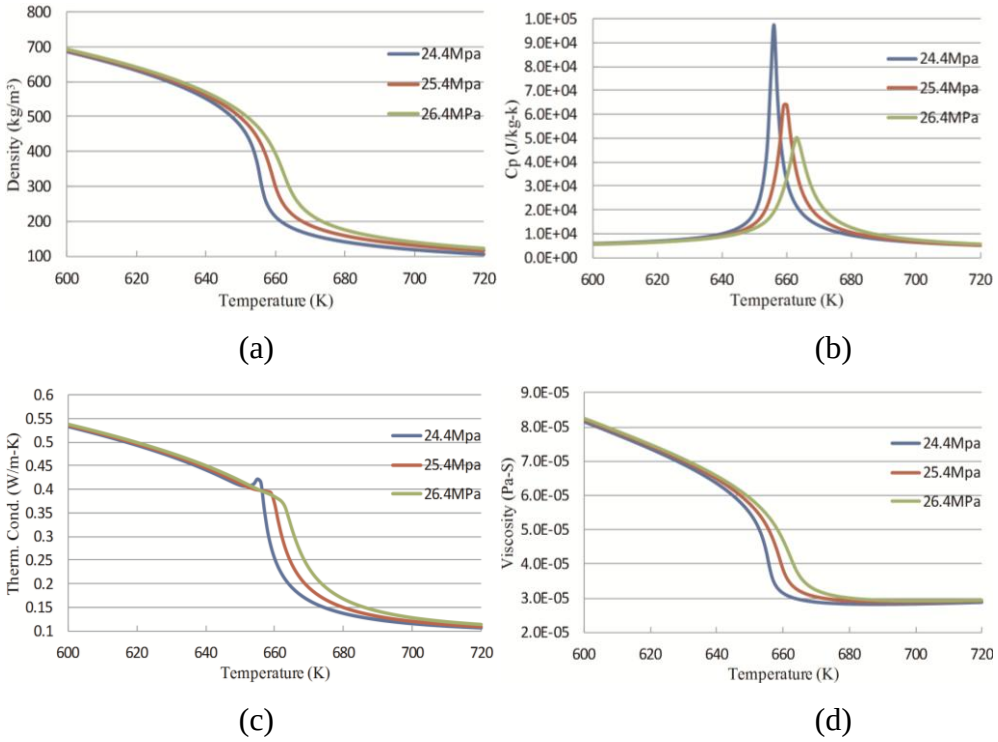

Fig.2.8 The variations of properties of water at different temperatures and pressures; (a) Density; (b) C_p; (c) Thermal conductivity; (d) Viscosity.

Since it was first discovered in 19th century, supercritical fluids have been deployed into many applications, such as oil extraction, biomass gasification, enrichment of natural tocopherols, and even cleaning (Brunner, 2010). The idea of using supercritical water (SCW) to increase the thermal efficiency of the power plant is dated back to 1950s. In the modern fossil-fired supercritical power plant, the thermal efficiency approaches 50% while the efficiency of nuclear power plant (NPP) in service is around 33~35% (Pioro et al., 2004[a,b], 2005). The SCW reactor concept was proposed as one of nuclear types for the next generation in the Generation IV international forum (GIF) for further development. The objective was to increase the thermal efficiency to 40% or even more, and make the nuclear energy more economic. To develop a reliable reactor, the understanding of the problems related to the supercritical fluid flow in the fuel assemblies is very important.

According to Pioro et al., (2004[a,b], 2005), the possibility of using supercritical water in nuclear reactors was investigated around 1960. After decades of research, many papers have been published on this topic. For example, there are 440 papers referenced in the book published by Pioro & Duffey (2007).

Most of the works published focused on the heat transfer to the supercritical fluid flow in a heated tube, which is different from the real geometric configuration of fuel assemblies in the reactor. The literature review here is focused on the supercritical fluid flow in a sub-channels-like geometry and the CFD simulations of the supercritical fluid flow, while the understanding of the supercritical fluids flow heat transfer phenomenon is very briefly discussed at the very beginning.

The heat transfer of supercritical fluid flow in a heated tube and rod bundles.

Many reviews on this topic are available. Early work can be found in Hall et al., (1967), Cheng & Schulenberg, (2001), Pioro et al., (2004[a,b]), Pioro and Duffey, 2005. More recent work is available in Kurganov et al. (2012&2013) and Yoo (2013). This section will provide a brief summary of the understanding of the SCP heat transfer.

Previous experimental data revealed that the heat transfer phenomenon in the supercritical pressured fluid flow is very complex. The heat transfer of flow under SCP can be classified into three modes (Pioro & Duffey, 2005 and Kurganov et al. 2012): 'normal', 'deteriorated' and 'improved'. A monotonic change of wall temperature can be observed in the 'normal' heat transfer mode, similar to the heat transfer far away from the pseudo critical point. A sudden heat transfer coefficient drop and the resulting sudden wall temperature increase occurs in certain part of the test section. This is referred to as heat transfer deterioration (HTD). An increased in HTC can be found in the 'improved' heat transfer mode. Heat transfer deterioration normally happens when the heat flux is high and mass flux is low. A sudden increase in wall temperature due to HTD can potentially damage the pipe or the clad of the fuel pin. Much research was devoted to understand this phenomenon. Flow acceleration and buoyancy force are important reasons that cause this to happen. Both can reduce the level of Reynolds stresses in the near wall region which leads to

the decrease of turbulent kinetic energy. As a result, heat transfer is impaired. (refer to Kurganove et al., 2012).

Numerous engineering correlations based on experimental data were proposed based on experimental data to predict the temperature distribution in the tube. Most correlations are based on Dittus-Boelter (1930), which relates Nusselt number to the Reynolds number and Prantl number. Other correlations, such as Bishop et al. (1964) and Jackson (2002), include the effect of density variations and geometry in the correlations as well. It was pointed out in the report by IAEA (2014) that the reliability of the correlations is dependent on the specific conditions. As a result, it is suggested in the report that the justification and validation of such correlations are required before they are applied to SCPW reactor design and safety analysis. Experimental data on the rod bundles are very limited. There were two early works (Dyadyakin & Popov, 1977 and Silin et al., 1993) included in the review by Duffey & Pioro (2005). Pressure oscillations were recorded in the experiments done by Dyadyakin and Popov (1977). After analysing the large database on the supercritical water flows in bundles created in Russian Scientific Centre 'Kurchatov Institute', Silin et al. (1993) claimed that the parameter range for HTD in rod bundles and tubes are different, albeit the experimental heat transfer data on the rod bundle can be reasonably predicted by a correlation obtained in the tube.

Recently, Richards et al., 2013[a,b] compared their experimental results of heat transfer of supercritical Freon R-12 flow in 7-element bundles with the correlations proposed by Bishop et al., (1964), Swenson et al. (1965), Dyadyakin et al (1977), Gorban et al. (1990), Jackson, (2002), Morkry et al. (2009), and Gupta et al. (2010). The HTD was observed to occur away from the spacer. Their main conclusion was that none of the correlations can predict the HTC number with $\pm 50\%$ of the experimental data. Wang et al. (2014) experimentally investigated the heat transfer of supercritical water flow in a heated 2×2 rod bundle. The obtained Nusselt number was compared with the results predicted using eight correlations. More details of the correlations can be found in the paper. Among them, only the correlation by Jacklson (2002) and Ornatsky (1970) can predict the Nusselt number within $\pm 25\%$ of the experimental

results. It was again demonstrated that the reliability of the existing correlations is poor under the various nuclear reactor conditions.

The effect of wrap wires on the rod was investigated in Li et al. (2009). The wire significantly improved the heat transfer in the pseudo-critical region, since the turbulence is enhanced by the wrap wire. The effect of spacers is dependent on the parameters tested as demonstrated in Richards et al., (2013[a,b]).

CFD method applied to SCP heat transfer.

Thanks to the rapid development in computer technology, computational fluids dynamics (CFD) becomes a popular and more economic tool to study the physics of turbulent convective heat transfer. The attempt of CFD to study supercritical fluid flow started with applying RANS models to flows in a tube in 1980s. Since then, much effort has devoted to find a good turbulence model to predict the heat transfer of supercritical fluids flow under various conditions with reasonable accuracy.

Many turbulence models can accurately capture the heat transfer of supercritical fluids flow in channels under the forced convection condition which was demonstrated in Dang and Hihara (2004a,b), Fard (2010), Hua et al. (2010), Lee (2010). This is because the buoyancy effect is excluded under such conditions, while the main influences on the turbulence are due to the variation of the fluids properties and thermal acceleration. Actually, many authors have proved that many the turbulence models can produce reasonably accurate heat transfer results as long as laminarization effect is small or negligible. For example, He et al. (2005) applied two low Reynolds number models to simulate the flow in a mini tube. Both models produced very similar results as laminarization effect induced by buoyancy force was insignificant. The turbulence models were also found to perform similarly in the studies of heat transfer of supercritical fluid flow in horizontal tubes, such as, Shang et al. (2008), Lee (2008), Du et al. (2010), Shang and Chen (2011), Lei et al. (2012). In these cases, the buoyancy effect was negligible. However, the performance of different models varies greatly as the laminarization effect of buoyancy force is strong. Many assessments on the performance of turbulence models have been done in the recent two decades.

Koshizuka et al. (1994) applied the Jones-Launder *k-ε* (JL) model to analyse the heat transfer deterioration in heated supercritical water flow at 24.52MPa. The Reynolds number of the flow was ~420,000 and the chosen heat fluxes on the wall were $2.33, 4.65\ and\ 9.30 \times 10^5\ w/m^2$. The obtained HTC and predicted HTD agreed well with the experimental results by Yamagata et al. (1972), only with a small under-prediction. A thicker viscous sub-layer due to increased viscosity was found to be responsible for the HTD when the mass flow rate is large; and laminarization effect due to buoyancy force is the reason for HTD when the mass flow rate is low. In the article by Lee and Howell (1998), they examined the performance of the mixing length scale model and JL model on prediction of the HTC by comparing their results to the work by Yamagata et al. (1972) and Koshizuka et al.(1994). The models can capture the trend of the HTC distribution, but the magnitude was over predicted in comparison with the experiment.

He et al.(2004 & 2008[a,b]) carried out a series of investigations to assess the performance of different low Reynolds number turbulence models on predicting the heat transfer and flow of supercritical CO_2 in a heated tube. The *k-ε* model proposed by Lauder & Sharma (LS), Chien (CH), Lam & Bremhorst (LB). Abe, Kondoh & Nagano (AKN), Myoung and Kasagi (MK) Yang & Shih and k-ω model due to Wilcox (WI), as well as V2F model by Behnia et al. (1998) were considered. To some extent, all of these models can reasonably predict the general trend of the buoyancy effect on heat transfer in the considered cases, while the performance on the prediction of the magnitude of such effect varies greatly from one to another. It was also revealed that the performance of the turbulence model is dependent on the flow conditions. For example, the V2F model is the best among the models considered in He et al. 2008[a], while AKN model significantly over-predicted the heat transfer deterioration due to a strong response to the buoyancy laminarization effect. However, the AKN is better than the V2F model under the conditions considered in He et al. (2008b). Most of the models cannot reproduce the recovery of heat transfer, even though some recovery of turbulence kinetic energy can be reproduced. It was also pointed out in the article (He et al., 2008[b]) that the effect of buoyancy on turbulence is largely dependent on the extent of the so-called large-property-variation (LPV) region, which is to describe the region around the pseudo-critical

temperature. A large turbulence reduction occurs only when the LPV region is spread to the buffer layer. The good performance of low Reynolds number models on predicting the HTD and the under-prediction on heat transfer recovery was also demonstrated in Sharabi et al. (2008a,b) and Sharabi & Ambrosini (2009). It was pointed out in the papers that the enhancement of heat transfer in supercritical fluid flow is just because of the steep increased specific heat around the pseudo critical point under the condition when buoyancy is weak.

Kao et al., 2010 compared the performance of the RNG k-ε model and a RSM model with an enhanced wall treatment on predicting the heat transfer enhancement (HTE) against the results by Yamagata et al. (1972). The predictions of the both models agreed well with the experimental results. Furthermore, the RSM model with enhanced wall treatment was also chosen to simulate the HTD observed by Shitsman (1963). The documented results show the capability of the selected model on prediction of HTD. They emphasised the importance of the treatment of turbulent Prandtl number on the prediction of HTD. Wen and Gu (2010 & 2011) showed that the performance of *SST*-k-ω model was as good as the *V2F* model. The former work considered the experimental conditions in Pis'menny et al. (2006) & Shitsman, 1963, while the experimental conditions used by Ornatskij et al. (1973) was considered in the later one. The good agreement between the numerical simulation by *SST*-k-ω model and experiment was also reported in Joromin and Anglart (2013) in which paper the experimental conditions in Shitsman (1963) and Ornatskij et al. (1973) was considered. They also agreed with the importance of turbulent Prandtl number on the predicting the HTD.

Having compared the performance of *SST* k-ω model with ABD model, LB model, LS model, YS model Abe model and V2F model in the simulation of mixed convection of supercritical water flow in annular and circular tubes, Liu et al., (2013[a,b]) claimed that SST model is most accurate under the condition of 23.5MPa, mass flux as 2200kg/m^2 and heat flux as 2410kW/m^2.

Although the RANS method can not accurately predict all of the aspects of the supercritical flow and heat transfer in heated channels, it is still a useful tool chosen by many authors who study the supercritical fluid flow in a rod-bundle-like geometry

Yang et al.(2007) assessed the accuracy of a series of turbulence models implemented in Star-CD on predicting the heat transfer of the supercritical water flow in a heated tube. Only the heat transfer enhanced case in the experimental work was considered. The numerical results were compared to the experiments done by Yamagata et al., (1972). It is shown that the *k*-ε turbulence model with a two layer wall function can predict heat transfer coefficient (HTC) more accurately. Moreover, they also investigated the supercritical fluids flow in a heated rod bundle using the same turbulence model. It was claimed in the paper that HTD would more likely to happen in the narrow gap of the subchannel, as the mass flow rate was small there. Strong non-uniformity of the circumferential distribution of the cladding surface temperature was observed in the square lattice bundle with a small pitch-to-diameter ratio (P/D). However, it does not occur in the triangular lattice bundle with a small P/D. This was also demonstrated by Cheng et al., (2007) who applied SSG-RSM model to simulate the supercritical water flow in the square and triangular fuel assembly configuration. It was also mentioned in the paper that the SSG-RSM model is better than the low Reynolds number ε-type of models in the simulation of supercritical fluid flow in rod bundles, since it can capture the anisotropic behaviour of turbulence in such geometric configuration, including the HTD. The same model was adopted by Gu et al. (2008 & 2010) for investigating supercritical water in a square and a triangular sub-channel. These two papers mainly discussed the secondary flow and turbulent mixing between the sub-channels. The effect of pitch-to-diameter ratio was studied. It should be mentioned here that the gap flow instability phenomenon, which can cause strong subchannel mixing as P/D is small, was not considered. It can be the reason why they found that the mixing due to the cross flow between the adjacent subchannels has a negative effect on the heat transfer, and enhances the non-uniformity of distribution of heat transfer and temperature on the rod surface. They also found that turbulence mixing was dependent on the pitch-to-diameter ratio, which is similar to the conclusion drawn by Zhang et al., (2011).

Shang (2009) utilized the Speziale quadratic non-linear high Reynolds number k-epsilon turbulence model with a two-layer near wall treatment proposed by (Hassid and Poreh) implement in STAR-CD to study the heat transfer of supercritical water

vertically flowing in three types of fuel assemblies arrangement, namely square, hexagon and cylinder, see Fig. 2.9. It was found that the wall temperature distribution around the rod wall in the hexagon geometry frame was more uniform than the other designs. They also found that a larger P/D would impair the heat transfer in the considered rod bundle, although it could result in a lower and more uniform wall temperature. Shang and Lo (2010 & 2011) published numerical results on the heated supercritical water flow in three horizontal fuel assemblies. The geometric configuration is the same as that mentioned above. They found that the orientation of the horizontal fuel assemblies would affect the temperature profile of the rod wall. The temperature was higher in the top half of the horizontal fuel assemblies, while the turbulence mixing would even out the temperature in certain regions.

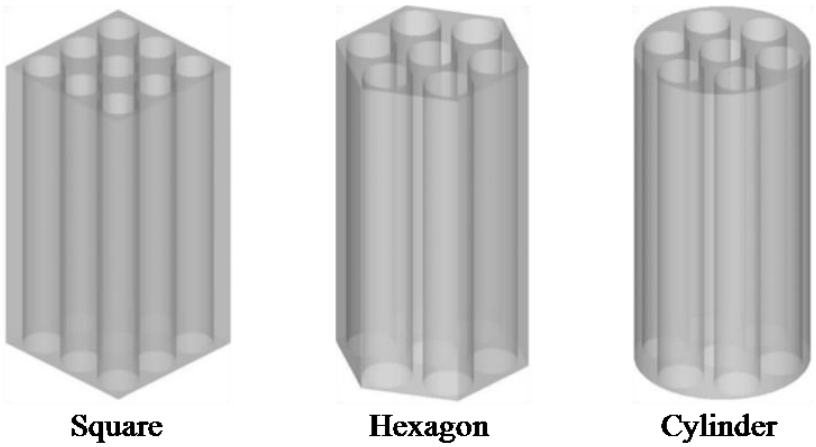

Fig.2.9 The three different fuel assembly considered by Shang (2009).

Zhang et al., (2014) numerically investigated the flow and heat transfer of a Freon R12 at supercritical pressure in a vertical 7-rod bundle subchannel. More details on the simulation are referred to the paper. They found that the heat transfer results were insensitive to the turbulence models used if the flow temperature is far away from the pseudo-critical point, while *SST-k-ω* and *ORS k-ω* model can predict the HTD near the pseudo-critical point. The HTD only occurred in the upwards flow. The buoyancy redistributed the mass flux in the geometry.

Podila and Rao (2014) numerically investigated the effect of wire wrap on the distribution of the rod temperature. The results suggest that the wire significantly

decreases the circumferential temperature difference. Podila and Rao 2015 chose *SST-k-ω* to model investigate the heat transfer in the Canadian supercritical water reactor bundle. Their results demonstrated the capability of *SST k-ω* model on capturing the HTD phenomenon.

Generally speaking, the low Reynolds number and RSM models can certainly capture some HTD induced by the buoyancy. However, there is no ultimate turbulence model that can resolve supercritical fluid flows under all conditions more accurately than others. So to further the understanding of the physic phenomenon of the supercritical fluids flow, DNS and LES have been used in some recent studies.

Bea et. Al, (2005) documented their DNS results of supercritical CO_2 flowing upwards and downwards in a tube. Instead of considering the fully compressible NS equations, the low speed incompressible NS equations were solved. It was assumed that the properties only vary with temperature not pressure. A fully developed isothermal turbulent flow was achieved by a spatially periodic non-heat domain located at the upstream of the main domain. It was revealed that positive streamwise turbulent heat flux was dominant in part of the domain, where turbulence also reduced significantly. It was pointed out that the buoyancy production term had a big impact on the Reynolds stresses and turbulence heat flux. Bae et al. (2008) focussed on the flow behaviour in the near wall region of a SCP CO_2 upwards flow in an annular passage. It was pointed out that the strong stabilizing effects of the property variation and buoyancy prevent the instability in the near wall region evolving into a self-sustained turbulence, when the pseudo critical temperature is between the wall and bulk temperature. In the meantime, a nearly flat temperature distribution and a strong radial turbulent heat flux co-existed in the viscous region due to high heat capacity of the fluid.

Kunik et al., 2010 applied the LES method to study the turbulent forced convection in a supercritical CO_2 flow. The flow was fully developed as it entered the heated part of the geometry. Three SGS models were considered, namely, Smagorinsky model, Kinetic energy SGS model and Dynamic kinetic energy SGS model. Their results showed that the best prediction was produced by the dynamic kinetic energy SGS model when the mesh was coarse. It is also suggested that DNS method is

necessary to be applied in the near wall region, in order to accurately predict the effect of property variation on the production of turbulence kinetic energy in the region

Niceno and Sharabi (2013) discussed the advantages and disadvantages of three SGS models, namely, Smagorinsky, Dynamic Smagorinsky and WALE SGS models. By considering the stability and the performance in the near wall region, the WALE model was selected. Is can damp the SGS viscosity in the near wall region which leads to a DNS simulation in the near wall region when the mesh is fine enough. (More detail on the WALE model can be found in Chapter 3) Dynamic Smagorinsky model also has this advantage but it is numerically unstable because negative SGS viscosity can be produced. A fully developed turbulent flow was generated at the isothermal part located at the front of the domain. The LES simulation has clearly shown a good performance on the prediction of the HTD and TKE. They also pointed out that the prediction of turbulence kinetic energy due to buoyancy contributed significantly to the total production in the upward flow, but it is small compared to the total production in the downward flow case.

DNS and LES can produce more accurate predictions of heat transfer and flow of supercritical fluid flow, but there are very expensive compared to the RANS method. The reliability of RANS method is dependent on the performance of turbulence models used. So it is necessary to assess the performance of different models on this topic.

Summary

After many years' development, the understanding of the heat transfer to fluids at supercritical pressure in a heated tube is well established. The heat transfer is always enhanced in the downward flow case, while the situation of the upward flow cases is more complicated. When the mass flux is low and the heat flux is high, HTD is more likely to happen. But the heat transfer can be enhanced due to the increased C_p, when the buoyancy is weak. Numerous correlations have been proposed to evaluate the wall temperature of the tube. But the knowledge of the supercritical fluid flow in rod bundles is still very limited. The correlations obtained by considering the circular

tube are not necessarily reliable on other geometries of the fuel assemblies in the nuclear reactor due to the non-uniform flow passage. Consequently, more experiments are needed.

Alternative to experiments, numerical simulations based on DNS and LES are very reliable tools to study such problems. In addition to lower cost, numerical simulations can reveal more details, especially on the flow field. Still DNS and LES studies are more likely to be carried out on the supercritical fluid flow in the round tube. According to the present author's best knowledge, no DNS or LES studies on heated supercritical fluid flow in rod-bundle-like geometry have been reported in the literature. RANS method is the common method used to investigate these problems. The accuracy of RANS is dependent on the turbulence models. Low-Reynolds number models can predict some aspect of phenomena such as HTD in an upward flow, but none of they can predict the problem quantitatively. When the detailed flow field is concerned, the predictions are even less reliable

One part of the present PhD study will be devoted to the understanding of a heated ascending supercritical water flow in a rod-bundle-like channel. . The study is focused on the large flow structures in tightly packed rod bundles and the buoyancy force is excluded. The results will be discussed in Chapter 6.

Chapter 3

Turbulence Theory, Statistical Methods and Turbulence Modelling

The theoretical background of turbulence flow, statistical tools and turbulence modelling is briefly summarized in this chapter. First of all, the turbulence theory is introduced. It starts with the characteristics of turbulent flow, followed by the concept of energy cascades, and finished by presenting some mathematic descriptions of fluid flow (Navier-Stokes equations). Secondly, the statistical tools which are used to study turbulent flow are discussed, while the turbulence modelling is included in the final section.

3.1 Brief introduction on turbulence theory

In general, fluids flows can be categorized into laminar flow and turbulent flow. Most of the flows around us are turbulent flows, e.g. a strong wind, the flow in the river, even the wind generated by funs. The turbulent flow is prevalent in industrial applications mainly due to its high mixing rate compared to laminar flow. For example, the flows in the nuclear reactor core or in the jet engine or in the pipe of oil refinery are all turbulent flows. The turbulence theory included in the section is very brief, more details can be found in several text books, for instance, Tennekes & Lumley (1972) and Pope (2000).

3.1.1 Characteristics of turbulent flow

Although the turbulent flow widely exists in the world and has been studied over a century, no one can give a precise definition of turbulence. However some common characteristics of it have been established, which are listed below.

Randomness All of the turbulent flows are random or irregular, which makes the statistical tools important in turbulence studies. However not all of the irregular flows are turbulence.

Diffusivity One of the main differences between the turbulence and laminar flow is that turbulence can result in more efficient fluids transport and mixing, which are important features concerned in many applications.

Rotational and three dimensional All of the turbulent flows contain high level of turbulent vortices. As a result, the irrotational random waves cannot be classified into turbulence.

Dissipation The kinetic energy of turbulence is dissipated by the viscous shear stress and added as internal energy to fluids. So the continuous supply of energy from the mean flow is needed to maintain the existence of the turbulence vortices.

Continuous Turbulence is a continuous phenomenon, governed by the Navier-Stokes equations **(**Tennekes & Lumley, 1972**)**

Turbulence is the characteristic of the flow Turbulence is a feature of the flow. It can be characterized by using the non-dimensionless parameter Reynolds number (Re), proposed by Osborne Reynolds (1894) and defined as $Re = UL/\nu$, where U and L is the characteristic velocity and length scale, and ν is the kinetic viscosity of the fluid. No matter what fluid it is, the dynamics of the turbulence is similar, if the Reynolds number is the same. According to the observation in Reynolds's experiment, the flow remains laminar when Re < 2300, but becomes turbulent when Re > 4000. The turbulence arises from the instability mechanism in the high Reynolds number flows, which would cause three-dimensional disturbances. The

local three dimensional disturbances would merge with each other forming a turbulence flow field (Tennekes & Lumley, 1972).

3.1.2 Energy cascade and turbulence scales;

In the turbulent flow field, large turbulence vortices break into smaller ones due to vortex stretching and finally dissipate into internal energy by viscous shear stress. This phenomenon is named as energy cascade. The idea of energy cascade was first suggested by Richardson, (1922) and later quantified by Kolmogorov (1941b).

According to Richardson's theory, the various turbulent vortices in the turbulent flow can be characterised by their length scale. For the eddies with a length scale l, its characteristic velocity can be written as u_l, and then, the time scale can be defined as $\tau = l/u_l$. The large scales vortices have the length scale l_0, which is comparable to the flow scale L, while their characteristic velocity u_0 has the same order of the r.m.s of the fluctuating velocity. So the time scale of the largest eddies can be defined as $\tau_0 = l_0/u_0$. The Reynolds number of these eddies is large, so the dissipation effect of molecular viscosity is small enough to be ignored.

However, the large eddies are unstable due to the existence of the strain field. They would break into smaller eddies with energy transfer. These smaller eddies follow the same mechanism, transferring the energy to even smaller eddies. This process continues until eddies are sufficiently small, while the molecular viscosity can effectively dissipate the kinetic energy. This means that the energy just dissipates at the end of process. The rate of dissipation ε is determined by rate of transfer of energy at the first step of the process, which can be written as

$$\varepsilon = \frac{u_0^2}{\tau_0} = \frac{u_0^3}{l_0} \tag{3.1}$$

There are some questions remaining in Richardson's theory. What is the size of eddies which molecular viscosity can effectively dissipate the energy from? What is the relations between the length scale of eddies and the characteristics velocity/time

scale? These questions were answered by Kolmogorov (1940b) in the form of three hypotheses.

Kolmogorov's hypothesis of local isotropy. The small scale turbulent motions are statistically isotropic, if the Reynolds number is high enough.

Kolmogorov's first similarity hypothesis. In every turbulent flow at sufficiently high Reynolds number, the statistics of the small-scale motions have a universal form that is uniquely determined by υ and ε. Then the so-called Kolmogorov scales can be defined as

$$\eta \equiv (\upsilon^3/\varepsilon)^{1/4} \tag{3.2}$$

$$u_\eta \equiv (\varepsilon\upsilon)^{1/4} \tag{3.3}$$

$$\tau_\eta \equiv (\upsilon/\varepsilon)^{1/2} \tag{3.4}$$

whereη, u_η and $\tau_\eta$are the length scale, characteristic velocity and time scale of smallest eddy. It is easy to conclude that the Reynolds number evaluated by the Kolmogorov scales is 1.

Combining equation (3.1) with equations (3.2) (3.3) (3.4), the relation between the scales of smallest eddy and largest ones can be written as

$$\eta/l_0 \sim Re^{-3/4} \tag{3.5}$$

$$u_\eta/u_0 \sim Re^{-1/4} \tag{3.6}$$

$$\tau_\eta/\tau_0 \sim Re^{-1/2} \tag{3.7}$$

Kolmogorov second similarity hypothesis. In every turbulent flow with sufficiently high Reynolds number, the statistics of the motion of scale of l in the range $\eta \ll l \ll l_0$ have a universal form that is uniquely determined by ε, independent of υ. The velocity scales and time scales can be formed by l and ε:

$$u_l = (\varepsilon l)^{1/3} \tag{3.8}$$

$$\tau_l = (l^2/\varepsilon)^{1/3} \tag{3.9}$$

The visualization of these different length scales is presented in Fig. 3.1. The l_{EI} and l_{DI} are defined as $l_0/6$ and 60η. l_{EI} is the demarcation between the anisotropic ($l>l_{EI}$) and isotropic eddies ($l < l_{EI}$). The eddy which satisfy $l< l_{EI}$ would fit the Kolmogorov first similarity hypothesis, and the range is named as the universal equilibrium range. The l_{DI} splits the universal equilibrium range into two subranges: the inertial subrange ($l_{DI}<l<l_{EI}$) and the dissipation range ($l<l_{DI}$). The dissipation ratio ε dominates the statistics of the motions of eddies in the inertial subrange, in the meantime, the energy of eddies are transformed into heat by the effect of molecular viscosity.

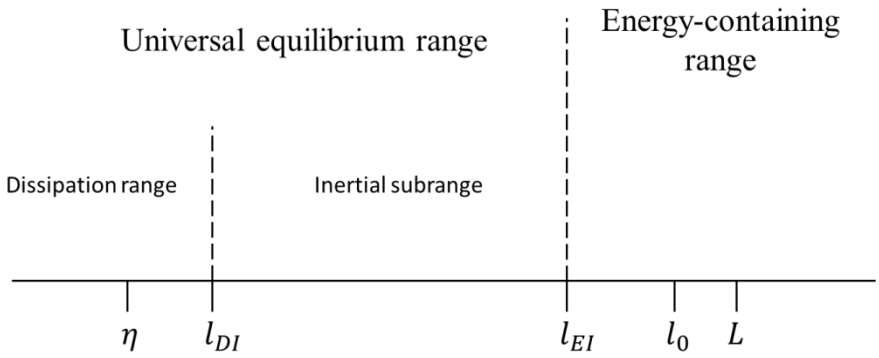

Fig.3.1 The various length scales of turbulent eddies and ranges (Pope, 2000)

3.1.3 Navier-Stokes equations;

The motion of fluids can be described by a set of equations, named after Claude-Louis Navier and George Gabriel Stokes, which are based on three basic physical principles: mass conservation, second Newton law and energy conservation. The compressible and incompressible forms of the equations are listed below.

Governing equations of compressible Newtonian fluids flow

Continuity equation:

$$\frac{\partial \rho}{\partial t} + \frac{\partial \rho U_i}{\partial x_i} = 0 \tag{3.10}$$

Momentum equations:

$$\frac{\partial \rho U_i}{\partial t} + \frac{\partial \left(\rho U_i U_j\right)}{\partial x_j} = -\frac{\partial P}{\partial x_i} + \frac{\partial \tau_{ij}}{\partial x_j} + S_M \tag{3.11}$$

Energy equation:

$$\frac{\partial (\rho E)}{\partial t} + \frac{\partial \left(\rho U_j E\right)}{\partial x_j} = -\frac{\partial P U_j}{\partial x_j} + \frac{\partial}{\partial x_j}\left(k \frac{\partial T}{\partial x_j}\right) + \frac{\partial}{\partial x_j}\left(\tau_{ij} U_i\right) + S_E \tag{3.12}$$

S_M and S_E are the body force and energy done by body force respectively. It also should be noted that *E* here represents the sum of internal energy and kinetic energy.

In the Newtonian fluid, τ_{ij} is defined as

$$\left(\tau_{ij}\right) = \mu\left[\left(\frac{\partial U_i}{\partial x_j} + \frac{\partial U_j}{\partial x_i}\right) - \frac{2}{3}\delta_{ij}\frac{\partial U_k}{\partial x_k}\right] \tag{3.13}$$

In the incompressible flow, the density is not dependent on pressure. The continuity equation can be rewritten as

$$\frac{\partial U_i}{\partial x_i} = 0 \tag{3.14}$$

Substitute equation (3.14) to (3.11), then the momentum equations can be rewritten as

$$\frac{\partial U_i}{\partial t} + U_j \frac{\partial U_i}{\partial x_j} = -\frac{1}{\rho}\frac{\partial P}{\partial x_i} + \nu \frac{\partial}{\partial x_j}\left(\frac{\partial u_i}{\partial x_j}\right) \tag{3.15}$$

where $\upsilon$is the kinematic viscosity.

And the energy equation can be rewritten as

$$\frac{\partial (T)}{\partial t} + \frac{\partial \left(U_j T\right)}{\partial x_j} = \frac{\partial}{\partial x_j}\left(\frac{\nu}{Pr}\frac{\partial T}{\partial x_j}\right) \tag{3.16}$$

where *Pr* is the Prandtl number.

No analytical solution of Navier-Stokes equations is supplied by the mathematicians. This is mainly due to the non-linear convective term and pressure gradient terms in the equations. However, these equations can be solved numerically. A brief introduction on the simulation and turbulence modelling is included in Section 3.3.

3.2 Statistical methods

As mentioned in previous sections, the ‘random’ nature is one of key features of the turbulent flow. The so called 'randomness' can be characterized in to three types -- random variables, random processes and random fields. Basically, random variables are a set of variables due to chance, and a random process is a set of time dependent random variables, whereas the random field is a set of position and time dependent variables. For example, the velocity signal at certain location in a turbulent flow is a random process, while the velocity field$\vec{U}(\vec{x},t)$ is a time dependent random field, which can be partially characterized by the statistical tools. The tools introduced here are a brief summary of those presented in Tennekes & Lumley (1972), Pope (2000), Nicolleau (2009) and the papers by Welch (1967). If more information is required, the original publications should be referred to.

3.2.1 The probability and probability density function

Considering a set of random velocity values $\zeta$and the event $A = \{U < V_a\}$, where U is the random variable and $V_a$is a certain velocity value. The probability p and the cumulative distribution function *F(V)* of *A* can be expressed as:

$$p = P(A) = P\{U < V_a\} = F(V_a) \tag{3.17}$$

where $0<p<1$.

The cumulative distribution function (CDF) *F(V)* has the following properties:

- $F \to 0$when $V \to -\infty$;
- $F \to 1$ when $V \to +\infty$;
- $F(V_a) > F(V_b)$, if $V_a > V_b$.

And, the probability density function (PDF) can be defined as the derivative of *F*:

$$f(V) = \frac{dF(V)}{dV} \tag{3.18}$$

*f(V)*has the following properties:

- Non-negative,$f(V) > 0$;
- Satisfying the normalization condition, $\int_{-\infty}^{+\infty} f\,(V)dV = 1$;
- $f(-\infty) = f(+\infty) = 0$.

Now, the probability *p* can be expressed as the interval of *f(V):*

$$p = P\{U < V_a\} = \int_{-\infty}^{V_a} f\,(V)dV \tag{3.19}$$

Then, the CDF and PDF of a random process *U(t)* can be defined as

$$F(V,t) = P\{U(t) < V\} \tag{3.20}$$

and,

$$f(V;t) = \frac{dF(V,t)}{dV} \tag{3.21}$$

3.2.2 Mean and Momentums

The mean of a data sample is evaluated as the average of the set. It can be expressed as a probability-weighted averaged of all possible value of *U*.

$$\langle U\rangle = \int_{\Omega} V\, f(V)dV \tag{3.22}$$

where*Ω*is the set of all possible values of *U*.

Particularly, the mean of the discrete velocity samples is

$$\langle U\rangle = \frac{1}{N}\sum_{i=1}^{N} U_i \tag{3.23}$$

where *N* is the total number of sample *U* and $U_i$is the components of set *U*.

The fluctuation of U is defined as

$$u = U - \langle U\rangle \tag{3.24}$$

The properties of the average operator can be explained by considering two random variables *U* and *V*, and two constant values *a* and *b*.

$$\langle a \rangle = a \tag{3.25}$$

$$\langle ab \rangle = ab \tag{3.26}$$

$$\langle aU \rangle = a\langle U \rangle \tag{3.27}$$

$$\langle U + V \rangle = \langle U \rangle + \langle V \rangle \tag{3.28}$$

The n^{th} moment of *U* is defined as the mean of the U^n,

$$\langle U^n \rangle = \int_{\Omega} V^n f(V) dV \tag{3.29}$$

Then, the n^{th} moment of turbulent velocity u can be written as

$$\langle u^n \rangle = \int_{\Omega} u^n f(V) dV = \int_{\Omega} (V - \langle U \rangle)^n f(V) dV \tag{3.30}$$

The 2^{nd} order moment of u is the variance of *U*,

$$var(U) = \int_{\Omega} u^2 f(V) dV = \int_{\Omega} (V - \langle U \rangle)^2 f(V) dV \tag{3.31}$$

The standard derivation is defined as the square root of the variance. In particular, the standard derivation of *U* in the turbulent flow is the root mean square (r.m.s) of the turbulent signal *u*, which indicates the strength of the fluctuations. Further, the turbulence intensity is defined as the ratio of the strength of fluctuation over the mean velocity.

$$\mathrm{I} = \frac{\sqrt{\langle u^2 \rangle}}{\langle U \rangle} \tag{3.32}$$

3.2.3 Correlations

The dependence of two set of random variables is measured by the covariance or correlation coefficient. The covariance is defined as the mean of the two random variables product (*U* and *V*) i.e.:

$$cov(U,V) = \langle (U - \langle U \rangle)(V - \langle V \rangle) \rangle \tag{3.33}$$

While, the correlation coefficient is defined as

$$corr(U,V) = \frac{cov\ (U,\ V)}{(var(U) * var(V))^{1/2}} \tag{3.34}$$

The velocity at one point in the turbulent flow field can be considered as three random processes $U_i(t)$ ($i = 1, 2, 3$) with $u_i(t)$ as the turbulent part. The correlation function of $U_i(t)$ with itself is named as autocorrelation, which is defined as

$$R(s) = \frac{\langle u_i(t) u_i(t+s) \rangle}{\langle (u_i)^2 \rangle}, \qquad i = 1, 2, 3 \tag{3.35}$$

It is easily to conclude that $R(0) = 1$, $|R(s)| <= 1$ and $R(-s) = R(s)$.

Now, considering one of velocity components $U(\vec{x}, t)$ at two locations $\overrightarrow{x_i}$ and $\overrightarrow{x_j}$, The correlation function of these two signals can be expressed as

$$R_{ij}(\overrightarrow{r},\ s) = \frac{\langle u(\overrightarrow{x_i}, t) u(\overrightarrow{x_j}, t+s) \rangle}{\sqrt{\langle \left(u(\overrightarrow{x_i}, t)\right)^2 \rangle} \sqrt{\langle \left(u(\overrightarrow{x_j}, t)\right)^2 \rangle}}, \vec{r} = \overrightarrow{x_i} - \overrightarrow{x_j}, i, j = 1, 2, 3 \tag{3.36}$$

when $\vec{r} = \vec{0}$, $R_{ij}(\vec{r}, s) = R(s)$.

Then the two points, one time correlation is defined as

$$R_{ij}(\vec{r}) = \frac{\langle u(\overrightarrow{x_i}, t) u(\overrightarrow{x_j}, t) \rangle}{\sqrt{\langle \left(u(\overrightarrow{x_i}, t)\right)^2 \rangle} \sqrt{\langle \left(u(\overrightarrow{x_j}, t)\right)^2 \rangle}}, \vec{r} = \overrightarrow{x_i} - \overrightarrow{x_j} \tag{3.37}$$

The velocity obtained in the real experiment or lab is discrete samples, it would be useful to introduce the discrete form of the correlations here.

Correlation of discrete-time signals

The built-in function in Matlab is used to calculate the correlation function between two discrete-time signals. The definition is as follows:

Considering the two discrete-time signals $X = \{X_0, X_1, \ldots, X_{n-1}\}$ and $Y = \{Y_0, Y_1, \ldots, Y_{n-1}\}$, the cross-correlation of X and Y is defined as

$$R_{xy}(l)\begin{cases} = \dfrac{\frac{1}{N-l}\sum_{n=0}^{N-l-1} X_{n+l}Y_n^*}{\sigma_X \sigma_Y}, l \geq 0; \\ R_{yx}^*(-l), l < 0 \end{cases} \tag{3.38}$$

where Y_n^* and R_{yx}^* is the complex conjugate of Y_n and R_{yx}. Furthermore, σ_X and σ_Y are the standard deviations of X and Y, respectively. If the signal X and Y are the same, the correlation defined by this equation is autocorrelation of X.

3.2.4 Fourier transform

Fourier series

Generally, the Fourier series is used to decompose a periodic function or periodic signal to a set of sine and cosine functions. For example, a random process $U(t)$ with period $T = 1/f$ can be decomposed as :

$$U(t) = a_0 + \sum_{n=1}^{\infty} [a_n \cos(2\pi nft) + b_n \sin(2\pi nft)] \tag{3.39}$$

or,

$$U(t) = \sum_{-\infty}^{\infty} c_n e^{2i\pi nft} \tag{3.40}$$

where a_0, a_n,b_n and c_n are defined by the following equations:

$$a_o = \frac{1}{2\pi} \int_{2\pi} U(t)dt \tag{3.41}$$

$$a_n = \frac{1}{\pi} \int_{2\pi} U(t)\cos(2\pi nft)dt \tag{3.42}$$

$$b_n = \frac{1}{\pi} \int_{2\pi} U(t)\sin(2\pi nft)dt \tag{3.43}$$

$$c_n = a_n + ib_n \tag{3.44}$$

Fourier transform

Fourier transform was developed for use with non-periodic functions.

The Fourier transform of U(t) is:

$$\tilde{U}(f) = \frac{1}{2\pi} \int_{-\infty}^{+\infty} U(t) e^{-2i\pi nft}\, dt \tag{3.45}$$

And the inverse transform is

$$U(t) = \int_{-\infty}^{+\infty} \tilde{U}(f) e^{2i\pi nft}\, df \tag{3.46}$$

3.2.5 Spectra

Generally, the power spectral density/energy spectrum of *U(t)* is the Fourier transform of its autocorrelation *R(s)*:

$$E(f) = \frac{1}{2\pi} \int_{-\infty}^{+\infty} R(t) e^{-2i\pi nft}\, dt \tag{3.47}$$

If the velocity measured along a line in the experiment or simulation, the correlation among the velocity at these points can be evaluated as *R(r).* The energy spectrum can be calculated as

$$E(\kappa) = \frac{1}{2\pi} \int_{-\infty}^{+\infty} R(r) e^{-2ikr}\, dr \tag{3.48}$$

where κ is the wavenumber and r is the spatial separation.

The spectra decomposes the functions/measured signals into waves of different frequencies/wavelengths. The value of the energy spectrum at certain frequency/wavelength is the mean energy in that particular wave (Tennekes & Lumley, 1972)).

Power spectrum density of the discrete time signal

The signals obtained from the experiments/simulations are discrete. In the current study, the energy spectrums of signals are estimated by using Welch's methodology. A brief description of the methodology is given below.

Considering the discrete equal interval time single $U = \{U_j, j = 0, 1, ..., N-1\}$. If the duration of the signal is T, then the interval is T/N. The whole signal set is split into K segments with a level of overlap and each segment contains L elements. Let $U_0 = \{U_j, j = 0, 1, ..., L-1\}$ then the following segments can be written as $U_D = \{U_{j+D}, j = 0, 1, ..., L-1\}$, $D = 0, 1, ..., K-1$. Then, a data window $W = \{W_j, j = 0, 1, ..., L-1\}$ needs to be selected, forming the sequence $U_D W$, $D = 0, 1, ..., K-1$.Finally, we can get K modified periodograms

$$I_k(f_n) = \frac{\mathrm{L}}{V}\left|\frac{1}{L}\sum_{j=0}^{L-1} U_{k-1}(j)W(j)e^{-2kijn/L}\right|^2, k = 1, 2, \ldots., K \tag{3.49}$$

where

$$f_n = \frac{n}{L}, n = 0, 1, \ldots., L/2 \tag{3.50}$$

and

$$V = \frac{1}{L}\sum_{j=0}^{L-1} W^2(j) \tag{3.51}$$

Finally, the estimated spectrum is the average of the periodograms:

$$\bar{E}(f_n) = \frac{1}{K}\sum_{k=1}^{k} I_k(f_n) \tag{3.52}$$

To convert f_n to frequency, it needs to be multiplied with sampling frequency calculated by time intervals between two adjacent data point. The power spectrum of the signals has been calculated using a built-in code in Matlab.

3.3 Turbulence Modelling and Numerical Method

The turbulent flow can be studied either by experiment or by numerical simulation. In comparison with the experimental method, the numerical simulation is generally cheaper and more efficient, but it is necessary to check the reliability of the numerical models using experimental results. The most accurate computational approach is *direct numerical simulation (DNS)*, which solves the Navier-Stokes equations directly and resolves the all the scales of turbulence. However the cost of this method is extremely high. The number of mesh elements required for resolving the three dimensional flow is proportional to $Re^{9/4}$. For example, to investigate a flow with Re=10,000, the total number of mesh element required by using DNS is in the order of 10^9, which makes this method too expensive for almost all industrial applications.

As mentioned previously, most of the turbulent kinetic energy is contained in the large scale eddies. It is reasonable to utilise a method which directly solve the large scale turbulence motions, while the influence of the small turbulent eddies is represent by using models. This methodology is named as *large eddy simulation (LES)*. The filtered NS equations, which are supposed to represent the large scale eddies, are solved with a model, which stands for the influence of small eddies. Compared with *DNS*, *LES* significantly reduces the requirement of computer resources, but it is still too costly in many engineering applications.

In engineering applications, the interest is focused on the time averaged flow properties, which can be achieved by the *Reynolds averaged Navier-Stokes (RANS)* method. In this methodology, the NS equations are time averaged, extra terms appearing in the equations, which makes the equations unclosed. Extra equation(s) is/are needed to solve the extra terms. More details on these three methods can be found in text books, such as Pope (2000) and Versteeg (2007).

The last two methods, *RANS* and *LES* are adopted in the present PhD study, which are briefly described in the following sub-sections.

3.3.1 Reynolds averaged Navier-Stokes (RANS) model

The RANS methodology is focused on the mean flow and the effects of turbulence on mean flow properties, Versteeg (2007). As mentioned in section3.2.2, the random process can be decomposed into the mean part and fluctuating part, which is referred to as the Reynolds decomposition. The instantaneous velocity U_i, pressure P and Temperature T can then be written as

$$U_i = \langle U_i \rangle + u_i \tag{3.53}$$

$$P = \langle P \rangle + p' \tag{3.54}$$

$$T = \langle T \rangle + T' \tag{3.55}$$

$$\rho = \langle \rho \rangle + \rho' \tag{3.56}$$

3.3.1.1 Reynolds averaged Navier-Stokes equations

Replacing the variables in the Navier-Stokes equations using four equations (3.53-3.56) and taking a time average yield the Reynolds Averaged Navier-Stokes equations. They can be expressed as:

$$\frac{\partial \langle U_i \rangle}{\partial x_i} = 0 \tag{3.57}$$

$$\frac{\partial \langle U_i \rangle}{\partial t} + \langle U_j \rangle \frac{\partial \langle U_i \rangle}{\partial x_j} = -\frac{1}{\rho}\frac{\partial \langle P \rangle}{\partial x_i} + \nu \frac{\partial}{\partial x_j}\left(\frac{\partial \langle U_i \rangle}{\partial x_j}\right) - \frac{\partial}{\partial x_j}\langle u_i u_j \rangle \tag{3.58}$$

$$\frac{\partial \langle T \rangle}{\partial t} + \frac{\partial \langle U_i \rangle \langle T \rangle}{\partial x_j} = \frac{\partial}{\partial x_j}\left(\frac{\nu}{Pr}\frac{\partial \langle T \rangle}{\partial x_j}\right) - \frac{\partial}{\partial x_j}\langle u_j T' \rangle \tag{3.59}$$

The newly appeared $\langle u_i u_j \rangle$ and $\langle u_j T' \rangle$ are named as the Reynolds stresses and turbulent heat flux. Additional equations are required to solve them. It should be noted that the equations shown above are for the incompressible Newtonian fluid. The compressible form can be found either in Versteeg (2007) or Fluent (2009).

3.3.1.2 Turbulent viscosity models

The Reynolds stresses terms in the Reynolds averaged Navier-Stokes equations can be determined either via a model based on turbulence viscosity

hypothesis/Boussinesq hypothesis (such as Sparlar-Allmaras model, k-ε model and k-ω model) or modelled directly (Reynolds stress model), refer to Pope (2000).

In the Boussinesq hypothesis (proposed by Bousinesq in 1877), the Reynolds stresses are proportional to the mean rate of deformation (Versteeg, 2007), namely, the mean strain rate and can be written as:

$$\langle u_i u_j \rangle = \mu_t \left(\frac{\partial \langle U_i \rangle}{\partial x_j} + \frac{\partial \langle U_j \rangle}{\partial x_i} \right) - \frac{2}{3} k \delta_{ij} \tag{3.60}$$

Sparlar-Allmaras model, *k-ε* model and *k-ω* model are based on the Boussinesq hypothesis. The main purpose of these models is to supply the value of μ_t which is used to reproduce the Reynolds Stresses in the RANS equations. In comparison with the Reynolds Stress Model, these models are relatively lower in computational cost. For instance, there are just two additional transport equations which needs to be solved in the *k-ε* model and μ_t is interpreted as the function of *k* and *ε*. However, the Reynolds Stress Model needs to solve the transport equations of six Reynolds stresses and an additional scale-determining equation.

The RNG '*k-ε*' model, proposed by Orszag et al. (1993), is a modified version of standard '*k-ε*' model by using renormalization group theory. It is similar to the standard 'k-ε' model, but including some refinements such as a higher accuracy for rapidly strained flows and swirling flows. It is used in many thermal hydraulic analyses (Liu et al., 2012; Yang et al., 2007). This model is applied to investigate the horizontal flow in the AGRs, of which results are presented in Chapter4. The following transportation equations of *k* and *ε* are solved in FLUENT (Fluent, 2009).

The transportation equation of turbulence kinetic energy, *k*

$$\frac{\partial}{\partial t}(\rho k) + \frac{\partial}{\partial x_i}(\rho k u_i) = \frac{\partial}{\partial x_j}\left(\alpha_k \mu_{eff} \frac{\partial k}{\partial x_j} \right) + \mu_t S^2 - \rho \varepsilon \tag{3.61}$$

The transportation equation of dissipation rate of turbulent kinetic energy, *ε*

$$\frac{\partial}{\partial t}(\rho\varepsilon)+\frac{\partial}{\partial x_i}(\rho\varepsilon u_i) = \frac{\partial}{\partial x_i}\left(\alpha_\varepsilon \mu_{eff}\frac{\partial \varepsilon}{\partial x_j}\right)+C_{1\varepsilon}\mu_t S^2\frac{\varepsilon}{k} - \left(C_{2\varepsilon}+\frac{C_\mu \eta^3(1-\eta/\eta_0)}{1+\beta\eta^3}\right)\rho\frac{\varepsilon^2}{k} \quad (3.62)$$

The inverse effective Prantl numbers, α_k and α_ε, are computed using the following formula:

$$\left|\frac{\alpha-1.3929}{1-1.3929}\right|^{0.6321}\left|\frac{\alpha+2.3929}{1+2.3929}\right|^{0.3679}=\frac{\mu}{\mu_{eff}} \quad (3.63)$$

And $a_k = a_\varepsilon \approx 1.393$ in the high Reynolds number flow as $\frac{\mu}{\mu_{eff}} \ll 1$, refer to Fluent (2009).

The turbulence viscosity is expressed as:

$$\mu_t = \rho C_\mu \frac{k^2}{\varepsilon} \quad (3.64)$$

And finally energy equation can be the written as:

$$\frac{\partial\langle E\rangle}{\partial t}+\frac{\partial\langle U_j\rangle\langle E\rangle}{\partial x_j}=\frac{\partial}{\partial x_j}\left(\kappa_{eff}\frac{\partial\langle T\rangle}{\partial x_j}\right)+S_E \quad (3.65)$$

where $S=\sqrt{2S_{ij}S_{ij}}$, $\eta \equiv Sk/\varepsilon$, $\eta_0 = 4.38$, $\beta = 0.012$, $C_\mu = 0.0845$, $C_{1\varepsilon} = 1.42$, $C_{2\varepsilon} = 1.68$, $\mu_{eff} = \mu + \mu_t$ and $\kappa_{eff} = C_p\mu_{eff}/Pr$.

3.3.2 Large Eddy Simulation and Sub Grid Scale (SGS) models

As discussed in the energy cascade in the turbulent flow, the three dimensional turbulent motions can be divided into large and small scale turbulent motions. Most energy is contained in the large scale turbulent motions. Instead of resolving all of the scales of turbulent motions as in direct numerical simulation (DNS), only the large scale turbulent eddies are resolved directly in the large eddy simulation (LES), while the small ones are modelled by the Sub Grid Scale (SGS) model. By introducing filtering operation, the velocity can be decomposed to a filtered part and

a sub-scale part. The filtered NS equations also include continuity, momentum and energy equations. In addition, some new terms, sub-grid stresses, show up in the momentum equations. A SGS model is required to solve these new terms. More details about LES are included in the following sections. The LES is utilized in the study of the buoyancy aided flow in the non-uniform channel (Chapter 5) and the forced convection of supercritical water flow in the heated non-uniform channel (Chapter 6).

3.3.2.1 The Filtered Navier-Stokes equations

Generally, the Filtered velocity can be defined as:

$$\overline{u_i}(x,t) = \int_D u_i\,(x',t)G(x,x')dx' \tag{3.66}$$

where '*D*' is the flow domain, and *G* is the filtering function.

The residual part of the velocity is defined as:

$$u_i'(x,t) = u_i(x,t) - \overline{u_i}(x,t) \tag{3.67}$$

So the original velocity can be decomposed as

$$u_i(x,t) = \overline{u_i}(x,t) + u_i'(x,t) \tag{3.68}$$

The form of this decomposition is similar to that of the Reynolds averaged. But the $\overline{u_i}$ is random and time dependant and the filtered $u_i^{'}$is not zero.

In commercial CFD software ANSYS FLUENT and the open source software Code_Saturne, the filtering function is

$$G(x,x') = \begin{cases} 1/V\,, x' \in v \\ 0, x' \notin v \end{cases} \tag{3.69}$$

where v is the local cell and *V* is the volume of the cell. Some brief introduction on the software is presented in section 3.4.

The filtered Navier-Stokes equations are obtained by subscribing equation(3.67) into the Navier-Stokes equations.

Continuity equations

$$\frac{\partial \rho}{\partial t} + \frac{\partial}{\partial x_i}(\rho \overline{u_i}) = 0 \tag{3.70}$$

$$\frac{\partial \rho}{\partial t} + \frac{\partial}{\partial x_i}(\rho u_i{}') = 0 \tag{3.71}$$

Momentum equations:

$$\frac{\partial}{\partial t}(\rho \overline{u_i}) + \frac{\partial}{\partial x_j}\left(\rho \overline{u_i u_j}\right) = -\frac{\partial \overline{p}}{\partial x_i} + \upsilon \frac{\partial^2 \overline{u_i}}{\partial x_j \partial x_j} - \frac{\partial \tau_{ij}}{x_j} \tag{3.72}$$

Scalar transport equation:

$$\frac{\partial \rho \overline{\theta}}{\partial t} + \frac{\partial \rho \overline{u_j}\,\overline{\theta}}{\partial x_j} = -\frac{\partial \tau_\theta}{\partial x_j} + \frac{\partial}{\partial x_j}\left(\delta_\theta \rho \frac{\partial \bar{\theta}}{\partial x_j}\right) \tag{3.73}$$

whereδ_θ is the diffusion coefficient, and τ_{ij} &τ_θ are the sub-grid stress tensor and sub-grid scalar flux, and they are defined by

$$\tau_{ij} = \rho \overline{u_i u_j} - \rho \overline{u_i}\,\overline{u_j} \tag{3.74}$$

$$\tau_\theta = \rho \overline{u_i \theta} - \rho \overline{u_i}\,\overline{\theta} \tag{3.75}$$

3.3.2.2 Sub Grid Scale (SGS) models

The sub-grid stresses due to the filtering operation are the new terms which need to be modelled. Since the smallest turbulent eddies are almost isotropic, Smagorinsky (1963) suggested that Boussinesq eddy viscosity hypothesis should be available to model the effect of the unresolved eddies on the resolved ones. The local SGS stresses can be expressed as SGS viscosityμ_{sgs} times the local rate of strain of the resolved flow, see the following equation:

$$\tau_{ij} = -\mu_{sgs}\overline{S_{ij}} + \frac{1}{3}\tau_{kk}\delta_{ij} = -\mu_{sgs}\left(\frac{\partial \overline{u_i}}{\partial x_j} + \frac{\partial \overline{u_j}}{\partial x_i}\right) + \frac{1}{3}\tau_{kk}\delta_{ij} \tag{3.76}$$

where δ_{ij} is the *Kronecker delta* and *i, j, k = 1, 2, 3*..

Several models were proposed by to evaluate μ_{sgs} in the past decades, e.g. Smagorinsky-Lilly model, dynamic models, and Wall-Adapting Local Eddy-Viscosity (WALE) Model. Only, Smagorinsky-Lilly model and WALE model are briefly introduced below.

Smagorinsky-Lilly Model

This model was firstly introduced by Smagorinsky (1963). The μ_{sgs} is interpreted by

$$\mu_{sgs} = \rho L_s^2 |\overline{S}| \tag{3.77}$$

where L_s is the mixing length for subgrid scales and $|\overline{S}|$ is the magnitude of the filtered rate of strain S_{ij}. They are defined as:

$$L_s = min(\kappa d, C_s \Delta) \tag{3.78}$$

where κ is the von Karman constant, d is the distance to the closest wall, C_s is the Smagorinsky constant and Δ is the local grid scale.

$$|\overline{S}| = \sqrt{2\overline{S_{ij} S_{ij}}} \tag{3.79}$$

It can be seen from the definition the performance of this model is highly dependent on C_S. So, C_s needs to be modified according to the different type of flows. Lily suggested a value of 0.17 for the homogeneous isotropic turbulence in the inertial sub-range. For an inhomogeneous flow a smaller value is required. Regarding to equations (3.79), the energy dissipation due to subgrid is only related to the strain rate of the resolved turbulent motions. But the energy dissipation in the domain, where local eddies override the irrotational strain, is not considered by the model. Furthermore, the μ_{sgs} exists as long as a non-zero velocity gradient exists. So the Smagrinsky model would lead to unrealistic energy dissipation in the near wall region, where all of the turbulent rotation disappears in reality.

Wall-Adapting Local Eddy-Viscosity (WALE) model

Nicoud and Ducros (1999) proposed a new subgrid viscosity model by considering the local rotational rate:

$$\mu_{sgs} = \rho L_s^2 \frac{\left(S_{ij}^d S_{ij}^d\right)^{3/2}}{\left(\overline{S_{ij} S_{ij}}\right)^{5/2} + \left(S_{ij}^d S_{ij}^d\right)^{5/4}} \tag{3.80}$$

where$L_s$and S_{ij}^d are defined as:

$$L_s = min\left(\kappa d, C_w V^{1/3}\right) \tag{3.81}$$

$$S_{ij}^d = \frac{1}{2}\left(\overline{g_{ij}}^2 + \overline{g_{ji}}^2\right) - \frac{1}{3}\delta_{ij}\overline{g_{ij}}^2, \qquad \overline{g_{ij}} = \frac{\partial \overline{u_i}}{\partial x_j} \tag{3.82}$$

where $C_w$is a constant.

As demonstrated in the article by Nicoud and Ducros (1999), the μ_{sgs} is zero in the so-called pure shear flow (e.g., $\overline{g_{ij}} = 0, if\ i \neq 1\ and\ j \neq 2$), which allows the subgrid scale (SGS) viscosity damping in the near wall region as dynamic models. Numerically, it is more stable than the dynamic model, since WALE model always generates a positive SGS viscosity, while a negative value can be generated by dynamic models.

3.3.2.3 Inlet boundary condition for the LES

Defining the inlet boundary condition for large eddy simulation is not a simple problem. Since the unsteady feature of LES, time-dependent turbulent or turbulent like motions are needed to be provided at the inlet. Tabor and Baba-Ahmadi (2010) provided a good review on methodologies developed to solve this problem. They highlighted the conditions which need to be met by the LES inlet boundary condition: (1) stochastically varying; (2) scales down to the filter size; (3) be compatible with Navier-Stokes equations; (4) having the structure of turbulence and coherent eddies across the range of spatial scales; (5) allowing the easy specification of turbulent properties; (6) being easy to implement and to adjust to new inlet condition. The following discussion is a brief summary of the work done by Tabor and Baba-Ahmadi (2010).

In general, the LES boundary condition can be classified into two kinds: synthesised turbulence methods and precursor simulation methods. The synthesised methods attempt to construct a random field at the inlet which agree with certain characteristics of turbulence by using mathematical models, while a precursor method is to generate the turbulence using an explicit simulation and feed the results at certain plane as the inlet of the main domain.

The simplest synthesised methods is adding the white noise to the mean velocity to create a random velocity at the inlet, however the white noise will quickly die out, because it does not include other key features such as the spatial and temporal coherence. To capture the coherent characteristic, the Fourier techniques are introduced to interpret the turbulence as the sum of the sine and cosine functions at the inlet of the main domain. Another method to produce turbulence like motions is using the basis functions obtained by using principal orthogonal decomposition (POD) method to reconstruct the majority information of turbulence described by the particular dataset. The most recently developed synthesised turbulence inlet method is vortex method and synthetic eddy method (SEM), which are based on the Lagrangian treatment of 2D vortices on the inlet plane while the streamwise turbulent velocity is generated by the Langevin equation. A virtual box surrounding the inlet boundary is considered in the SEM method, which can provide a coherent flow with a target mean velocity and Reynolds stresses at the inlet.

The precursor method is to generate a library of turbulent data by running a separate or precursor calculation of an equilibrium flow and introducing it to the main channel as the inlet boundary condition. The most widely used precursor method is to create a periodic domain to generate a fully developed flow in the channel/pipe. However, periodic boundary conditions cannot be applied to simulate the developing flow, such as a supercritical fluids flow in a heated channel/pipe. One of the methods to solve this problem is creating a data library by using an auxiliary computational domain then feed it as the inlet boundary of the main channel. One of the modifications of this method is to run the precursor calculation with the main simulation simultaneously. This method rescales the velocity profile from several boundary-layer thickness downstream of the inlet and feed it as the inlet at the main domain. Another modification is the so-called internal mapping, which is to copy a

downstream flow profile back to the inlet. A mechanism to drive the fluid flow in the domain with certain mass flow rate is required in the last two methods mentioned above. One method is to correct the mapped velocity by using the target mass flux.

Tabor and Baba-Ahmadi (2010) also presented an assessment of the different LES inlet methodologies. They concluded that most accurate results can be achieved using the precursor method, due to the use of the actual turbulence in this method. The synthesis method cannot create real turbulence at the inlet. It can also be the case in certain implementations of the library method if the library does not match the required inlet flow. They also suggested that internal mapping is the best way to generate turbulence inlet boundary conditions. This method is chosen to generate a fully developed inlet flow in the simulation of the forced convection of supercritical water flow in a heated non-uniform geometry (see Chapter 6).

3.3.2.4 Criteria of model performance

Since the turbulence is only partially solved in the LES, the validation of the results is necessary. There are two ways to measure the performance of the model, *a priori* and *a posteriori*. The former uses the experimental or DNS results to examine the assumptions of the model, while the latter compares the resolved flow field with experimental or DNS results. As we know the accuracy of an LES simulation is dependent on many facts, such as the grid, filter width and SGS model. Pope (2000) mentioned that a subgrid model can present bad results on the *a priori* test, but good results on *a posteriori*. Pope (2000) also suggested that a good LES should resolve at least 80% of the turbulent energy everywhere.

Geurts and Frohlich (2002) quantified the modelling turbulent energy by LES respect to DNS results using the so-called subgrid-activity parameter:

$$s = \frac{\langle \varepsilon_{sgs} \rangle}{\langle \varepsilon_{sgs} \rangle + \langle \varepsilon \rangle_{\mu}} \tag{3.83}$$

where ε_{sgs} and ε_{μ} are the energy dissipation due to the SGS viscosity and the molecular viscosity.

This parameter is based on the assumption that the turbulent kinetic energy ratio equals to the dissipations. By definition $0 \leqslant s < 1$with s = 0 corresponding to DNS results and s = 1 to LES at infinite Reynolds number. Celik et al. (2005) proposed a more simplified parameter by linking the energy dissipation to molecular and turbulent viscosities:

$$s \simeq \frac{\langle \mu_{sgs} \rangle}{\langle \mu_{sgs} \rangle + \langle \mu \rangle} \tag{3.84}$$

where$\mu_{sgs}$is the SGS viscosity and $\mu$is the molecular viscosity.

Geurts and Frohlich (2002) suggested that the error of the LES can be decomposed to the modelling error and numerical error. The magnitude of numerical error increases with the increase of $r = h/\Delta$.(h is the size of grid and $\Delta$is the width of filter.) The numerical error dominates when *r = 1.*By considering this fact, Celik et al. (2005) suggested another parameter:

$$s^* = \frac{\langle \mu_{sgs} \rangle + \langle \mu_{num} \rangle}{\langle \mu_{sgs} \rangle + \langle \mu_{num} \rangle + \langle \mu \rangle} \tag{3.85}$$

where μ_{num} is the numerical viscosity. The problem about how to evaluate the numerical viscosity had been risen up here.

It was demonstrated in Celik et al. (2005) that the criteria *s* is not sensitive to the change of grid size in the high velocity gradient flow such as mixing layer. By considering the gird resolution and the Kolmogorov length scale, they proposed another quality index for the large eddy simulation:

$$LES\_IQ_v = \frac{1}{1 + \alpha_v \left(\frac{s^*}{1-s^*}\right)^n} \tag{3.86}$$

where $\alpha_v \simeq 0.05$ and $n \simeq 0.53$. When LES_IQ_v is larger than 0.8, the LES is normally considered as good, when it is equal or above 95% the simulation can be considered as DNS. The challenge brought by this definition is to find a way to evaluate the numerical viscosity. Celik et al., 2005 proposed the following equation to evaluate it:

$$\mu_{num} = C_v h \sqrt{k_{num}} \tag{3.87}$$

where, h is the filter length and C_v is a constenat.

It was demonstrated in Celik et al., (2005) that the high Reynolds number homogeneous isotropic turbulence resolved with a sharp cut-off filter with resolution $L/\Delta \simeq 14.5$(L *is the characteristic length of turbulence, defined as* $k^{2/3}/\varepsilon$). When 80% of k is resolved together with assuming the half of unresolved k is dissipated due to the numerical dissipation, namely $k_{num}/k_{resolved} \simeq 0.125$. The μ_{num} is about 14.7 times the μ_{sgs} by considering the following relationship between μ_{sgs} and $k_{resolved}$.

The μ_{sgs} can be evaluated by using the following equations:

$$\mu_{sgs} = 1.12C_s^2\left(\frac{\Delta}{L}\right)^{4/3} L(k_{resolved})^{1/2} \tag{3.88}$$

Finally, by considering $C_s = 0.17$, $k \cong \Delta$ and C_v = 0.55, the relationship between the numerical viscosity and the SGS viscosity can be approximated as:

$$\mu_{num} = 14.7\mu_{sgs} \tag{3.89}$$

In Celik et al., (2009), numerical kinetic energyk_{num} is defined as a function of SGS kinetic energy k_{sgs} in:

$$k_{num} = C_n r^2 k_{sgs} \tag{3.90}$$

while,k_{sgs} is defined as:

$$k_{sgs} = \left(\frac{\mu_{sgs}}{C_v \Delta}\right)^2 \tag{3.91}$$

By substituting equations (3.90) and (3.91) in to (3.87), the relation between ν_{num} and ν_{sgs} can be established:

$$\frac{\mu_{sgs}}{\mu_{num}} = \sqrt{\frac{1}{C_n}}\left(\frac{\Delta}{h}\right)^2 \tag{3.92}$$

C_n is of order of 1. With $\Delta = h$, it can be concluded as:

$$\mu_{num} \approx \mu_{sgs} \tag{3.93}$$

It should be noted the relationships between μ_{sgs} and μ_{num} mentioned above are the guesses based on different assumptions. They can only be used to show the estimations not the accurate results.

3.4 A Brief introduction on the CFD software package (FLUENT and Code_Saturne)

Two CFD software packages are chosen in the research documented in the following chapters. A popular commercial CFD software, FLUENT, is adopted in the study of horizontal flows in the advanced gas-cooled reactor and the investigation of a buoyancy-aided flow in a non-uniform geometry, while Code_Saturne , an open source software developed by the EDF R&D, is utilised to simulate the forced convection of supercritical water flow in a non-uniform geometry. These two software packages are based on the finite volume method, which can use many types of cells and grid structures.

Fluent, written in C language, is currently supported by the ANSYS. It is widely used in industries such as aerospace, automotive and energy, since it includes various models which can be used to model fluid flow, heat transfer or chemical reactions in complex geometries. The software also offers some flexibility on modifying or even adding new models by using the user defined function (UDF). Fluent allows efficient execution, interactive control and flexibility between the different types of machines or operation systems such as Linux and Windows. The limitation of the software is obvious. The number of computer cores allowed in the parallel computing is based on the kinds of licenses used. For example, only 48 cores can be used in the parallel computing under the academic license. So it is not suitable to run the simulation case with a big mesh, such as the supercritical fluids case.

There is no limit on the number of cores in the parallel computing by using Code_Saturne, which is available under the GNU General Public license. The code is based on a combination of Fortran, C language and Python. It can solve the incompressible or weakly compressible flow with or without heat transfer and

turbulence. A wide range of turbulence models are included in the code, including two equation models, Reynolds stress models, large eddy simulation with Smagorinsky model, a dynamic model and the wall adapted local eddy viscosity (WALE) model, and so on. Some specialized models are also included in the code such as radioactive heat transfer, combustion and two phase flow. As FLUENT, the models can be changed or added by modifying or creating some subroutines in Code_Saturne. The code is only available in the Linux or Unix environment. Different partition libraries, which significantly affect the parallel computing coefficient, can be compiled and chosen in the Code_Saturne. More information on the performance of parallel computing with different partition libraries on the parallel computing can be found in Shang (2013).

Chapter 4

Horizontal Flows in the Advances Gas-Cooled Reactor

4.1 Introduction

As mentioned in the introduction, the Advances Gas-Cooled Reactor (AGR) is the most common design of nuclear reactors operating in the UK. It normally contains over three hundreds fuel channels in the reactor core. Each fuel channel is made of eight vertically connected fuel elements surrounded by vertically connected graphite moderator bricks. Each of the fuel elements contain a cluster of 36 fuel pins, covered by the graphite sleeve. On the outer surface of the sleeve, there are rectangular ribs, with a height of 0.51 to 0.76mm and a width of 0.38 to 0.64mm. The rib-to-rib distance varies from 4.70 to 5.08mm. The purpose of the ribs is to reduce charge/discharge vibrational activity from the high gas flows during on-load refuelling. The moderator bricks of each fuel channel are connected with those of neighbouring channels through the radial key/keyway system located on the outer surface of the bricks, see Fig. 4.1. The square graphite which sits in the middle of four fuel channels is named as the interstitial brick, while the smaller graphite brick sitting between two moderator bricks is referred to as the loose bearing key. The detailed horizontal arrangement of the fuel channels can be seen in Fig. 4.1.

The fast neutrons released from the fission reaction are slowed down by the graphite moderate brick. As a result, some energy deposits in the moderator bricks, which leads to a temperature rise. As illustrated in Fig. 4.1, there are two flow passages in the core region to cool the heated bricks. The one bounded by the moderator brick

and interstitial brick is named as the arrowhead passage (AP). The other is the annular flow passage (Ann) between the graphite sleeve and the moderator brick.

The configuration is such that the main cooling flow is vertically down through Ann and AP, mixed with the coolant flowing through the bottom of the reactor core, and then, vertically up through the fuel pins. However, due to the horizontal pressure gradient in the reactor, there is a horizontal cross flow (CF) from peripheral fuel channels to inner fuel channels through the narrow gap between the outer surfaces of the moderator bricks. Such flow is referred to as the cross flow. In the meantime, there is a leakage of flow from AP to Ann through the gaps between two axially connected moderator bricks which is named as horizontal inter-brick leakage (HIBL) flow. These two types of horizontal flows become stronger over the life time of the reactor since the graphite will lose weight and shrink in the reactor core as the reactor ages, which results in bigger gaps between the moderator bricks.

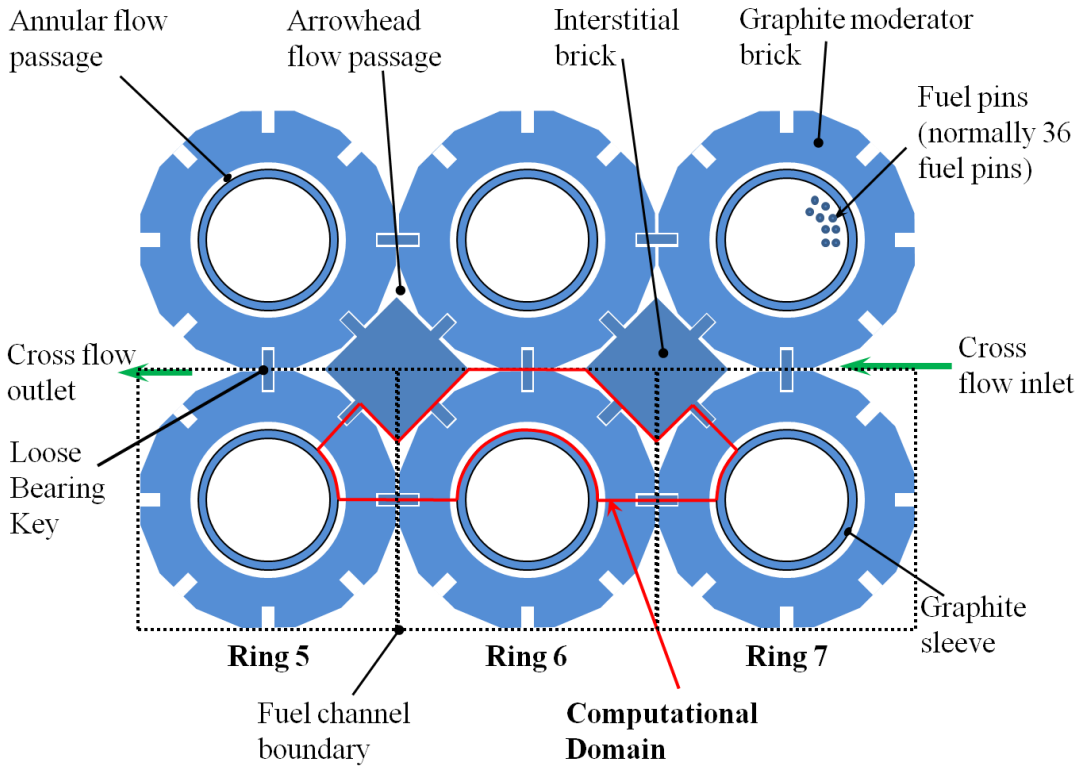

Fig.4.1Top view of the fuel channels in the AGR reactors.

The temperature of the coolant and graphite in the core is predicted by using the sub-channel code PANTHER AE at EDF Energy. The time to calculate the temperature

of all fuel channels (~330) in the core region is just about several seconds. It is known that the prediction of the moderator brick temperature using PANTHER AE is higher than the measurement by the thermocouples in some of the reactors, such as Torness/Heysham 1&2/Hartlepool. The simplified treatment of the cross flow across fuel channels is thought to be responsible for this over-prediction. Ganesan et al. (2013) demonstrated that this is true for moderator brick design adopted in the Torness/Heysham 2 reactor. The geometric configuration of the moderator brick in Hartlepool/Heyshame 1 reactor is much more complex than in Torness/Heysham 2. Furthermore, the horizontal inter-brick leakage (HIBL) flow was ignored in Ganesan et al. (2013), since it is very small in the reactors considered there. However, this is not the cases for Harlepool/Heysham 1 reactors. The main purpose of this study is to investigate the effect of cross flow on cooling in the more complex moderator brick geometry encountered in some AGRs to further our understanding of such phenomenon, and to analyze the impact of HIBL flow on the cooling of the moderator brick in the AGRs. The geometry of the moderator brick and cooling passages in this study is based on those in the Hartlepool/ Heysham1 AGR power stations.

4.2 Methodology

4.2.1 Geometry considered

A fuel channel located at the half radius of the reactor core (Ring 6 shown in Fig. 4.1) is chosen to be the central channel for the simulations. Ring 6 and 1/8 of its two neighbouring channels (Ring 7 and Ring 5) with the arrowhead and annular flow passages attached to them formed the computational domain, which is outlined in Fig. 4.1.

The geometry of the moderator brick considered in this study is based on the moderator brick in the Hartlepool/Haysham 1 (HAR/HEY1) reactor, which has two main differences compared to the bricks used in Torness station (considered by Ganesan et al., 2013). Firstly, the keyways in HAR/HEY 1are much shorter than those at the Torness station. In the meantime, the cross flow through the clearance between key/keyways is negligible, because the clearance is much smaller in

HAR/HEY 1. Secondly, there is a large cut-out located at the bottom of each moderator brick, which allows a large cross flow through it.

The geometry of the moderator brick is simplified in the CFD simulations, see Fig. 4.2. The keys are located at the top of the brick. Since the size of the key/keyway clearance can be ignored, the keys are attached to the brick with no gaps. So the moderator brick is directly connected to the interstitial brick and other moderator bricks through the keys located at the top. The cut-out is faithfully represented in the CFD model. The region with the keys is named as ‘blocked region’ in the following discussions. The cross section of the flow passage at this level can be seen in Fig. 4.2 I. The arrowhead flow passage for most of the moderator brick height consists of the main arrowhead flow passages (the central wider channel) connected by the narrow gaps, as illustrated in Fig. 4.2 II. The flow passage at the cut-out part is much bigger than at other levels, see Fig. 4.2 III.

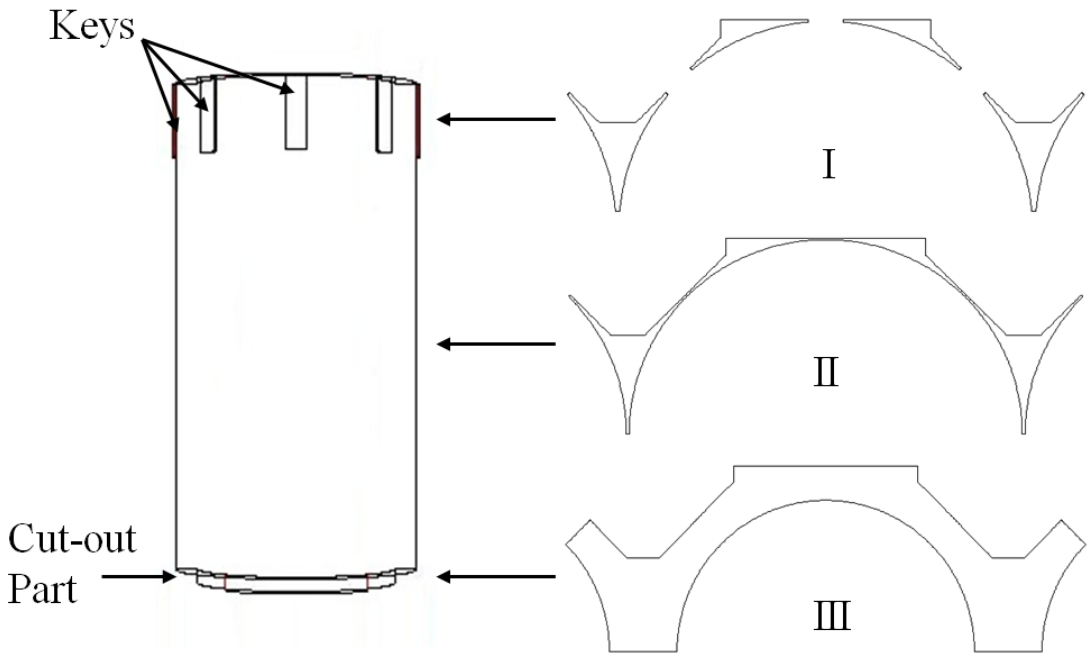

Fig.4.2 The overview of the moderator brick’s geometry and the shapes of the arrowhead flow passage (AP) at different level in each layer in the CFD model; 'I' indicates the AP at key/keyway blocked region, while 'II' and 'III' stand for AP without blockage and AP at Cut-Out part respectively.

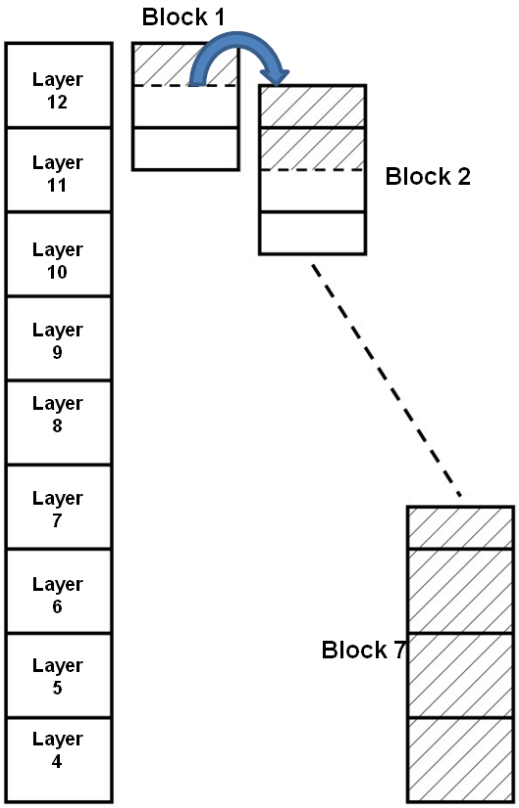

Fig.4.3 The schematic diagram of the methodology.

The total length of the considered fuel channel is 8.2768m, which covers eight fuel elements, sitting in axially connected moderator bricks. One moderator brick together with the attached flow passages (AP & Ann) form one brick layer of the domain. The requirement on the computer resource for the whole fuel channel is more than ten times the model used in Ganesan et al. 2013. This is because more mesh elements are required for each layer of the domain due to the axial variation of the moderator brick geometry. As a result, simulating the entire fuel channel just in one model becomes impractical unless a coarse mesh is adopted, but then the accuracy of the simulation will suffer. Since the flow in the channel is predominately one directional and the influence of the downstream flow on the upstream flow is limited, it is reasonable to develop a methodology to simulate the whole domain by considering each layer separately. A general schematic diagram of the methodology is illustrated in Fig. 4.3. The modelling starts from the top brick of the fuel channel and moves downwards to the lower ones, with the result obtained from the middle of the upper layer passed to the lower layer as the inlet boundary conditions. To reduce the end effect, the model of each layer also contains a half of the neighbouring layers,

so each model contains two layers, except for the 1st layer (1.5 layers) and bottom three layers (3.5 layers), see the arrangement shown in Fig. 4.3. The model of each layer is named as a block in the following discussion. For instance, Block 2 contains ½ layer 12 + layer 11 + ½ layer 10, as illustrated in Fig. 4.3. Severn blocks have been created to model the entire fuel channel. Because the flow at the bottom 3 layer regions is found to be unsteady in some of the simulations and the transfer of the boundary condition from block to block of unsteady model is inaccurate, it is necessary to combine the last 3 layers in the fuel channel together as one block.

4.2.2 Mathematical models

The three dimensional flow and heat transfer in the arrowhead and annular flow passages are simulated by using the incompressible Reynolds Average Navier-Stokes (RANS) methodology and the energy equation. The latter is also solved for the conduction through the moderator brick. Since the flow is found to be unsteady in Block 7 in one of the simulations, the unsteady RANS methodology is used in this particular block. Meanwhile, the effect of buoyancy is deemed negligible on assessing the cross flow effect on the cooling of the moderator brick. Hence, the body force is not taken into consideration in this study. As it had been approved by Ganesan et al. (2013), the performance of standard k-ε model is good at predicting the cooling effect of cross flow. A k-ε type model is also chosen as the turbulence mode in the stud. Considering the complexity of moderator brick geometry (the blocks and cut-out part on the moderator brick), a modified k-ε model, the RNG k-ε modelby Orszag et al. (1993), is utilized to simulate the effect of the turbulence on the main flow. This type of k-ε model contains some refinement on predicting stained flows and swirling flows (Ansys Fluent 12.0 theory guide, 2009), which makes the model more suitable for modelling the flow in complex geometry compared to the standard k-ε model. The near wall region flow is represented using the standard wall function.

The energy transferred by radiation in the annular passage is modelled by using the discrete transfer radiation model (DTRM). The model solves the radiation transfer equation (RTE) for some representative rays fired from the domain boundaries. The

model is based on the assumption that the radiation leaving the surface element in a certain range of the angles can be approximated by a single ray. The main advantage of this model is that the accuracy can be improved by increasing the mesh element, but it cannot be used in the parallel computing. More details about this radiation model can be found in the theory guide supplied by Ansys (Ansys Fluent 12.0 theory guide, 2009). The emissivity value at both sleeve outer surface and moderator brick inner surface is set as 0.76, which is consistent with the value adopted by PANTHER AE code.

The effect of the ribs on the sleeves is modelled by using the Fluent rough wall boundary conditions. Two parameters required are the roughness height (sand-equivalent) and the roughness constant, which are set as 1 mm and 1 respectively.

4.2.3 Simulation models

In the reactor, there is a net increase of mass flow in the flow passage down the fuel channel Ring 6 due to cross flow, since the mass flow rate of the incoming cross flow from Ring 7 is greater than the outgoing flow to Ring 5. To evaluate the cooling effect of the cross flow on the moderator brick, two sets of models have been created. One is the 'No Cross Flow', referred to as the NoCF model later. The other one is 'Cross Flow' (CF) model. The difference between these two types of models lie in the method used to treat the cross flow. Instead of directly modelling the cross flow, only the imbalance of the mass and energy associated with the cross flow are modelled by using the source terms in the NoCF model, which is to represent the method used in PANTHER AE. The energy added associated with cross flow sink is evaluated by $E_{cf} = C_p M_{cf} (T_{cf} - T_{ref})$. Here, C_p is the heat capacity of the coolant at temperature T_{cf}, while M_{cf} stands for the change of the mass flow rate due to the cross flow. T_{ref} is set as 298.15K. It should be noted T_{cf} is obtained by PANTHER AE. The mass and energy sink due to cross flow are 'injected' at two discrete regions in the arrowhead passage, which is similar to the arrangement in the PANTHER AE. The regions and the magnitude of the mass sink are illustrated in Fig. 4.4. The cross flow is truthfully represented in the CF model, uniformly inlet and outlet velocity are set at the right and left side of the computing domain, respectively. The cooling

effect of the cross flow is evaluated by using the temperature obtained in 'NoCF' model minus that in 'CF' model. More details about the settings of models are listed below.

4.2.4 Input data and boundary conditions

The inlet boundary conditions (including velocity, turbulence and temperature distributions) at the top of each block except block 1 are obtained from the results of upper block. The inlet boundary conditions of Block 1 are formulated from the results obtained by using PANTER AE. A mass flow rate of 2.116kg/s with a temperature of 560.5K is set at the inlet of the arrowhead passage of Block 1, while the mass flow rate and temperature for the inlet of annular flow passage are 2.123 m/s (counted as 0.8586 kg/s) and 582.2K, respectively. In the meantime, the turbulence intensity is set to be 10% at both the arrowhead and annular flow passage inlets, but the hydraulic diameters are set as 0.022m and 0.03m, respectively. Zero pressure is set at the outlet of the arrowhead and annular flow passage in each block. The adiabatic boundary condition is set at the top of the moderator brick in Block 1 and the bottom of brick in each block.

Furthermore, the mass flow rate loss due to the so called horizontal inter-brick leakage (HIBL) flow in the AP is significant in the HAR/HEY 1 reactor design concerned herein. The total mass flow rate loses from the AP to the Ann in the CFD model is 1.1397kg/s which is obtained from PANTHER AE output. It means that the mass flow rate at the bottom of the fuel channel is just ~50% of that at the inlet, when the added mass flow rate due to cross flow is not considered.The mass and energy imbalance related to the HIBL flow is modelled by using the sink and source terms respectively at several axial heights. The same method used to model energy change associated with cross flow is applied here. In other words, some of the mass flow rate and the associated energy are removed from the AP, which is then injected into Ann by using the source terms in the continuity equation and energy equation. This is achieved by using the 'User-Defined Function' (UDF) in Fluent. The magnitudes of the mass imbalance due to the HIBL flow at different levels are plotted inFig. 4.4. To make the model more consistent with the arrangement in

PANTHER AE, the axial levels of the mass imbalance associated with the cross flow in NoCF model and HIBL flow are made the same as those used in PANTEHR AE, even though these deviate from the real situation. For example, HIBL is introduced at the interfaces of the Heat Transfer Meshes in PANTHER. The CFD model uses these same locations, but instead of adding/removing mass at isolated points, the mass sources are spread over a height equivalent to the size of the small PANTHER Heat Transfer Mesh (i.e, ~17cm). This method is the same as the added mass for cross flow in AP in NoCF simulations, except the height covered is ~10% of the moderator brick. Consequently, there is an approximation introduced into the CFD calculations in that physically the HIBL enters the annulus at discrete axial heights whereas in the CFD model the HIBL is introduced over regions that are ~17cm in axial length. The effect of this approximation on the cross flow effect is small as it is present in both the NoCF and CF calculations.

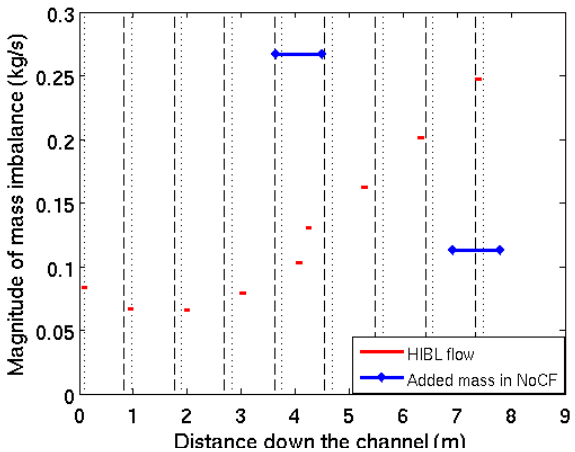

Fig.4.4 Magnitude of the mass imbalance due to cross flow in NoCF case and horizontal inter brick leakage (HIBL) flow in both cases.

In addition to the input data for the flow passages, the following boundary conditions for a whole channel are obtained from PANTHER AE subchannel code, i.e.,: (i) non-uniform heat fluxes at the sleeve outer surface; (ii) heat fluxes through the surface of the interstitial bricks; (iii) direct heat generation in the moderator bricks due to neutron and gamma heating. These boundary conditions were specified to the CFD domains by using User Defined Function (UDF) in Fluent (Fluent, 2009). Furthermore, the top surface of layer 12 brick, which is included in CFD Block1, and

the brick outlet surfaces of each CFD block are approximated by using the adiabatic boundary condition for simplicity.

4.2.5 Property of the graphite and the coolant (CO2)

The thermal conductivity (κ_g) data of graphite as a function of temperature which is set to be the same as that used in the PANTHER AE subchannel code for consistency between the CFD models and the industrial code. These data are represented by using linear interpolation in Fluent (Ansys Fluent 12.0, 2009). The properties of the coolant (CO_2) are obtained from the NIST Standard Reference Database 23 (REFPROP) Version 7 (Lemmon, 2002). Ten data points for temperature range from 500K to 1000K at a constant pressure of 4.45MP have been given as input to Fluent and linear interpolation is used in the CFD model.

4.2.6 Mesh and numerical method

Structured mesh is applied for the flow passages and the outer region of the moderator brick, while the inner region of moderator brick is meshed by an unstructured mesh to reduce the number of mesh elements. A plan view (cross section) of the mesh is shown in Fig. 4.5. There are about 15,000 cell elements for the radial-circumferential cross section. Vertically, there are 52 mesh elements in the axial direction for each layer of the computational. Each layer, which includes one moderator brick and the associated flow passages, contains 0.8 million mesh elements. So there are ~1.6 million mesh elements in the blocks, except Block 1 (1.2 million) and Block 7 (3 million). The y+ value on the interstitial wall is from 5 to 140, while it is 5~200 on the outer surface of the moderator brick. The y+ on the outer surface of sleeve and inner surfaces on moderator brick is 74 ~122. The low values of the y+ on the interstitial wall and outer surface of moderator brick are centered in the narrow gap regions.

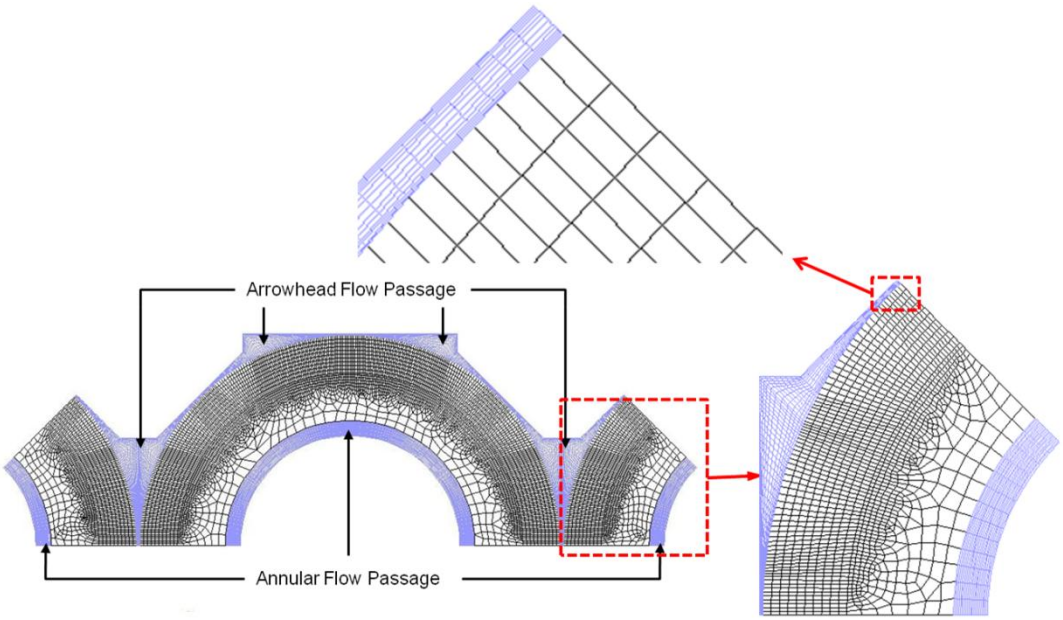

Fig.4.5 Top view of the mesh.

Mesh independence is checked by performing a simulation with a coarser mesh of about 50% of the original mesh points. The highest difference between the brick temperatures predicted by the two meshes is about 5~10 ℃, which is not a significant difference. More details about the mesh sensitive study can be found in the Appendix 1.

The first order upwind discretization scheme is utilized to solve the transport governing equations, while the SIMPLE scheme is used for coupling of the pressure and velocity. The main reason of using the first order upwind scheme it to increase the numerical stability in the simulations. Further, the effect on the accuracy of the simulation is considered to be small, since very fine mesh is generated and the cooling effect of cross flow is evaluated by using NoCF minus CF. Steady model is used for both NoCF models and CF model, except Block 7 in the NoCF model, where an the unsteady flow is simulated. In the unsteady model for Block 7, the time step is set as 0.0001s corresponding to CFL (Courant-Friedrichs-Lewy) number, ($U_b \Delta t/\Delta x$) of 0.129 to 1.69, while U_b is the averaged bulk velocity of the arrowhead passage in Block 7 of the NoCF model.

4.3 Results and Discussion

To illustrate the azimuthal heat transfer at different parts of the brick outer surface, the surface has been split into 9 faces, as shown inFig. 4.6.Several locations on the inner and outer surfaces are selected to show the axial variation of the temperature of the brick. ‘AH1’, ‘AH2’, ‘AH3’ and ‘AH4’ (referred ‘AHs’ as a group), located on the brick outer surfaces within the main arrowhead flow passage, see Fig. 4.7 (a). ‘NG1’, ‘NG2’ and ‘NG3’ (referred ‘NGs’ as a group) are the locations on the outer surface facing the centre of the narrow gap, see Fig. 4.7 (a). There are three locations in the narrow gap ‘NG-C6’, ‘NG-C7’ and ‘NG-C8’,seeing Fig. 4.7 (b), which are used to display the temperature within one brick layer. These three locations are close to the locations defined in the narrow gap, ‘C6’, ‘C8’ and ‘C7’, which are used to present the axial distribution of the velocity in the narrow gap of the AP, see Fig. 4.7 (b). All heights at which data are presented are measured down from the top of the model.

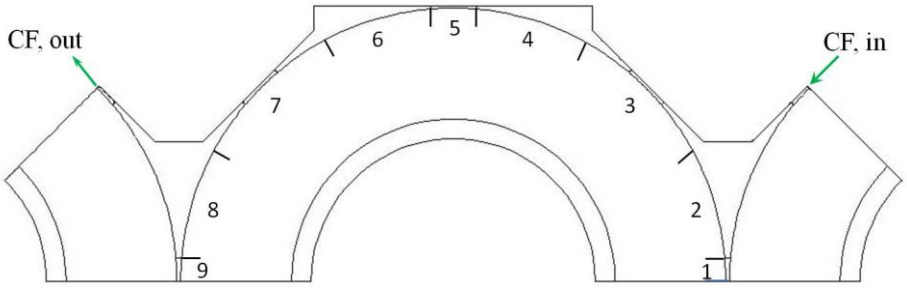

Fig.4.6 The numbered faces on the outer surface of moderator brick.

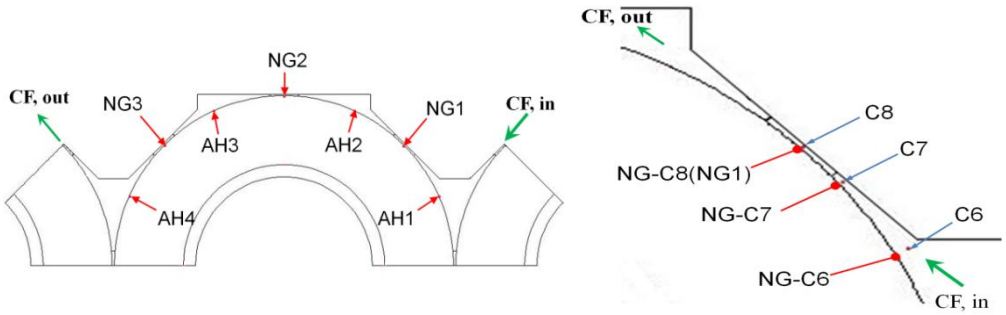

(a) (b)

Fig.4.7 (a) locations on the brick outer surface (AH1, AH2, AH3 & AH4 and NG1, NG2 & NG3) to shown the axial profiles of heat transfer results down the channel;

(b) Locations used to the present axial variation of velocity in the arrowhead passages and brick temperature on the outer surface.

4.3.1 Comparison of the NoCF case setting and results with those of PANTHER

As the NoCF case is to reproduce the method adopted in PANTHER on modelling the cross flow. This section is to produce the comparison of the certain results of the CFD models with prediction obtained by PATHER.

Fig. 4.8 shows the axial variation of the bulk temperature of the annular flow predicted by the CFD model (CF & NoCF cases) compared with the Panther output (TAN). Generally speaking, the distributions of temperature in the two models agree well with each other. There are some discrepancies between NoCF case and AE results starting from the middle of the channel. These discrepancies can be explained by reasons already discussed above in relation to the gas outlet temperature. There are also differences between the NoCF and CF results which are caused by the cross flow. The CF results are quite close to the PANTHER results but this is purely coincidental.

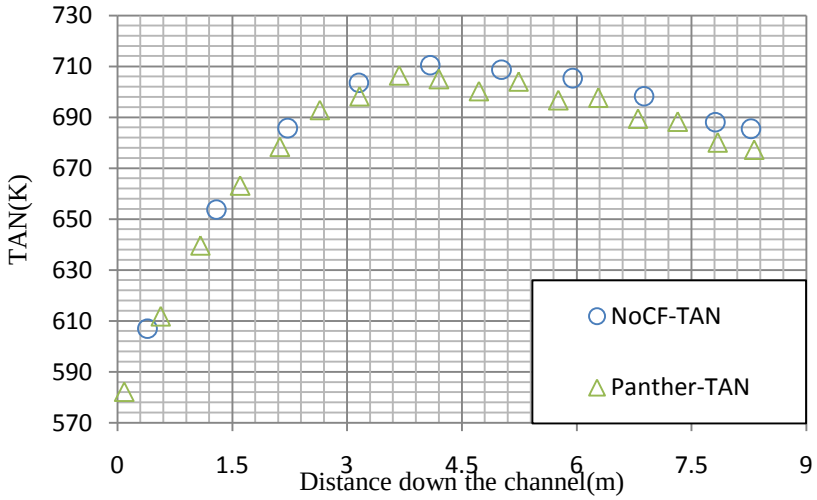

Fig.4.8 Bulk temperature of the annular passage flow - comparison between PANTHER and NoCF model.

Fig.4.9 shows the axial variation of the bulk temperature of the arrowhead passage flow of the CFD models and AE value (TAP). The results from the CFD NoCF model and PANTHER agree reasonable well. As a trend, the axial variations are consistent with the AP outlet gas temperatures discussed above based on Table 7 and potential reasons for the small discrepancies are already explained.

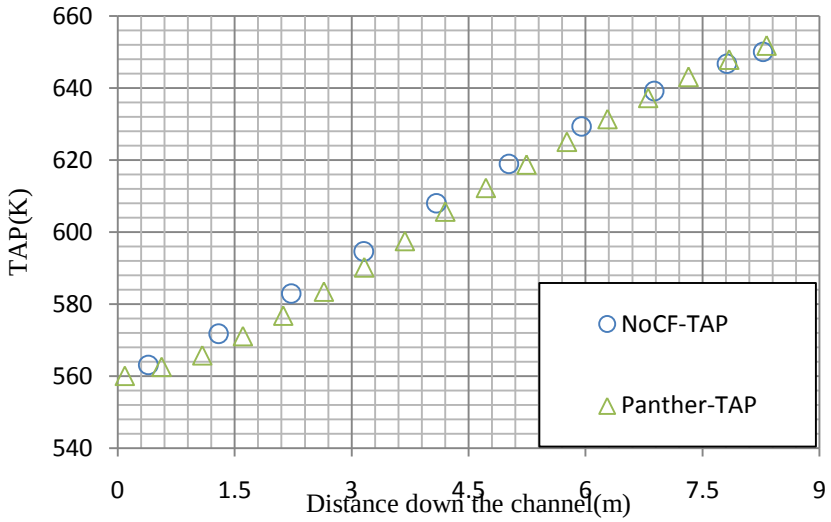

Fig.4.9 Bulk temperature of the arrowhead passage flow - comparison between PANTHER and NoCF model.

Fig.4.10 shows the comparison between the predictions of the temperature on the inner and outer surfaces of the brick using the CFD NoCF model and those of the PANTHER. Due to the irregularity of the arrowhead passage, the temperature on the outer surface of the brick varies along its perimeter. The group of locations (AH*)is used to show the temperature variations (referring to Fig 2.3).Because PANTHER is a subchannel code, only the hydraulic diameter is considered, while AH1 to 4 are close to the main arrowhead passage. As a result, AH1 to 4 of the CFD model are probably more relevant when compared with PANTHER. The shape of the axial profiles of the temperature on the outer surface predicted by the CFD model agrees very well with that of the PANTHER, yet there is an up-shift in all of them. In this case, the temperature on the outer surface (AH1 to AH4) is up to 10℃ higher than that in the PANTHER (TM2).

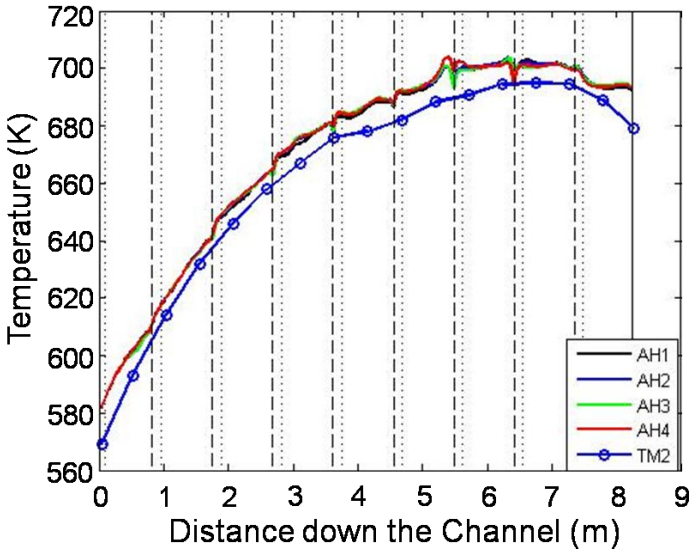

Fig.4.10 Axial temperature profile on the brick outer surface in NoCF base case and PENTHER.

In conclusion, the CFD NoCF model predictions of the coolant temperature in the arrowhead and annulus, and those of the brick inner and outer surfaces agree reasonably well with the PANTHER data. There are noticeable differences in the predictions of the brick temperatures which result from the very different modelling approaches and some small inconsistent settings. But these are insignificant as far as the purpose of this study is concerned and the model is therefore considered fit for purpose.

For ease of referencing, a summary of the main differences in the CFD and PANTHER models which significantly contribute to the differences in the results is given below:

- The height of the ribs on the sleeve outer surface in the CFD model is about half of the real value. This is a result of using a fine mesh for the annular passage because the height modelled in the FLUENT CFD model can only be as big as the first node. This causes the sleeve temperature predicted at the top of the channel (the first 2m) to be significantly higher than it should be which causes a higher radiation heat flux from the sleeve, but it has no direct

effect on the total flux from the sleeve which is a boundary condition imposed on the CFD model.

- Even though the intension of the CFD approach in modelling the horizontal leakage flow is to mimic the PANTHER approach, the simulation in the CFD model is rather complicated as described earlier and there are detailed differences in the two models, which will contribute to the discrepancies in the brick temperatures

- In PANTHER, the brick is smeared to a concentric cylinder and the arrowhead passage is modelled as an annular passage, whereas in the CFD model, the brick and the arrowhead passage are truthfully represented. In addition the CFD model takes into account the cut-out section at the bottom of each brick whereas the PANTHER neglects their existence.

4.3.2 Cooling effect of the cross flow

4.3.2.1 Temperature distributions

Fig. 4.8shows the cross sectional contour plots of the brick temperature at height z = 4.13m (the middle of the fuel channel.) in both NoCF case and CF case, while the comparison between azimuthal variations of the outer surface temperature in both cases and the temperature differences between NoCF case and CF case at level z = 4.13m are presented in Fig. 4.9.

As shown in Fig. 4.8, in the NoCF case,the temperature distribution on the inner surface of the brick is more or less axis-symmetric, and that on the outer surface of the brick is periodic. The highest temperature is located on the part facing the center of the narrow gaps and the lowest located close to the center of the main arrowhead flow passage. Such regular distribution no longer exists in the CF case, where the temperature is clearly lower on the right (facing the incoming cross flow) and higher on the left. Also, the peak temperature is lower and temperature distribution is more uniform in comparison to the NoCF case. The circumferential variation of the

temperature on the brick outer surface is shown inFig. 4.9 (a). It further demonstrates that the periodic and non-periodic temperature distribution on the outer surface of the brick in NoCF and CF cases, respectively. In the NoCF case the temperature troughs and peaks are related to the better and worse well cooled regions of the brick perimeter respectively. For instance, the peaks are always located at the centre of narrow gap (such as x=0m), while the toughs are located at the position facing the main arrowhead flow passage (such as x=0.08m). Although the azimuthal variation of the temperature distribution on the outer surface can still be observed in CF case, the locations of the troughs and peaks have been moved round the brick in the direction of the cross flow. Considering faces 4, 5 & 6, the original peak at face 5 in NoCF case moves to face 6 while the tough on face 4 in NoCF case moved to the face 5 in CF case. In the CF case the peak to trough difference is smaller than in NoCF since the effect of the cross flow is to improve cooling in the narrow gaps.

Quantitative information on the cross flow effect (defined as NoCF-CF) is obtained by studying the differences between the brick temperatures in the NoCF and CF cases. The circumferential variation of the differences between temperature on the outer surface at z = 4.13m in two cases (NoCF-CF) is presented in Fig. 4.9(b). The higher temperature difference (cross flow effect) is at the narrow gaps and the lowest in the middle of the main arrowhead passage. The positions of the peaks/troughs are inline with the positions of the max/min temperatures in the NoCF case. The differences at this level range from about 10 ℃ to 37 ℃, which makes the averaged value as 25 ℃

The axial variation of the temperature at the location on the outer surfaces of moderator brick in the NoCF case is shown inFig. 4.10. As illustrated in the figure, the temperatures at ‘AHs’ (locations close to main arrowhead flow passage) almost overlaps with each other in the NoCF case. Similar behaviour can also be found in the temperature profile at ‘NGs’ (locations facing the centre of narrow gap). As expected, the temperature values at ‘NGs’ are higher than those at ‘AHs’.

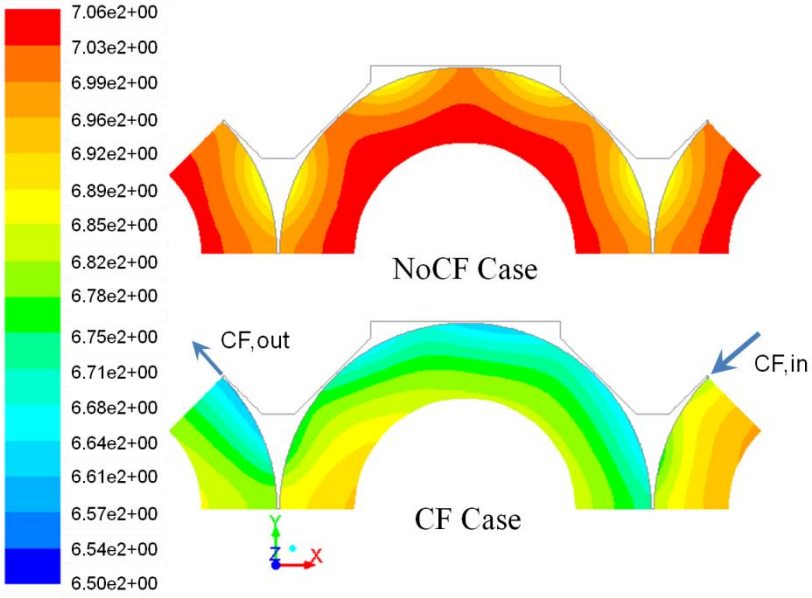

Fig.4.11 Fuel brick temperature contours at 4.13m from top of the whole modelled channel, the upper one is from NoCF base case, while the lower one is from CF base case.

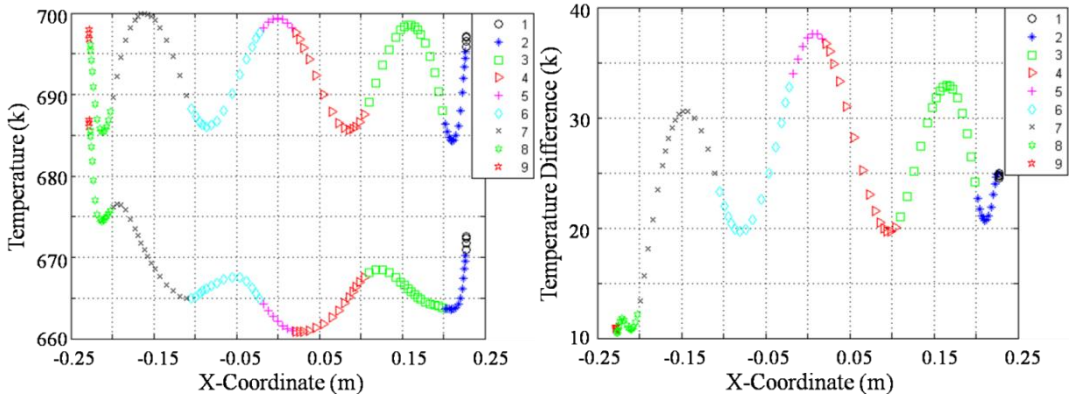

(a) (b)

Fig.4.12 (a) Azimuthal variation of moderator brick outer surface temperatureat level z=4.13m in NoCF/CF case; (b) Difference of outer surface temperature atlevel z=4.13m (NoCF-CF).

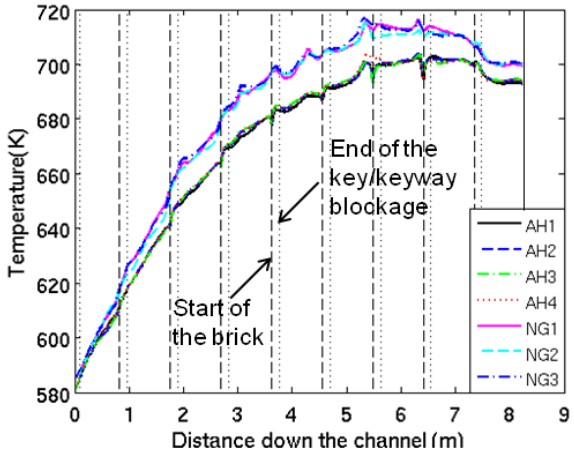

Fig.4.13 Axial temperature profile at locations on the bricks' outer surface in NoCF case (Each long dashed line: start of brick; each short dashed line: end of key/keyway blockage)

The moderator brick outer surface temperature distributions down the channel in the CF case at various locations are plotted inFig. 4.11. To make a good comparison, vertical temperature distributions at 'AH2' and 'NG2' in the NoCF case are presented in the same figure. Except for the top two bricks where there is no cross flow, the brick temperature in the CF case is significantly reduced everywhere in comparison with the NoCF case. Generally speaking, the reduction in the brick temperature is greatest in the narrow-gap region of the outer surface, while the reduction is smaller in the main-arrowhead region of the main brick. The temperature profile at locations with different angles, say 'AH1' to 'AH4' no longer overlaps with each other, which is consistent with the non-periodic temperature distribution observed in the contour plot and the distribution of the azimuthal temperature distribution on the outer surface. The figure also reveals a striking difference compared to the case studied by Ganesan et al. (2013). There is a strong non-monotonic axial variation of temperature within each brick layer here. It does not exist only in the CF case but also in NoCF case, although it is much weaker in the latter.

Quantitative information on the cross flow effect down the channel at the 'AHs' and 'NGs' is illustrated in Fig. 4.12. Fig. 4.12 (a) shows the cross flow effect varies greatly vertically within each brick. The cooling effect of cross flow at location 'AHs' is strongest at the two ends of each brick and the lowest in the middle, see Fig.

4.12(a). The median is ~ 20 ℃ (evaluated from z = 2.5m to 7.5m). Moreover, the effect is much stronger at locations 'AH1' to 'AH3' than at the location 'AH4'. The temperature reductions on the surfaces close to the narrow gap, referred to as 'NGs', is much higher, see Fig. 4.12(b). The median of the reduction is ~35 ℃. Also, the reduction in the narrow gap decreases rapidly within the blockage region, then increases from the end of the blockage and reaches the highest value close to the bottom of the each brick at these locations.

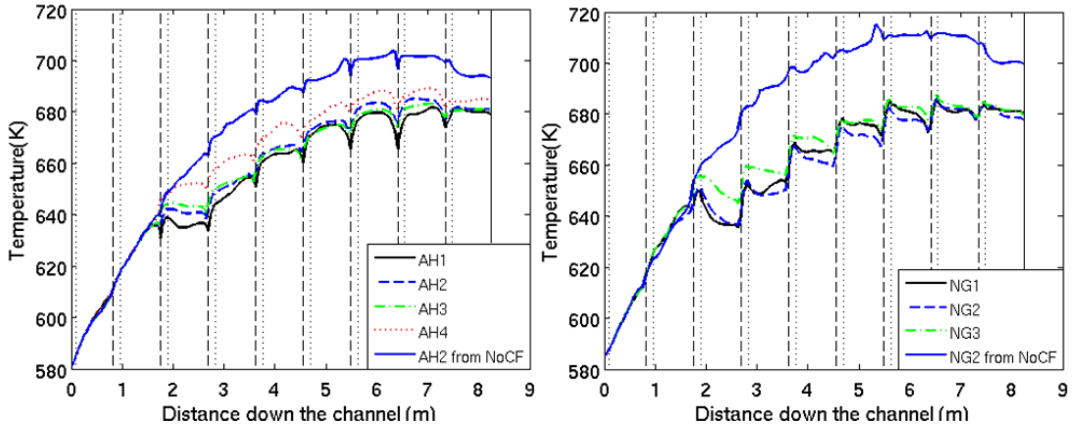

(a) (b)

Fig.4.14 Axial temperature profile at different locations (a) AH1, AH2, Ah3, & AH4; (b) NG1, NG2, and NG3 in CF case and comparison with that of NoCF case.

A summary of the cross flow effect in each brick layer, based on the temperature reduction at 'AH2' and 'NG2', is given in theTable 1.Although the cross flow in layer 10 can also affect the lower part of layer 11 brick, the magnitude is small and localized, see Fig. 4.12.The cross flow effect at the top two layers like layers 12 & 11, as shown in Fig. 4.12, is considered as zero, since no cross flow is considered in these two layers. The values at these two layers are not shown in the table. The average values are obtained by straight averaging the maximum and minimum values to obtain the representative values. The cooling effect is more significant in the middle three bricks i.e. brick layers 9 to 7, being around 29 ℃, but decrease to 19.63 ℃ at the bottom brick layer, which makes the overall averaged temperature reduction due to cross flow to be ~ 25.34 ℃.

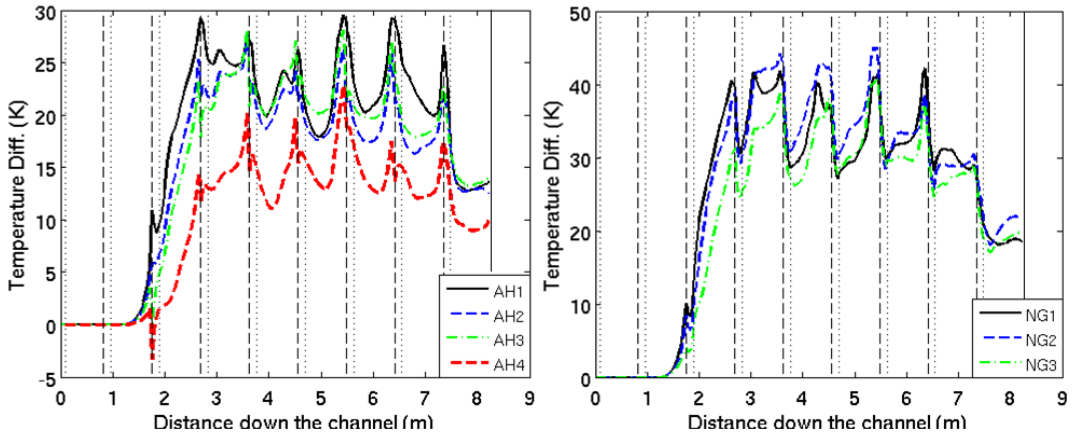

(a) (b)

Fig.4.15 The vertical temperature difference (NoCF minus CF) profile at (a) AH1, AH2, AH3, & AH4; (b) NG1, NG2, and NG3.

Table 4.1 Cross flow cooling effect (NoCF case minus CF case).

Brick Layer	Outer Sufaces (main arrowhead), ℃			Outer Sufaces (narrow gap), ℃			Average within One Brick, ℃
	Minimum	Maximum	Average	Minimum	Maximum	Average	
10	25	6	15.5	7	40	23.5	19.5
9	21	27	24	28	44	36	30
8	18	24	21	30	43	36.5	28.75
7	17	25	21	29	45	37	29
6	17	24	20.5	28	38	33	26.75
5	16	23	19.5	26	30	28	23.75
4	12.5	20	16.25	18	28	23	19.63
						Overall Average:	25.34

4.3.2.2 Heat flux and heat transfer coefficient

The heat flux and heat transfer coefficient on the outer surface of the moderator brick are discussed in this section to further understand the cross flow effect. Vertical heat flux variation at selected locations (‘AHs’ and ‘NGs’) in two cases is illustrated in Fig. 4.13 and Fig. 4.14 respectively, while the azimuthal variations of heat transfer on the circumference of horizontal section at z = 4.13m are presented in Fig. 4.15.

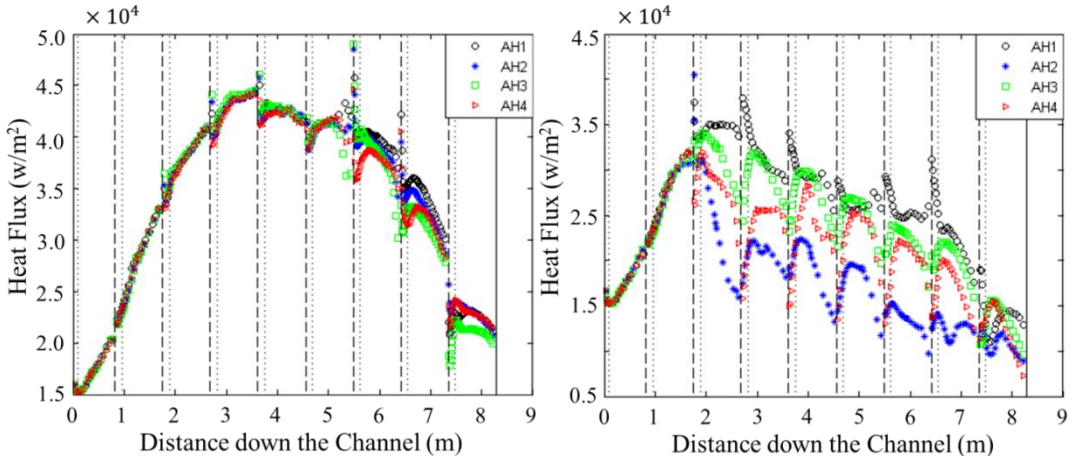

Fig.4.16 Vertical variation of heat flux at AH1, AH2, AH3, and AH4 in (a) NoCF case, (b) CF case.

As shown in Fig. 4.13 (a), the overall trend is that the heat flux at 'AHs' down the fuel channel in NoCF case peaks in the middle. The distributions at different locations almost overlap with each other over most part of the channel but diverge from each other in the bottom three brick layers. The deviation can be due to the strong unsteady feature of the flow in bottom of the fuel channel in NoCF case, which appears to break the symmetric distribution of flow and heat transfer. In addition, the variations within each brick layer due to the axial variation of the geometry are also evident in the figure. The vertical distribution of heat flux at AHs in the CF case is quite different from the NoCF case, see Fig. 4.13 (b). There is an overall decreasing trend, which starts from brick layer 10, where the cross flow starts functioning. Meanwhile, the profiles at different locations are separated from each other in the layers with cross flow. Hence the azimuthal symmetry no longer exists as discussed earlier in relation to the brick temperature, which is also attributed to the effect of cross flow. Moreover, the variation within each brick is stronger than in the NoCF case. The strong variation of the distribution of the vertical and cross flow velocities within the layer can be the reason. More details on the effect of the brick's axial variation will be discussed later.

The heat flux in the narrow gap ('NG') is about an order of magnitude lower than it at 'AHs' in NoCF case as illustrated in Fig. 4.14 (a). This is expected. It is interesting however that the negative heat flux, implying energy is transferring from

the coolant to the moderator brick, can be found at the levels coinciding with the HIBL flow. It can be due to several reasons. One is that the energy sink due to HIBL flow implemented in the CFD model is based on the flow temperature obtained by PANTHER, which can potentially be smaller than the local CFD temperature. That is, the energy sink is too small, equivalent to a positive energy source, which can result in heat transfer from coolant to the brick. Furthermore, the HIBL flow together with blockages can cause the flow redistribution, decrease axial velocity or even reverse the flow. As a result, fluid with higher temperature from downstream or a higher temperature region may be drawn to the area, leading to localised reversed heat transfer. The effect of the HIBL flow will be further discussed later. The reversed heat transfer has almost completely disappears in the CF case, except for at the ends of the bricks of the top/bottom as presented in Fig. 4.14 (b). In the meantime, the magnitudes of heat flux are significantly increased. These can reach the same level or even higher than heat flux at 'AHs' in CF case.

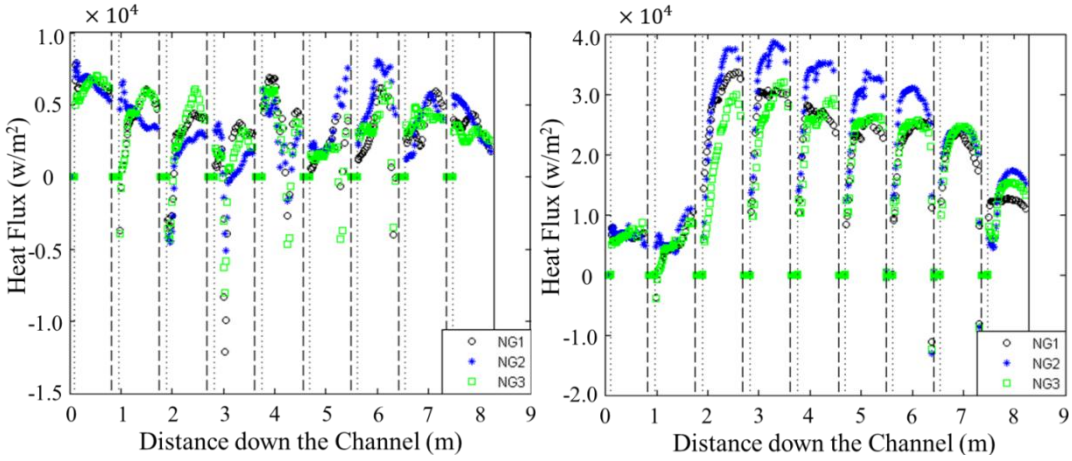

(a) (b)

Fig.4.17 Vertical variation of heat Flux at NG1, NG2 and NG3 in (a) NoCF case, (b) CF case.

The circumferential distribution of the heat flux on the brick perimeter at z=4.13m in NoCF case is illustrated inFig. 4.15 (a). Similar to the circumferential distribution of temperature, it changes periodically on the brick, being lowest in the narrow gap; say on face 5 and at the center of faces 3 and 7. The highest heat flux is on faces 4 and 6 which is facing the main arrowhead flow passage. The lowest and highest values are about one order of magnitude apart. The heat flux distribution at this level is

symmetric regarding x=0m. Heat transfer in the narrow gap regions has become very effective in CF case, as shown in Fig. 4.15 (b). Heat flux in these regions (face 5, middle region of faces 3 and 7) is close to the maximum values. In the meantime, in the CF case, heat transfer on some of the surfaces in the main arrowhead passage is no longer as effective but it remains effective on other surfaces. This is dependent on whether the surface is facing the jet (of the cross flow) or in the wake of the jet. When the surface faces the jet, the main axial flow is pushed towards the surface and the heat transfer is enhanced, whereas when it is in the wake of the cross flow, the main axial velocity is reduced, making the heat transfer less effective. Consider face 4 for example, the heat flux is low on the right but peaks on the left. Moreover, heat transfer is much more uniform in the CF than in the NoCF. For example, the heat flux varies from $1.5x10^4$ to $3.6x10^4$ W/m^2 in most part of the surface at 4.13m in the CF case, which can be compared with the range 0 to $4.5x10^4$ W/m^2 in the NoCF case.

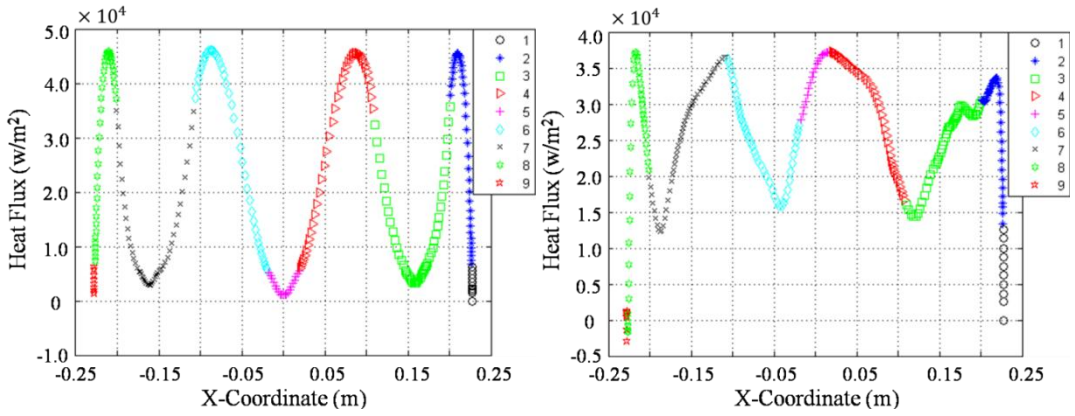

(a) (b)

Fig.4.18 Heat flux on outer surface of the brick at axial level z=4.13m; (a) NoCF case, (b) CF case.

The overall heat transfer coefficient (HTC) of the moderator brick outer surface at different levels down the channel in both cases are shown in the Fig. 4.16. The data presented in the figure is evaluated at the center of each brick layer. As shown in the figure, the HTC is significantly increased once the momentum of the cross flows is functioning in CF case. In the NoCF, the HTC decreases from the top of the channel, and remains more or less the same from brick layer 9. Thanks to the cross flow, the HTC steadily increases from brick layer 10 and stays more or less the same from

layer 9, in CF case, and the value is about doubled that at the same level obtained in the NoCF Case.

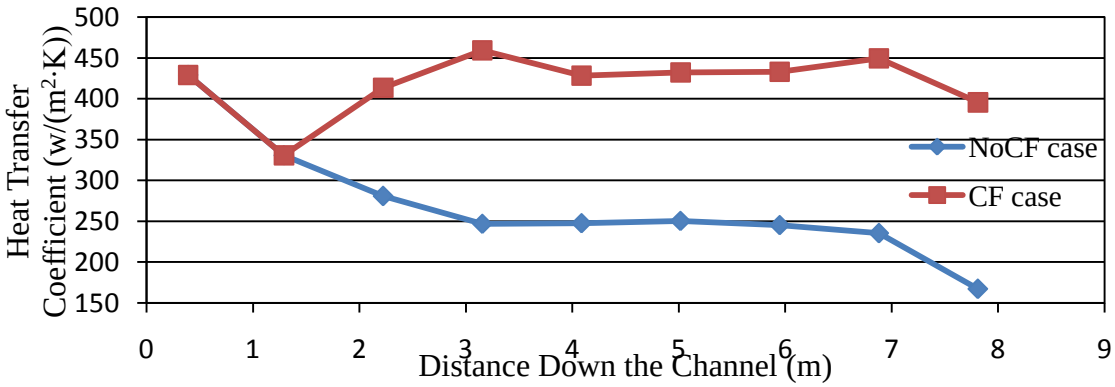

Fig.4.19 The heat transfer coefficient (HTC) at different levels.

4.3.2.3 Flow pattern

The axial variation of the geometry of the arrowhead flow passage results in a very complex and three dimensional flow field even in the NoCF case. Also, the horizontal inter-brick leakage (HIBL) flow has significant effect on the flow, especially at the three layers (layer 6, 5, 4), where the HIBL flow is the biggest and the downwards arrowhead flow is smallest. More details on the impact of the axial geometry variation and HIBL flow will be discussed later. In fact, the flow becomes unstable in the last three layers in the NoCF case. The results presented for these three layers are based on an average over 9 seconds. The overall velocity distribution, including the axial velocity and cross flow velocity $\sqrt{V_x^2 + V_y^2}$ in AP at z=4.13m in both cases is presented in Fig. 4.17. Then, the vertical profile of velocities at locations C6, C7 and C8 will be discussed to further the understanding, referring to Fig. 4.18 and Fig. 4.19.

Since the flow passage is symmetric about plane x =0m, only the left half of the flow passage is shown in the figure. As illustrated in Fig. 4.17 (a), the axial velocity peaks are located at the centre of main arrowhead flow passage, and the velocity distribution is symmetric regarding x = 0m in the NoCF case. Due to the cross flow, the axial velocity peak is shifted to one side of the AP in the CF case. As a result, the axial velocity significantly increases on the side of the main arrowhead flow passage

facing the cross flow inlet, but is reduced on the other side. As illustrated in Fig. 4.17 (b), certain level of cross flow can also be found in the NoCF case. But the value is very small and mainly exists in the narrow gap. The axial geometry variation and the HIBL flow are the main reasons for such cross flow. The magnitude of the cross flow is much stronger in the CF case. It is strongest in the narrow gap and much smaller in the main arrowhead flow passage.

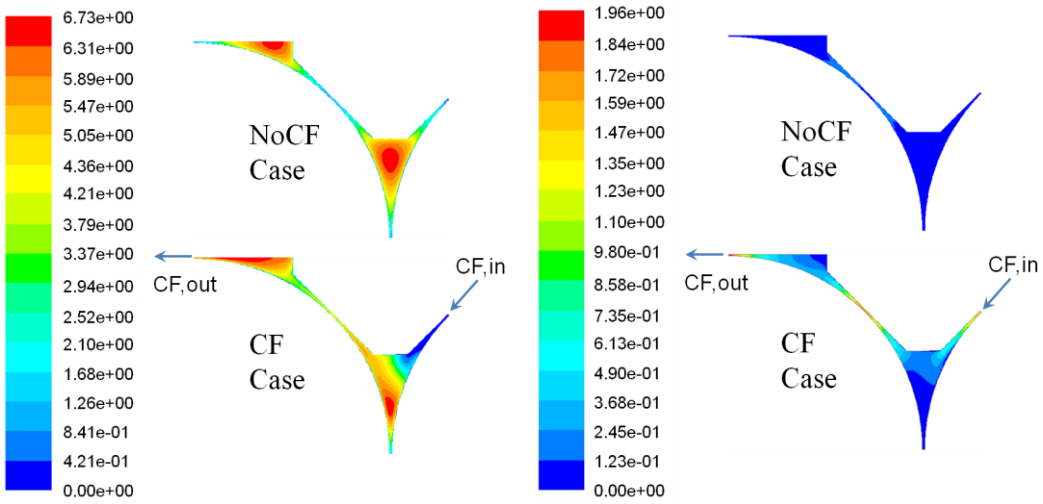

(a) (b)

Fig.4.20 Contours of velocity components magnitude at height 4.13m from both cases in (a) axial velocity; (b) cross flow velocity.

Additional and more detailed information on the flow field can be obtained by studying the vertical distribution of the axial velocity and cross flow velocities, refer to Fig. 4.18 and Fig. 4.19. As shown in Fig. 4.18, there is a positive relationship between the axial velocity and the size of the flow passage observed in the NoCF case. The magnitude of the axial velocity decreases with the location moving to the centre of the narrow gap as shown in Fig. 4.18 (a). Overall, the axial velocity at 'C6' is higher than at 'C7' which is followed by that at 'C8' down the channel. However, the axial velocity around the centre of the narrow gap is significantly increased in the CF case. The magnitude of the velocity at 'C7' and 'C8' is comparable to the value at 'C6', especially in the bottom layers. Here the axial velocities at these three locations almost overlap with each other.

The vertical distribution of the cross flow velocity on C6, C7 & C8 presented in Fig. 4.19 also demonstrates the existence of non-zero but localized cross flow velocity in the NoCF case. However, the maximum value is just ~0.5m/s and very localized. The velocity is much smaller over most of the channel height. The cross flow velocity in CF case is significantly increased from the layer where the cross flow starts functioning. The maximum value is up to 3.2m/s. Meanwhile the cross flow velocity is negatively correlated with the size of the gap in the CF case. The magnitude of cross flow velocity at the flank of the narrow gap ('C6') is smaller than at the centre of the narrow gap.

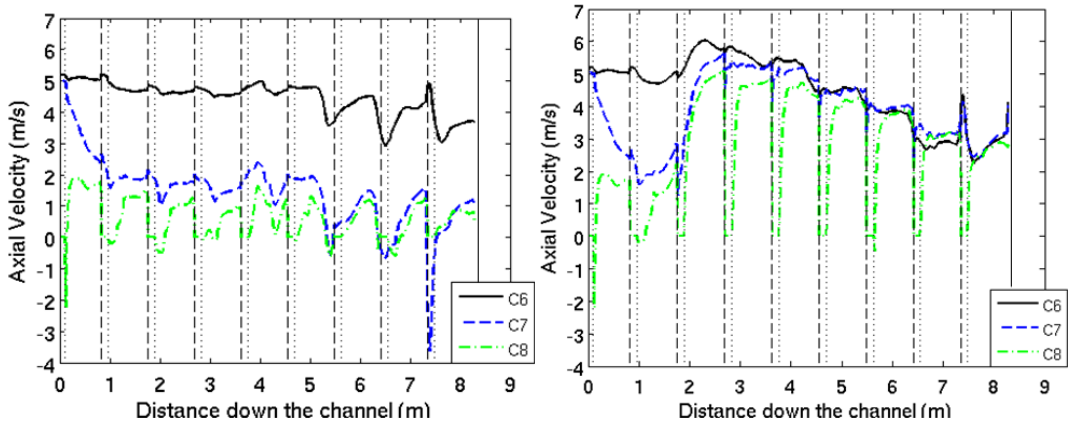

(a) (b)

Fig.4.21 Profiles of velocity component of Vz down the channel at locations C6 to C10; (a) NoCF (b) CF. (Each long dashed line: start of brick; each short dashed line: end of key/keyway blockage)

The asymmetric distribution of the axial flow is one of the reasons for the asymmetric temperature and heat flux distributions discussed earlier. The large cross flow velocity in the narrow gap is the main reason for the great decrease of the temperature on the faces close to the narrow gap, which also makes the faces no longer the peak temperature region. This can also be used to explain the greatly increased heat flux in the narrow gap in CF case. It should also be noted that the axial distribution of the vertical/cross flow velocity reveals the strong non-monotonous change within each layer. More details will be discussed later.

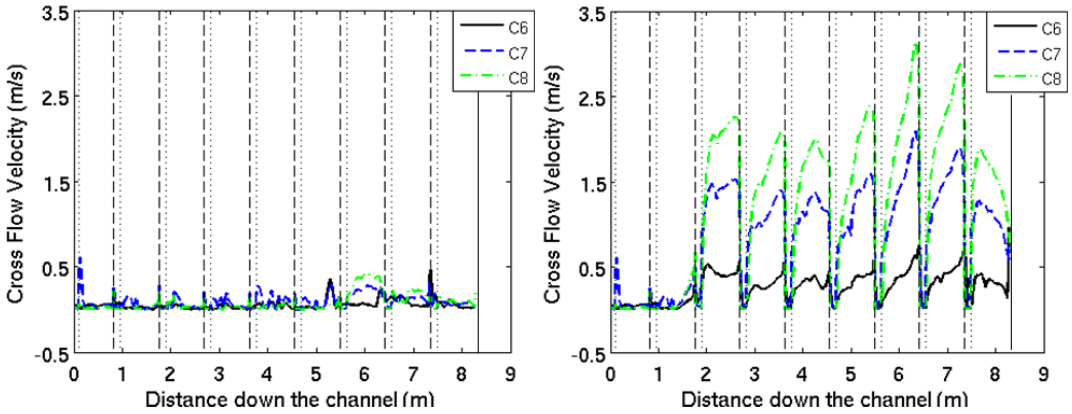

(a) (b)

Fig.4.22 Profile of cross flow velocity ($\sqrt{V_x^2 + V_y^2}$) down the channel at locations C6 to C10; (a) NoCF case, (b) CF case.

4.3.2.4 Effect of increasing the cross flow rate

The graphite moderator brick would shrink away from each other within the lifetime of the AGR reactor, which would cause a significant increase of the cross flow rate. It is useful to investigate the effect of doubling cross flow rate with all the other parameters kept the same. Again two cases have been investigated, i.e. a 200% NoCF case and a 200% CF case.

The vertical distribution of the outer surface temperature at selected locations ('AHs' and 'NGs') in 200% NoCF Case is plotted in Fig. 4.20, with the results at 'AH2' and 'NG2' in the references NoCF case for comparison. As expected, the differences between the two cases start at brick layer 8 (5th brick from top).It is related to the injection location of the mass and energy imbalance associated with the cross flow. The general temperature reduction in 200% NoCF case is up to 7 ℃ in comparison with NoCF case, and this reduction is much smaller in some locations. It should be noted that the higher temperature reduction is mainly in brick layers 8 and 7. The lower temperature in the 200% NoCF case is because of extra added mass resulting in an increased axial velocity which enhances the heat transfer and leads to a cooler brick.

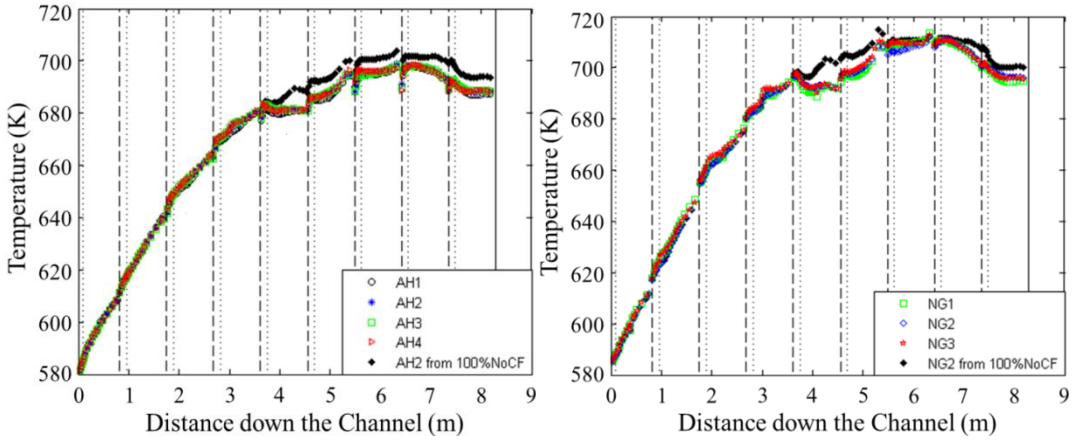

(a) (b)

Fig.4.23 Axial temperature profile on the brick outer surface in 200% NoCF case and 100% NoCF at (a) 'AH1', 'AH2', 'AH3' & 'AH4'; (b) 'NG1', 'NG2' & 'NG3'.

The comparison between the temperatures at selected locations ('AHs' and 'NGs') obtained in the 200% NoCF case and 200% CF case is shown in Fig. 4.21. As expected, a strong heat transfer enhancement has been observed in the 200% CF case. The quantitative information is shown in Fig. 4.22.

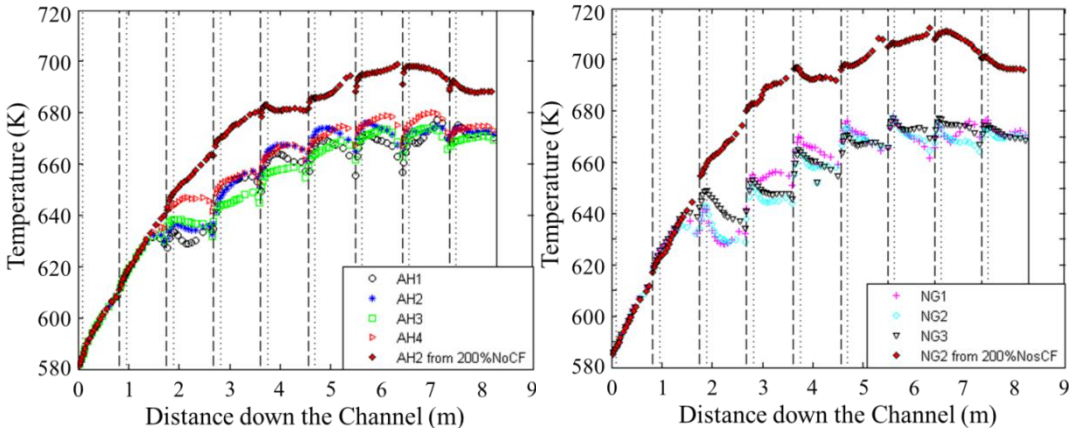

(a) (b)

Fig.4.24 Axial temperature profiles on the brick outer surface at (a) 'AH1', 'AH2', 'AH3' & 'AH4'; (b) 'NG1', 'NG2' & 'NG3'in 200% CF case,in comparison with that of 200% NoCF Case;

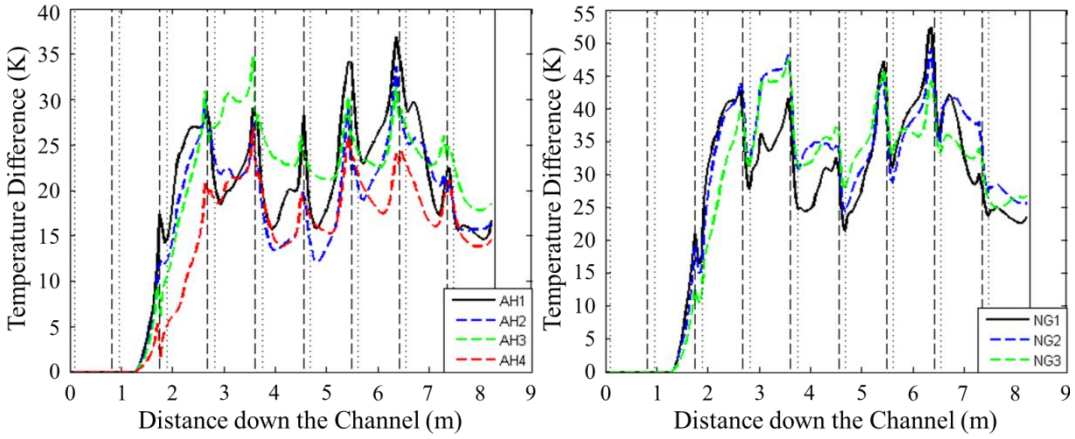

(a) (b)

Fig.4.25 The vertical temperature difference (200% NoCF minus 200% CF) profile at (a) 'AH1', 'AH2', 'AH3', & 'AH4'; (b) 'NG1', 'NG2', and'NG3'.

As illustrated in Fig. 4.22**,** the overall trend of the cross flow effect is about the same as that discussed in the 100% cross flow rate cases. Within one brick, the cross flow effect (temperature difference) is strongest at the two ends of the brick, and modest in the middle. In the meantime, the temperature drop at the locations in the centre of narrow gap ('NGs') is greater than that in main arrowhead passage ('AHs').

Following the same procedure mentioned earlier, the average cooling effect in each brick layer in the 200% cross flow rate cases is obtained, see Table 2. A smaller temperature reduction (~27.25 ℃) is seen in brick layers 8 and 7, while the average magnitude of the cross flow cooling effect is ~32 ℃ in brick layers 9, 6, and 5.The impairment of the cooling effect at brick layer 8 & 7 is mainly due to the heat transfer enhancement due to the sudden injection of mass flow rate, which results in the disturbances and a redistribution of the axial velocity at the injection and further down the channel. As a result, the cooling effect evaluated by using 200% NoCF minus 200% CF decreases. The overall average of the temperature reduction in all bricks is about 28.5 ℃, which is just about 3.0 ℃ higher than the 100% cross flow rate. Although the cross flow rate is doubled, the heat transfer enhancement in 200% CF is very limited, which is similar to the finding by Ganesan et al. (2013). So it is reasonable to conclude that the cross flow cooling effect is largely insensitive to the cross flow rate between 100% and 200% cross flow rate.

Table 4.2 Cooling effect of doubled cross flow rate (200% NoCF case minus 200% CF case).

Brick Layer	Outer Surfaces (main arrowhead), ℃			Outer Surfaces (narrow gap), ℃			Average within One Brick, ℃
	Minimum	Maximum	Average	Minimum	Maximum	Average	
10	12	29	20.5	15	44	29.5	25
9	20	29	24.5	32.5	48	40.25	32.38
8	13	29	21	32	35	33.5	27.25
7	12	28	20	24	45	34.5	27.25
6	19	34	26.5	29	48	38.5	32.5
5	20	34	27	33	42	37.5	32.25
4	15	23	19	25	28	26.5	22.75
						Overall Average:	28.48

4.3.3 Impact of the axial geometry variation and horizontal inter-brick leakage (HIBL) flow

As mentioned above, there are keys and cut-out parts at the top and bottom ends respectively of each moderator brick (see Fig. 4.2(b)). Since the clearances between the key/keyways are neglected in the CFD model, the keys act as a blockage for the cross flow (for both the axial and the cross flows). The part of the fuel channel, which contains the keys (blockage), is named as the blockage region. The variation of the geometry significantly affects the temperature distribution and flow pattern in the arrowhead passage. Meanwhile, the horizontal inter-brick leakage (HIBL) flow causes a significant reduction in the mass flow in the arrowhead passage. The impact of such flow is discussed in this section. The effect of HIBL flow is strongest at the bottom of the fuel channel, where the magnitude of HIBL is big and the downward mass flow rate is small. The results from layer 6,(which is the 7^{th} layer from the top) are shown in this section.

Impact of the axial geometry variation

The temperature variation within one layer is somewhat different on the surfaces next to the main arrowhead flow passage and those next to the narrow gaps in the CF case. We consider the vertical temperature profile on the outer surface of each brick facing the main arrowhead flow passage (‘AHs’), e.g., from 3.7m to 4.6m down the

fuel channel, refer to Fig. 4.11 (a). The temperature is lower at the two ends of the moderator brick. Starting from a rather low value at the top of each brick, the temperature rises quickly to a much higher value before increasing more slowly with distance until the end of the brick, where it drops quickly to a much lower value. The pattern then repeats itself in the next layer. The trend of the temperature variation in the narrow gap region (referring to 'NG1' to 'NG2') within one brick is different, but the magnitude of the variation is similar to the main arrowhead flow passage, see Fig. 4.11(b). The temperature of moderator outer surface along most part of the brick tends to remain more or less the same or even reduce a little down the channel.

The temperature contour on the outer surface of the moderator brick in layer 6 is presented inFig. 4.23. It can be seen from the figure that the temperature on the moderator brick outer surface is periodic in the NoCF case (seeing Fig. 4.23(a)). The highest temperature is located in the narrow gap, while the lowest value can be found on the part of the surface facing the main arrowhead flow passage. Furthermore, strong asymmetric distribution of the temperature can be observed in the CF case, (seeing Fig. 4.23 (b)). As illustrated in the figure, the cross flow, coming from the left, shifts the highest temperature region from the centre of the narrow gap to the downstream of the cross flow.

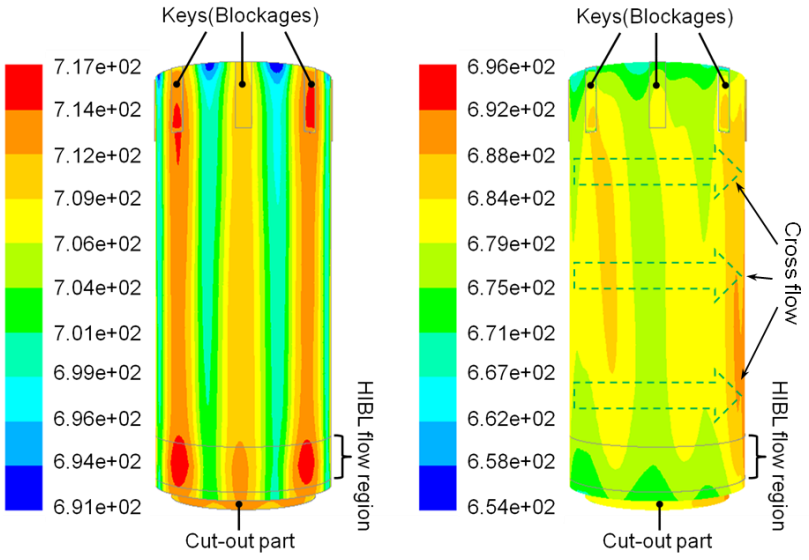

(a) (b)

Fig.4.26 The temperature contour of the outer surface of the layer 6's moderator brick (the 7th from the top) in (a) NoCF case, (b) CF.

The vertical temperature variations at locations ‘AHs’ and ‘NG-Cs’ (‘NG-C6’ to ‘NG-C8’) within layer 6 are presented in Fig. 4.24. The temperature increases quickly in the blockage region in both cases. The overall temperature variation within a brick is much greater in the CF case, which demonstrates the strong influence of the axial geometry variation on the cooling effect of cross flow within the layer. It also shows that the temperature profiles at different type of locations (‘AHs’ & ‘NGs’) are different in both cases. In the NoCF case, the magnitude of wall temperature increment in the blockage region varies with different locations. For instance, (~ 6 ℃ to the increment of the wall temperature at the region at ‘AHs’ is ~ 6 ℃, but ~2 ℃ at‘NG-C8’ (see Fig. 4.24 (a)). In CF case, however, the temperature increment in the blockage region appears to be the same at the various locations, including ‘AHs’ and ‘NG-Cs’. More interestingly, the wall temperature at locations ‘NG-Cs’ converges to the same value as the location moving towards the cutout part of the brick (see Fig. 4.24 (b)).

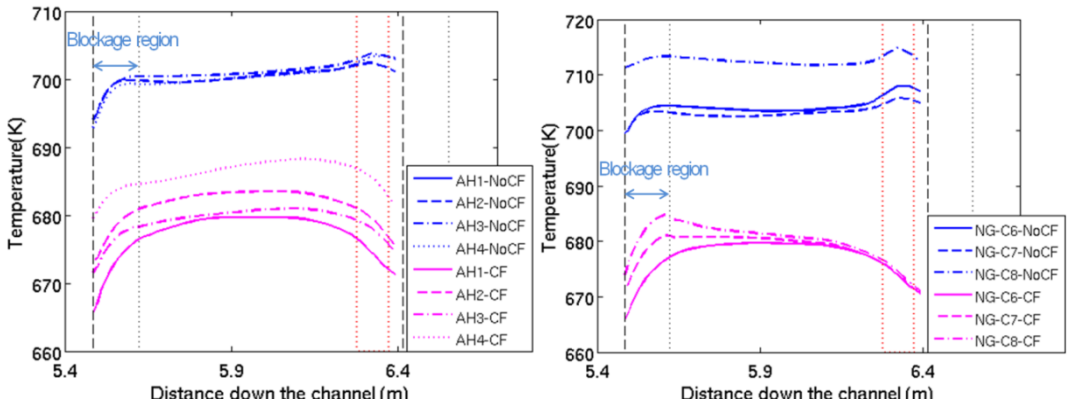

(a) (b)

Fig.4.27 The axial temperature profile on brick outer surface at locations (a) AH1, AH2, AH3 and AH4); (b) NG-C6, NG-C7 and NG-C8 in both cases in the layer 6, locations are shown in Fig. 4.7. (Long dashed line: start of brick; Short dashed line: end of key/keyway blockage; red dash box indicating the HIBL flow region)

There is a sudden increase in the temperature in the region where the HIBL is applied in NoCF as presented in Fig. 4.24, which will be explained in the next section. With the location moving towards the end of the brick, there is a change of trend, the temperature reduces slightly in the NoCF case. This can be explained by

the existence of the cut-out part at the end and the blockage on the next brick. Both of them would disturb the thermal boundary layer or even redistribute the flow velocity which would again disturb the thermal boundary layer and lead to an enhancement in heat transfer. In the CF case, the great decrease of wall temperature at the low level of the brick is also due to the existence of the cut-out part of the brick, which does not only break the thermal boundary layer created by the upstream flow, but also allows more coolant cross flow through, results a stronger cooling and hence a big reduction of temperature toward the end of a brick. Meanwhile the cross flow is stopped by the key/keyway blockage which results in an even more rapid temperature increase in the blockage region. The combination of the effects mentioned above causes the temperature variation within each brick to increase significantly in the CF case compared to the NoCF case, as observed in Fig. 4.24.

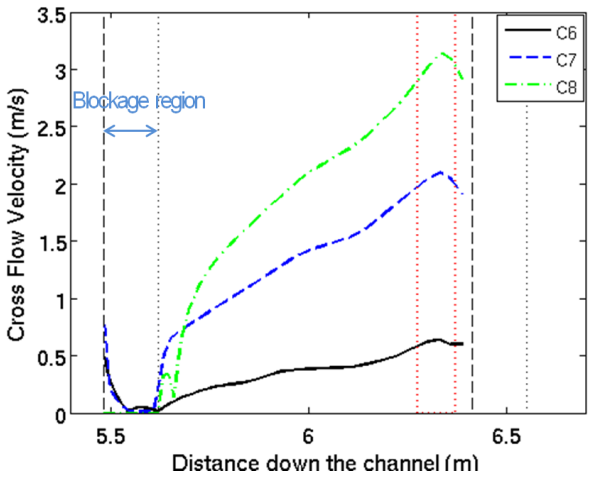

Fig.4.28 Cross flow velocity distributions from CF case in the layer 6 of the modelled fuel channel;

The cross flow velocity profiles at locations in the narrow gap (C6 to C8) within one layer in the CF case are shown in Fig. 4.25. As illustrated in the figure, the cross flow velocity drops rapidly to zero in the blockage region even at C6 which is away from the key/keyway blockage. Then the velocity gradually increases from the end of the blockage region to the end of the brick. The increasing rate and the magnitude of cross flow velocity increase as the location moves from the flank of the narrow gap (C6) to the centre (C8), which results in more efficient heat transfer in the gap centre. This effect can explain the more uniform temperature distribution in the narrow gap of the lower part of the moderator brick in CF case mentioned early.

Effect of the horizontal inter-brick leakage (HIBL) flow

As shown in Fig. 4.23, the temperature on the brick surface in the narrow gaps clearly shows peaks in the HIBL flow region in the NoCF case but not in the CF case. The temperature rise in this particular region in the NoCF case is also shown in the line plot in Fig. 4.24 (a). There is also a temperature increase in the arrowhead passages albeit with a smaller amount. This can be explained by the negative effect of the HIBL flow on the axial velocity in this region, which is shown in Fig. 4.26. In NoCF Case, the sudden and strong velocity reduction is recorded at the HIBL flow region in the narrow gap, and it is more significant when the gap becomes narrower and even creates a reverse flow (negative value in Fig. 4.26 (a)) around the centre of narrow gap, which can induce the hotter fluid from down- stream. This can explain the more significant temperature increase in the HIBL region narrow gap. However, the negative effect of HIBL flow on the axial velocity in the CF case is much smaller. This result further demonstrates that under the presence of the cross flow which pushes the axial flow into the narrow gap region, the effect of the HIBL is much weakened.

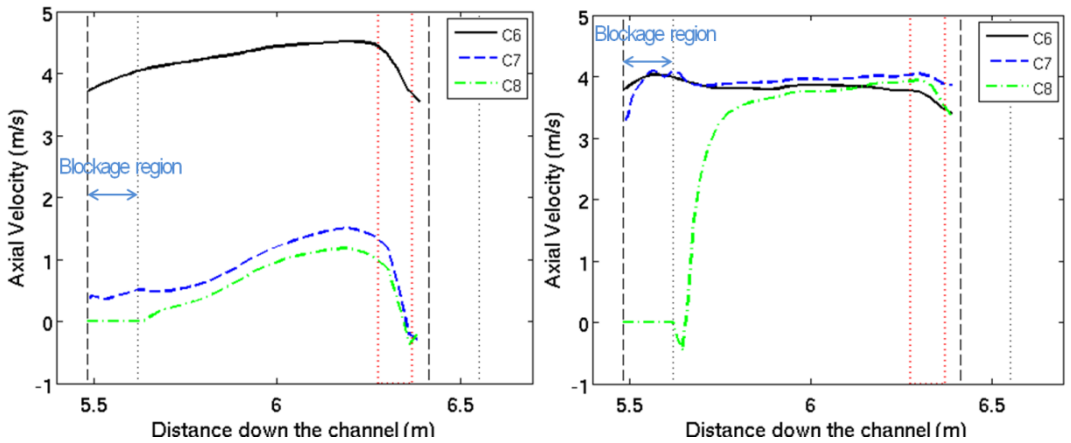

Fig.4.29 The vertical profile of axial velocity in layer 6 of modelled fuel channel in (a) NoCF case, (b) CF;

4.3.4 Flow instability as the bottom of the fuel channel

The instantaneous velocity history is recorded at three points at different levels on 'C6', which is presented in Fig. 4.27. The points are located at 6.71m, 6.96m, 7.26m down the channel, respectively. As illustrated in the figure, a strong periodic oscillation of the axial velocity in the narrow gap is recorded. Although the amplitude of the axial velocity oscillation is about 25% of the mean value, the effect of such flow instability on the brick temperature is negligible, as shown in the Fig. 4.28, which can be due to the thermal inertia of the brick. It acts as a low pass filter which makes the temperature rather insensitive to the periodic changes in the velocity.

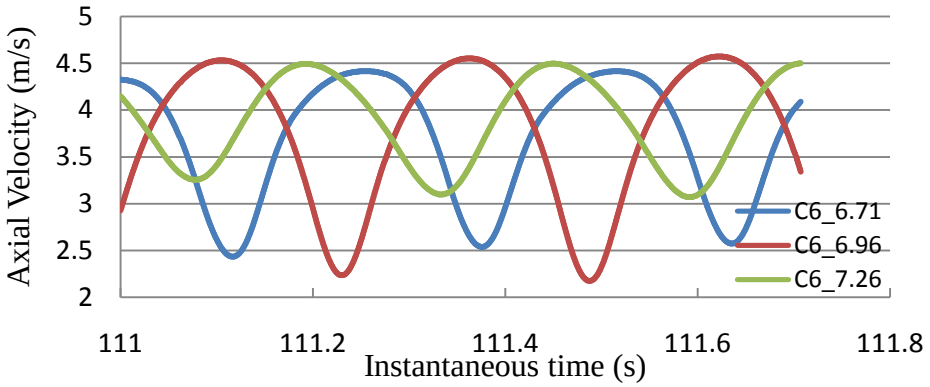

Fig.4.30 The instantaneous axial velocity profile of three locations on C6 in block 7 from NoCF case.

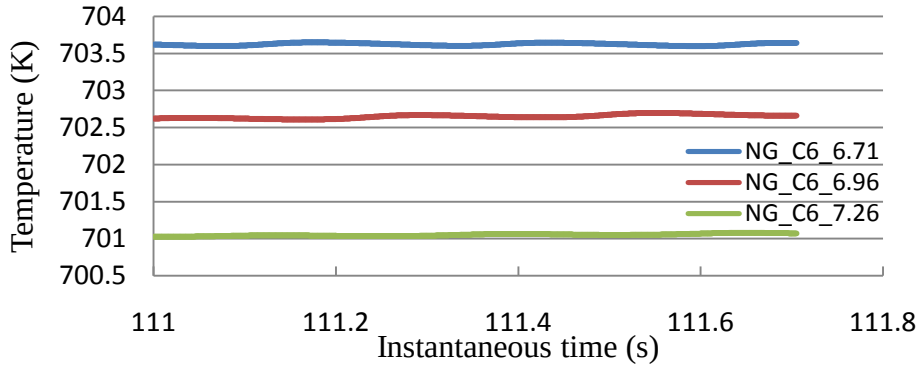

Fig.4.31 The instantaneous temperature of the 3 points on NG-C6 from NoCF case.

As already mentioned earlier, the unsteady behaviour of the flow only exists in the modelled fuel channel in the NoCF model not in the CF case. As a result, it is

reasonable to conclude that the cross flow can significantly moderate the flow instability, simply because the strong cross flow can redistribute the flow in the arrowhead flow passage, resulting in a more uniformly axial velocity distribution. The high velocity gradient in the azimuthal direction, which is the driving force of the flow instability in the tightly pack tubes, would be hugely moderated in the CF case. When the cross flow is not strong, the velocity distribution can be similar to that in the NoCF case, and the flow at bottom of the fuel channel might be unstable.

4.4 Conclusions

The horizontal flows in one of the designs of the AGR reactor cores have been studied by using Fluent. 12.0. Appropriate CFD models have been developed.

Compared with the model which only considers the mass imbalance and mass/energy imbalance due to the cross flow, the overall reduction of brick temperature varies from 20℃ to 35℃ in the model which considers the momentum of the cross flow. The reductions remain more or less the same in brick layers9 to 5, but are lower in other part of the channel. The heat transfer coefficient is nearly doubled in CF case in comparison with that in the NoCF case.

The temperature reduction is stronger on the wall close to the narrow gap than that facing the main arrowhead flow passage. Meanwhile, it is strongest on the part of the brick where the cross flow enters the domain, but weakest where is leaves. Furthermore, the heat transfer rate enhancement within the brick is higher at the ends of brick and lower in the middle. The within-brick axial temperature variation is from 5℃ to 10°C. The overall cooling effect is only 3˚C higher with the cross mass flow rate doubled.

The mechanisms of the cross flow cooling effect are listed below:

- The strong cross flow in the narrow gap greatly increases the heat transfer rate in the region; The cross flow also pushes the axial flow into the narrow

gap, which again increases the heat transfer coefficient on the wall in the narrow gap;

- The cross flow also reduces the flow temperature in the narrow gap thanks to the mixing with the flow from the main arrowhead flow passage, which further improves the heat transfer in such region.
- The cross flow redistributes the axial velocity in the arrowhead flow passage, shifting the maximum velocity toward the wall facing the incoming cross flow, which also results in an increased heat transfer ratio for this part of the brick. However, it also results in an impaired heat transfer on the surfaces facing the discharge of cross flow;

The vertical variation of the moderator brick geometry has significant impact on the cooling effect of the cross flow within each brick layer in Hartlepool/Heysham 1 reactor. The keys can significantly reduce the cooling effect of the cross flow, because it hugely reduces the cross flow velocity in the region, especially in the narrow gaps. However the cut-out part of the brick can enhance the cooling effect of cross flow at the bottom of the brick by allowing more fluids to flow through it.

The horizontal inter-brick leakage (HIBL) flow significantly reduces the axial flow in the narrow gaps or even creates some reverse flow which will induce hotter fluids from downstream in the NoCF case. This is why HIBL flow can results in a moderate temperature increase on the part of brick surface close to the narrow gaps (~5 ℃) in such case. This effect is small in the main arrow heat flow passage.

It is possible that flow towards the bottom of fuel channel is unstable when the cross flow is small. However its effect on the moderator brick temperature in the considered reactors is negligible. The flow instability was found to have disappeared when the cross flow is strong, which causes a more uniform axial velocity distribution in the arrowhead flow passage and reduces the velocity gradient in the azimuthal direction.

Chapter 5

Numerical Investigation of Flow and Heat Transfer in the Heated Non-uniform Geometry under the Buoyancy Aided Condition.

Inspired by the discovery of the flow instability in the narrow gaps formed by two fuel channels, the present research is extended to investigate the flow behaviour in tightly pack rod bundles. As shown in the literature review, much understanding of the flow behaviour in such non-uniform geometry had been established using experiments and numerical simulations. The features include the existence of large coherent flow structures, which are driven by high velocity gradients present in the vicinity of narrow part of the flow passage. The strength of the structures is mainly dependent on the geometry configuration.

It is noted, however, that almost all of the studies were carried out for an isothermal flow or under the forced convection conditions, even though the buoyancy effect is unavoidable in the real world, especially in a nuclear reactor. Due to the non-uniformity of the geometry, the strength of the buoyancy force at the different part of the flow passage would be different, which would result in a redistribution of the velocity in the geometry. Consequently, it is useful to study the effect of the buoyancy force on the behaviour of the coherent flow structure in the narrow gap. Meanwhile, the impact of the buoyancy force on the heat transfer rate is also interesting, since most early studies on the mixed convection focused on the uniform geometries like tube and channels, as shown in the literature review.

The effects of the buoyancy force on the coherent flow structure and the overall heat transfer rate of the tightly pack rod bundle has been studied by using the CFD method. To obtain accurate and detailed flow field, the large eddy simulation (LES) with wall-adapting local eddy viscosity model (WALE) is chosen. The simulations are carried out by using the commercial CFD software ANSYS Fluent 14.5. The obtained results are presented and discussed in this chapter.

5.1 Case Description

5.1.1 Geometry and Dimensions

Instead of a full rod bundle, a simplified geometry configuration is considered. The geometry can be seen in Fig. 5.1. It is a trapezoid channel with a rod mounted in it, which is the same as the channel adopted in the experimental work done by Wu & Trupp (1993). The diameter of rod D is 0.0508m. The size of the narrow gap S is 0.004m while the ratio S/D is 0.079. The lengths of the two trapezoid bases are 0.0548m and 0.127m, and the height as 0.066m. Then the hydraulic diameter (D_H) of channel is calculated to be 0.0314m. Since the periodic boundary condition is applied in the simulations, a relative short computing domain is considered (the length of the computing domain L is $10D_H$ = 0.314m). This configuration contained a narrow gap close to bottom edge and a relatively bigger gap at the opposite side. The two gaps are connected to each other through the main channels which were located both sides of the rod.

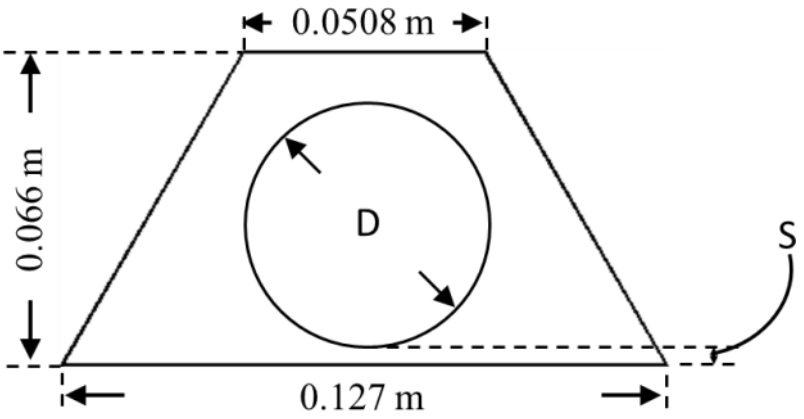

Fig.5.1 The Scheme of the considered geometry D = 0.0508m and S = 0.004m.

5.1.2 Simulations and numerical details

To investigate the effect of various buoyancy forces on the performance of the large coherent structures, four simulation cases have been created. The first (Case 1) is a forced convection case, while the following three (Case 2, 3 & 4) are mixed convection cases with different thermal boundary conditions. In all of the cases, the air at atmosphere pressure is adopted as the working fluid which flows at upwards with a bulk velocity U_b as 2.45 m/s. The mass flow rate and Reynolds number are 0.11527 kg/s and 5270 respectively. Periodic boundary condition is chosen to allow the flow to develop. Instead of considering all the variation of the fluids properties, the Boussinesq approximation is utilized to simulate the effect of the buoyancy force. The expansion coefficient β is set as $0.001\frac{1}{k}$ in the simulations. The gravity acceleration is 0 m/s^2 in Case 1 to ensure the strength of buoyancy force is zero, while it is set as -9.8m/s^2 in the other three cases. To avoid the extreme temperatures appearing in the sharp corner of the geometry, the constant wall temperatures instead of the heat flux are set in the cases (800k, 650k, 1427k and 6250k in Case 1, 2, 3, & 4 respectively). And, the computed buoyancy parameter Bo* (proposed by Jackson, 1989) is *0*, *1.5x10^{-6}*, *2.4x10^{-6}*and*1.7x10^{-5}*in the cases, respectively. So the liminarization effect of the buoyancy force is expected in Case 2 and 3, while the turbulence recovery regime is expected in Case 4.

Because of the use of LES with WALE model, a relatively fine mesh is required to resolve the flow in the near wall region. To control computing resources of the simulations, the mesh with non-equivalent element size has been generated. The mesh size is small in the near wall region but bigger in the main channel. An overview of the mesh can be seen in Fig. 5.2.The first near wall mesh nodes are in the range of $5 \leq \Delta x^+ \leq 17$, $0.13 \leq y^+ \leq 0.2$ and $10 \leq \Delta z^+ \leq 16$. It should be noted here that Δy, Δx and Δz are the non-dimensional size of mesh in wall normal, azimuthal and streamwise direction. There are at least 15 cells located between wall and y^+ = 20, (counted in the Case 1). The total number of the mesh elements is 7.8 million. The time step is set as 0.0001s in the cases, with a CFL number of~0.2. To reduce the numerical dissipation, the momentum equations are solved by using the

bounded central differencing scheme; the *second order upwind* scheme is applied to solve the energy equation, while the *bounded second order implicit* method is used to solve the transient component. And, the *SIMPLE* scheme is chosen for the pressure-velocity coupling.

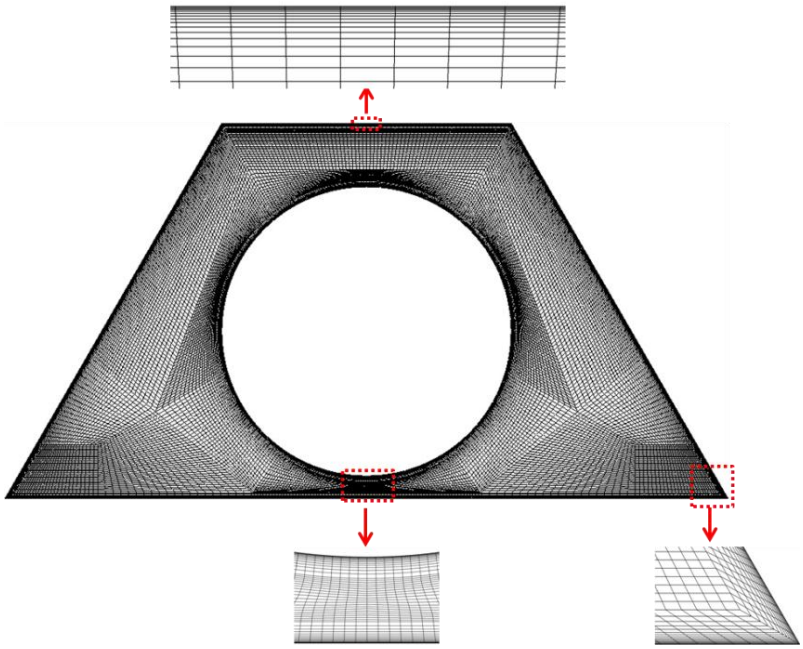

Fig.5.2 The overview of the mesh.

5.1.3 The locations used to extract the results

Before discussing the results, it is necessary to introduce the various locations and lines defined in the domain to present the results. The details of turbulence statistics are plotted along the blue lines shown in Fig. 5.3 (a), such as 'P1' to 'P3' and 'ML1' to 'ML3'. It would be useful to point out here that lines, 'ML1', 'ML2', and 'ML3', are the lines on the equal distance plane between rod and trapezoid channel wall. And 'P2' is started from the rod wall and ended at the geometrical centre of the main channel. The extension of the line can pass the circle centre of rod. There are monitors set at the black points like 'MP1' and 'MD', see Fig. 5.3 (a), which are used to record the temporal history of the velocities and temperature, which would be used for spectrum analysis and correlation analysis to study the moving feature of the flow structure. In addition, the instantaneous velocities are also recorded at 30

points located on 'ML1'. The same arrangement is set at location 'MP1' and 'MD' except the points are located axially at the different levels.

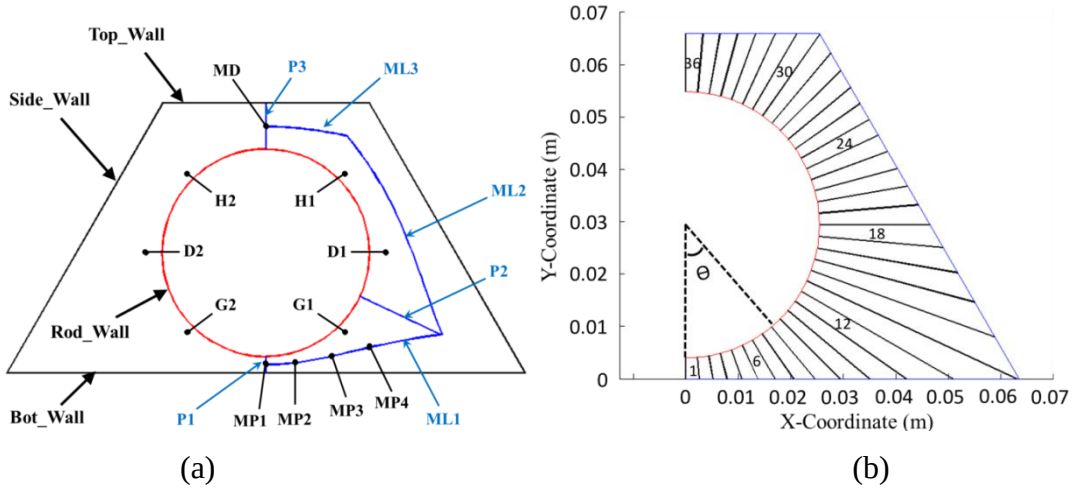

(a) (b)

Fig.5.3 Scheme of the flow passage, predefined lines and selected locations.

The local heat transfer coefficient and friction coefficient are more related to the local averaged values. The left part of the geometry was divided into 36 sections uniformly in terms of the angle. These sections are used to obtain the local mass flow rate or local mass flow rate weighted averaged values. They are numbered in the anti-clock direction. The first section is located in the narrow gap while last section is located in the top of the big gap; see Fig. 5.3 (b).

5.2 Results

First of all, the quality of the results is discussed. Since no DNS results or experimental data are available for the same geometry with Re = 5270. (The experiment done by Wu & Trupp, 1993 was based on the flow with Re = 52700.) The dimensionless velocity w^+ from Case 1 and the LES quality criteria mentioned in Chapter 3 are used to examine the accuracy of the simulations. Secondly, the instantaneous velocity field, correlations and power spectra density of velocities are utilized to investigate the performance of the flow structures in the channel under the different buoyancy conditions. Then, the results of the heat transfer rate and friction factor are documented. The last subsection is devoted to report and discuss the turbulence statistics, starting with the averaged velocity field and ending at the

discussion of the shear production term and body force production term in the turbulent kinetic energy.

5.2.1 Results quality

5.2.1.1 Dimensionless velocity profile

The non-dimensional streamwise velocity w^+ in Case 1 is plotted against y^+ as shown in Fig. 5.4. The results of the simulation are compared with log-law and the DNS result of You et al (2003), in which a buoyancy aiding flow in the pipe with Re = 5300 was studied. The mean velocity profiles show reasonably good agreement between the results obtained using different methods. It should be noticed that there is a drop of the velocity at the end of the line. This is mainly because the location of the maximum velocity does not match with the geometrical centre of the main channel.

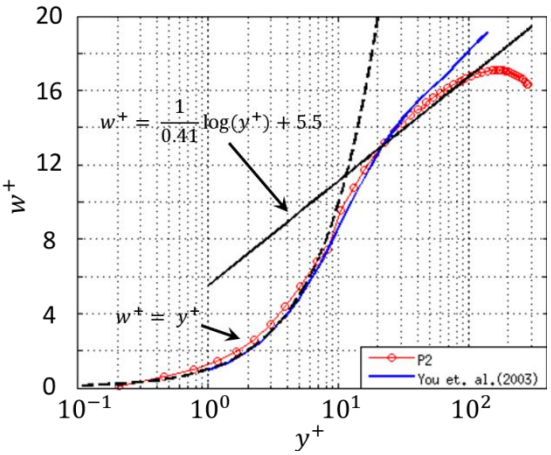

Fig.5.4 w^+ along the P2 in Case 1.

5.2.1.2 LES quality criteria

Since there is a lack of experimental or DNS data under similar conditions, using LES quality criteria to evaluate the quality of the results is necessary. There are two types of criteria considered in this section, the first (*S*) is proposed by Geurts and Frohlich (2002). When *S* approaches 0, the LES result is more accurate. The other is the LES_IQ_v proposed by Celik et al (2005). In this definition when LES_IQ_v is

closer to 1, the LES simulation approaches DNS. More details about these two criteria can be found in the Chapter 3.

Instead of using LES_IQ_v directly, two sub-versions are considered, namely*LES_Q01* and *LES_Q02*. The difference between these two criteria lies in the evaluation of the μ_{num} in LES_IQ_v. While the μ_{num} in the former one is considered as $\mu_{num} = \mu_{sgs}$, it in *LES_Q02* is $14.7\mu_{sgs}$. It should be noted these two values are the artificial numerical viscosity due to numerical dissipation. A more detailed discussion on these criteria is presented in Chapter 3.

Fig. 5.5, Fig. 5.6 and Fig. 5.7 show contour plots of the different criteria. Due to the symmetry of the geometry, the figures only show the contours at the left part of the channel. Since both of types criteria considering the SGS viscosity, which is a function of the size of mesh elements, the values of the criteria are also related to the size of the mesh elements. The shapes of the criteria values in the main channel, illustrated in the three figures, are actually representing the non-uniform distribution of the mesh element in the region. As shown in Fig. 5.5, very low values of *S* (close to 0) is located in the near well region, while the highest value of S is ~0.11 centred in the main part of the channel. It should be reminded that S is stand for the fraction of the turbulence kinetic energy modelled by the LES. As Pope (2000) had pointed out that good LES simulation should resolve at 80% of the turbulence kinetic energy. Consequently the simulations are of high quality. Further, the values of *LES_Q01* and *LES_Q02* approach 1 in the near wall region and ~0.97 in the main channel, which also demonstrates the good quality of the simulations, see Fig. 5.6 and Fig. 5.7.

Again, the peak value of *S* is decreased in Cases 2 & 3, but bounce back in Case 4. The opposite performance is found for the other two criteria in Fig. 5.6 and Fig. 5.7. The values of *LES_Q01* and *LES_Q02* increase in Cases 2 & 3, but decrease in Case4. These all demonstrate lesser SGS/numerical dissipation in Case 2 & 3, than in Cases 1 & 4.

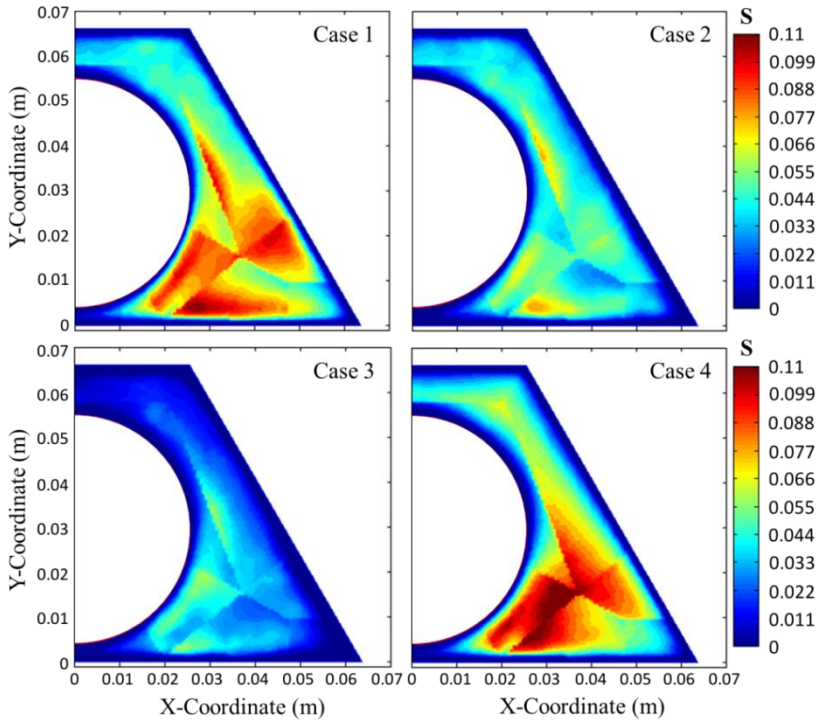

Fig.5.5 Large eddy simulation quality criteria *S*.

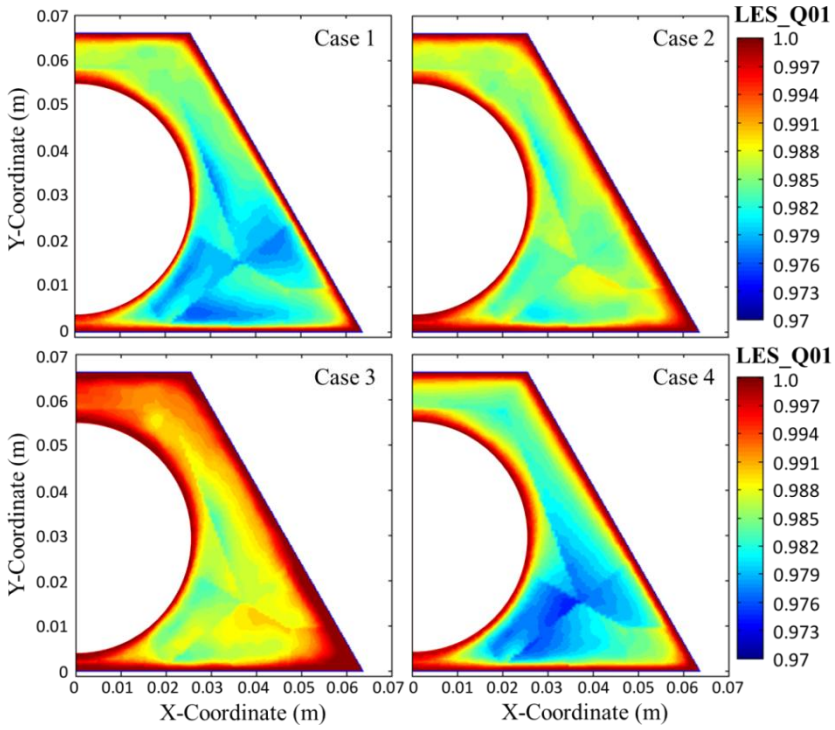

Fig.5.6 Large eddy simulation quality criteria *LES_Q01*.

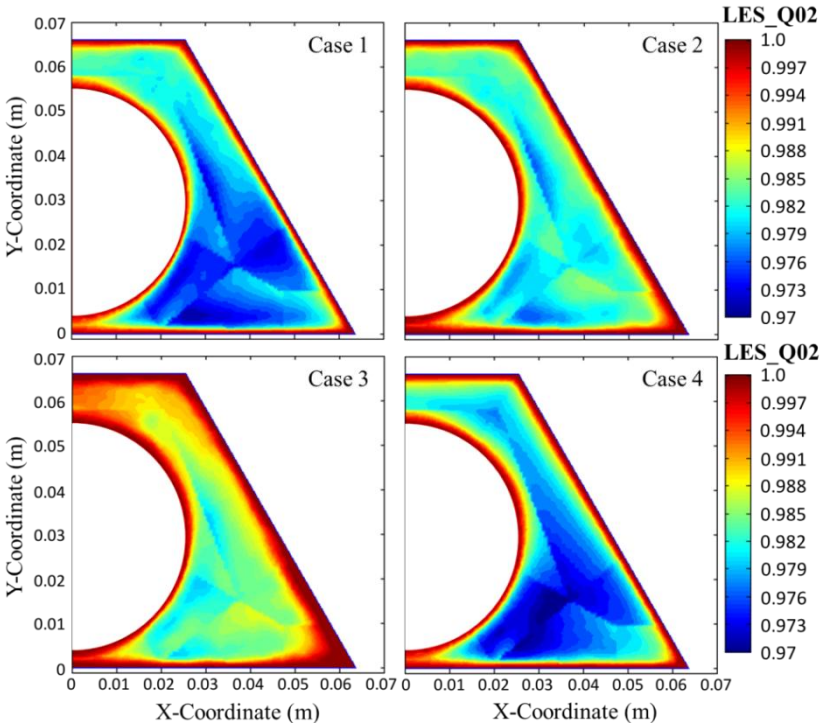

Fig.5.7 Large eddy simulation quality criteria *LES_Q02*.

Table 5.1 The maximum value of S and minimum value of *LES_Q01* and *LES_Q02.*

Cases	S_max	LES_Q01_min	LES_Q02_min
1	0.112	0.977	0.933
2	0.079	0.981	0.945
3	0.061	0.983	0.952
4	0.130	0.974	0.927

The maximum value of *S* (*S_max*) and the minimum values of *LES_Q01* (*LES_Q01_min*) and *LES_Q02* (*LES_Q02_min*) are listed in Table 5.1. The lowest value of S_max and highest value of LES_Q01_min and LES_Q02_min are in Case4 (0.13, 0.974 and 0.927 respectively). Although these values are worse than in other cases, they still indicate that fairly accurate simulations have been carried out for Case 4. It is also interesting to note that the *S_max* decreases while *LES_Q01_min* and *LES_Q02_min* increase with the increase of buoyancy force in Cases 2 & 3. This can be explained by the different effects of the buoyancy force in these 3 cases. The laminarization effect starts in Case 2, while it becomes strong in Case 3 resulting in a further reduction of the turbulence level. However, turbulence is regenerated in Case 4 thanks to the sufficiently high heat flux. It is noted that the *LES_Q02* in each case

does not change much compared to *LES_Q01*, even when severe artificial numerical dissipation is considered in *LES_Q02*.

5.2.2 Flow pattern

5.2.2.1 Instantaneous velocity field

The contours of the instantaneous temperature, streamwise/z-direction velocity component (w) and azimuthal/x-direction velocity component (u) at equal-distance plane, and the horizontal cross sections at different levels, are shown in Fig. 5.8. The contours clearly illustrate the existence of swinging flow structures in the vicinity of the narrow gap region in all of the cases. As found by other authors previously, such flow pulsations are not perfectly periodic but with some jittering, which can also be seen in Fig. 5.8. The wavelength of the swinging flow structure is not constant in Case 1/2/3. Furthermore, the general patterns of flow structures in the narrow gap region are similar in Case1, 2 & 3, but it is significantly different in Case 4. No wave is captured in the contour of *w* in Case 4 except some localised recirculation. Meanwhile, the streamwise velocity is higher in the narrow gap than in the main channel in Case 4. The shape of the waves, seen in the temperature contours and *w* contours agree very well with each other in all of the cases, which indicate a good correlation between the instantaneous streamwise velocity and temperature.

In order to investigate such flow structures with more details, representative time history of normalised fluctuating azimuthal velocity ($u^{'}/U_b$) and streamwise velocity ($w^{'}/U_b$) at 'MP1' and 'MD' are presented in Fig. 5.9andFig. 5.10.

As shown in Fig. 5.9 (a), there are strong and almost regular oscillations of spanwise velocity in the narrow gap in all of the cases. But velocity from Case 4 is more irregular than others. The amplitude of the oscillations can reach as high as ~35%U_b in Case 1. The amplitude of the oscillation decreases slightly with the increase of the buoyancy force in Case 2 (~25% U_b) and Case 3 (~20% U_b) but recovers in Case 4. It is shown in Fig. 5.9 (a) that the period of the oscillation is not perfectly constant in the cases, which is consistent with the finding of the change of the wavelength in the

above instantaneous velocity contours. The dominant periods of the oscillations in Cases 1 & 2 are similar to each other. It decreases a little in Case 3, but significantly increases in Case 4.

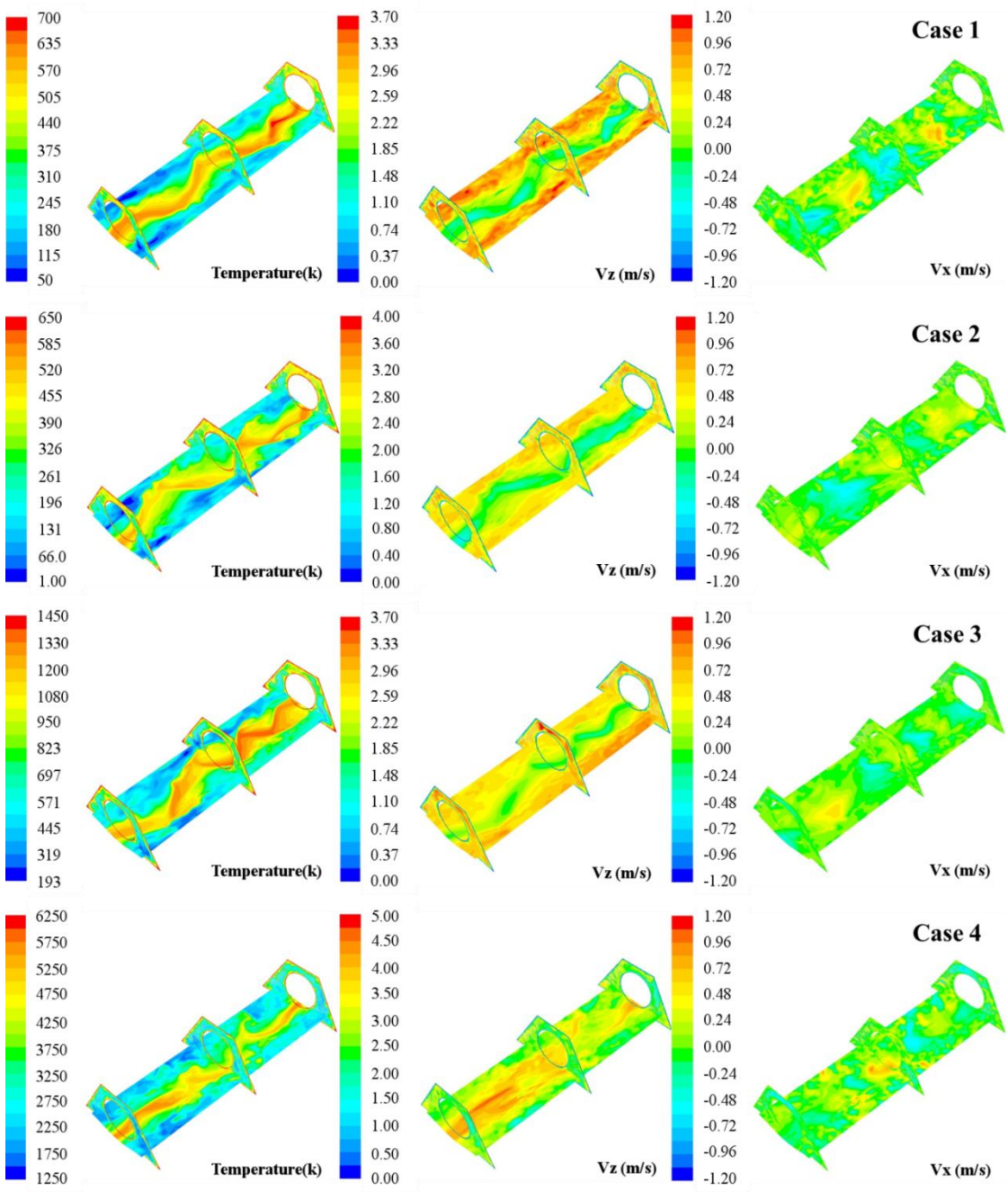

Fig.5.8 Instantaneous flow fields of all of the cases.

Regarding the signal of u' at MD, there is a very weak periodic oscillation with strong turbulent noise containment at 'MD' in Case 1, refer to Fig. 5.9 (b). The period is different from the oscillation in the narrow gap. Such oscillations are hugely

suppressed and almost vanish in Case 2, but strengthened in the other two cases, especially in Case 4. It is interesting to note that the dominant periods of such oscillations at 'MD' in the different cases are very similar to each other.

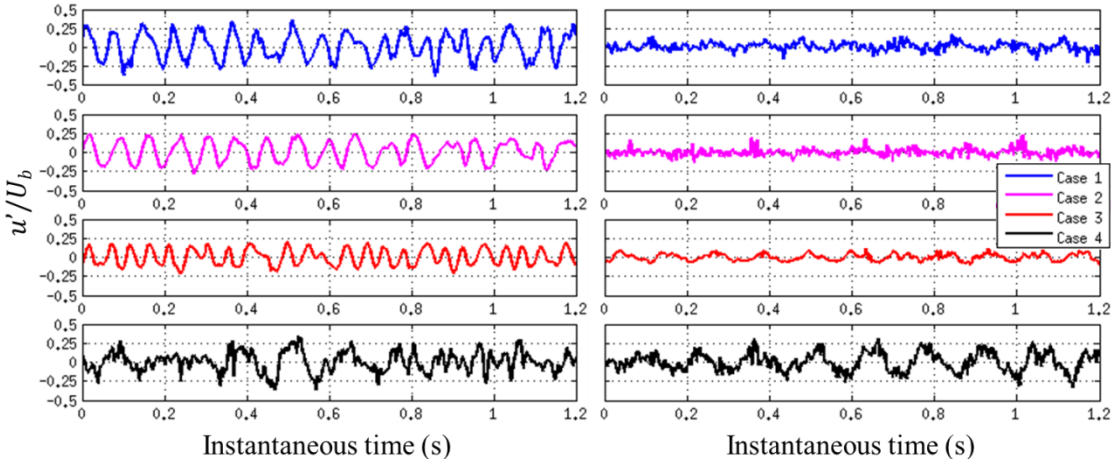

(a) (b)

Fig.5.9 The ratio u'/U_b at (a) MP1; (b) MD in all of cases.

Similar to u'/U_b, the quasi-periodic oscillations also exist in the history of w'/U_b at 'MP1' in the cases, see Fig. 5.10 (a). The variation of the period of the oscillations is more profound in the history of w'. The behaviours of the signals in Case 1 and Case 2 are again very similar to each other, refer to Fig. 5.10 (a). Furthermore, the dominant periods of w'/U_b at MP1 in the cases are about a half of that of u'/U_b, except for Case 4. In Case 4 such period is more or less the same as that of u'/U_b. This is because, in Case 1, 2 & 3, the flow in the vicinity of the narrow gap swings from one side to the other side, as shown in the countors. It means that the streamwise velocity at the centre of narrow gap changes twice, with the flow oscillating for a full cycle. However it is not the case in Case 4. More details on the flow structure in the vicinity of the narrow gap will be discussed in the following sections.

Regarding the w'/U_b at 'MD', the regular oscillations are absent in Case 1 and Case 2, while they can be found in Case 3 and Case 4, refer to Fig. 5.10 (b), which are more clearly shown in the spectrum. It is however shown that the signal in Case 4 is heavily affected by turbulent noise. This can be explained by the regeneration of the turbulence in the case. Combining with the behaviour of u' at 'MD', it is reasonable

to assume that there is also a flow structure passing in the big gap. Although it is weak under the force convection condition or weak buoyancy condition, it is enhanced with the increase of buoyancy force.

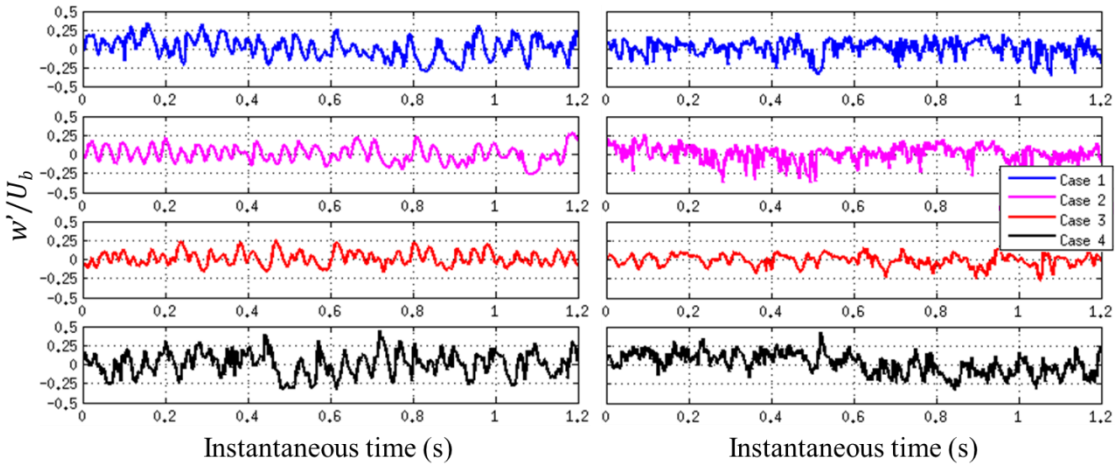

(a) (b)

Fig.5.10 The ratio w'/U_b at (a) 'MP1'; (b) 'MD' in all of cases.

5.2.2.2 PSD of fluctuating velocity component

It is difficult to determine the exact value of the dominant frequency of the flow structures just by studying the instantaneous velocity history. The power spectra density is a useful and accurate tool to characterize frequency of the large flow structures. The Welch's power spectral density estimate (more details above this method can be found in Chapter 3) is utilized to obtain the power spectra density of the instantaneous signals as 'MP1' and 'MD' shown in the above section.

Fig. 5.11shows the energy spectrum of u', w' at selected locations ('MP1' and 'MD') of the four cases. The colours are used to discriminate the results from the different cases. To make the results from different cases more distinguishable, the original results from Cases 1, 2, 3 and 4 are multiplied by a factor of '10^0', '10^2', '10^4' and '10^6' respectively. The power spectral densities of u', w' are noted as 'PSDX', 'PSDZ' while 'f_p' stands for the peak/dominant frequency in the following discussion.

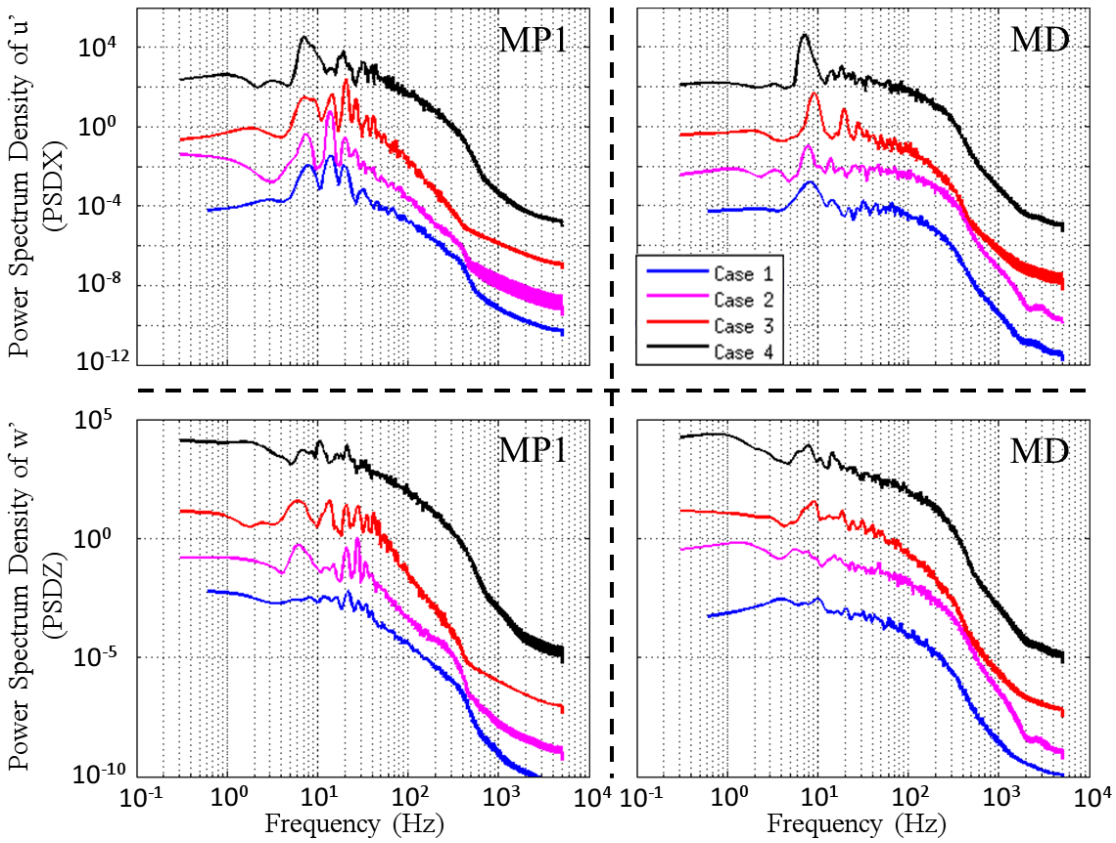

Fig.5.11 Power spectral density of the $\boldsymbol{u'}$ (PSDX) and $\boldsymbol{w'}$ (PSDZ) at 'MP1' and 'MD' in all of the cases. The results of Cases 2, 3 and4 are multiplied by a factor of 10^2, 10^4 and 10^6, respectively.

Similar to the results of experimental work done by Wu and Trupp (1993), the pronounced peak in PSDX is not only found in the narrow gap, referring to location 'MP1', but also at the centre of the big gap 'MD' in all of the cases, including Case 2. This again implies the existence of a large flow structure passing the bigger gap. Regarding PSDX at MP1, it is also interesting to note that there are secondary peaks located at both sides of the dominant peaks in the cases, except Case 4. This suggests that the coherent flow structures in the narrow gap are complicated. They are likely to be affected by other structures in the channel as well. The f_p of u' at MD in Cases 1, 2 and 3 is every similar to the frequency of the sub-peak located at the left of the dominant peak, which means that the influence of the flow structures passing the big gap can spread to the narrow gap in these three cases. It should be mentioned that that peak frequency of u' at MP1 in Case 4 is the same as it in the centre of narrow gap. It is reasonable to infer that the structures in the narrow gap and big gap are strongly correlated in this particular case.

The f_p values of PSDX at 'MP1' and 'MD' in all cases are listed in Table 5.2. In Cases 1 & 2 such peak frequencies at 'MP1' are very close to each other (13.4 Hz and 13.7 Hz, respectively), while they are increased in Case 3 (~20.75Hz), but decreased in Case 4 (~7.32 Hz). So, the dominant periods of the flow structure in the cases are 0.075s, 0.073s, 0.048s and 0.137s, respectively. The value of this f_p remains the same with the location moving away from the centre of the narrow gap for f_p 'MP2', 'MP3' and 'MP4', which mean that the impact of the flow structures in the narrow gap spreads into the main channel. The peak frequency of u' at 'MD' is changed by very little under the influence of buoyancy force. The highest PSDX at 'MD' is 9.16Hz in Case 3. The smallest is 7.32 Hz in Case 4. The values in Cases 1 and 2 are 8.55 Hz and 7.93 Hz. The dominant periods of the flow structures in the big gap in Case 1, 2, 3, and 4 are 0.117s, 0.126s, 0.109s and 0.137s respectively.

Table 5.2 The frequencies (Hz) of peaks in the power spectrum density of u' at selected locations:

Locations	Case1	Case2	Case3	Case4
MP1	14 Hz	13.7 Hz	20.75 Hz	7.32 Hz
MP2	14 Hz	13.7 Hz	20.75 Hz	7.32 Hz
MP3	14 Hz	13.7 Hz	20.75 Hz	7.63 Hz
MP4	14 Hz	13.7 Hz	20.75 Hz	20.14 Hz
MD	8.55 Hz	7.93 Hz	9.16 Hz	7.32 Hz

Considering the PSDZ at 'MP1', the peak is much weaker than its counterpart in PSDX. It is also found that the values of f_p are nearly double these of PSDX in Case 1 and 2, but there is no pronounced peak shown in Case 3, while the value in Case 4 is very similar to its counterpart (f_p of PSDX at 'MP1'). The reasons have been discussed in the above section. In Cases 1, 2 & 3, the centre of the narrow gap is also the centre of the swinging flow structures. So the axial velocity changes twice, when the spanwise velocity changes once. Meanwhile, the magnitude of the w' oscillation is small due to the limited variation of the flow passage size in the vicinity of narrow gap, which makes the value of PSDZ weaker as well. In Case 4, the original flow structure is fundamentally changed, which will be discussed in the following sections.

In contrast to the absence of spikes in PSDZ at 'MD' in Cases 1 & 2, there are visible spikes in PSDZ at 'MD' in Cases 3 and 4. Meanwhile, the f_p of PSDZ at 'MD' in Case 3 and 4 is similar to f_p of PSDX at the same locations. This again implies that the structures passing 'MD' are different from the dominant structures in the narrow gap.

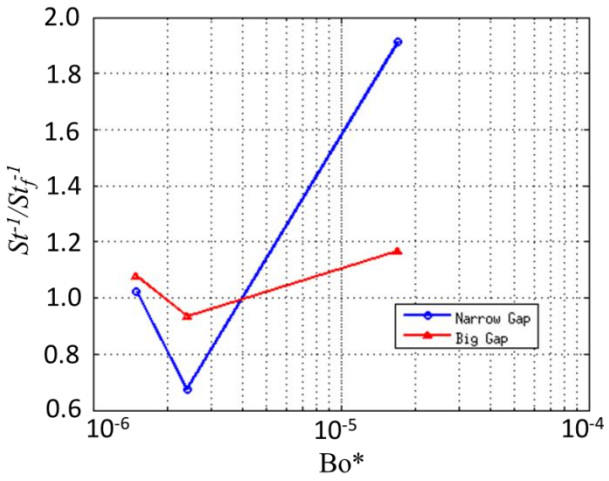

Fig.5.12 Ratio of St^{-1} in buoyancy influenced case over St_f^{-1} in forced convection case.

Consistent with findings by others in experiments and numerical simulations before, the peak frequency in the spectra of the flow in narrow gap of similar geometric configurations depends on the geometry and flow velocity, while the non-dimensional frequency Strouhal number (*St*), which is defined as fD_h/u^* (where f is the peak frequency, D_h is the hydraulic diameter of the channel and u^* is the friction velocity) is just dependent on the geometry configuration. In the current simulation the St^{-1} evaluated in Case 1 is 0.3787, which is about double the value (0.16) in Wu and Trupp (1993) for the same geometry configuration. However, the St_{Ub}^{-1} evaluated by using the bulk velocity is 5.57, which is very close to the experimental value of 5.20. A possible reason to explain this inconsistency is that the relationship between the friction velocity and Re number is not linear. It also indicates the *St* is more correlated with U_b than with friction velocity. To avoid confusion, the *St* mentioned below is evaluated by using bulk velocity. The relationship between St^{-1}/St_f^{-1} and buoyancy parameter Bo^* is shown in Fig. 5.12. Here, *St* is the Strouhal number in buoyancy influenced cases and St_f is from Case 1.

A negative relationship between St^{-1} and Bo^* is demonstrated in Fig. 5.12 when the buoyancy force is small, see the values of St^{-1}/St_f^{-1} in Case 2 & 3. But St^{-1} increases

with the rise of the buoyancy force as Bo^* is beyond certain value. Meanwhile, it can also be seen from the figure that St^{-1} in the big gap follows the same trend, but the response of St^{-1} to the change of Bo^* is more moderate. It is interesting to note the relationship between St^{-1} and Bo^* is similar to the relationship between Nu and Bo^* in the buoyancy aiding mixed convection as shown in the literature review of the mixed convection.

5.2.2.3 Correlations Analysis

Correlation analysis is used to further the understanding of the flow structure in the channel. The cross correlation functions of u' (XR_{uu}) between 'MP1' and 'MD' is shown in Fig. 5.13, and XR_{uu} between locations G1, G2, H1 and H2 are presented in Fig. 5.14.

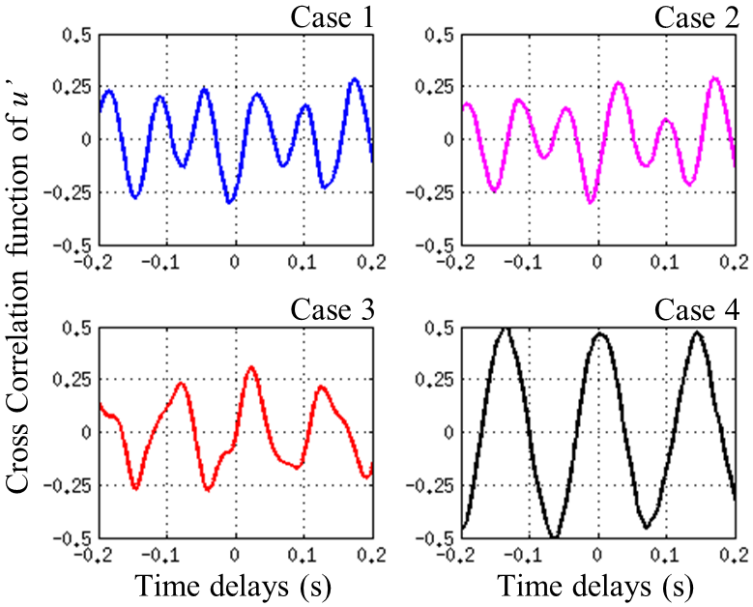

Fig.5.13 The cross correlation function of $\boldsymbol{u'}$ between 'MP1' and 'MD'. The legend is the same as shown in Fig. 5.10.

As illustrated in Fig. 5.13, u' at 'MP1' is correlated with that at 'MD' in all of the cases. And, the correlation is very strong in Case 4 but weaker in Cases 1 & 2. In Case 4, the maximum value is at 0s delays. Statistically, flow passes these two locations in the same direction (regarding x-coordinate). Meanwhile, the maximum/minimum value of the XR_{uu} is away from 0s delays in the other three cases,

which is much more obvious in Case 3.It means that there is a phase difference between the flow structures at 'MD' and 'MP1'. So it is reasonable to guess that the flow structures in the narrow gap and big gap in these three cases are separated but linked with each other due to the continuity.

The *u'* at ‘G1’ and ‘G2’ are strongly correlated with each other in Cases 1, 2 & 3, see in Fig. 5.14 (a). Meanwhile, the cross correlation of u' at locations ‘G1’ and ‘G2’ reach the maximum with zero time lag, which means that the flow on either side of the gap moves in the same manner, namely they are part of a large flow structure. It again suggests that the dominant flow structures in the narrow gap are the flow swing from one side to the other side in these three cases. It is also shown in the figure that the period of XR_{uu} between ‘G1’ and ‘G2’ remains about the same in Cases 1 and 2, while it is apparently diminished in Case 3. However, the XR_{uu} between ‘G1’ and ‘G2’ is very small in Case 4. This indicates the size of the flow structures in the region significantly decreased.

As illustrated in Fig. 5.14 (b), the flow structures in the big gap are enhanced in Cases 3 and 4. The XR_{uu} between ‘H1’ and ‘H2’ in Cases 3 & 4 are much stronger and more regular than their counterparts in Cases 1 & 2. Similar to the observation at ‘G1’ and ‘G2’, maximum of XR_{uu} with zero time lag again indicates that these two locations are covered by the same flow structure. Furthermore, it is reasonable to infer that these two locations are dominated by the flow structures passing 'MD', not the flow structures crossing the narrow gap.

The XR_{uu} between ‘G1’ & ‘H1’ or ‘G2’ & ‘H2’ are very similar to each other. In Cases 1 & 2, the negative XR_{uu} can be observed at the zero delays. It suggests that the fluid passing ‘G1’ & ‘H1’ or ‘G2’ & ‘H2’ statistically moves oppositely regarding x-direction. This is again indication that ‘G1’ & ‘H1’ or ‘G2’ & ‘H2’ are involved in the same flow structures The irregular shape and the smaller value of the cross correlation of u’ at these two sets of locations in Case3 show the weak link between the structure passing ‘G1’ & ‘H1’ or ‘G2’ & ‘H2’. In Case 4, the strong positive correlation occurs at the zero delays. Considering the continuity, ‘G1’ &‘H1’ or ‘G2’ & ‘H2’ must involve in one type of flow structures or two types of highly

correlated separate flow structures. It is also interesting to note that correlation at these two sets of the location is even stronger than it between the ‘G1’ & ‘G2’.

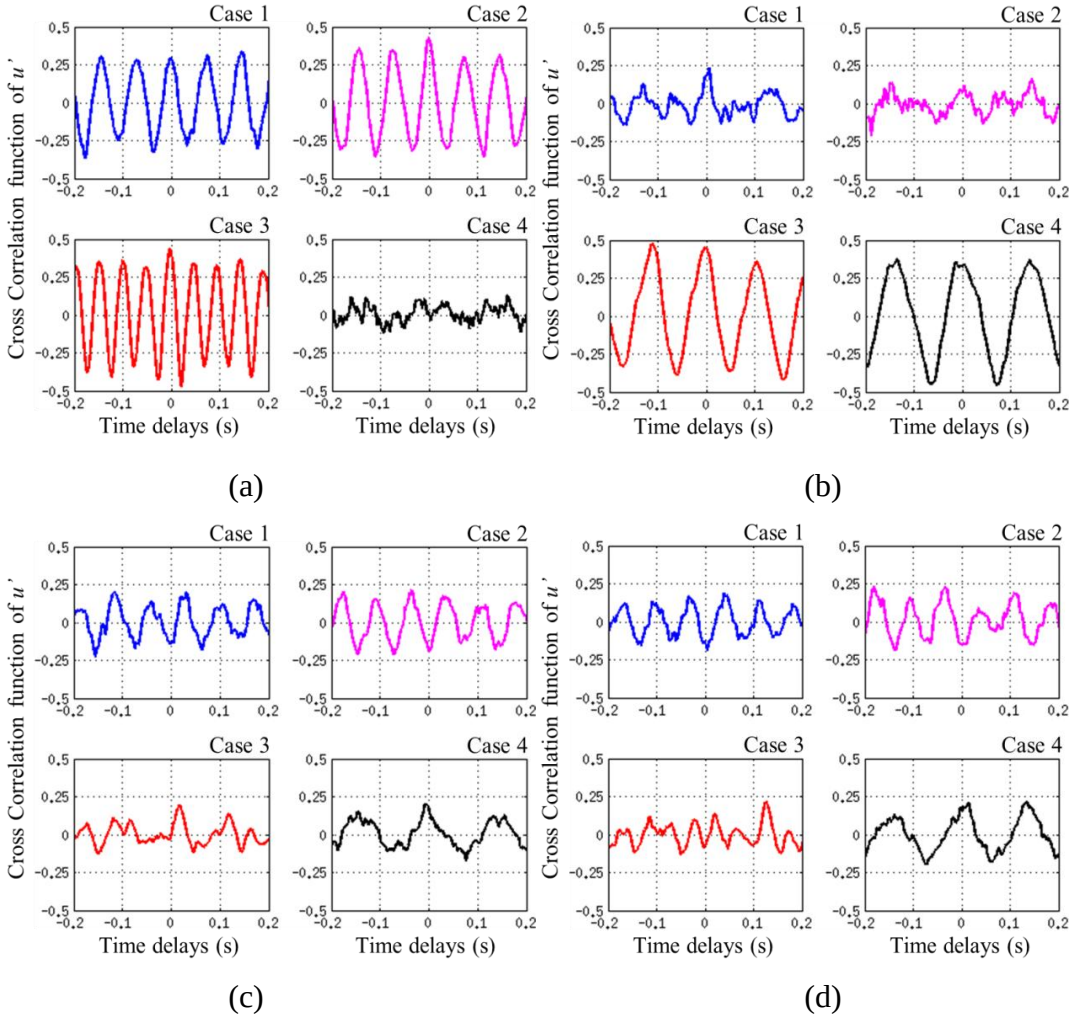

Fig.5.14 Cross correlation functions of u' at locations (a) ‘G1’ and ‘G2’; (b) ‘H1’ and ‘H2’; (c) ‘G1’ and ‘H1’; (d) ‘G2’ and ‘H2’.

From the above discussion, it is reasonable to conclude that there are at least two large flow structures co-existing in the considered channel in Cases 1, 2 & 3. In the narrow gap region, the dominant flow structure is the continuous swinging wave about the centre of the narrow gap. There is another flow structure dominant the big gap region. These two types of flow structures are correlated with each other. But visible phase differences again indicate they are separate. Although, the dominant frequency of the flow structures in the narrow gap and big gap is almost the same and the strong correlation can be observed in the at difference sets of location ‘MA’ & ‘MD’, ‘H1’& ‘G1’, and ‘H2’ & ‘G2’ as mentioned above. But the flow structures

is still separate from the flow structures in the big gap, as the week link between the flow structures passing ‘G1’ & ‘G2’ in the case.

The azimuthal size of the large flow structure in the narrow gap can be studied using the cross-correlations of u' between 'MP1' and the other 30 points on 'ML1' (see Fig. 5.15), while the axial size of the dominant flow structure passing narrow/big gap can be assessed by using the cross correlation of u' between the point located axially at MP1 and MD down the channel, see Fig. 5.16.The value 0.2 is regarded as the minimum correlation used to indicate the size of the structure. The spread of the structure at the spanwise direction is almost the same in the first 3 cases, while a visible shrink can be seen in Case 4. As shown in Fig. 5.16, the wavelength of the large flow structure in the narrow gap is about same in Case 1 and Case 2 (0.16m), but reduced about ~60% to ~0.1m in Case 3, while it is hugely increased in Case 4, see Fig. 5.16 (a). The wavelength of the flow structure passing the large gap is so big only one wave is captured in Cases 3 & 4. However it is not captured in Case 1 and 2, see Fig. 5.16 (b). This probably is due to the weakness of such flow structure and strong contamination due to the turbulent eddies in Case 1 & 2.

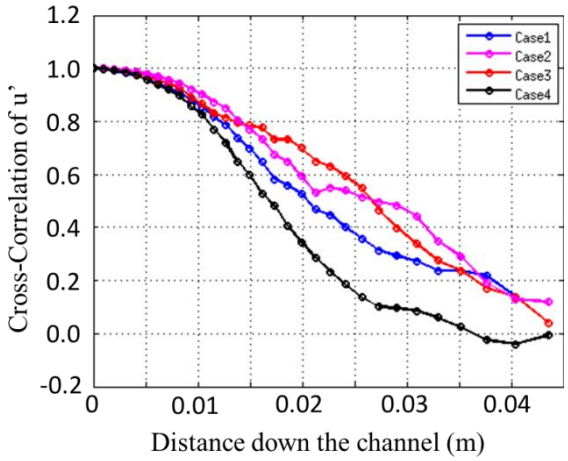

Fig.5.15 Cross Correlation of *u'* at centre of narrow gap and different positions moving toward the centre of main channel.

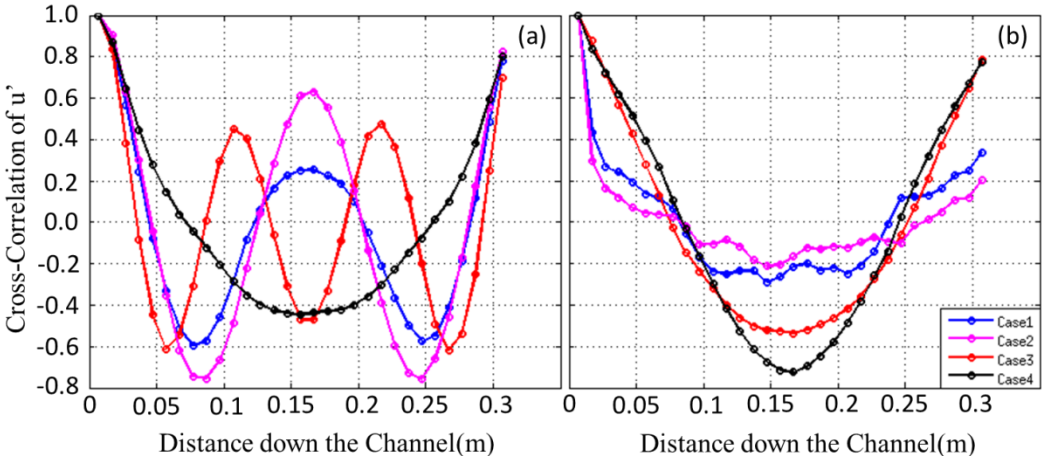

Fig.5.16 Cross correlation of *u'* at different axial points located in the middle of narrow gap and big gap.

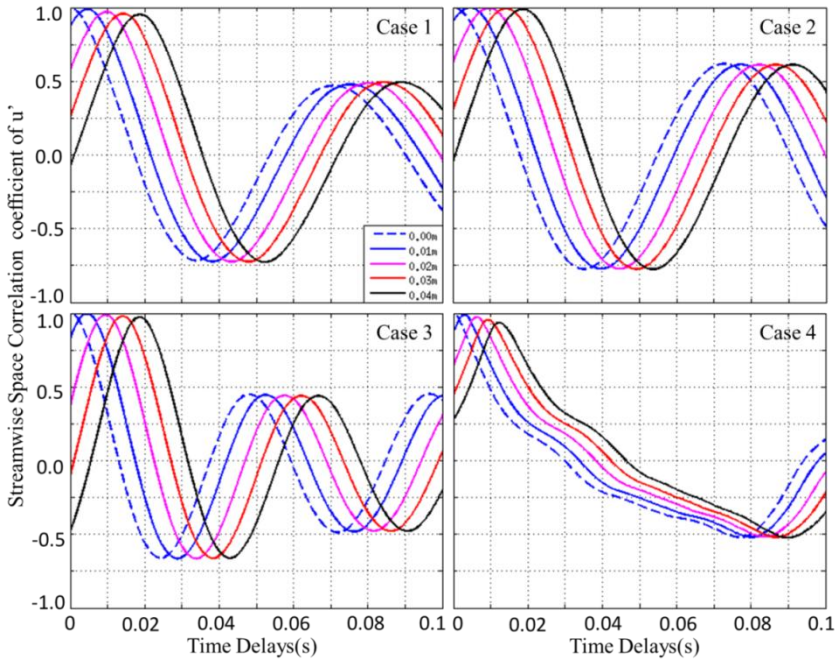

Fig.5.17 The streamwise space-time correlation function of u' between point at 0.07 and other points down the channel at centre of narrow gap in all of the cases.

More accurate wavelength of the dominant flow structure can be evaluated by using its convective velocity and the dominant frequency. The convection velocity of the vortices can be evaluated by the ratio of streamwise distance and time delay of the maximum correlation between the two axially aligned points. Fig. 5.17 is a representative plot of the streamwise space correlation of u' in the centre of the narrow gap as a function of time delays, in all cases, whereas, Fig. 5.18 shows that in the centre of the big gap. It should be noted, the reference point is located at the

0.007m down the channel. The values in the legend of the figures are the distances between the points to the reference point. The Fig. 5.17 again illustrates the almost regular and continuous waving flow structures existing in the narrow gap in all the Cases.

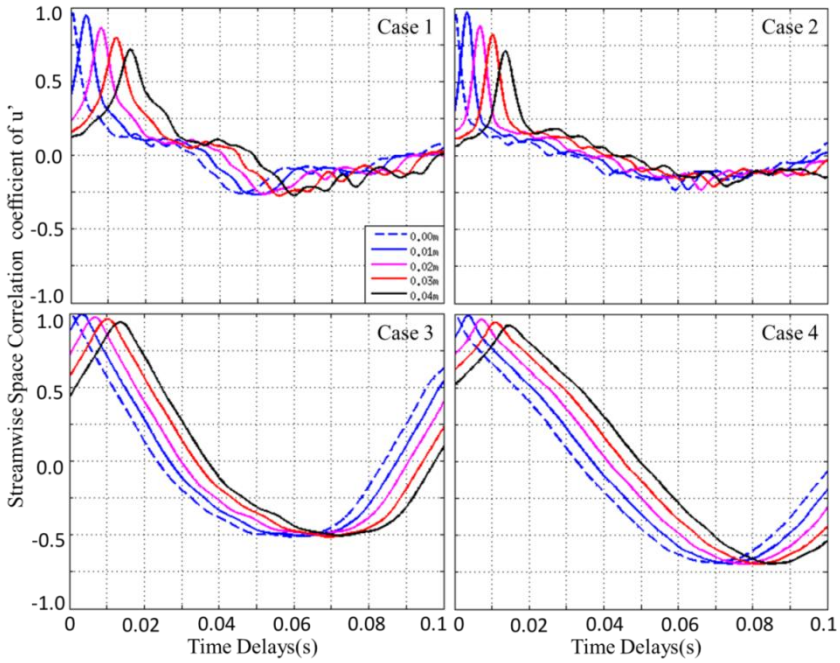

Fig.5.18 The streamwise space-time correlation function of u' between point at 0.07 and other points down the channel at centre of big gap in all of the cases.

However, such continuous flow structures in the big gap are only established in Cases 3 & 4, see Fig. 5.18. The convection velocity and normalized wavelength of flow structure in the narrow gap and big gap are listed in the Table 5.3. The wavelength is considered as convection velocity (U_c) divided by the dominant frequency (f_p) of the flow structure times hydraulic diameter (D_h). The convection velocity of the wave in the narrow gap remains similar (~2.16m/s) in the laminarization cases, Cases 1, 2 & 3, but the wavelength decreased from $5D_h$ to $3.33D_h$ in Case 3. Whereas, the wavelength in Case 4 is greatly increased (~$14D_h$), while the convection velocity is 50% higher (~3.31m/s).The difference among convection velocities of flow structures through big gap in cases is very small (from ~2.5m/s to 2.9m/s), and the wavelengths in the different cases are very close to each other as well. The shortest wavelengths is in Case 1 (~ $9D_h$) and the longest in Case

4 (~11.7D_h) which is similar to that in Case 2 (~11.5D_h), but higher than ~10D_h in Case 3.

Table 5.3 The convection velocity and wavelength of flow structures in narrow gap and bigger gap.

	Narrow Gap		Big Gap	
	Convection Velocity (m/s)	Wave Length/Dh	Convection Velocity (m/s)	Wave Length/Dh
Case1	2.159	4.912	2.488	9.267
Case2	2.156	5.013	2.857	11.473
Case3	2.176	3.339	2.913	10.127
Case4	3.313	14.412	2.689	11.697

Note: '*Dh*' is the hydraulic diameter of the considered channel.

5.2.3 Mixing factor

Due to the existence of the flow structures, the turbulence mixing between the either sides of narrow gap is enhanced. It is useful to explore the mixing factor due to the narrow gap flow. As mentioned in the literature review, the mixing factor can be evaluated by the equation introduced by Rehme (1992). More details can be found in the Chapter 2. It is useful to recall the equation adopted to calculate the mixing factor induced by the swinging flow structure at the bottom of the channel.

The mixing factor is evaluated by

$$Y = \frac{u_{eff}\,\delta_{ij}}{\bar{\varepsilon}} \tag{5.1}$$

where δ_{ij}, in the equation above, is the distance between the subchannels, the value of which value is 0.09m the same as proposed by Wu and Trupp (1994). u_{eff} and $\bar{\varepsilon}$ are the effective mixing velocity and reference eddy viscosity, which are evaluated by the following equations:

$$u_{eff} = \sqrt{\int_{f_p-\frac{f_p}{4}}^{f_p+\frac{f_p}{4}} E_{uu}\,(f)df} \tag{5.2}$$

where f_p is the peak frequency in the power spectra density, $E_{uu}(f)$ the power spectra density function.

$$\bar{\varepsilon} = 0.0177 \nu Re \sqrt{f_t} \tag{5.3}$$

whereν is the kinematic viscosity and f_t is the friction factor. The value of f_t is 0.03712, which is converted from the You et al, (2003). So $\bar{\varepsilon}$ is $2.6 * 10^{-4}$.

Moller (1992) found that the spectral density decreases as the location moves away from the centre of the gap. Meanwhile, u_{eff} is usually calculated away from the centre, at the location $x/\delta_{ij} = 0.2$ as proposed by Rehme (1992). Most available spectral density data are located at the centre of the narrow gap. A correlation was suggested by Rehme (1992) for the gap between a rod and a wall:

$$u_{eff} = u_{eff,x=0} 10^{-0.78((S/D)-1)^{-0.33}(x/\delta_{ij})} \tag{5.4}$$

The value of u_{eff} obtained at 'MP1' ($x/\delta_{ij} = 0$) and other two locations 'MP2' ($x/\delta_{ij} = 0.08$) and 'MP3' ($x/\delta_{ij} = 0.18$) are documented in Table 6. The u_{eff} at the 'MP1' in Case 1 is 0.331 which is very similar to the value of 0.34, published by Wu and Trupp (1994). It is different from the assumption suggested by Rehme (1992) and accepted by Wu and Trupp (1994) and Chang and Tavoularis (2008), which indicates u_{eff} is the proportional to $Re^{0.9}$.

With the location moving away from the centre of the narrow gap, u_{eff} decreases. This is mainly due to the decreased peak power spectra value. The values in the table also clearly indicate that the u_{eff} at all of the locations decrease with the increase of the buoyancy force. It is interesting to note that the rate of decrease is different at different range of Bo^*. Y decreases very slowly from Case 1 to 2, or, from Case 3, to 4, but drops rapidly from Case 2 to 3.

According to the values shown in Table 5.4, Rehme's correlation can predict the u_{eff} away from the centre of narrow gap with reasonable accuracy. At 'MP3' the ratio between the prediction of correlation and simulation ($0.08^*/0.08$) is around 0.85. With the location moving further away to 'MP2' the accuracy of the correlation is

more likely affected by the buoyancy force. The ratio varies from 0.088 to 1.26. This is because the buoyancy force decreases the azimuthal size of the flow structure in the bottom of the channel.

Table 5.4 u_{eff} at certain locations and the ratio between values calculated from simulation and correlation.

	u_{eff}					Ratio [Eq.(4)/simulation]	
Cases	x/δ_{ij} = 0	x/δ_{ij} =0.08	x/δ_{ij} =0.08*	x/δ_{ij} =1.8	x/δ_{ij} =1.8*	x/δ_{ij} =0.08	x/δ_{ij} =0.18
1	0.331	0.268	0.237	0.178	0.157	0.885	0.880
2	0.327	0.272	0.234	0.170	0.155	0.861	0.913
3	0.206	0.182	0.148	0.130	0.098	0.810	0.752
4	0.199	0.170	0.143	0.075	0.094	0.837	1.261

Note: * means the values are calculate by using equation (4).

Since the subchannels are connected with each other through the symmetric plane of the geometry and the azimuthal size of the structure varies with the imposed buoyancy force, it is more reasonable to calculate the mixing factor Y using u_{eff} at the centre of narrow gap. The mixing factors calculated by using the u_{eff} at 'MP1' are listed in the Table 5.5. Y_f is the mixing factor from Case 1, the value of which value is 113.5. It is about 7.5 times the value of 15.4 shown in the article by Wu and Trupp (1993), due to the almost unchanged u_{eff} in the current study. Y decreases with the increase of the buoyancy force. It is decreased rapidly before Bo_0^* (Y decreases rapidly when the Bo^* increases from $1.5*10^{-6}$ to $2.4*10^{-6}$ in Case 2 and 3), however the decreasing ratio reduces rapidly beyond Bo_0^*.

Table 5.5 Mixing factor from cases;

Cases	Y	Y/Y_f
1	113.50	1
2	112.04	0.987
3	70.692	0.623
4	68.224	0.601

Note: Y_f is the Y of Case 1.

All in all, the results obtained in the current study illustrate the effective mixing velocity u_{eff} is unrelated to the Reynolds number. But it changes with the distance between the locations. And, it does decrease with the increase of the buoyancy force which is similar to the relation between Y and Bo^*. Also, the decreasing ratio is different at different range of Bo^*.

5.2.4 Performance of the heat transfer and Friction Coefficient

5.2.4.1 Performance of heat transfer

In spite of enormous amount of heat transfer data on the mixing convection in vertical pipes or channels, the knowledge on the channels similar to the current geometry configuration is still limited. The heat transfer data of the present cases are discussed in this section.

The influence of the buoyancy force on the heat transfer of mixed convection in the current channel is compared to the mixed convection in pipe. The DNS data credited to You et al.(2003) and results obtained by using Launder-Sharma model by Kim et al.(2008) have been chosen here for this purpose. The DNS study considered here was devoted to investigating the fully developed turbulent mixed convection due to air flowing upwards in a vertical pipe with the Re number of 5300. The work done by Kim et al. (2008) was to investigate the performance of the different models on predicting the mixed convection under conditions as reported in You et al. (2003). Again, buoyancy aided flow was considered, which is the same as the current investigation.

To obtain a general picture of the forced and mixed convection heat transfer, the Nusselt number (*Nu*) of the considered cases and results of the forces convection case reported by You et al. (2003) have been show in Fig. 5.19(a), and the effect of buoyancy force on Nu of current geometry configuration and pipe (You et al. (2003) and Kim et al. (2008)) are shown in Fig. 5.19(b).

The *Nu* of forced convection in the current geometry is very similar to DNS result of heated pipe. The difference between the values in the two geometries is just 0.52 (~2.86%), refer to Fig. 5.19 (a). It also shows that *Nu* firstly decreases with the increase of the buoyancy force. It increases again when the heat flux is sufficiently high. Such trend is the same as the buoyancy aided pipe flow. However, the significance of buoyancy effect on the mixed convection in these two geometries is different. In general, the heat transfer deterioration is less severe and recovery occurs much earlier than in the pipe flow, which is the same as demonstrated in the Forooghi et al. (2015).As shown in Fig. 5.19 (b), Nu/Nu_f in the present cases is slightly smaller than that of pipe as $Bo^* \cong 1.6 \times 10^{-6}$, Case 2), while Nu/Nu_f is generally much higher than the values of the heat flow in the pipe under the buoyancy aided condition as $Bo^* > 2 \times 10^{-6}$. The value of the buoyancy parameter at which the strongest heat transfer deterioration occurs is more or less the same in two types of channels.

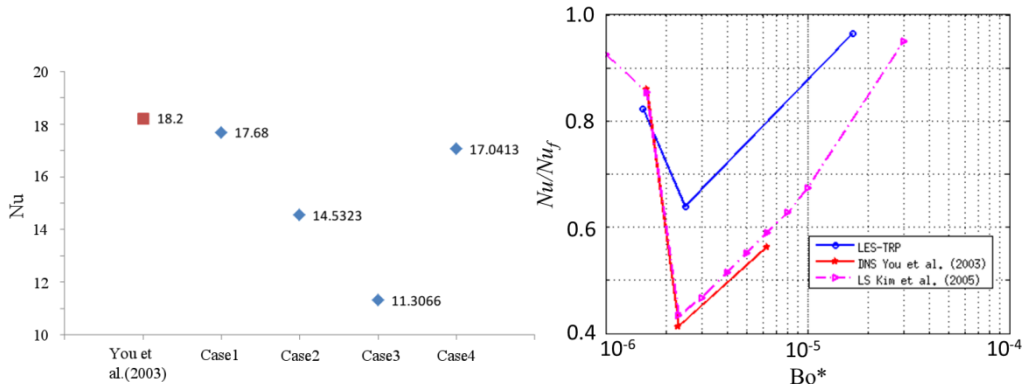

(a) (b)

Fig.5.19(a) Nu of the current simulation Cases. (b)Influent of buoyancy on heat transfer in buoyancy cases and references simulations

The local heat flux and heat transfer coefficients on the walls ('Bot-Wall', 'Top-Wall', 'Side-Wall' and 'Rod-Wall') of the current simulations are shown in Fig. 5.20 and Fig. 5.21, respectively. It needs to be mentioned here that 'Bot_Wall'/'Top_Wall' starts from the symmetric panel of the geometry. 'Side-Wall' starts from the corner of the bottom wall to the corner of the top wall, while the leading point of 'Rod_Wall' is located at the symmetric panel. The panel is indicated by ‘P1’ and ‘P3’ illustrated in Fig. 5.3 (a). The local heat fluxes (HF_{loc}) are normalized by the averaged heat flux

(HF_{avg}) in each cases. HF_{avg} are 6154 W/m^2, 3656W/m^2, 5904W/m^2& 40210 W/m^2, in Cases 1, 2, 3 & 4, respectively. The local heat transfer coefficient h_{loc} of all of the cases is normalized by overall heat transfer coefficient (h_f) from the forced convection case, 'Case 1'. The h_{loc} is evaluated by using local heat flux and the local mass flow rate and weighted average temperature in the predefined sections, refers to Fig. 5.3 (b).

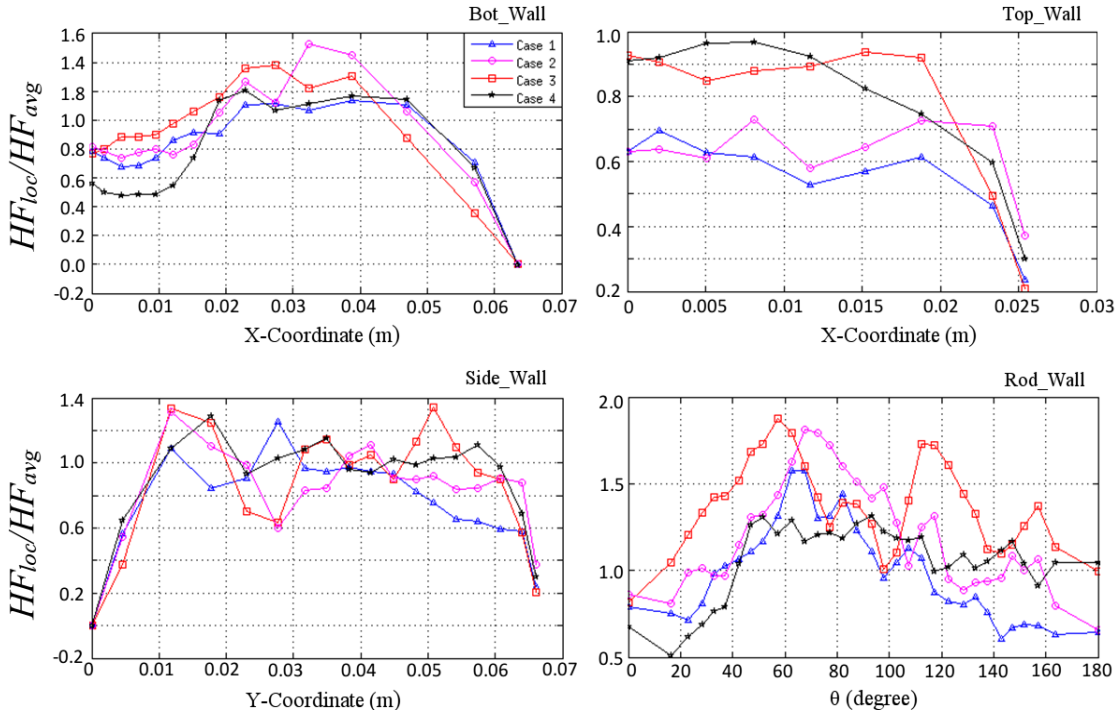

Fig.5.20 Normalized heat flux (HF_{loc}/HF_{avg}) on the walls.

As illustrated in Fig. 5.20, HF_{loc} on the 'Bot_Wall' close to the narrow gap is relatively low in all of cases. It increases with the location moving always from the centre of the narrow gap, reaches the maximum at the location around 0.35m, which is close to the main channel. Then HF_{loc} decreases to zero as the location moves towards the corner. The distribution of HF_{loc} on 'Top_Wall' is more or less uniform in first three cases, except the region around the top corner of the trapezoid wall, while the value of HF_{loc} decreases in the region 0.01m to 0.024m in Case 4. The distribution of HF_{loc} on the side wall can be classified into two types according to its different performances. In the Case 1 & 4, the heat flux remains more or less the same on most of 'Side_Wall', except the region close to the corners. However, there is a 'V' type change between 0.02m and 0.04m in Cases 2 & 3. This region indicates

the part of 'Side_Wall' close to diverge part of the main channel, see Fig. 5.5. As mentioned in the distribution of HF_{loc} on 'Bot_Wall', the heat flux on the part of 'Rod_Wall' close to the narrow gap is relatively low. Then it general rises up as the location moves away from the centre narrow gap ($\theta = 0°$) in all of the cases. The value reaches the peak around $\theta = 60°$ in Cases 1, 2 & 3 ($\theta = 60°$ indicates the part of the wall facing the bottom corner, see Fig. 5.3(b)). When the heat flux decreases from the peak as the locations moves around to the middle of the top gap ($\theta = 180°$) in Cases 1 & 2, the 'W' trend can be observed between $\theta = 60°$ and 110° in Case 3, before it reduces as the location moves $\theta = 180°$. It should also be noted, there is a small peak at the part of the 'Rod_Wall' facing the top gap ($\theta = 158°$) in Case 3. Compared to other three cases, the heat flux on 'Rod_Wall' in Case 4 is much more uniform from $\theta = 60°$to 110°.

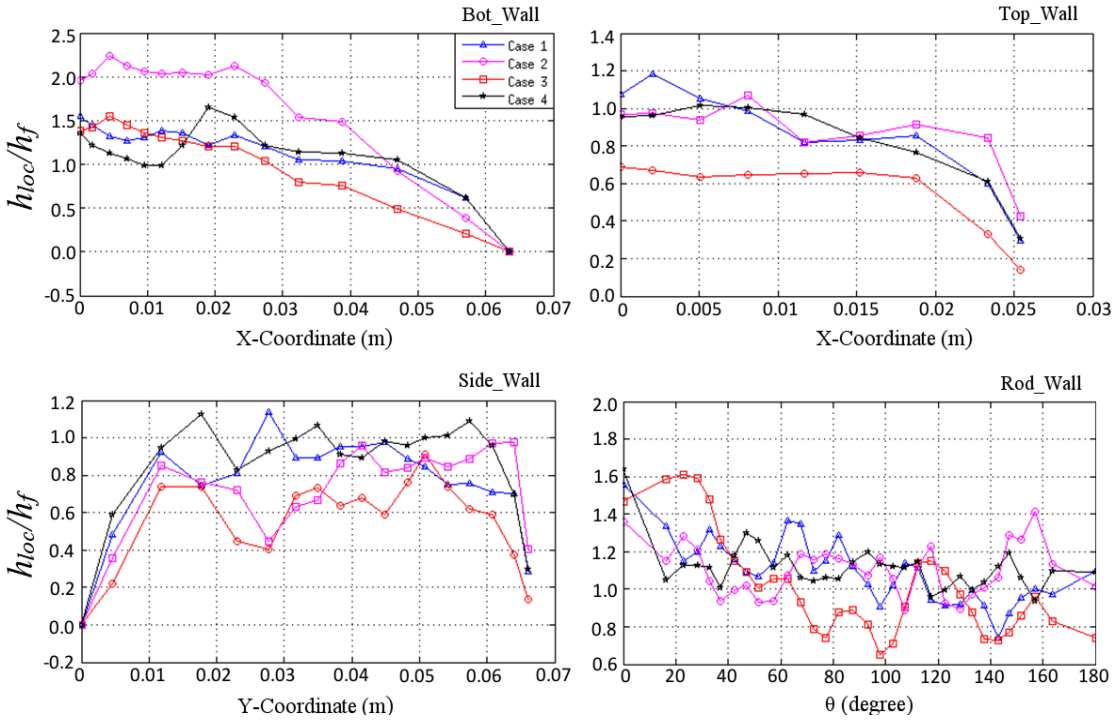

Fig.5.21 Heat Transfer Coefficient ratio (h_{loc}/h_f) on the walls.

As expected, extremely small values of h_{loc}/h_f are located at the corners, see Fig. 5.21. The highest heat transfer coefficient occurs in the narrow gap region in all the cases; see value in the range 0m to 0.02m on the 'Bot_Wall'. Generally the value decreases steadily with the location moving towards the corner. It is interesting to note that the h_{loc} on the bottom wall is strongest in Case 2, the value is double of h_f in the narrow

gap region. The values of h_{loc} in the narrow gap in Cases 1 and 3 are comparable to each other while the value is even smaller in Case 4 than in other cases.

Regarding the distribution of h_{loc} on the 'Top_Wall', the value in the big gap region (from 0m to 0.01m) is more or less the same as h_f in all the cases, except for Case 3. h_{loc} on the 'Top_wall' significantly decreased in Case 3, amounting to 65% to 70% of h_f. It can also be seen from the figure that h in the region close to the top corner is improved in Case 2.

The distribution of h_{loc} on the 'Side_Wall' is very similar in Case 1 and Case 4, except at the region close to the top corner. h_{loc} increases in this region in Case 4. Similar distribution can be found in Case 2. The decrease of the h_f happens on the part of the wall facing the main channel (0.02m to 0.03m), which is similar to Case 3. The value at this particular part can reach as low as 40% of h_f, which is very close to the lowest level of Nu of turbulent buoyancy-aided convection in a tube, see Fig. 5.19 (b).

In contrast, the h_{loc} on 'Rod_Wall' is more or less the same in Cases 1, 2, and 4. A high heat transfer rate can be found at the centre of narrow gap (see the value as 0 degree). It drops quickly with the location moving away from the centre for $\theta < 20°$. Considering the local heat transfer value in Case 1, a visible drop of h_{loc} can be found between 30°to 70°, while a significant increase occurs from 140° to 160°. While the value of h_{loc} in Case 4 is close to that in Case 1. Considering the h_{loc} in Case 3, the value climbs up a little from the narrow gap centre to the range of the narrow gap ($0° < \theta < 30°$), followed by a rapid drop from 30° to 100°.

It is reasonable to conclude that heat transfer impairment due to buoyancy force in the turbulent mixed convection in the non-uniform geometry configuration is more moderate than in the tube. The effect of the buoyancy force on heat transfer rate varies at the different parts of the channel due to the non-uniformity of the geometry.

5.2.4.2 Friction Coefficient

The friction coefficient C_f and ratio C_f/C_{f0} of all of the cases and the DNS results are shown in Fig. 5.22. C_{f0} is the overall friction coefficient in Case 1. Since Launder-Sharma model cannot accurately capture the friction coefficient, refer to Kim et al., 2008. The result from the RANS model is not shown here. The friction coefficient is 0.00919 in Case 1, very close to the forced convection result (0.00928) obtained by using the DNS in the pipe, see Fig. 5.22 (a). It is also clear in Fig. 5.22 (a) that the lowest value of C_f occurs in Case 2. With the increase of the buoyancy force, C_f increases monotonically. Similar trend can be found in Fig. 5.22 (b). Instead of having dropped to a lower value with Bo^* increasing to 2.5×10^{-6}, which happens in the tube, the C_f/C_{f0}increases a little. Then it keeps rising as the buoyancy keeps increasing.

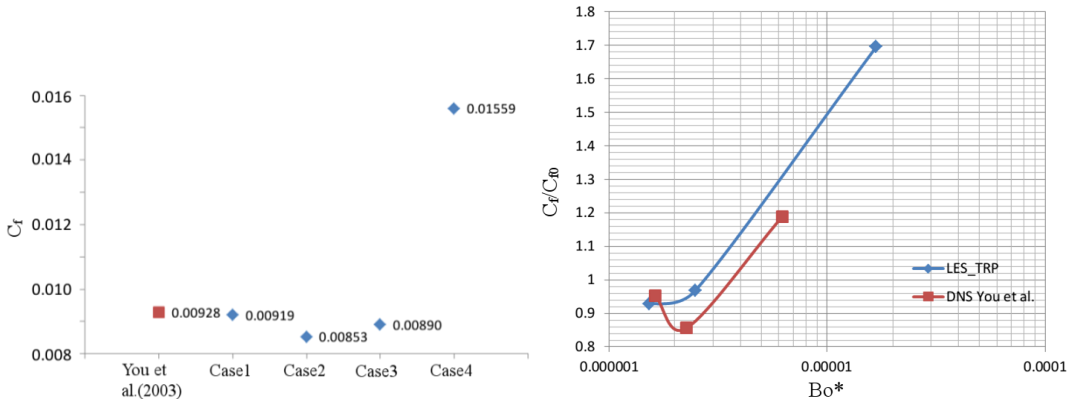

(a) (b)

Fig.5.22 (a) Skin friction coefficient and (b) skin friction coefficient ratio from simulations, the current large eddy simulation and DNS results (You et al., 2003).

The local friction coefficients are evaluated by considering the local wall shear stress over dynamic pressure in the pre-defined sections. The results normalized by C_{f0}= *0.00919* are shown in Fig. 5.23.

Compared to other cases, a more uniformly distributed C_f can be found in Case 4. The value varies from 150% to 200% of C_{f0}, which is normally higher than in other cases (normally around the value of C_{f0}), except in the vicinity of narrow gap. The maximum value is achieved in the region in Cases 1, 2 & 3, while the value drops greatly with the location moving away from the narrow gap. The C_f in the centre of the narrow gap can be more than three times C_{f0}, see the plot on the 'Bot_Wall' and

'Rod_Wall'. Meanwhile, the distributions of C_f are inter-weaved with each other in Cases 1, 2 and 3, except on 'Top_wall'. The C_f/C_{f0} on the 'Top_wall' in Case 1 is about 20% higher than corresponding values in Cases 2 and 3. The distribution of C_f/C_{f0} on the rod is very uniform from 60° to 180° in Cases 1, 2 & 3, while the value is about 1.

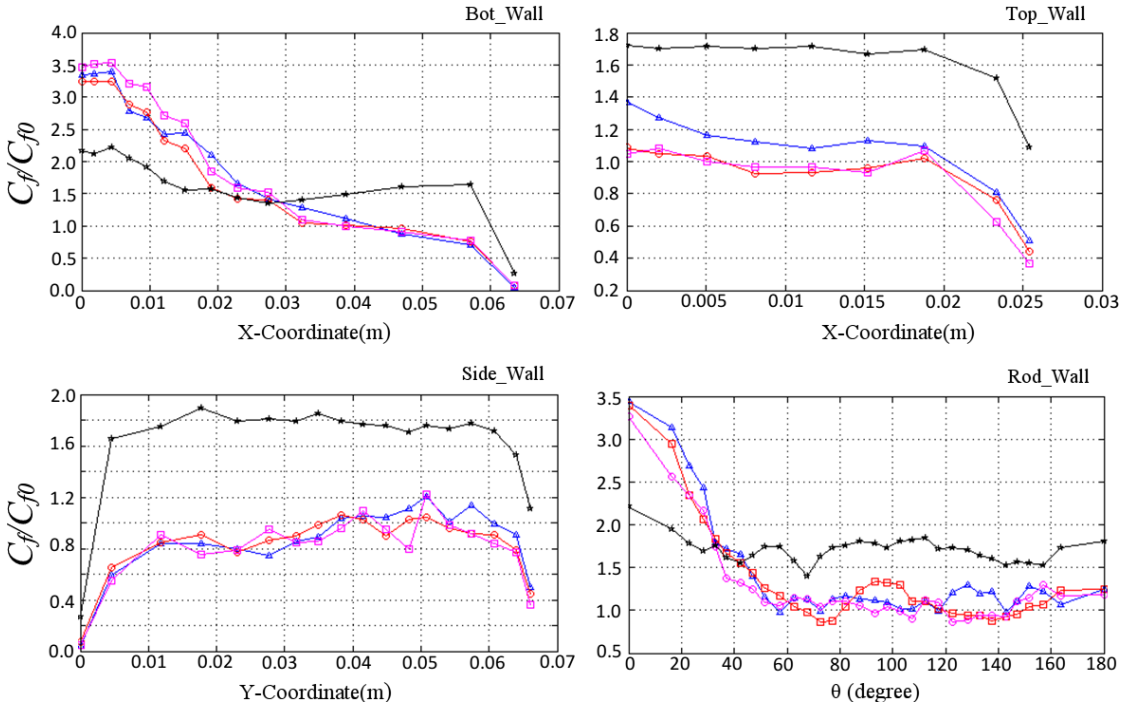

Fig.5.23 Skin friction coefficient ratio (C_f/C_{f0}) on the walls.

5.2.5 Turbulence statistics

5.2.5.1 Reynolds averaged velocity field

The mass flow rate through the predefined sections in Fig. 5.3(b) is illustrated in Fig. 5.24. As presented in the figure, the buoyancy force dose not redistribute the mass flow rate much in Case 2 and 3. However the mass flow rate in the section at the vicinity of the narrow gap is visibly increased. Especially, in the narrow gap region, the value of mass flow rate is nearly doubled, although the magnitude is small compared with the peak.

The contours of the axial velocity distribution in the cases are shown in Fig. 5.25. As expected, the high velocity patch is located in the main channel in the forced convection case. The velocity decreases as the flow passage becomes narrower. Such velocity distribution is modified as the buoyancy force is introduced into the system. For example, high velocity patch is moved to the top corner and spreads to the top big gap in Case 2. With the increase of the buoyancy force, the high velocity patch is also moved towards the main channel; see the velocity contour of Case 3.When the buoyancy force is sufficiently high, the velocity in the bottom narrow gap and the corners is greatly accelerated; as demonstrated in Case 4. It is similar to the prediction by Forooghi et al. (2015).

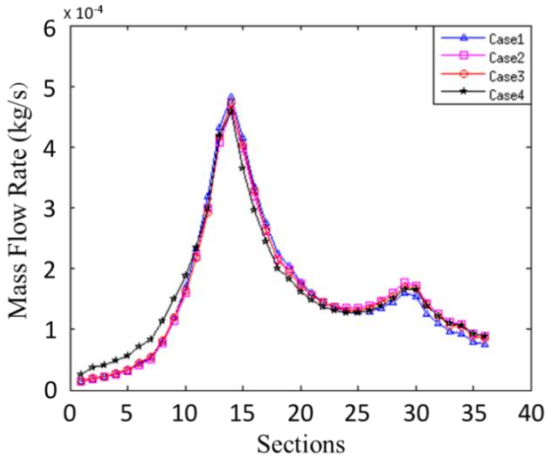

Fig.5.24 The local mass flow rate through each pre-defined sections.

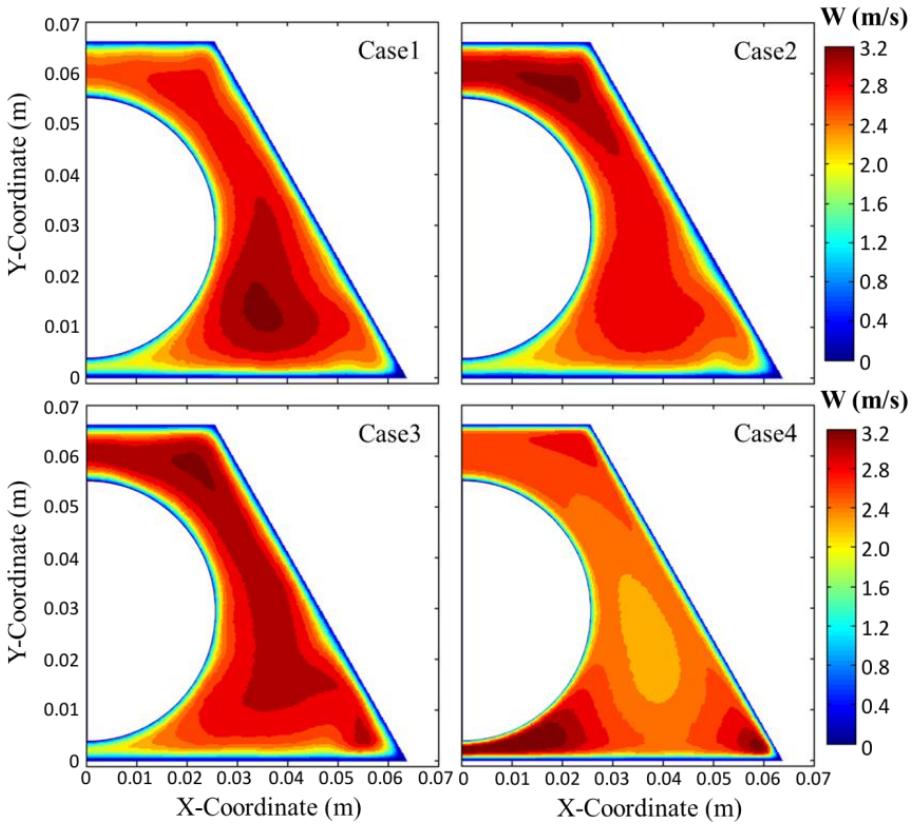

Fig.5.25 Contours of streamwise velocity 'W'(m/s).

More details can be seen from the velocity profile on the pre-defined lines (ML1, ML2, ML3 and P1, P2, P3), see Fig. 5.26 (a). Considering the velocity distribution on the equal-distance lines ('ML1', 'ML2' and 'ML3') in Case 1, the velocity increases gradually from the centre of the narrow gap, reaches the first peak in the main channel, after which it starts to decrease until the location moves to another relative bigger opening of the channel (the end of ML2), the velocity decreases again with the location moving to the centre of big gap. The shape of velocity distribution along ML1 is similar in Case 2 and 3. The velocity continues decreasing along ML2 even though at a much slower rate. The velocity along ML3 in these two cases decreases with the location moving to the centre of narrow gap, but with a very small rate, that is much smaller than in Case 1. The picture is completely different in Case 4. As shown in the figure the maximum velocity is located at the vicinity of the narrow gap. There, the velocity decreases until the channel starts to narrow up again, refer to 0.06m in Fig. 5.26 (a). The velocity increases beyond this point, until it reaches a flat level along ML3. A very uniform velocity distribution can be found along the centreline of the narrow gap.

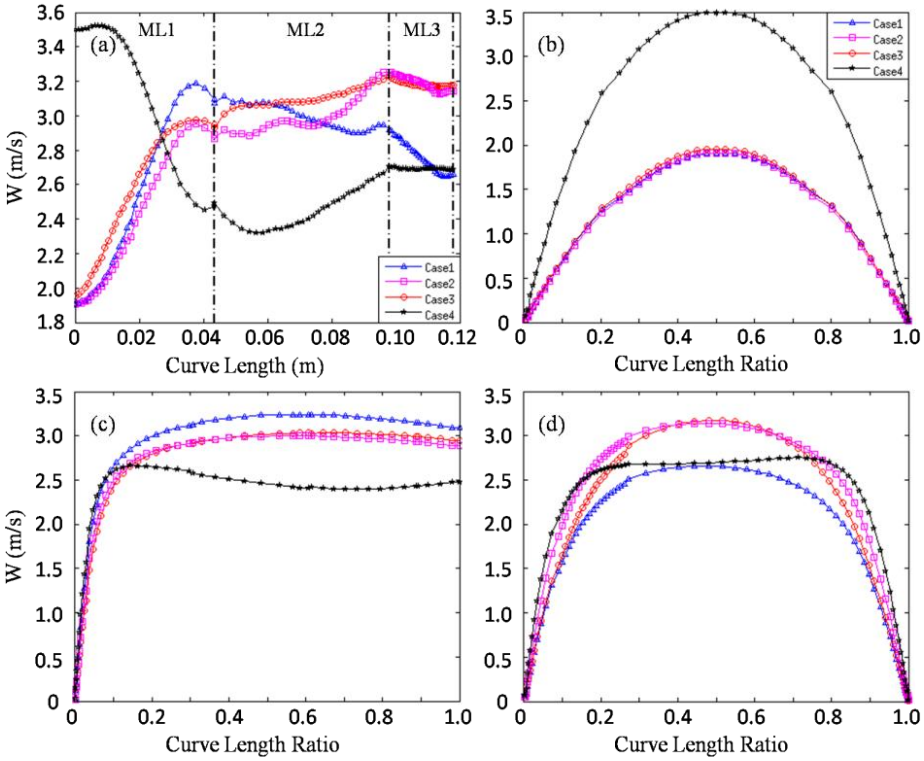

Fig.5.26 Reynolds averaged streamwise velocity *W* (m/s) along lines(a) ML* (b) P1; (c) P2; (d) P3.

The velocity distributions on 'P1', 'P2' and 'P3' from all of the cases are shown here to further the understanding on the influence of buoyancy force on local velocity profile. Generally speaking, the effects of body force on the profile of velocity on the lines in the different region are quite different.

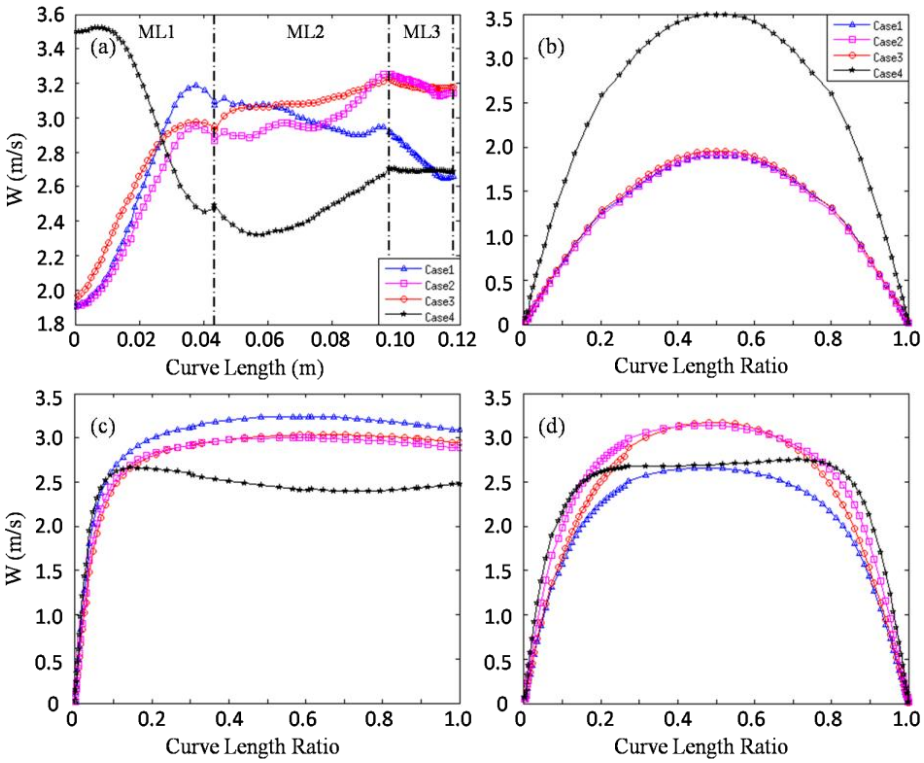

Fig.5.27 Reynolds averaged streamwise velocity *W* (m/s) along lines(a) ML* (b) P1; (c) P2; (d) P3.

The velocity profiles on 'P1' in the first 3 cases almost overlap with each other, while it is stretched greatly in Case 4, in which case the highest velocity magnitude on 'P1' is about double the value than that in other three cases; see Fig. 5.26 (b). This change would lead to an increase in the wall shear stress in the narrow gap in Case 4. Although, the velocity in the region is about double than the value in other 3 cases, a lower friction coefficient is seen in the narrow gap region in Case 4. The shape of the velocity profile along 'P2' is again very similar to each other in the first three cases, while velocity magnitude and gradient in the near wall region is slightly lower in Cases 2 & 3 due to the buoyancy force. Meanwhile, the velocity magnitude is smaller than the value in Case 1 in the centre of the channel in these two cases. As the heat flux is sufficiently high as in Case 4, the velocity in the near wall region is recovered and a concavity is developed in the velocity profile, see Fig. 5.26 (c). As shown in Fig. 5.26 (d), the velocity profile along 'P3' is stretched in Case 2 and 3, compared to the profile in Case 1.This can explain the lower friction coefficient on the top wall in these two cases. The velocity profile is turned into a 'M' shape in Case 4, which would result in regeneration of turbulence. In comparison with Case 1, the

velocity gradient along 'P3' in the near wall region is firstly increased in Case 2, returns to the magnitude of Case 1 in Case 3, but is increased again in Case 4.

5.2.5.2 Turbulence Quantities

Due to the symmetry of the geometry, only a half of the channel (the right half) is used to show the contours of turbulence quantities for all of the Cases. Firstly, the data of normalized turbulent kinetic energy (k/U_b^2) is shown in Fig. 5.27, which is followed by the turbulence intensity $\langle w' \rangle / U_b$, $\langle u' \rangle / U_b$ and $\langle v' \rangle / U_b$ in Fig. 5.29, Fig. 5.31 and Fig. 5.33. Meanwhile the distribution of k/U_b^2, $\langle w' \rangle / U_b$, and $\langle u' \rangle / U_b$ on the predefined lines are illustrated in Fig. 5.28, Fig. 5.30, and Fig. 5.32.

It can be seen in Fig. 5.27 that there is a high turbulence kinetic energy region, which is located in the vicinity of the narrow gap in Case 1. This is similar to that found in the experimental work by Wu and Trupp (1993). The magnitude of such high turbulence kinetic energy is reduced in Case 2 and 3. It can be explained by the *laminarization effect* due to buoyancy force. With a further increase in the buoyancy force, turbulence is regenerated, which can be detected from the contours of k/U_b^2 inCase4. It is also interesting to note that the size of high turbulence region in the near gap region in Case 4 is much bigger than in other three Cases. Meanwhile, the high turbulent patch in the near wall region is disappeared, while a general increase of turbulence kinetic energy level in the core region of the whole channel can be seen from the contours of k/U_b^2 inCase4.

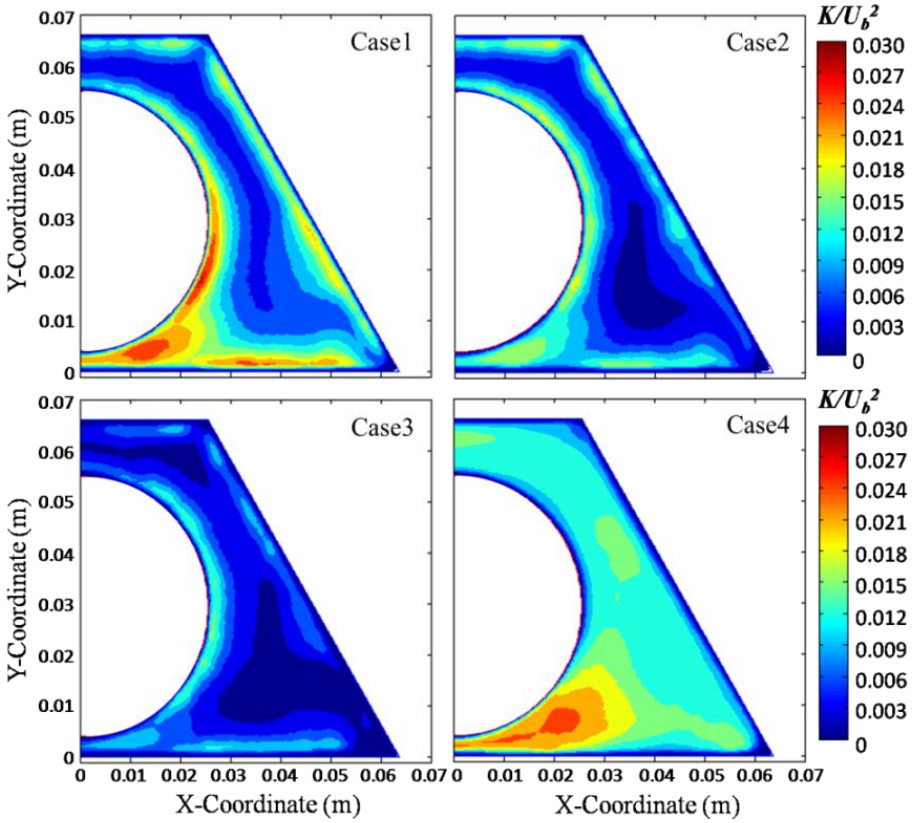

Fig.5.28 The contour plot of turbulent kinetic energy ($\boldsymbol{k/U_b^2}$) in different cases

The profiles of k/U_b^2 along the 'ML*' (referring to 'ML1', 'ML2' and 'ML3'), 'P1', 'P2', and 'P3' are illustrated in Fig. 5.28. The peak of k/U_b^2 along 'ML1' in Case 2 is just 70% of its value in Case 1, while it further drops to 50% in Case 3. The value of *k* along 'ML2' and 'ML3' is generally smaller in Case 2 and 3, but the reduction is smaller compared to the value on 'ML1'. While the turbulent kinetic energy on 'ML1' recovers in Case 4, it is almost tripled on 'ML2' and 'ML3' compared to the value obtained in Case 1. The same trend can be seen from the distribution of k/U_b^2 on 'P1': Turbulence reduction occurs in Case 2 and 3, but it recovers in Case 4. The reduction of *k* in the near wall region along 'P2' occurs in all of buoyancy influenced cases. The k/U_b^2 on 'P2' reduces with the increase of buoyancy force in Case 2 & 3, while the peak of *k* in Case 4 is similar to that in Case 2 and the location moves away from the near wall region. Meanwhile, the value of k/U_b^2 in Case 4 is more than triple its value in Case 1 in the core region. The location of that of k/U_b^2 peak on P3 in Cases 1, 2 & 3 is closer to the wall than in Case 4. Interestingly, k/U_b^2 in the vicinity of the wall in Case 2 is increased but is significantly decreased in Case 3. The peak value

of k/U_b^2 in Case 4 is similar to that in Case 2. Again a high turbulent kinetic energy can be found in the centre of big gap in Case 4.

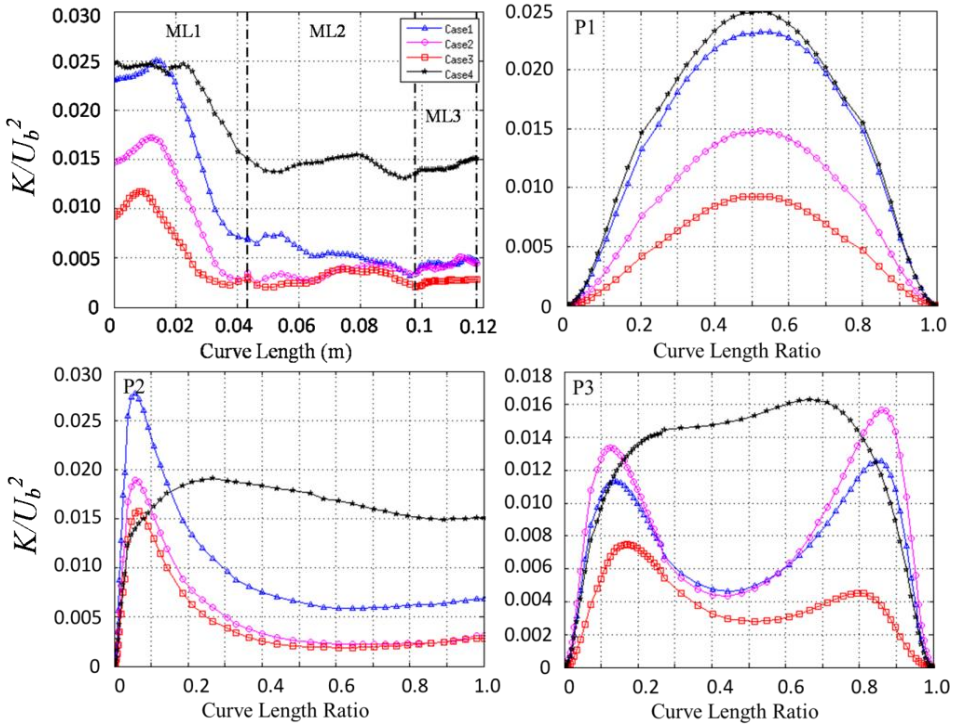

Fig.5.29 The turbulent kinetic energy ($\boldsymbol{k/U_b^2}$) on predefined lines 'ML*', 'P1', 'P2' and 'P3'.

The contours of axial components of turbulent intensity $\langle w' \rangle / U_b$ show a similar picture as turbulence kinetic energy distributions, see Fig. 5.29. The high value patches are located near the wall and the region close to the narrow gap. In comparison with Case 1, the magnitudes and size reduced in Case 2 and a more significant shrink occurs in Case 3. When the body force is sufficiently strong, the value of turbulence intensity recovers as seen in Case 4. Furthermore, the $\langle w' \rangle / U_b$ value in the core region in Case 4 is much higher than in other cases. The contours show that the high value patch penetrates into the acute-angle corner in Case 4.

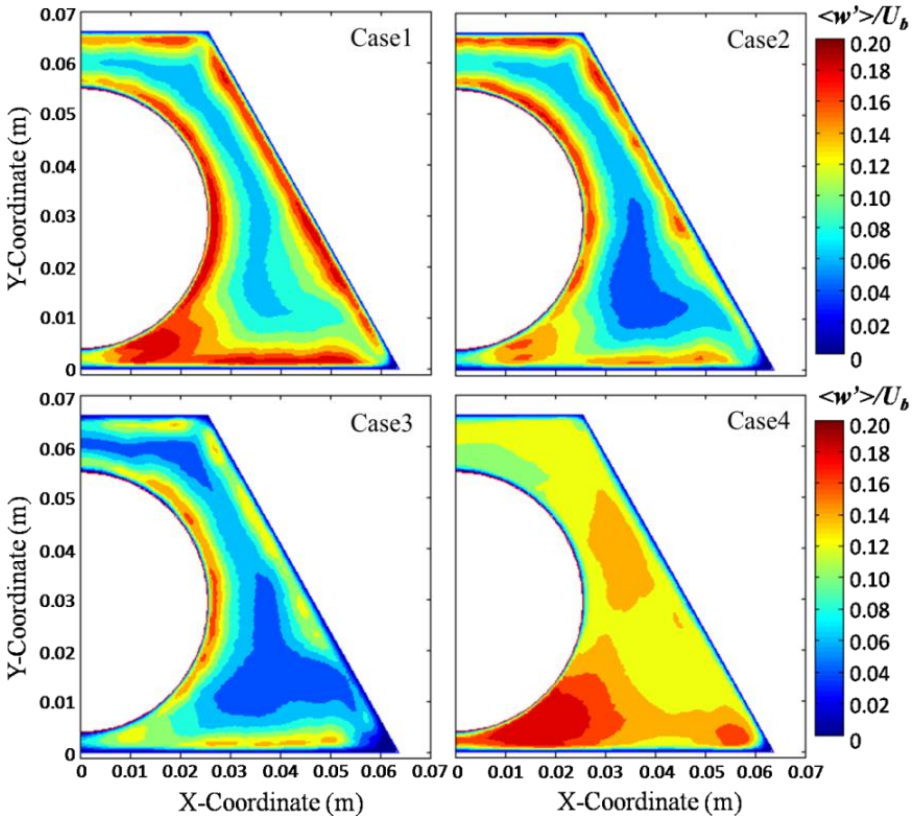

Fig.5.30 The contour plot of the axial component of turbulence intensity ($\langle \boldsymbol{w'} \rangle / \boldsymbol{U_b}$) in different cases.

The distribution of $\langle w' \rangle / U_b$ on the selected lines ('ML*', 'P1', 'P2'&'P3') are illustrated in Fig. 5.30. Generally speaking, there are high values of $\langle w' \rangle / U_b$ located along'ML1', but away from the narrow gap centre in cases. The magnitude of$\langle w' \rangle / U_b$ on 'ML1', 'ML2' and 'ML3' is generally higher in Case 4, which is followed by Case 1, Case 2 and Case 3, sequentially. It indicates that the level of $\langle w' \rangle / U_b$ in the centre of the channel decreases with the increase of heat transfer rate when $Bo^* < Bo_0^*$, but recovers or even is significantly increased when $Bo^* > Bo_0^*$. The peak value of $\langle w' \rangle / U_b$ on 'ML1' is decreased by ~17% in Case 2, ~33% in Case 3. And the location of peak moves towards the centre of narrow gap with increase of body force. The peak reflects the strongest production of k which is associated with the largest velocity gradient. The $\langle w' \rangle / U_b$ on 'P1' and 'P2' are similar as the turbulence kinetic energy distributions on these lines. It is though interesting to point out that the values of $\langle w' \rangle / U_b$ on P2 in Case 2 & 3 almost overlap each other. The value of $\langle w' \rangle / U_b$ on P1 in Case 4 is 30% higher than that in Case 1. And $\langle w' \rangle / U_b$ in the main channel is almost double the value in Case 1. Like the distribution of k/U_b^2 on P3,

the peak of $\langle w' \rangle / U_b$ in Cases 1, 2 & 3 are in the vicinity of the wall. Compared to Case 1, the peak is highest in Case 2, while it reduces in Case 3. Furthermore the magnitude of $\langle w' \rangle / U_b$ on P3 in the near wall region is lower than that in Case 1, but the peak value of $\langle w' \rangle / U_b$ is located in the middle of the gap.

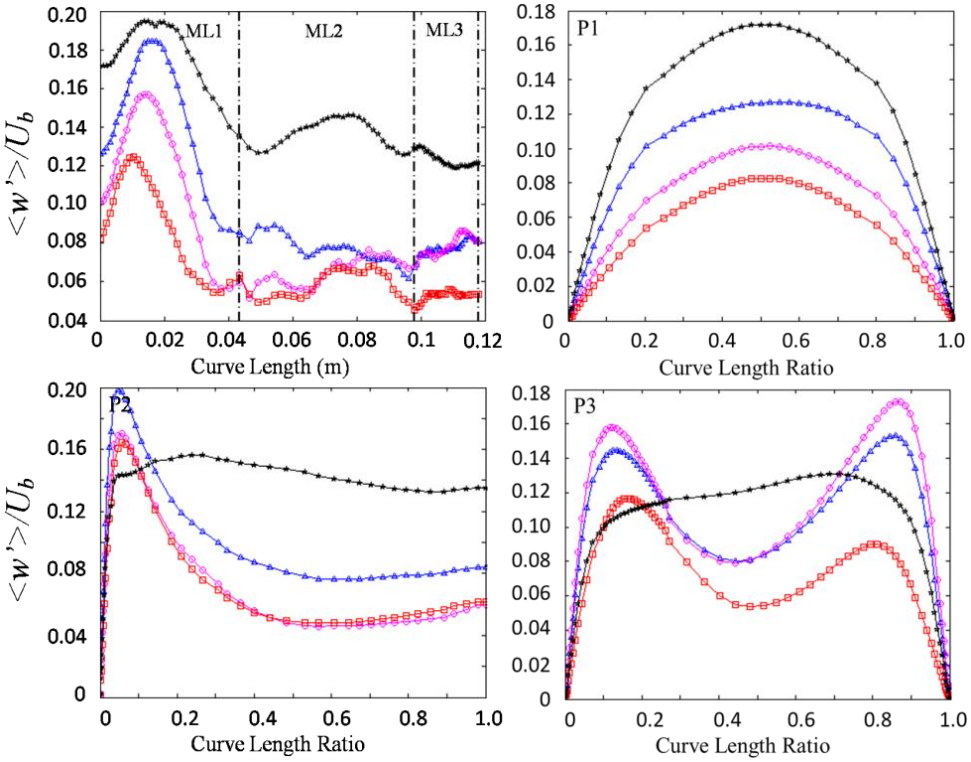

Fig.5.31 The axial component of turbulence intensity ($\langle \boldsymbol{w'} \rangle / \boldsymbol{U_b}$), See nomination inFig. 5.28.

It can be seen in Fig. 5.31, the high value patches of $\langle u' \rangle / U_b$ are located in the narrow gap in Cases 1, 2 & 3, while an additional patch is also visible in the big gap in Case 4. Like the contours of k/U_b^2 and $\langle w' \rangle / U_b$ shown above, the size of the high value patch is reduced with the increase of buoyancy force in the Cases 2 & 3 but it becomes much bigger in Case 4, although the magnitude in Case 4is smaller than that in the forced convection case.

As illustrated in Fig. 5.32, the highest values of $\langle u' \rangle / U_b$ are located in the middle of the narrow gap in the cases. Its magnitudes are comparable to peak $\langle w' \rangle / U_b$ in Case 1, but smaller in other cases. The value in the cases reduces continuously as the location moves away from the centre of the narrow gap on 'ML1'. It decreases

slightly along 'ML2' in Case 1. The decreasing trend on 'ML2' remains in Cases 2 and 3 but the rate of decrease is very small, while a 'V' trend can be found in Case 4. The visible increase of $\langle u' \rangle / U_b$ on 'ML3' can be found in all of the cases, especially in Case 4. As shown in the figure on the distribution of $\langle u' \rangle / U_b$ on 'P1', the maximum values are located in the centre of the narrow gap in the cases. $\langle u' \rangle / U_b$ which is most significant in the forced convection case, decreases with the increase of buoyancy force in Case 2 (about 20% lower) and Case 3 (about 40% lower), the value is recovered in Case 4 (the profile almost overlaps that in Case 2). $\langle u' \rangle / U_b$ on 'P2' and 'P3' in Case 4 is higher than its counterpart in other cases but smaller than the value in the near wall region in Case 1. In first three cases, the values of $\langle u' \rangle / U_b$ decrease as the location moving towards the centre. However, the value of $\langle u' \rangle / U_b$ increases from wall and remains more or less the same in Case 4. Regarding the $\langle u' \rangle / U_b$ on 'P3', the flat distribution can be found in all the cases, except in Case 3, in which a peak is located close to the centre of the big gap. Meanwhile, its value in Case 4 is almost triple the value in the other three cases.

As shown in Fig. 5.33**,** the high value patches of y component of turbulence intensity are in the near wall region facing the main channel close to the rod. By comparing Cases 1, 2, & 3, it can be clearly seen that the size of the high value patch reduces with the increase of buoyancy force. The magnitude of the y-component of turbulence intensities recovers in Case 4 and the size of high value patch is much bigger than that in Case 1. The peak of $\langle v' \rangle / U_b$ is located close to the wall in these 3 cases, while it is moved away from wall in Case 4. Its magnitude in the core region here is much bigger than in the other three Cases.

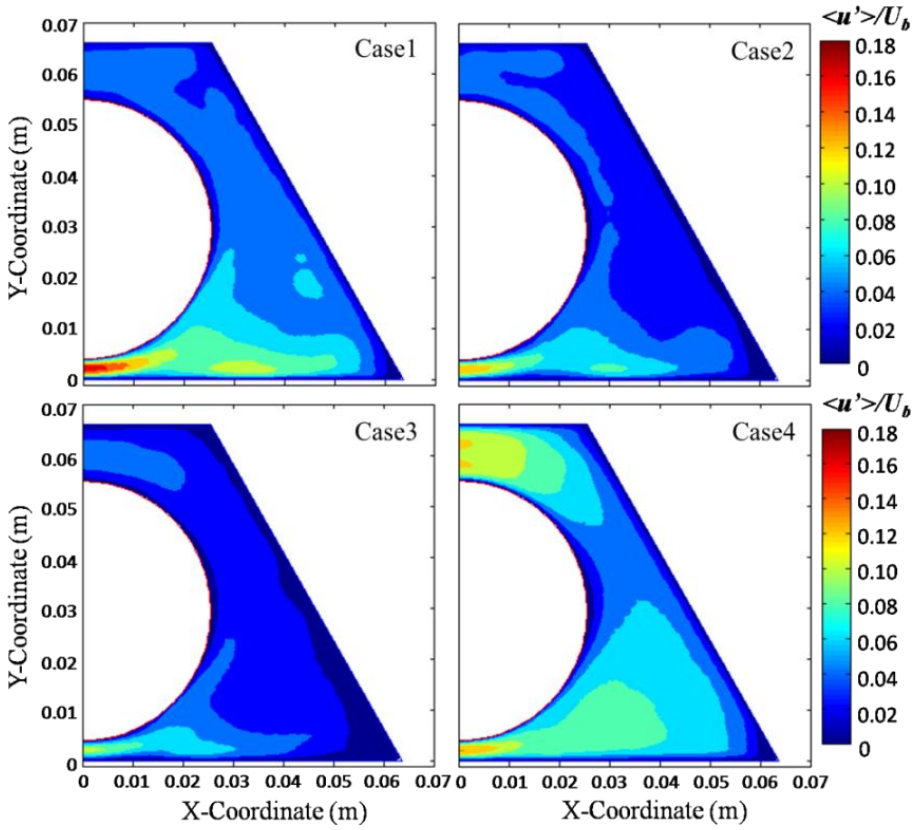

Fig.5.32 The contour plot of the azimuthal component of turbulence intensity ($\langle u' \rangle / U_b$) in different cases.

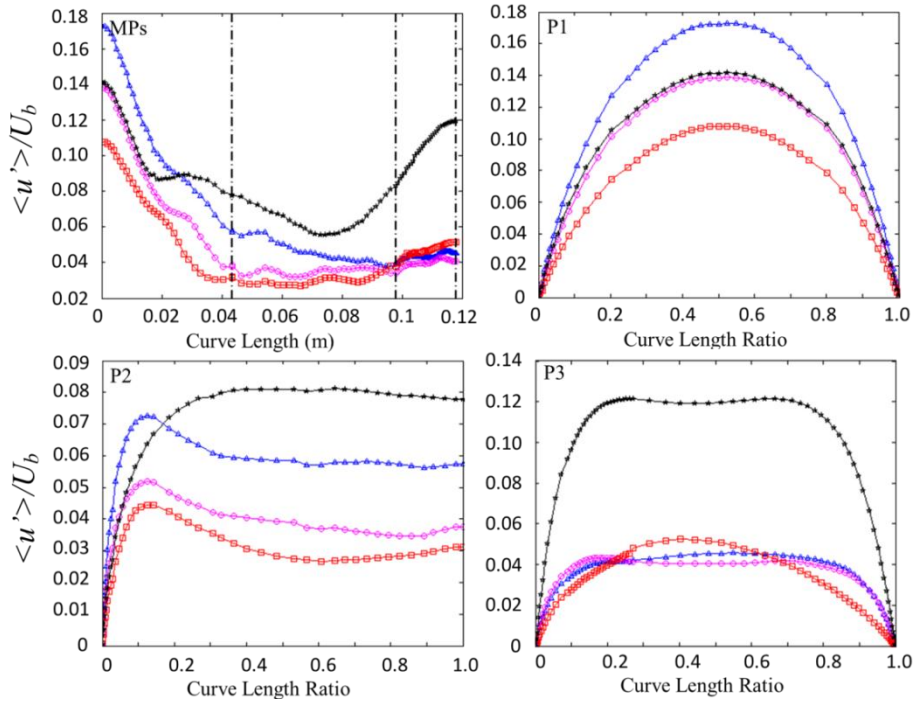

Fig.5.33 The azimuthal component of turbulence intensity ($\langle \boldsymbol{u'} \rangle / \boldsymbol{U_b}$), See nomination in Fig. 5.28.

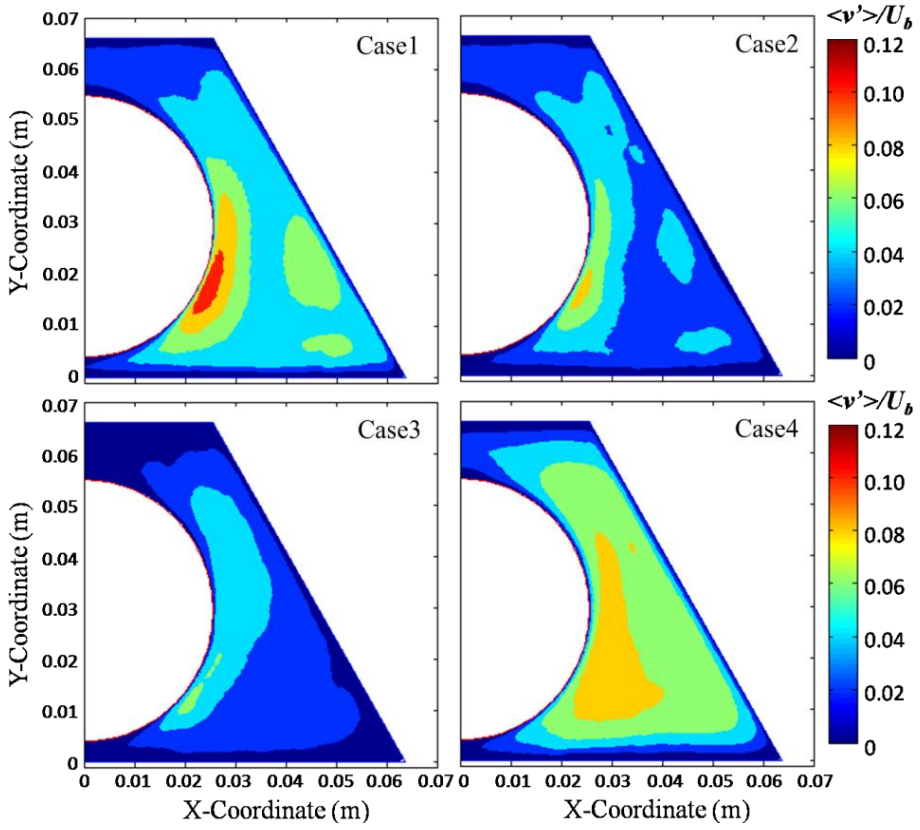

Fig.5.34 The contour plot of azimuthal component of turbulence intensity ($\langle v' \rangle / U_b$).

As discussed above, high turbulent quantities are mainly located on the 'ML1'. Shear stresses production terms of the kinetic energy along 'ML1', 'P1', 'P2' and 'P3' are shown in Fig. 5.34. A peak of the turbulence production on 'ML1' can be found in all of the cases. The peak value is greatest in Case 1, while it decreases with the increase of buoyancy force in the other 3 cases. Meanwhile the location of the peak on 'ML1' moves towards the narrow gap centre in Case 2 and Case 3, but moves away in Case 4. Overall the reduction of the peak value can be more than 50% in the buoyancy influenced cases. The weakest peak is in Case 4, although the peak values of only slightly higher in cases 2 & 3. The trend remains similar for the distribution of turbulent production rate on 'P2', but not on 'P1' and 'P3'. The turbulence kinetic energy productions are mainly occurred in the near wall region along all the three lines, 'P1', 'P2' & 'P3'. On 'P1', the most significant peak value (~4.8 m^2/s^3) is found in Case 4, which is almost double the value (~2.4 m^2/s^3) than that in Case 1, while the value can be less 0.8(m^2/s^3) in Case 2 and around 0.3 (m^2/s^3) in Case 3. The highest value of the peak (~7m^2/s^3) of turbulence production on P3 is found in Case

2, the lowest (~2 m^2/s^3) again found in Case 3, while it is (~5.4 m^2/s^3) and (~2.8 m^2/s^3) in Case 1 and Case 4, respectively.

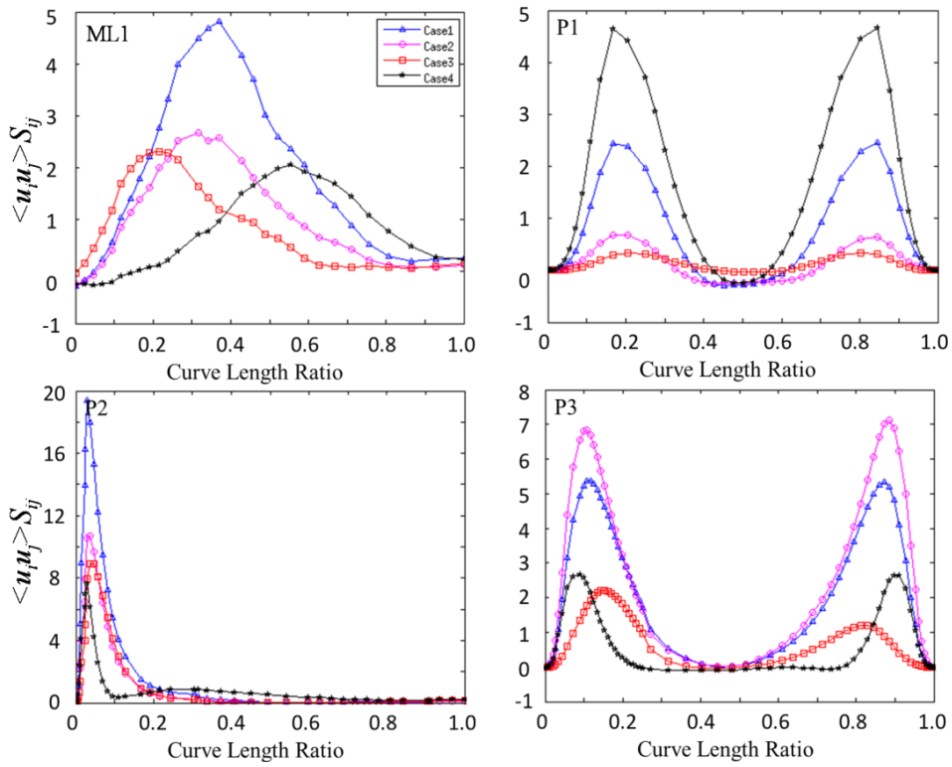

Fig.5.35 The shear stress production of the turbulence kinetic energy.

The buoyancy production of the turbulence kinetic energy on selected lines is shown in Fig. 5.35. Since g = 0 m/s^2 in Case1, the buoyancy production term in Case 1 is 0 m^2/s^3. Generally speaking, the body force plays a negative role in Cases 2 & 3. The locations of the minimum values on 'ML1' are similar to that of the peak of $\langle w' \rangle / U_b$ on each selected lines in these two cases and the negative value is more significant in Case 3. Such negative effect is stronger in Case 3. A strong and positive buoyancy production can be found in Case 4. The value in Case 4 increases from the centre of narrow gap and reaches a peak at a location where the highest *k* is located. The peak value is the same as that of the production due to the Reynolds shear stresses. Again a positive buoyancy production can be found on 'P1' in Case 4, especially in the centre of narrow gap, while a negative production (i.e. a sink) can be found in Cases 2 and 3. Although a negative production can be found in Case 4 in the near wall region on 'P2' and 'P3', a significant positive buoyancy production can be found in the region far from the wall. However, the value is mainly negative on 'P2' and 'P3' in Cases 2 and 3, especially in the near wall region.

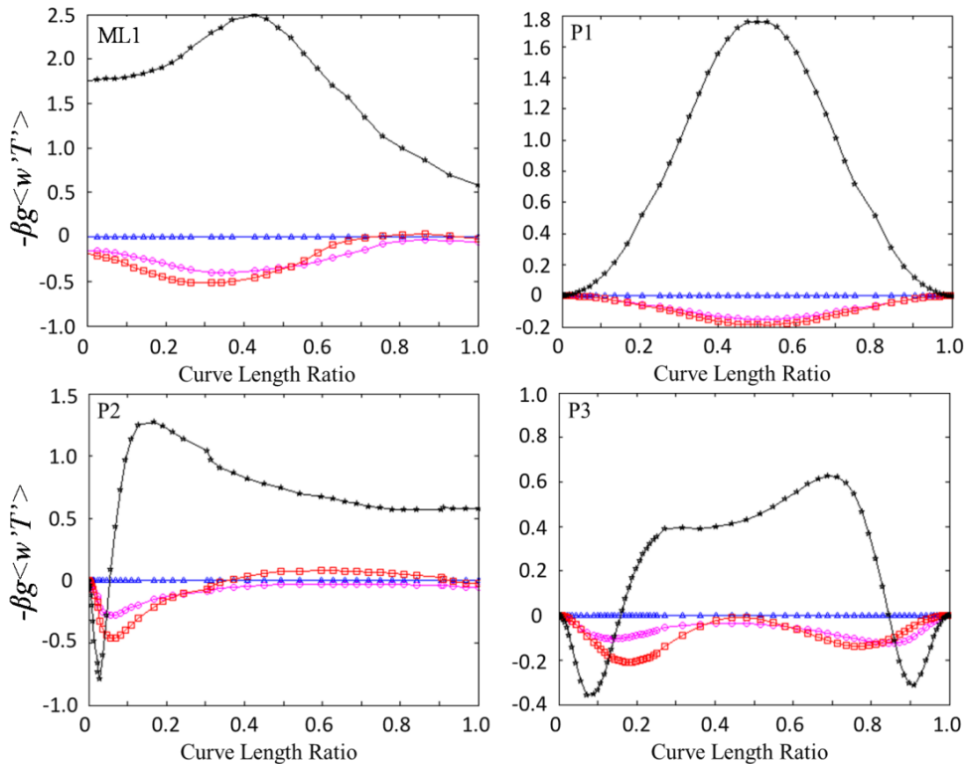

Fig.5.36 Gravity production of the turbulent kinetic energy.

Overall, turbulence is reduced with the increase of heat transfer when $Bo^* < Bo_0^*$, and it recovers when the heat flux is further increased as $Bo^* > Bo_0^*$. When $Bo^* < Bo_0^*$, the buoyancy force does not just decrease the magnitude of the turbulence production by modifying the shear stress, but also plays a negative role in the turbulence production due to the negative value of the buoyancy production. When the heat flux is sufficient high, the buoyancy production is very high in the region away from the wall, which results in high turbulence generation in the core region. The strength of buoyancy effect on turbulence in the non-uniform flow passage is location dependent. Under particular thermal boundary conditions, turbulence can be even enhanced at certain regions while it is suppressed by the body force in the other places. Because of this, the laminarization effect of buoyancy flow is much weaker in the non-uniform channel, which result in a more gentle heat transfer impairment compared to that in a tube at the same Bo^*.

The existence of the vortex in the vicinity of the narrow gap in the case results in more turbulence generated in the narrow gap. Such an effect is reduced by the

buoyancy force when $Bo^* < Bo_0^*$, although the form of the large flow structure is not changed much by the buoyancy force. The reduction is not just due to the decreased shear production, but the negative buoyancy production. Due to the strong positive buoyancy production, turbulence in the region can be as high as the value in the forced convection case.

5.3 Conclusion

The buoyancy-aided flow in a heated non-uniform flow passage with different heat flux on the wall is studied by using large eddy simulation (LES). The subgrid scale viscosity is modelled using the Wall-adapting local Eddy Viscosity (WALE) model. The accuracy of the simulations is demonstrated by using local velocity profiles and the LES criteria suggested by Geurt and Frolich (2002) and Celik et al. (2005). It also was demonstrated in the discussions that the numerical models is accurately predict the performance of the flow structures under the isothermal condition. The same as mentioned in the work by Wu and Trupp (1993), the numerical model also demonstrated that the flow structures do not just exist in the narrow gap of the flow passage but also in the big gap. And, the flow structures in the narrow gap resulted strong r.m.s of *w'* and *u'* around the region. Also the St^{-1} of such flow structures predicted in the narrow gap is the same as it revealed in the experimental work, which is again the key feature of these flow structures under the isothermal conditions. It is worth to remind that the main objectives of this study is to provide the some pioneering understandings of the effect of buoyancy force on the flow structures and heat transfer of the flow in the tightly packed rod-bundles. The key conclusions are summarized below:

1. Effect of buoyancy force on the flow structures in the consider geometry

Generally, there are at least two large flow structures existing in the considered flow passage in the forced convection case. The first is the large flow structures existing in the vicinity of the narrow gap. The other passes the big gap in the channel. These two large structures are weakly correlated with each other in this case.

As suggested by Krauss and Meyer (1998), the flow structure in the narrow gap is formed due to the mean flow and the two streets of counter rotating turbulent vortices located at either sides of the narrow gap. They were generated by the velocity gradient existing in the region. It should be noted that velocity profile cross the narrow looks like a 'V'. The velocity is much higher in the main channel than it in the narrow gap. The vortex is driven by the high velocity gradient $\partial W/\partial x$and fuelled by the high velocity in the main channel. The vortices are rotating from the main channel to the narrow gap. Furthermore, the sizes of the vortices are big enough to cross the narrow gap centre, so the two streets of the vortices strongly correlate with each other. As mentioned above, the dimensionless frequency Strouhal number (S_t) of such flow structures in the current numerical simulation is quite similar to the experiment by Wu and Trupp (1993), although the Reynolds number of the current consideration is just 10% of the original experiments. It does again prove that the S_t is determined by the geometric configuration.

When the gravity is introduced into the system, the flow model of the two large flow structures is maintained when the buoyancy parameter is smaller than the critical buoyancy parameter Bo_0^*. The flow structure passing the big gap around the rod is strengthened with increasing heat flux, when $Bo^* < Bo_0^*$. The correlation between the two structures becomes stronger as well. In the meantime, the azimuthal size of the flow structure in the narrow gap remains more or less the same, while the axial wavelength of the structure can be reduced by the body force with the increase of heat flux, as $Bo^* < Bo_0^*$.

For the case when $Bo^* > Bo_0^*$, the velocity in the narrow gap region is accelerated by the body force. In fact, the peak velocity was relocated into the vicinity of the narrow gap, once the heat flux is strong enough. As a result, the velocity profile changes from the 'V' type to the 'A' type in the region. There are still turbulent vortices exist in the region. According to the correlation analysis, the size of the turbulent vortices decreases. Because the high velocity region is located in the narrow gap, it is reasonable to guess the vortices rotate from the narrow gap to the main channel as shown in Fig. 5.36. These vortices are unstable. As the results, the centres of the vortices does not align at the straight line and their size can be

different as well. In the meantime, such flow structures are strongly correlated with the structures passing the big gap. Actually, the dominant frequencies of these two types of structures are about the same as the heat flux is strong enough.

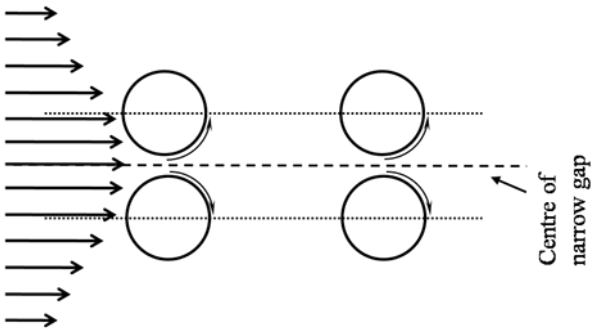

Fig.5.37 Flow model of the turbulent vortices in the narrow gap when heat flux is sufficiently high in the turbulent buoyancy aided mixed convection case.

Consistent with results shown in the previous studies, high turbulence is produced by the flow structures in vicinity of the narrow gap. Again, these turbulence quantities are reduced by the buoyancy force when $Bo^* < Bo_0^*$, while the value of turbulence quantities will recover, once $Bo^* > Bo_0^*$, due to the strong buoyancy production. The effect of buoyancy force on the mixing factor due to the narrow gap flow structure is also discussed. The results show a rapid decrease just before Bo_0^*, but the decrease ratio reduces when $Bo^* > Bo_0^*$. It should also be pointed out that the mixing velocity calculated in the forced convection case of current study (Re = 5270) is very similar to that obtained from the experimental work done by Wu and Trupp (1994).

2. Heat transfer and friction coefficient in the non-uniform geometry.

Overall, heat transfer impairment due to the laminarization effect of the buoyancy force is less significant in the non-uniform geometry considered herein than that in a heated circular tube, while the recovery of heat transfer rate is stronger than in the tube when the buoyancy is very strong. The buoyancy effect varies with circumferentially.

The heat transfer coefficient (*h*) of wall close to the narrow gap is generally higher than the other part of the wall. It can be 50% or even higher than the overall heat

transfer coefficient of the forced heat transfer case. This can be explained by the high turbulence level and the enhanced flow mixing between the fluids in the narrow gap region and main channel caused by the large structures. Hot fluid is brought away by the large structures while cooler fluid from main channel is transported into the narrow gap.

While the overall Nusselt number (*Nu*) decreases with increase of buoyancy when $Bo^* < Bo_0^*$, the overall C_f remains almost the same at this stage, which is different from that in a circular tube. A rapid increase appears just beyond Bo_0^*. It is interesting to note that the distribution of C_f is more uniform when the heat flux is sufficient high. This can be explained by the redistributed mass flow in the geometry. Especially, the mass flow rate through the narrow gap region is nearly doubled in Case 4.

Chapter 6

Forced Convection of Supercritical Water Flow in the Non-uniform Geometry.

As already demonstrated in the Chapter 5, the behaviour of the flow structures in narrow gaps of a non-uniform geometry, such as tightly packed rod bundles, can be significantly modified by buoyancy force once the heat flux is sufficiently high. The main reason for this is the non-uniform distribution of the buoyancy force in the cross section altering the streamwise velocity. In the real world, strong buoyancy force normally coexists with the strong thermal expansion and strong variations of other fluids properties such as the conductivity and specific heat. These effects are particularly strong in a supercritical fluid flows in a vertical heated channel. Especially, the significant changes of fluid properties are expected around the pseudo-critical temperature. It is of interest to understand how they influence the large flow structures in the narrow gaps existing in tightly packed fuel assemblies which is the typical design of the fuel assembly for the SCWR/HPLWR. The main objective of the study documented in this chapter is to provide some preliminary understanding of the effect of the thermal expansion and the variations of other thermal properties such as C_p and λ on the large flow structures. Buoyancy effect is excluded in this study by omitting the gravitational term. The cross section of geometry considered here is the same as that used in Chapter 5, but the geometry is much longer. It is still worth to mention that this geometry arrangement represents the triangular fuel assembly.

To make this research more practical, the supercritical water at 25MPa is chosen as the working fluid. Again, LES with WALE SGS model is chosen as the numerical

tool. All of the simulations are carried out by using the open source code Code_Saturne, which is developed by the EDF R & D. A brief introduction of this code can be found in the Chapter 3.

6.1 Case Setting

As mentioned in Chapter 3, it is necessary to introduce turbulence at the inlet for the large eddy simulation (LES). The internal mapping, namely integrating a turbulence generator at the front of the domain, is chosen in this study, which is the good way to create a fully developed incoming flow in the domain. The simulation started with a uniform velocity profile before the internal circulation being turned on after several time steps. The schematic diagram of this method is illustrated in Fig. 6.1. The velocity at $L_c = 5D_H$ is copied at the end of each time step and fed to the inlet of the domain for the next time step. To ensure the targeted mass flow rate to be reached, the inlet velocity profile is corrected using the targeted mass flow rate. The inlet velocity will gradually become one that is typical of a fully developed profile after sufficient time steps of simulation. Hence, the turbulence will generate in the domain. The subroutine of this internal circulation is included in the Appendix 2. To avoid the influence of the heated domain on the inflow generator, a $5D_H$ long isothermal domain is placed before the main domain. Namely the total length of turbulence generator is $10D_H$, which occupies 1/4 of the whole domain, length of which is $40D_H$. The rest of the domain ($30D_H$) is heated by a constant heat flux imposed on the walls.

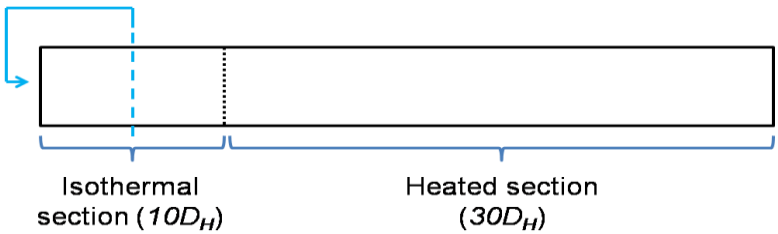

Fig.6.1 The scheme of the internal mapping for creating a fully developed inlet boundary condition for LES.

The cross section of the geometry considered here is the same as that studied in Chapter 5. There is a narrow gap contained in the channel. The hydraulic diameter of the flow passage is 0.0314m. The properties of the water at 25 MPa is obtained by

NIST (2009) and integrated in the Code_Saturne by using a subroutine. The pseudo critical temperature of water at 25MPa is ~658K. The temperature of the incoming flow is set as 633K, while the Reynolds number of the incoming flow is chosen to be 10540 which is double the value of that used in the previous chapter. The bulk velocity U_b, evaluated by using the water properties at T_b = 633K and 25.0MPa, is *0.0388m/s*and the mass flow rate is 0.08775kg/s, which makes the mass flux to be 22.85 kg/s-m^2. Four cases are included in this study. The properties of water at T_b = 633k and 25.0MPa are utilized in Case 1 (constant property case) and the heat flux is set as 7.5×10^4 W/m^{2}on both walls in the heated section of the domain. The properties are allowed to vary with temperature in the other three cases (Case 2, 3 & 4). The difference among these three cases lies in the imposed heat flux at wall of the heated section in the domain. The magnitudes of heat flux are set as 1.0×10^4 W/m^2, 5.0×10^4 W/m^2, and 7.5×10^4 W/m^2 respectively.

Again a non-uniform mesh is adopted in this study; a fine grid is located close to the wall, while big elements are placed in the centre of the main channel. Since the Reynolds number of the flow is double that of the flow in Chapter 5, the mesh in the near wall region is refined compared to that used earlier, while the size of the mesh element in the centre of channels remains the same. The first near wall mesh nodes are in the range of $5 \leq \Delta x^+ \leq 17$, $0.13 \leq y^+ \leq 0.2$ and $\Delta z^+ \approx 23$. There are about 13 cells located between the wall and y^+ = 20, while ~9 cells located in the range $0 \leq y^+ \leq 10$. It should be noted that these numbers are evaluated in the isothermal sub-domain. In total, there are 33 million mesh elements in the domain. The time step is set as 0.01s in the Case 1, while it is reduced to 0.001s, 0.0005s and 0.0005s in Cases 2, 3 and 4, respectively, since the flow is accelerated in these three cases. The CFL number in Case 1 is < 0.4, while it is < 0.7 in the other three cases. The momentum and energy equations are solved using the *second order upwind scheme*, while the *SIMPLE* scheme is chosen for pressure-velocity coupling.

To facilitate discussion, several locations and lines are predefined in the domain to display results, see Fig. 6.2. In addition, instantaneous velocities are also recorded at 30 points at locations ‘MP1’ and ‘MD’ down the channel from 0.385m to 1.10m. These values are used to study the behaviour of the flow in the narrow/big gaps and

investigate the changes in size and dominant frequency of the flow structures in the regions. The lines, 'ML' together with 'P1', 'P2', 'P3', are to present the local distributions of the turbulence statistics such as the mean velocity and turbulence quantities.

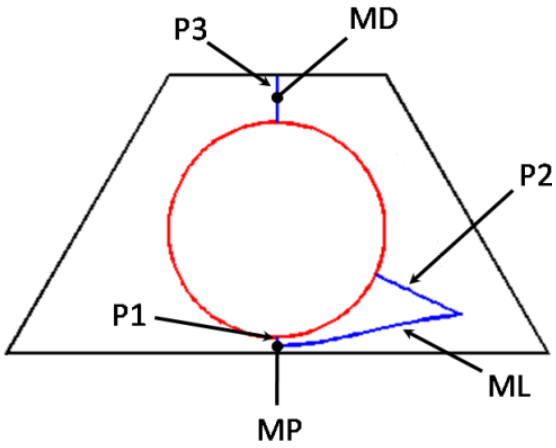

Fig.6.2 The predefined locations in the domain.

6.2 Results and discussions:

6.2.1 Quality of the results

Before discussing the results, it is always necessary to check the quality of the results first. As most severe thermal expansion occurs in Case 4, the quality of the results in this case can be a good indicator for other cases. Consequently, only the results in Case 4 are presented in this section. As no experiment results or DNS results are available, the quality of the results are assessed using the distribution of non-dimensional streamwise velocity w^+ on 'P2' against the theoretical functions and contours of three quality criteria of LES at different levels down the channel.

Velocity profile

The non-dimensional velocity along 'P2' at z = 0.157m is shown in Fig. 6.3. No heat flux is imposed at this level. As shown in the figure, the predicted velocity profile agrees well with the log law distribution.

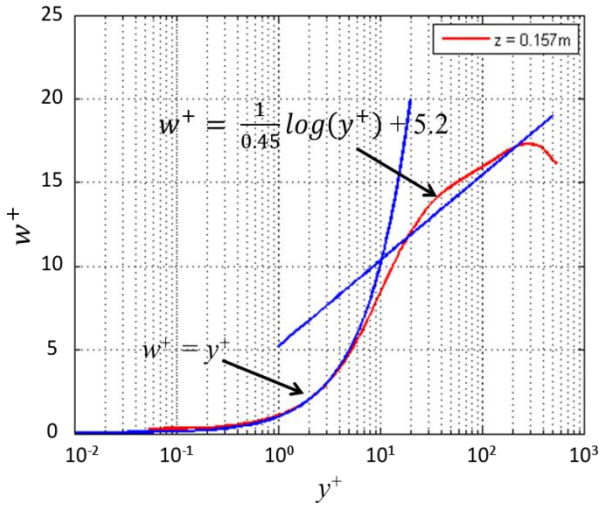

Fig.6.3 The velocity profile along 'P2' at z = 0.157m.

LES quality criteria

Same as in Chapter 5, the LES quality criteria (*S*) proposed by Geurts and Frohlich (2002) and two sub-versions of the criteria proposed by Celik et al. (2005) are used to address the quality of the results. The former criteria (*S*) is defined as the ratio of the SGS viscosity ($\langle\mu_{sgs}\rangle$) and the total viscosity ($\langle\mu_{sgs}\rangle + \langle\mu\rangle$), while the other one is based on the comparison of the grid resolution and the Kolmogorov length scale. The definition of these two criteria can be found in Chapter 3. The numerical dissipation, represented by the numerical viscosity μ_{num}, is included in the criteria suggested by Celik et al. (2005). It is difficult to know the real numerical viscosity from the simulations. Normally, it is evaluated by making some assumptions. The differences of the two sub-versions (*LES_Q01* & *LES_Q02*) of criteria proposed by Celik et al. (2005) rooted in the evaluation of the numerical viscosity. The two assumptions are $\mu_{num} = \mu_{SGS}$ in *LES_Q01*, and $\mu_{num} = 14.5\mu_{SGS}$ in *LES_Q02*. More details can be found in Chapter 3.

Fig. 6.4 shows the contours of *S* at different distances down the channel in Case 4. Overall, the values of *S* gradually increase with the distance down the channel. At z=0.157m, where no heat flux is imposed on the wall, the values of *S* in the near wall region are very close to 0, while they are around 0.2-0.4 in the gaps. Hence a good resolution is achieved in the non-heated section. The values in the main channel can

be as high as 0.8. The area with the values of S > 0.8 becomes bigger down the channel. The region of $S > 0.8$ spreads almost all of the cross section at z = 1.10m. This indicates dissipation of turbulence kinetic energy due to μ_{sgs} dominates at this level of the channel in Case 4, which is probably due to the increased turbulence level down the channel.

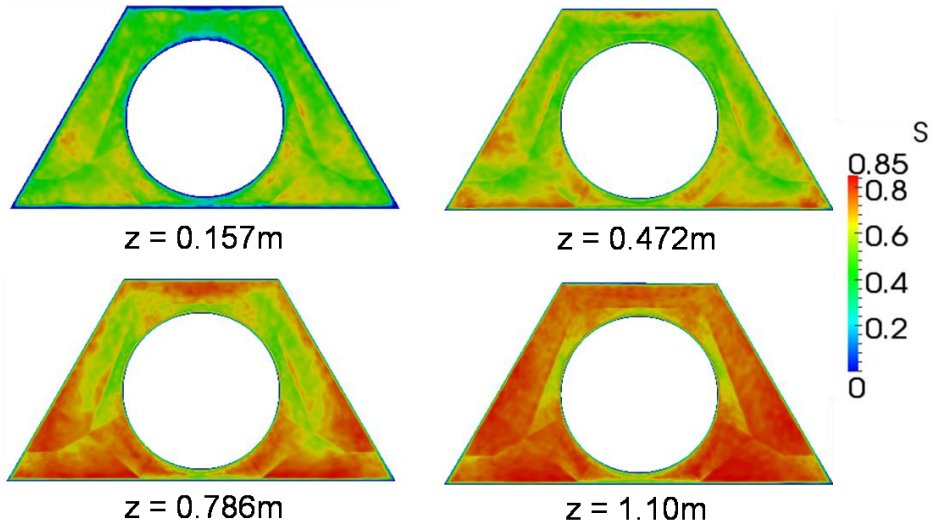

Fig.6.4 Contours of *S* at difference levels down the channel in Case 4

The counters of *LES_Q01* and *LES_Q02* at four levels are shown in Fig. 6.5 and Fig. 6.6, respectively. The overall values of these two criteria decrease with the distance down the channel, which can also be due to the increased turbulence level in the heated part of the channel. As mentioned in Celik et al. (2005), the quality of LES is considered as good if $LES\_IQ_v > 0.8$. It can be clearly seen in Fig. 6.5 that the value of *LES_Q01* at 0.157m ranges from 0.9 to 1.0. The minimum value of *LES_Q01* at other levels is ~0.85. It means that the quality of the simulation is reasonable according to *LES_Q01*. However the lowest value of *LES_Q02* at 0.157m decreases to 0.75 centralized in the main channel, while the value in most part of the cross section is still above 0.8. Moreover, the value in the near wall region is still ~1 at this level. Further down the channel, the minimum value of *LES_Q02* becomes even smaller. The range reduces to 0.65-0.8 at z = 1.10m. But it should be remembered that a very strong artificial numerical viscosity is assumed in the *LES_Q02*, which may not be true in the real case.

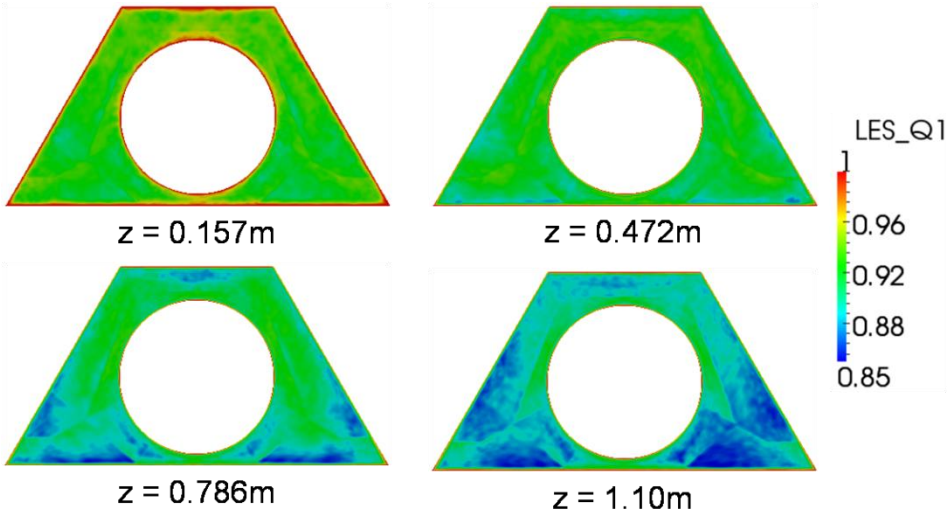

Fig.6.5 Contours of *LES_Q01* at difference levels down the channel in Case 4

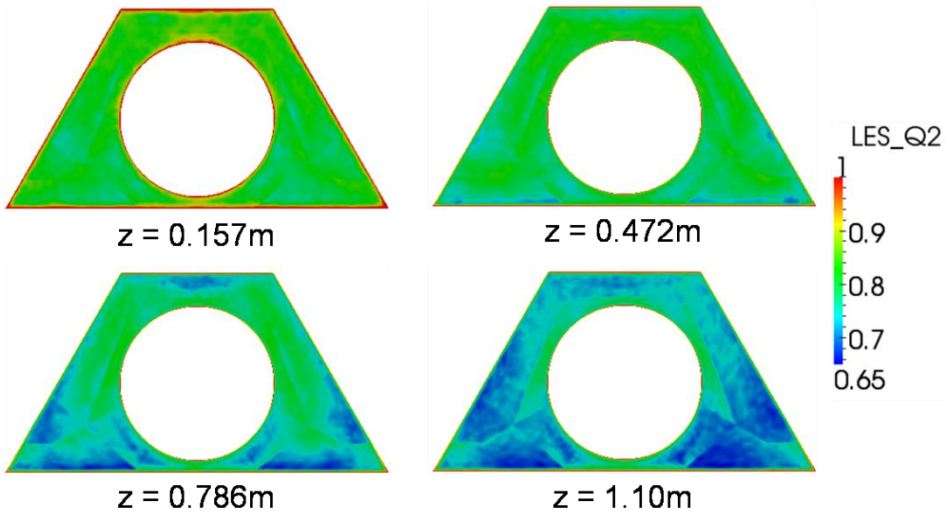

Fig.6.6 Contours of *LES_Q02* at difference levels down the channel in Case 4.

In summary, the good agreement between the predicted velocity profile and theoretical distribution and the good performance of the different criteria in the isothermal part of the domain indicate that the flow in this section is solved with good accuracy. For the heated section, the values of *S* are generally higher than the criterion (S<0.2) for a well resolved LES. *LES_Q01* indicates a good simulation (*LES_Q*> 0.8) throughout the whole channel. The value of *LES_Q02*, with $\mu_{num} = 14.5\mu_{sgs}$, is mostly smaller than 0.8 at z = 1.10m down the channel but by much. It is also worth to note that the results shown here are for Case 4, in which case more turbulence due to high flow temperature is expected at the lower part of the channel. As will be shown later it is not true in other cases.

6.2.2 Bulk parameters

Although the primary objective of this study is to investigate the thermal expansion effect on the gap flow instability, it is still useful to look at the bulk parameters, which would help us understand the performance of the large flow structures in the channel later.

As the density of the supercritical water varies around T_{pc} greatly, the mean quantities are evaluated by using the Favre averaging. The Favre-average mean of a variable φ and its fluctuation, φ'' are defined as follows:

$$\tilde{\varphi} = \langle \rho\varphi \rangle / \langle \rho \rangle \text{ and } \varphi'' = \varphi - \tilde{\varphi} \tag{6.1}$$

The '<>' indicates the Reynolds averaging.

Then the bulk velocity and bulk temperature are defined as:

$$W_b = \int_A \langle \rho w \rangle dA \Big/ \int_A \langle \rho \rangle dA \tag{6.2}$$

$$T_b = \int_A \langle \rho w \rangle \tilde{T} dA \Big/ \int_A \langle \rho w \rangle dA \tag{6.3}$$

Fig. 6.7 shows distribution of the wall temperature (T_w), flow bulk temperature (T_b) and heat transfer coefficient (*HTC*) down the channel. The significant variation of properties in the heated section of the domain is expected to occur in Cases 3 & 4, as the condition of $T_b < T_{pc} < T_w$ is maintained in the heated section, except at the very start of the section, see Fig. 6.7 (a) & (b). The gentle change of properties can be expected in Case 2 as $T_b < T_w < T_{pc}$. The monotonic increase in the wall temperature is observed in all of the cases. The increase rate of the wall temperature is much more significant in Cases 1 & 4 in comparison with Cases 2 & 3. Higher heat flux in Cases 1 & 4 is the main reason. The zig-zag in the wall temperature distribution is likely due to inefficient data.

Similar to the wall temperature, the bulk temperature increases monotonically in all of the cases, refer to Fig. 6.7 (b). It should be noted that the increase is much steeper in Case 1 than in other three cases. The positive relationship between the increase rate and the heat flux is established by comparing the results for Cases 4, 3 & 2. Although $T_b < T_{pc}$ in Cases 3 & 4, it is still possible that the local temperature in some region, such as the near wall region and the vicinity of the narrow gap, can be higher than T_{pc} in these two cases, especially at the low levels of the channel. Furthermore, the bulk temperature at certain level down the channel in Case 4 is lower than in Case 1, which implies a reduction in HTC in Case 4.

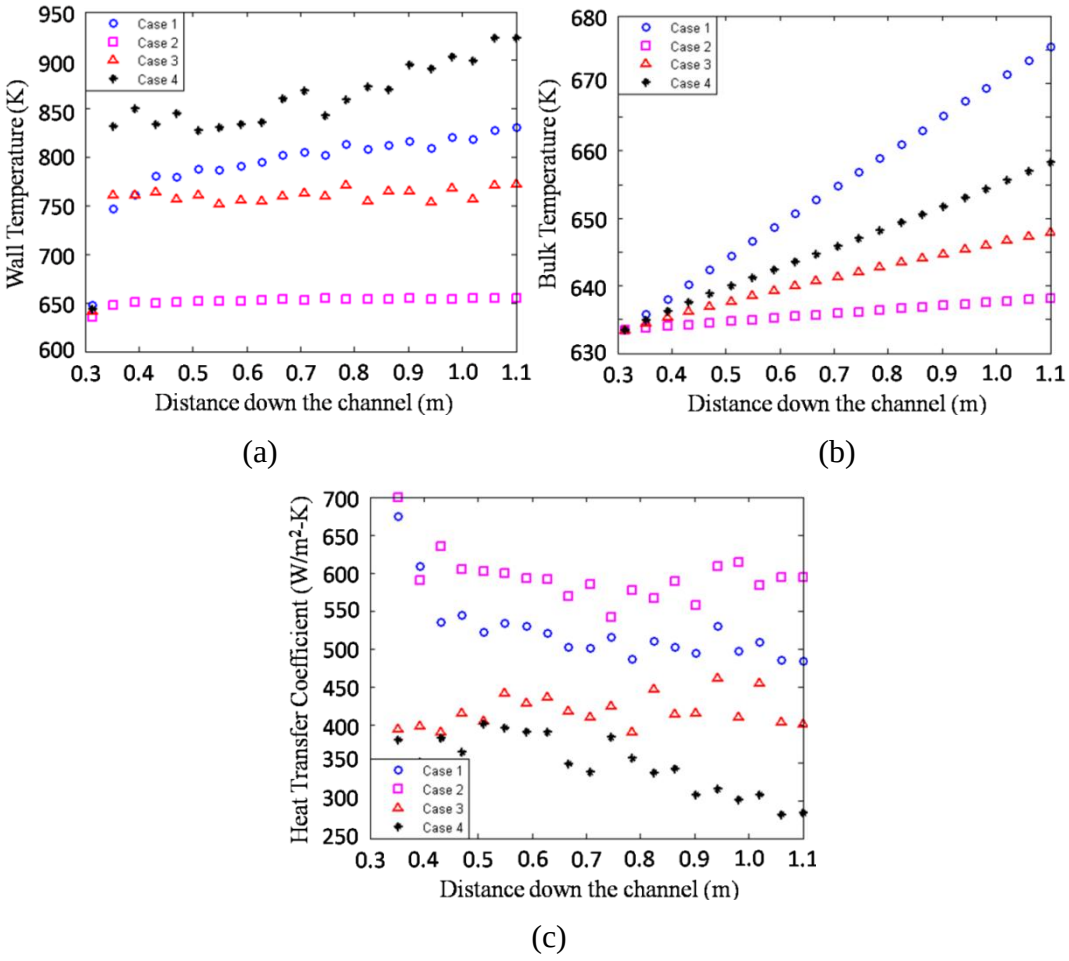

Fig.6.7 Streamwise distribution of (a) wall temperature; (b)bulk temperature and (c) local heat transfer coefficient.

The streamwise distribution of HTC is illustrated in Fig. 6.7 (c). It is highest in Case 2, then Case 1 and followed by 3, while the lowest value can be seen in Case 4. After the steep drop at the beginning of the heated section, the HTC in Cases 1 & 2

remains at the same level throughout the channel, while the HTC in Case 3 remains more or less the same in the heated section and HTC in Case 4 drops from the middle section of the section. The increased HTC in Case 2 is due to the increased Prandtl number in the near wall region which is ~2.16 in comparison with 1.183 in Case 1. (These values are obtained by using the wall temperature in the cases). The Prandtl number in the near wall region of Cases 3 & 4 is similar to that in Case 1. However the greatly reduced thermal conductivity is the potential reason for the decrease of HTC in these two cases.

The distribution of bulk velocity down the channel is illustrated in Fig. 6.8. The bulk velocity remains the same in Case 1; it increases steadily in all other cases due to the temperature dependent density. In Case 4, the increase becomes steeper moving down the outlet. Due to the significantly increased bulk velocity in the lower level of the channel, a large velocity change in the near wall region is expected in Cases 3 & 4.

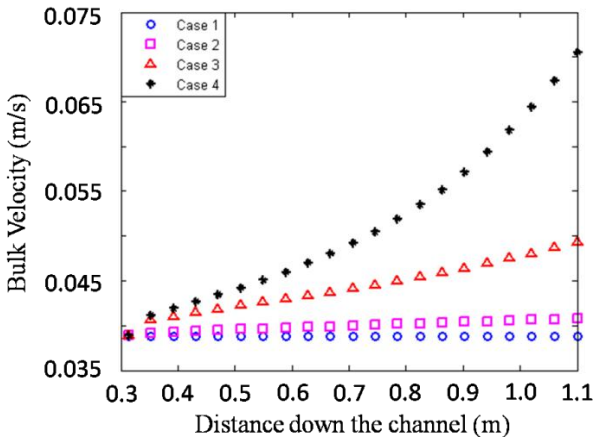

Fig.6.8 Streamwise distribution of bulk velocity down the channel

6.2.3 Velocity field

Instantaneous flow field

To demonstrate the performance of the large flow structures in the narrow gap region, the contours of the instantaneous temperature field at the equal-distance plane between the rod and bottom edge of the trapezoid channel is illustrated in Fig. 6.9. A

regular swinging flow structure is clearly shown in Case 1. The shape of the flow structure remains the same in Case 2, but becomes more irregular in the lower part of the channel in Case 3 and Case 4.

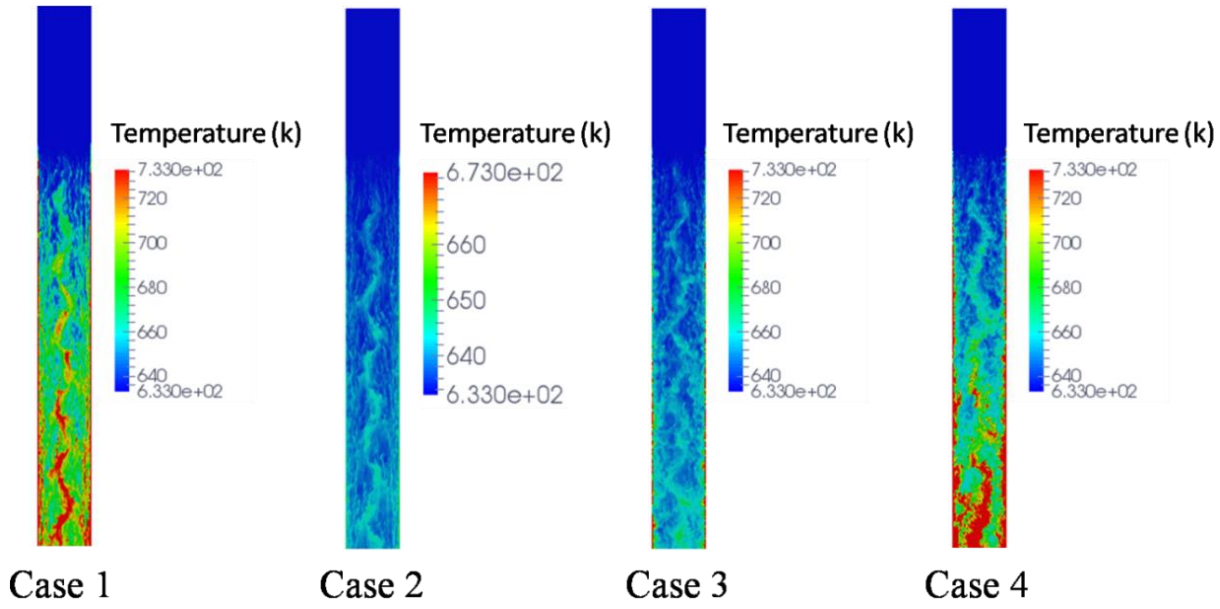

Fig.6.9 Contour of the instantaneous temperature field at equal-distance plane.

To provide more details of the instantaneous feature of the flow structure, the instantaneous turbulent spanwise velocity/x-velocity (u') at 'MP' and 'MD' at different levels of the channel are shown in the Fig. 6.10 and Fig. 6.11, respectively. Similar to the information shown in the contours, regular oscillations of u' at 'MP' are observed in Cases 1 & 2 at different levels down the channel. The dominant periods of the oscillations are similar at all of the levels and in both cases, which are ~4.5s. Similar regular oscillations are also recorded at the high levels of the channel ($z = 0.471m$ & $0.628m$) in Cases 3 & 4. As the temperature increases with the distance down the channel, the local flow temperature in the narrow gap can rise beyond the T_{pc}, which would lead to severe property changes in the narrow gap. As a result, stronger noises can be observed in the signals recorded at the levels further down the channel (z = 0.785m, 0.942m & 1.10m) in the narrow gap. In the meantime, the dominant frequency of the oscillation is hard to be obtained from the instantaneous history at these levels due to the strong noises.

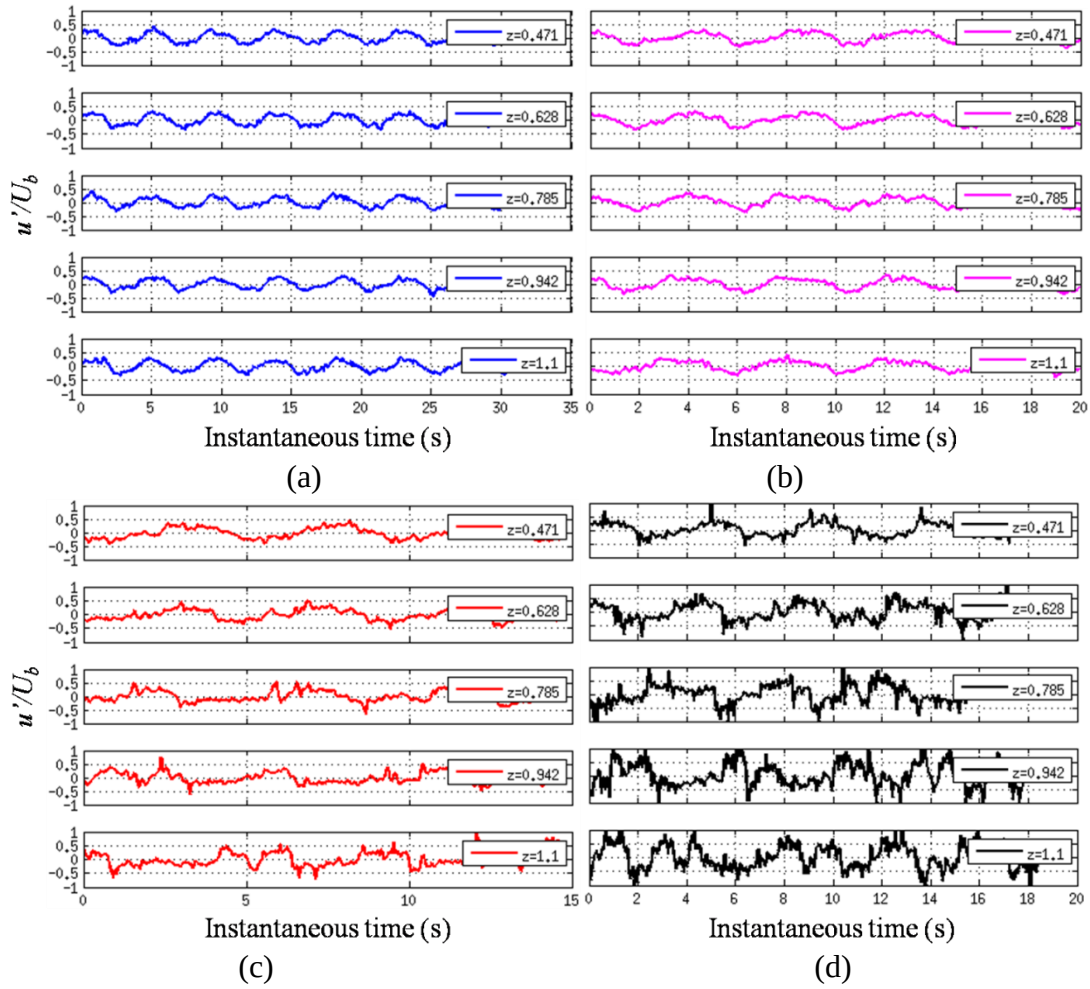

Fig.6.10 Instantaneous x-velocity at 'MP' at four levels for (a) Case 1; (b) Case 2; (c) Case 3; (d) Case 4.

As mentioned in the Chapter 5, there are large flow structures passing the big gap as well. A regular oscillation of the signal should be recorded at the 'MD'. However, it is very difficult to see any regular oscillations of *u'* at 'MD' in all the cases, except *u'* at z = 1.10m in Case 4, the dominant frequency period of which is 5*s*, similar to that at '*MP*' mentioned above. The disappearance of the regular oscillations is probably due to the high turbulence level at the bigger gap in the channel, together with the weak strength of the flow structure.

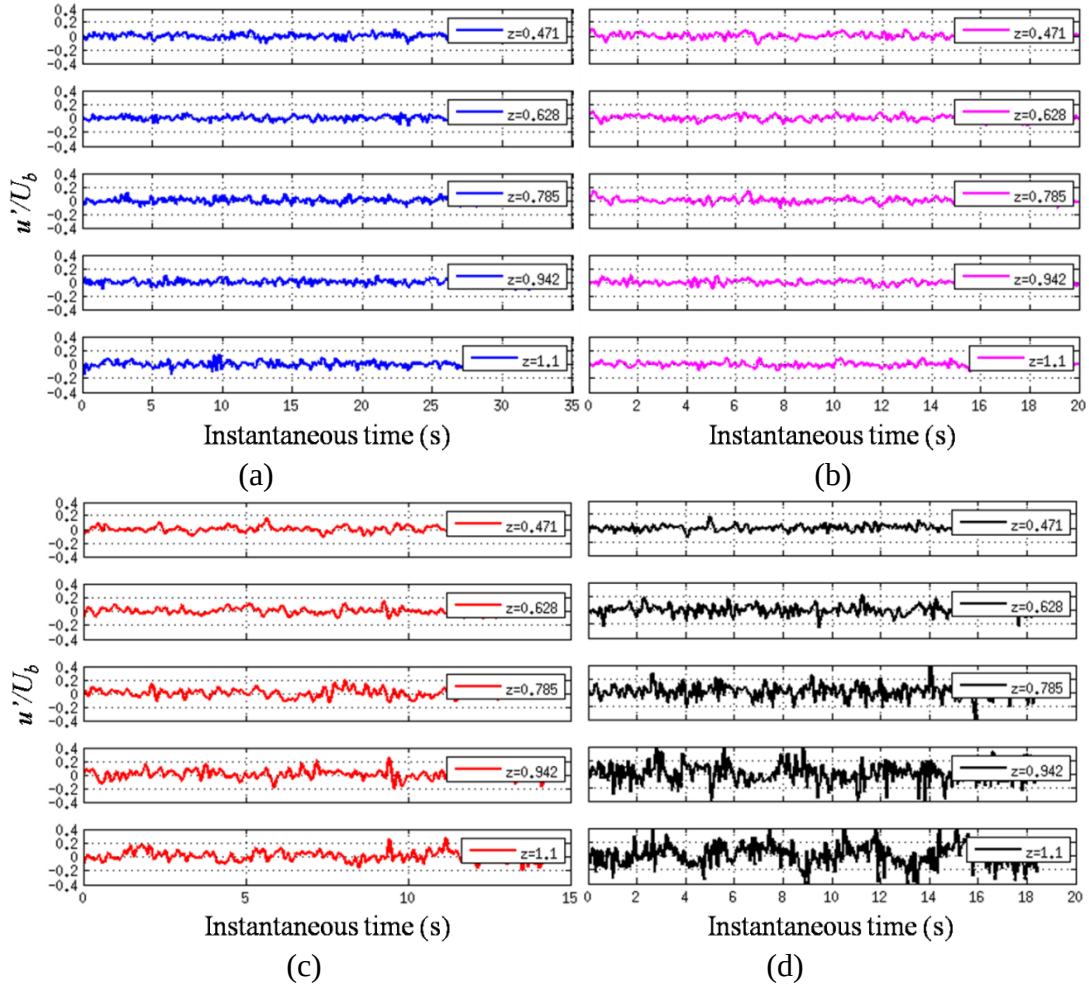

Fig.6.11 Instantaneous x-velocity at 'MD' at four levels for (a) Case 1; (b) Case 2; (c) Case 3; (d) Case 4.

6.2.4 PSD and correlation analysis

To quantify the dominant frequency of the flow structures, the power spectrum density (PSD) of *u'* at 'MP' & 'MD' at different levels down the channel is analysed, the results of which are presented in Fig. 6.12 & Fig. 6.13, respectively. As shown in Fig. 6.12, there are the visible peaks in the distribution of the PSD of *u'* at 'MP' at all of the levels in the cases. The frequency of the peaks (f_p) which is the dominant frequency of the structures remains the same throughout the channel in the cases. The values for the different cases are very similar to each other (~0.22Hz). The calculated Strouhal number $St^{-1} \cong 5.61$. (It should be noted the number is evaluated by using the bulk velocity at the unheated section of the domain.) This value is almost the same as the St^{-1} (~5.57) obtained in the forced convection case

studied in Chapter 5. This again proves that the Strouhal number is more related to the bulk velocity rather than the friction velocity. It is also worth to remind the readers here that the current working fluid is liquid water in Case 1 and supercritical water in the other three cases, and the Reynolds number of the incoming flow here is double the value considered in Chapter 5. As a result, the results of the current study again confirmed that St^{-1} is only dependent on the geometry configuration in a buoyancy free system. The effect of the force due to thermal expansion is rather limited.

The peaks can also be seen in the PSD of u' at 'MD' at some levels, but disappear in other levels in all the cases, as shown in Fig. 6.13. For example, the peak of PSD of u' at 'MD' disappears at the z = 1.10m in Case 1 and z = 0.157m in Case 4. The weak strength of the flow structures and short sampling interval are likely to be the reason. Furthermore, there are two sets of peaks that can be found in the figure, the first ranges from 0.2Hz to 0.3Hz, while the second peak can be found between 0.4Hz to 0.7Hz.

The value of f_p for the first set of peaks is very similar to f_p of the flow structures in the narrow gap. Similarly to f_p of swinging flow structure, they do not change much as the heat flux varies from 10^4 to $7.5x10^4$ in Cases 2, 3 & 4. Consequently the flow structures passing the 'MD' associated with the first peak are potentially linked to the swing flow structure in the narrow gap region. To simplify the discussion, such flow structures in the big gaps will be referred to as the first flow structures. In addition, the secondary peaks at certain levels indicate the possibility of the existence of other structures in the big gap. These flow structures will be referred to as the second flow structures later. Again no systematic trend of relationship between the dominant frequency of the second flow structures and heat flux is revealed in the figure. Different from the observations in Chapter 5, the dominant frequency of the second flow structures are smaller than the first flow structures and the energy of the first flow structures is significantly greater than that of second flow structure. The dominant frequencies of the rotating flow structures mentioned in the last chapter are not here. As mentioned in the previous chapter, the frequency of the rotation flow structure is much bigger than that of the swinging flow structure in the narrow gap. But the number of samples recorded in this study is not enough to

capture the rotating flow structure. The second peak shown here is probably due to another flow structures passing the big gap.

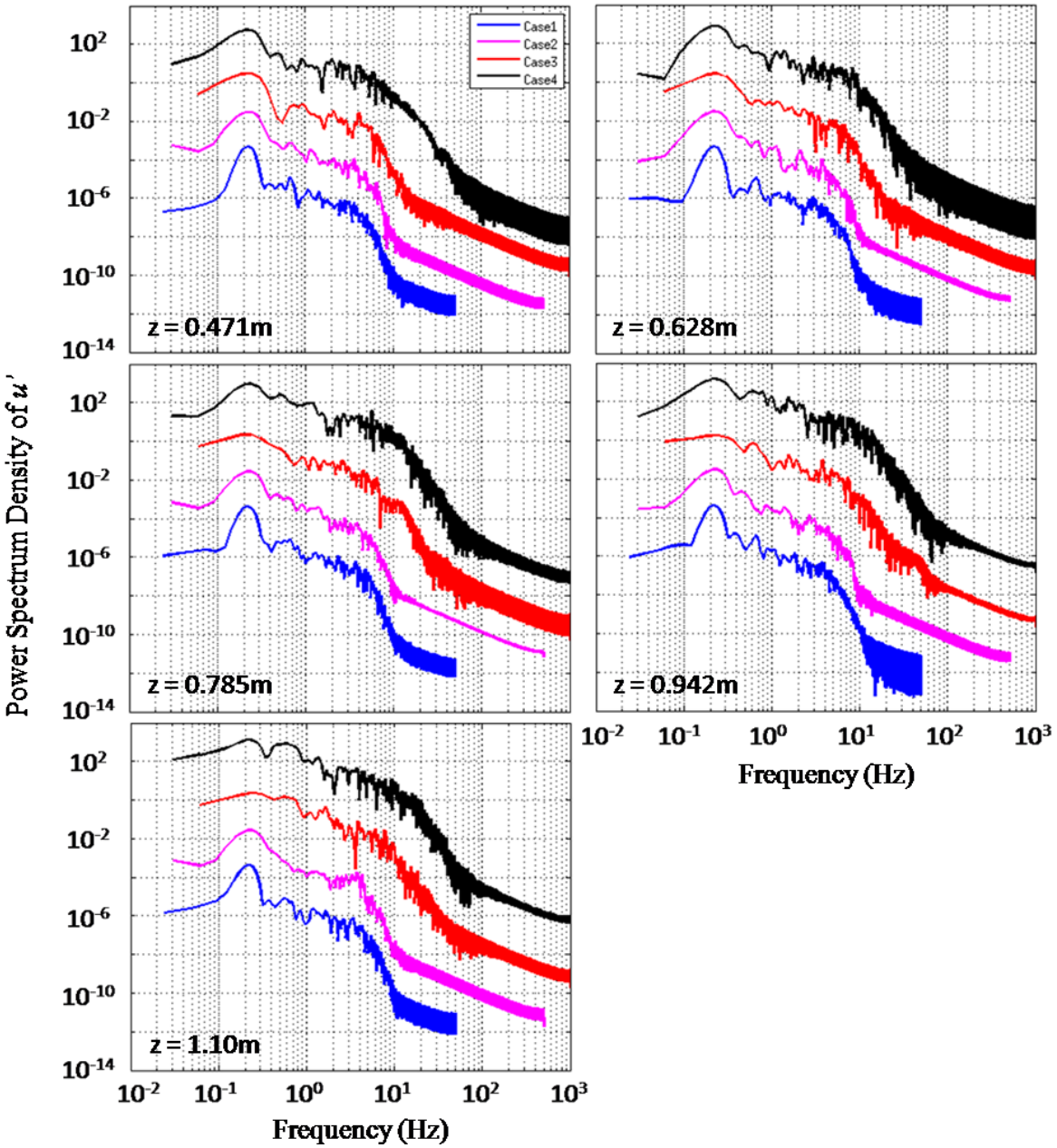

Fig.6.12 Power spectrum density of ***u'*** at 'MP' at different levels for all of the Cases.

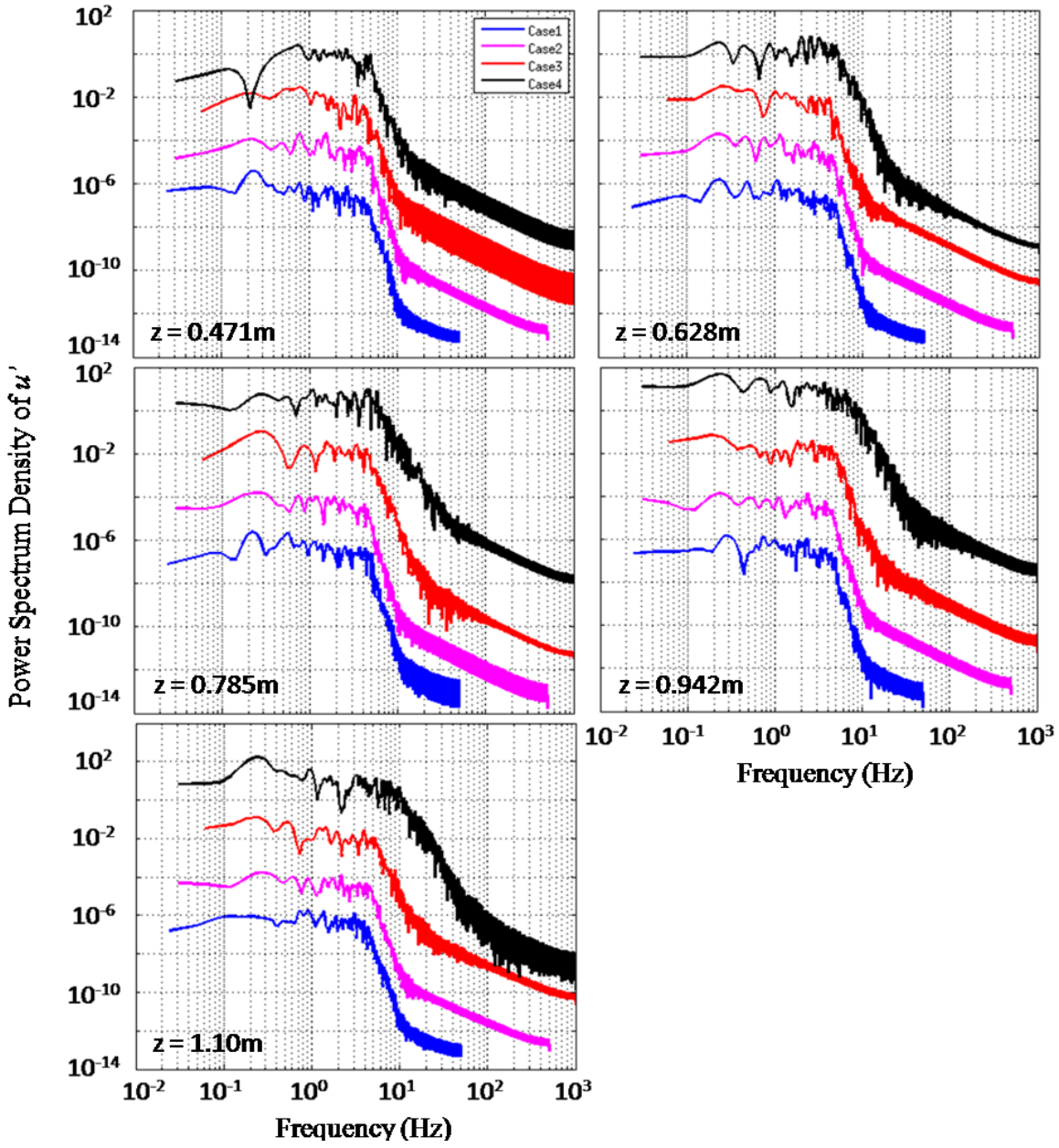

Fig.6.13 Power spectrum density of ***u'*** at 'MD' at different levels for all of the Cases.

The link between the structures passing the big gap and narrow gap can be established by studying the cross correlation functions between the *u'* at 'MP' and 'MD', which are shown in the Fig. 6.14. The strong correlation between the signals of *u'* at 'MP' and 'MD' at different levels (0.471m, 0.624m, 0.785m, 0.948m and 1.10m) has been demonstrated in the figure. The cross correlation function of *u'* takes a similar pattern at different levels of all the cases, except z =1.10m in Case 4. The strongest negative correlation between *u'* at 'MP' and 'MD' can be observed at zero time delay at all of the levels, except at z = 1.10m in Case 4. It is reasonable to

conclude that the direction of flows passing ‘MP’ and ‘MD’ are statistically opposite with respect to the x-direction. Namely, as the flow passing ‘MP’ moves towards the right x-coordinate, the flow passing ‘MD’ will lead to the left. As the configuration of the flow passage cross section is the same as that studied in the previous chapter, it is reasonable to assume that there are rotating flow structures around the rod existing in the cases considered here. The shift of the minimum negative correlation from zero time lag at z = 1.10m in Case 4 indicates a phase difference between the signal of *u’* at ‘MP’ and ‘MD’ in the bottom of the channel.

Together with the behaviour of the PSD of *u’* at ‘MD’, it can be concluded that there are large flow structures passing the big gap. They are strongly correlated with the flow structures in the narrow gap. Different from the flow structures in the narrow gap, the flow structures passing the big gap is potentially dependent on the Reynolds number and working flow properties.

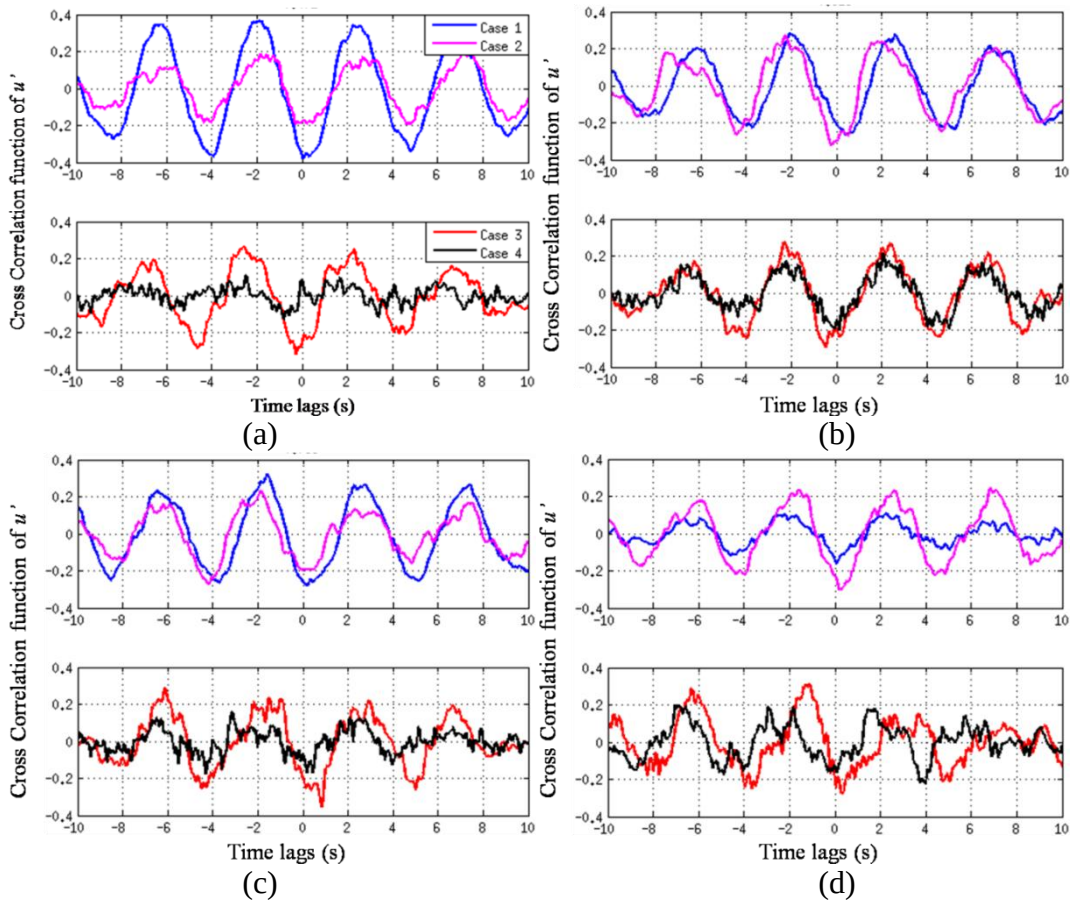

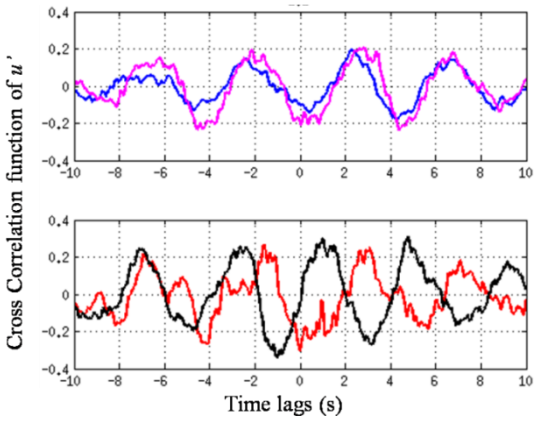

(e)

Fig.6.14 The cross correlation function of $\boldsymbol{u'}$ between 'MP1' and 'MD' at level (a) 0.471m; (b) 0.628m; (c) 0.785m; (d) 0.948m; (e) 1.10m.

As discussed above, the dominant frequencies of the flow structures in the vicinity of narrow gap keep more or less the same in all of the cases throughout the channel. However, the flow velocity is accelerated in all the cases which consider the properties variation of the supercritical water. So, the wave length of the flow structures in the narrow gap increases in Cases 2, 3 & 4. To demonstrated this, the cross correlations of between the *u'* at 'MP' and 'MD' at z = 0.345m and other levels down the channels are presented in Fig. 6.15. As shown in Fig. 6.15 (a), the wavelength of the flow structure passing 'MP' is ~0.2m, which remains the same for z < 0.8m in Case 2, but increases a little for z > 0.8m. A similar trend can also be observed in Cases 3 & 4 although a visible elongation of the wave length occurs much earlier in these two cases, starting around 0.5m down the channel. Consequently a positive relationship between the heat flux and the wavelength is established.

Different from the observation of the cross-correlation of *u'* at 'MP', it is hard to see any regular waves from Fig. 6.15 (b) for 'MD'. Some high positive values can be found at certain levels in Cases 1, 2 & 3, but not in Case 4. These results show that the flow structures (if any) in the larger gap are much weaker. However, lack of data points may also contribute to the weak correlation shown in Fig. 6.15 (b). Nevertheless, the distance between intervals of the burst values shown is very similar to that at 'MP' in the upper levels of the heated section (z < 0.7m) in the various cases. It is also worth to note that there are some small peaks that can be found

between two significant peaks, such as the peak located at ~0.45m or 0.6m down the channel in Cases 2 and 3. It is probably due to the existence of some secondary flow structures in the big gaps.

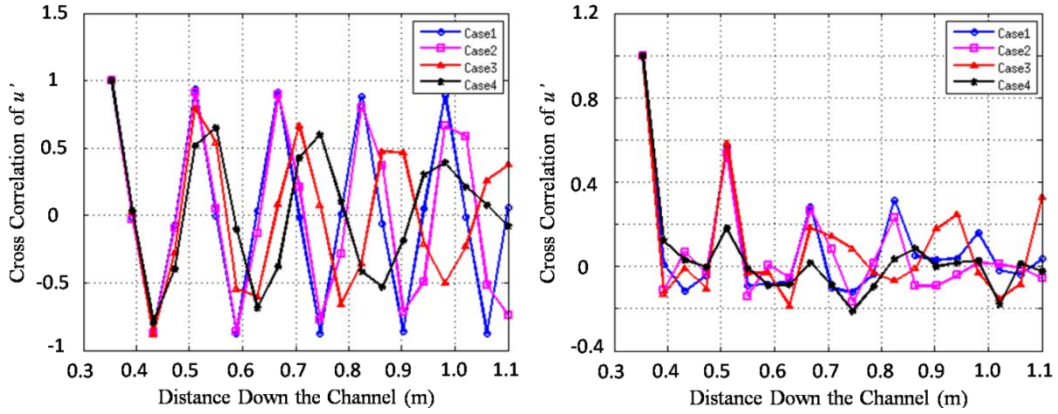

Fig.6.15 Cross correlation of u' at different axial points located in the middle of narrow gap and big gap.

Summary

Now, it is reasonable to conclude that there are different flow structures existing in the considered cases in this chapter. The swinging flow structures dominate in the vicinity of the narrow gap in the channel, while there are other flow structures passing the big gap in the channel. Although the velocity is redistributed in the cross section due to the temperature dependent properties in the high heat flux case, the characteristics of swinging flow structure do not change much, except for elongated wavelengths. The Strouhal number (St^{-1}) of the swinging flow structure remains the same in all of the cases.

The flow structures in the big gap are much weaker than the swinging flow structures in the small gap. Two dominant frequencies can be found in the PSD of u' at MD, which means there are potentially two types of flow structures with different frequencies existing in the big gap. These flow structures are strongly correlated with the swing flow structures in the narrow gap, which is the same as that discussed in the Chapter 5. The dominant frequency of the first structures in the big gap is very similar to the swing flow structure, which suggests that the two structures are likely

to be directly related. The phase difference between the flow structures in the big and narrow gap can occur when the thermal expansion is very strong.

6.2.5 Turbulence quantities

Statistics flow field

The statistics of flow field at different levels of the flow passage in all of the cases will be discussed in this section to show the thermal expansion on the flow distribution in the non-uniform channel.

Thanks to the symmetry of the horizontal cross section about the plane x = 0m, only the right side of the cross section is shown here. As presented in Fig. 6.16, the velocity distribution at different levels in the channel is very similar to each other in Cases 1 and 2. This is because the property changes are small in Case 2 as $T_b < T_{wall} < T_{pc}$ is maintained. The velocity increases everywhere in the cross section in Case 3 and 4 as the condition $T_b < T_{pc} < T_{wall}$ is maintained. The velocity is particularly high in narrow gap and in the corners, see the contour at 0.785m and 1.10m in Cases 3 and 4.

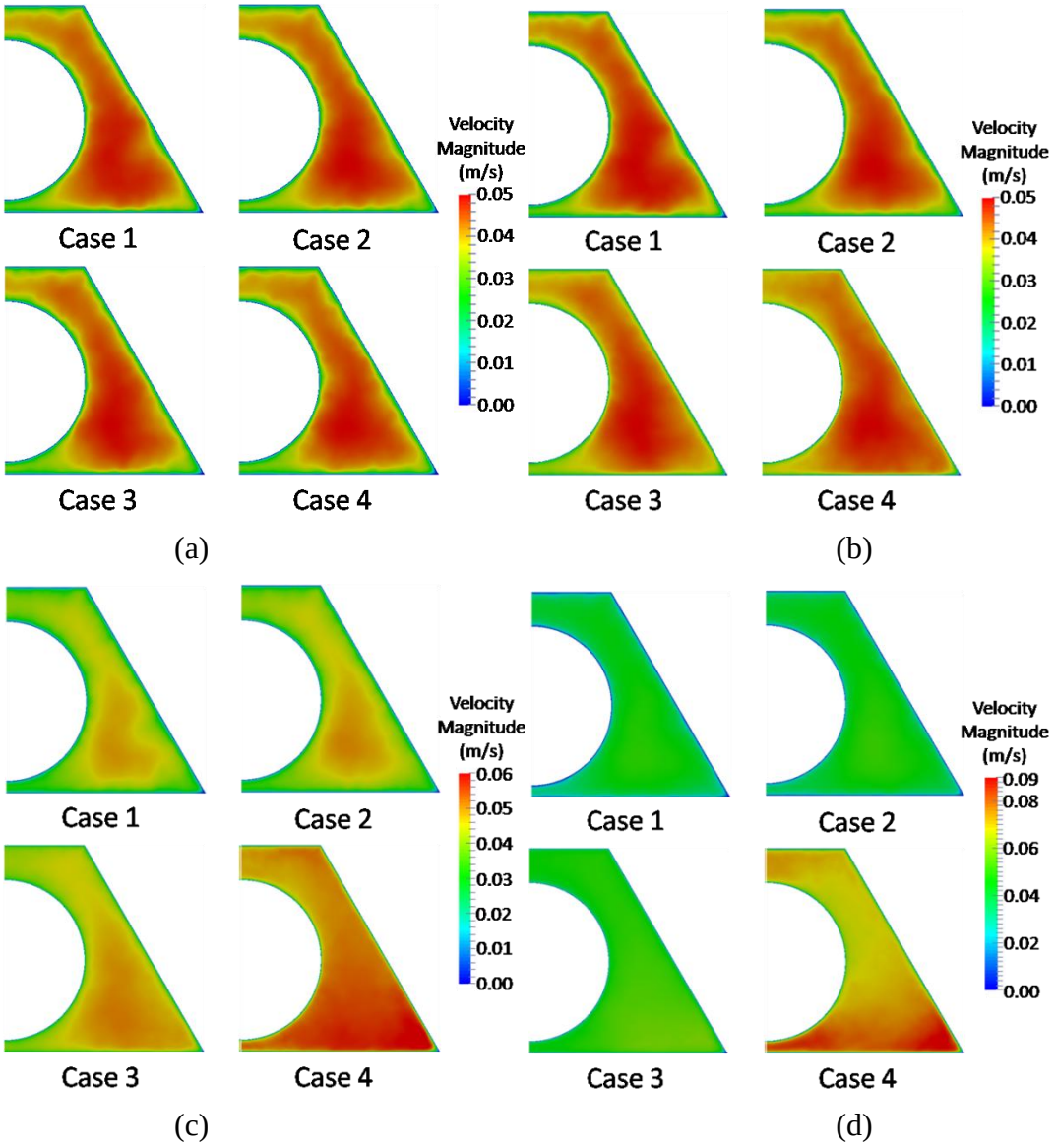

Fig.6.16 The velocity distribution at level (1) 0.157m; (b) 0.471m; (c) 0.785m and (d) 1.10m for all of the cases.

Fig. 6.17 shows the mean velocity distributions in the narrow gap ('P1'), the wider gap ('P3'), along ('P2') and the equal-distance line from the narrow gap to the centre of the main channel ('ML'). The profiles at four locations down the channel are shown here. It can be seen that the velocity profile in the narrow gap ('P1') in the isothermal case (Case 1) is typical of the laminar flow at all vertical locations. The velocity profiles in Case 2 are only slightly increased down the channel due to heating. In Cases 3 & 4, however, the velocity is significantly increased with distance down the channel. In addition, the profiles deviate from the typical laminar

profile becoming flatter in the centre. The flow acceleration is much greater in Case 4 than in Case 3 towards the low end of the channel simulated. It can be seen from Fig. 6.17 (b) that the velocity profile in the wider gap in the isothermal flow (Case 1) is typical of a turbulent flow. Again, the velocity profile in Case 2 deviates little from that of Case 1, whereas, it becomes much flatter, with an increased velocity close to the walls in Case 3. The overall magnitude of the velocity remains however little changed until towards the bottom of the simulated channel (z = 1.10m). That is the effect of heating on velocity is largely limited to the walls. In Case 4, the flattening of the velocity profile is even stronger and in addition, the overall magnitude also increases significantly at lower levels (z = 0.785m & 1.10m). Hence the heating causes large flow acceleration in the larger gap in this case.

It can be seen from Fig. 6.17 (c) that the velocity profile in Case 1 along 'P2' (i.e. that in the main channel) is typical of a turbulent flow. The velocity profiles in all cases agree with each other well at z = 0.471m and only some flow acceleration is seen in Cases 4 at z =0.785m. At z=1.10m flow is slightly accelerated in Case 3 and is significantly accelerated in Case 4. Fig. 6.17 (d) shows how the velocity varies from the narrow gap to the main channel along 'P2'. It can be seen that at z = 0.471m, the flow is only slightly increased close to the narrow gap, in Cases 3 & 4. At z = 0.785m & 1.10m, flow acceleration can be seen everywhere in Cases 3 and 4, and is much higher in the latter. In fact, at the lowest level (z = 1.10m) the velocity in the narrow gap is higher in the main channel, showing a strong heating effect in the narrow gap.

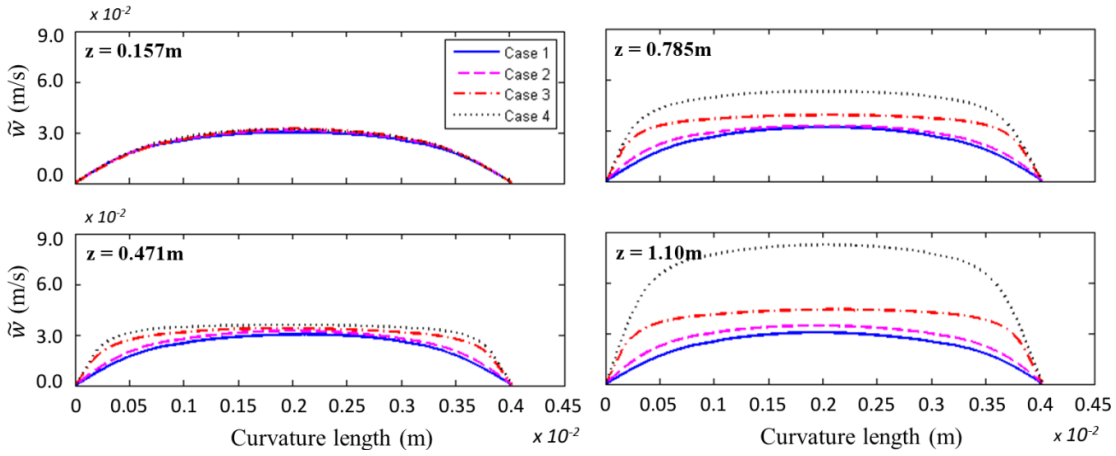
x 10-2
z = 0.157m
Case 1
Case 2
Case 3
Case 4
z = 0.785m
z = 0.471m
z = 1.10m
w̃ (m/s)
9.0
6.0
3.0
0.0
0 0.05 0.1 0.15 0.2 0.25 0.3 0.35 0.4 0.45
Curvature length (m)
x 10-2

(a)

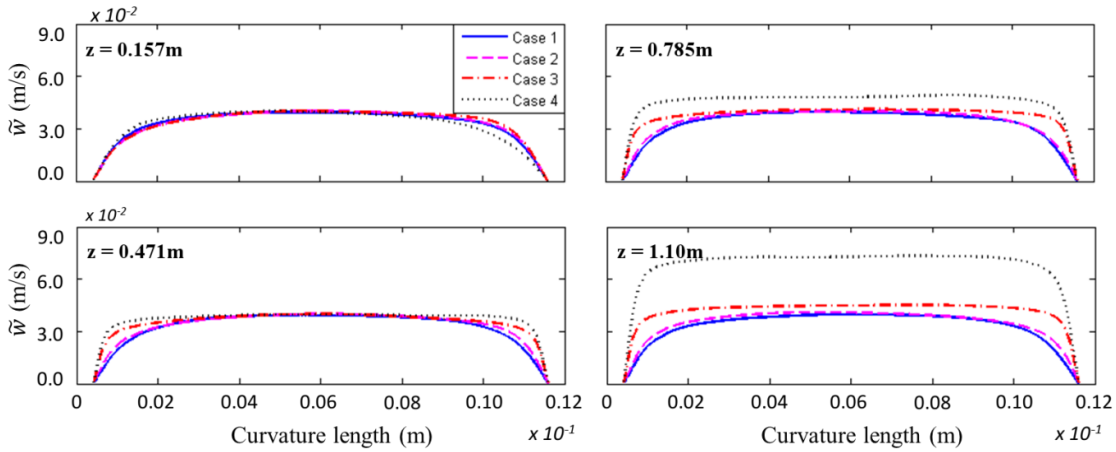
x 10-2
z = 0.157m
Case 1
Case 2
Case 3
Case 4
z = 0.785m
z = 0.471m
z = 1.10m
w̃ (m/s)
9.0
6.0
3.0
0.0
0 0.02 0.04 0.06 0.08 0.10 0.12
Curvature length (m)
x 10-1

(b)

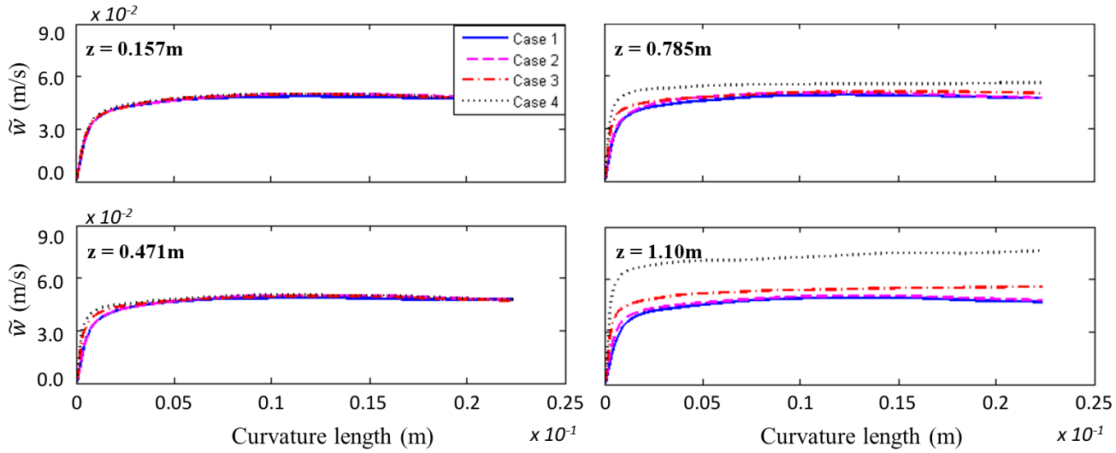
x 10-2
z = 0.157m
Case 1
Case 2
Case 3
Case 4
z = 0.785m
z = 0.471m
z = 1.10m
w̃ (m/s)
9.0
6.0
3.0
0.0
0 0.05 0.1 0.15 0.2 0.25
Curvature length (m)
x 10-1

(c)

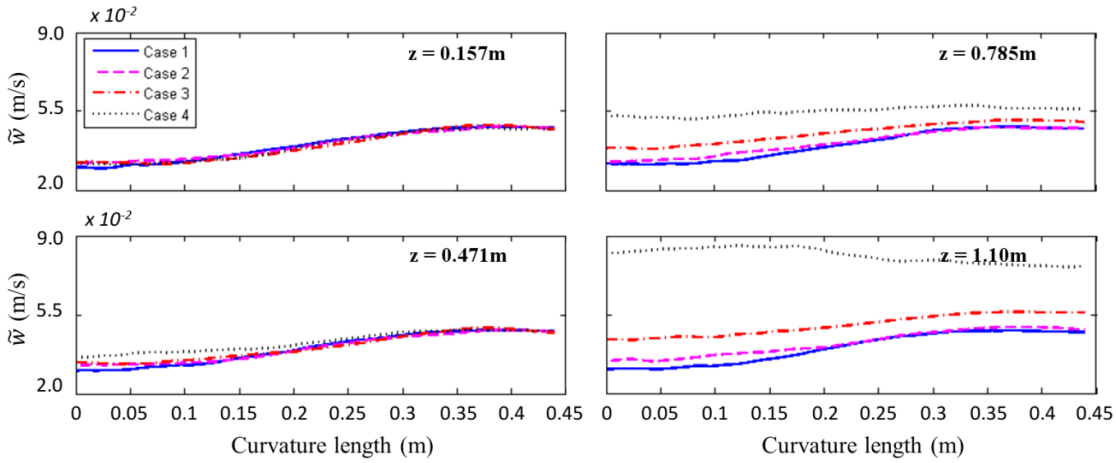

(d)

Fig.6.17 The velocity distribution along (a) 'ML', (b) 'P1'; (c) 'P2'; (d) 'P3' at four levels in the channel.

General distributions of turbulent quantities

A general view of the distribution of $0.5 * \langle \rho u_i'' u_i'' \rangle, i = 1, 2, 3$ in the cross sections at different levels down the channel can be seen in Fig. 6.18. It should be noted that u_1'' here stands for u'', u_2'' for v'', and u_3'' for w''. The cross section at levels z = 0.157m, 0.471m, 0.785m & 1.10m down the channel are selected. Thanks to the swinging flow structure in the vicinity of narrow gap, a patch of a relative high value of $0.5 * \langle \rho u_i'' u_i'' \rangle$ can be observed in the narrow gap region at all the selected levels in all the cases. By comparing the results for last three cases, it can be seen that the turbulence increases in the heated section with increase of heat flux in cases 2 to 4. However, it is believed that the very high values of $0.5 * \langle \rho u_i'' u_i'' \rangle$ in the narrow gap region at z = 0.157m in Case 4 are due to insufficient sampling data.

Interestingly, $0.5 * \langle \rho u_i'' u_i'' \rangle$ increases greatly at the corner on the bottom edge of the channel in the lower half of the heated section, see results for Cases 3 & 4 at levels z = 0.785m & 1.10m. This deviates from the expectation that turbulence is expected to decrease or die out in the corner. A strongly accelerated velocity in the region can be the main reason for this. The velocity is greatly accelerated in the corner due to the high local temperature resulting in an enhanced the shear stresses which then leads to a high turbulence level in the corner.

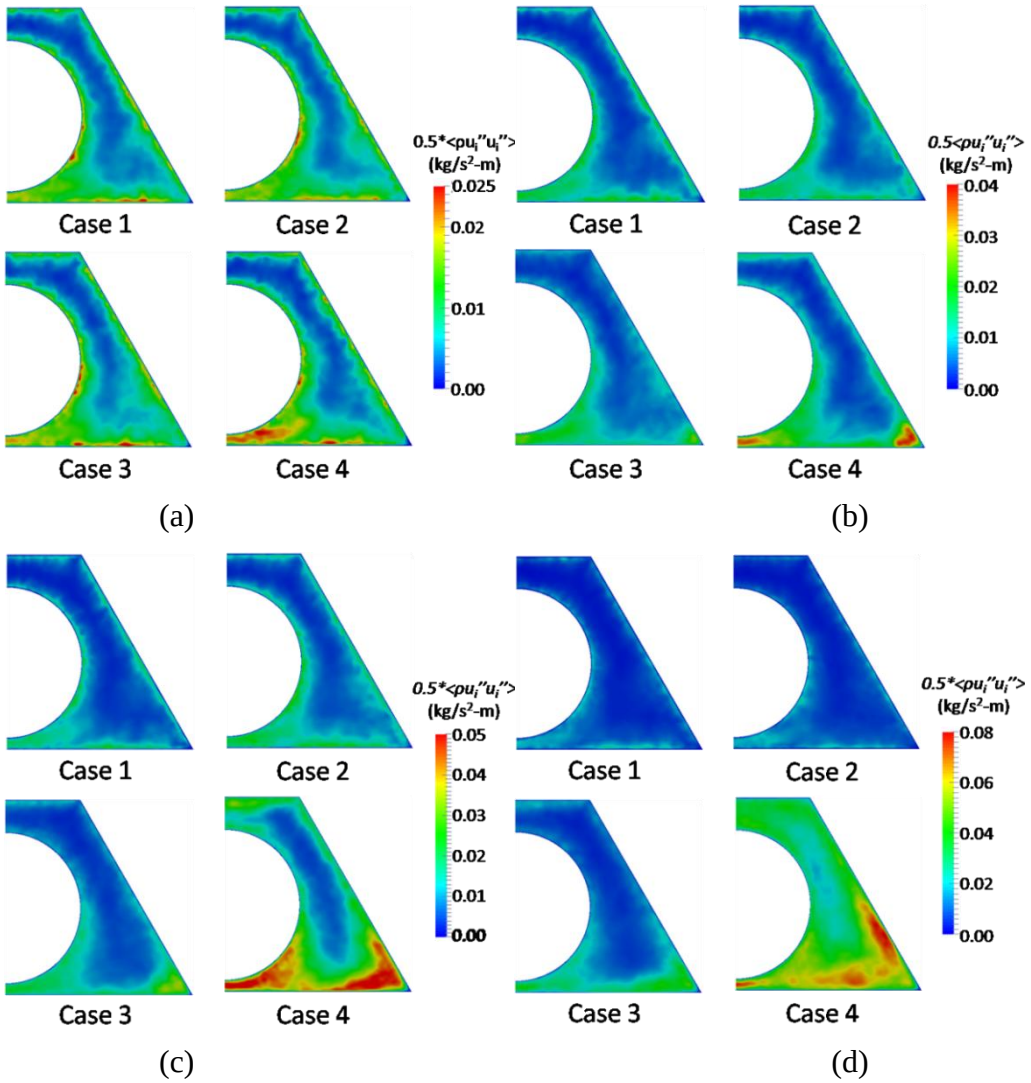

Fig.6.18 Distribution of $\mathbf{0.5} * \langle \boldsymbol{\rho u_i^{''} u_i^{''}} \rangle$at (a) 0.157m; (b) 0.471m; (c) 0.785m; (d) 1.10m down the channel.

The general view of the distribution of $\langle \rho w'' w'' \rangle$ in the cross section at different levels down the channel can be seen in Fig. 6.19. As already shown in the contours of other turbulent statistic parameters, the general view of the distribution of $\langle \rho w'' w'' \rangle$ at level z = 0.157m is very similar to each other in all of the cases, seeing Fig. 6.19(a), although some inconsistencies can still be observed. The reason for it has been explained above. As expected, the high value patch of $\langle \rho w'' w'' \rangle$ can be found just outside the narrow gap, seeing Fig. 6.19(a). Again, the similar distributions of the contours of $\langle \rho w'' w'' \rangle$ can be found in Cases 1 & 2 and it keeps more or less the same throughout the channel. However, the picture changes as the level of the cross section moving towards the outlet of the channel in Case 3 & 4. First, the size and the magnitude of high value patch increases as the levels moves

down. Furthermore, the other high value patches would appear in the vicinity of the corner on the bottom wall of the channel in these two cases. These size patches in the corner grow along the edges of the corner as the location moves further down the channel. The magnitude of $\langle \rho w'' w'' \rangle$ in the corner can even over-ride the value of the patches located just out the narrow gap, seeing the contour at z = 1.10m for Case 4. The increased shear stress due to the high flow temperature in corner should be the main reason for this.

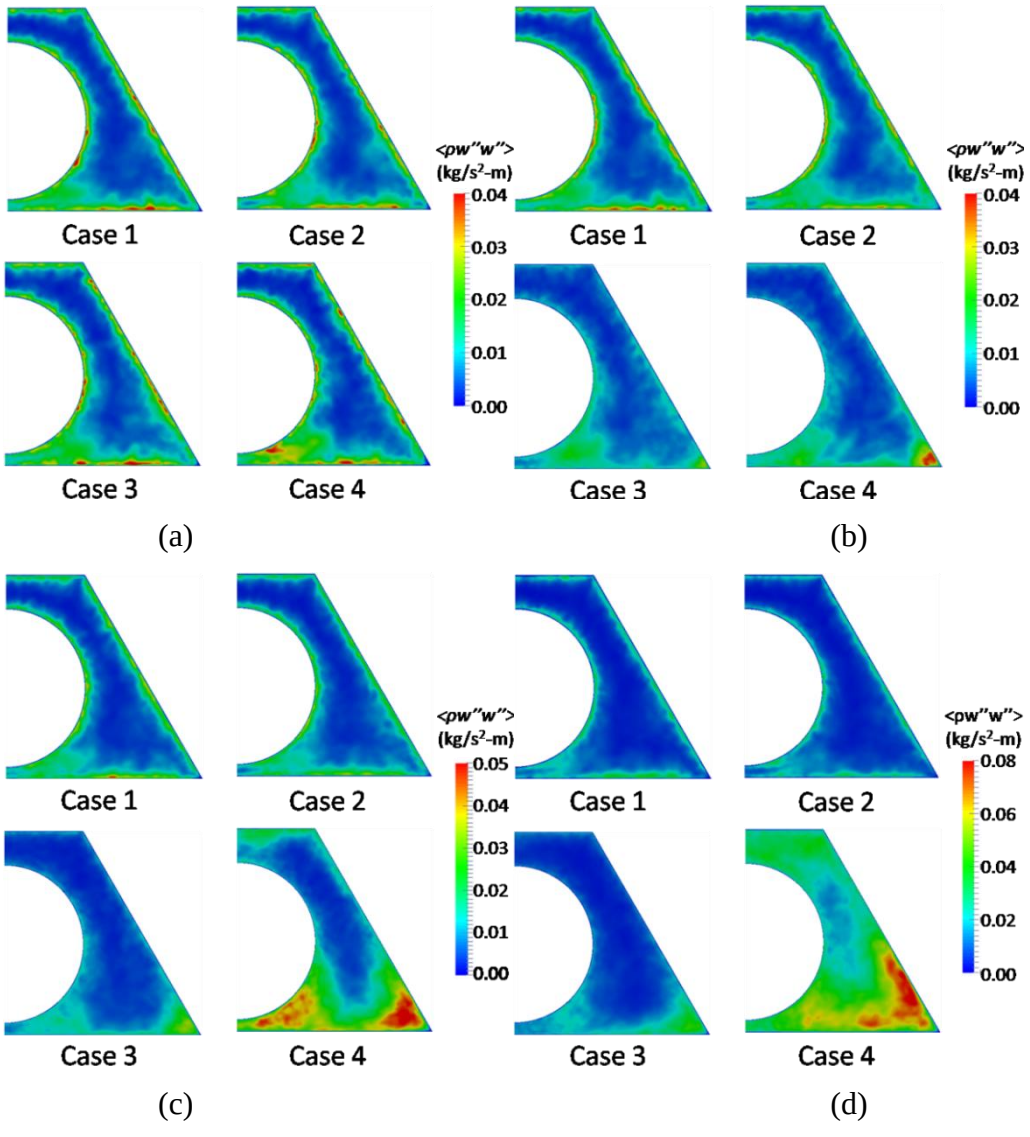

Fig.6.19 Distribution of $\langle \boldsymbol{\rho w'' w''} \rangle$ at (a) 0.157m; (b) 0.471m; (c) 0.785m; (d) 1.10m down the channel.

The distributions of the normal shear stress $\langle \rho u'' u'' \rangle$ in the cross sections at different levels down the channel are illustrated in Fig. 6.20. As expected, a high value patch

of $\langle \rho u'' u'' \rangle$ can be observed in the narrow gap region in all of the cases. The inconsistency of the values at z = 0.157m is also shown in the contours of $\langle \rho u'' u'' \rangle$. The reason for this inconsistency has been mentioned above which is due to the lack of samples. For the heated section, a similar trend to that of the turbulent kinetic energy is shown. The magnitude of $\langle \rho u'' u'' \rangle$ in the vicinity region also increases as the heat flux increase, when the condition $T_b < T_{pc} < T_{wall}$ is maintained, for instance in Cases 3 & 4. And it is more significant at the low levels in the channel. It is also interesting to note that the magnitude of $\langle \rho u'' u'' \rangle$ is visibly increased in the region away from the narrow gap at z = 1.10m down the channel in Case 4. Enhanced flow structures in the region are expected to be one of the reasons for this.

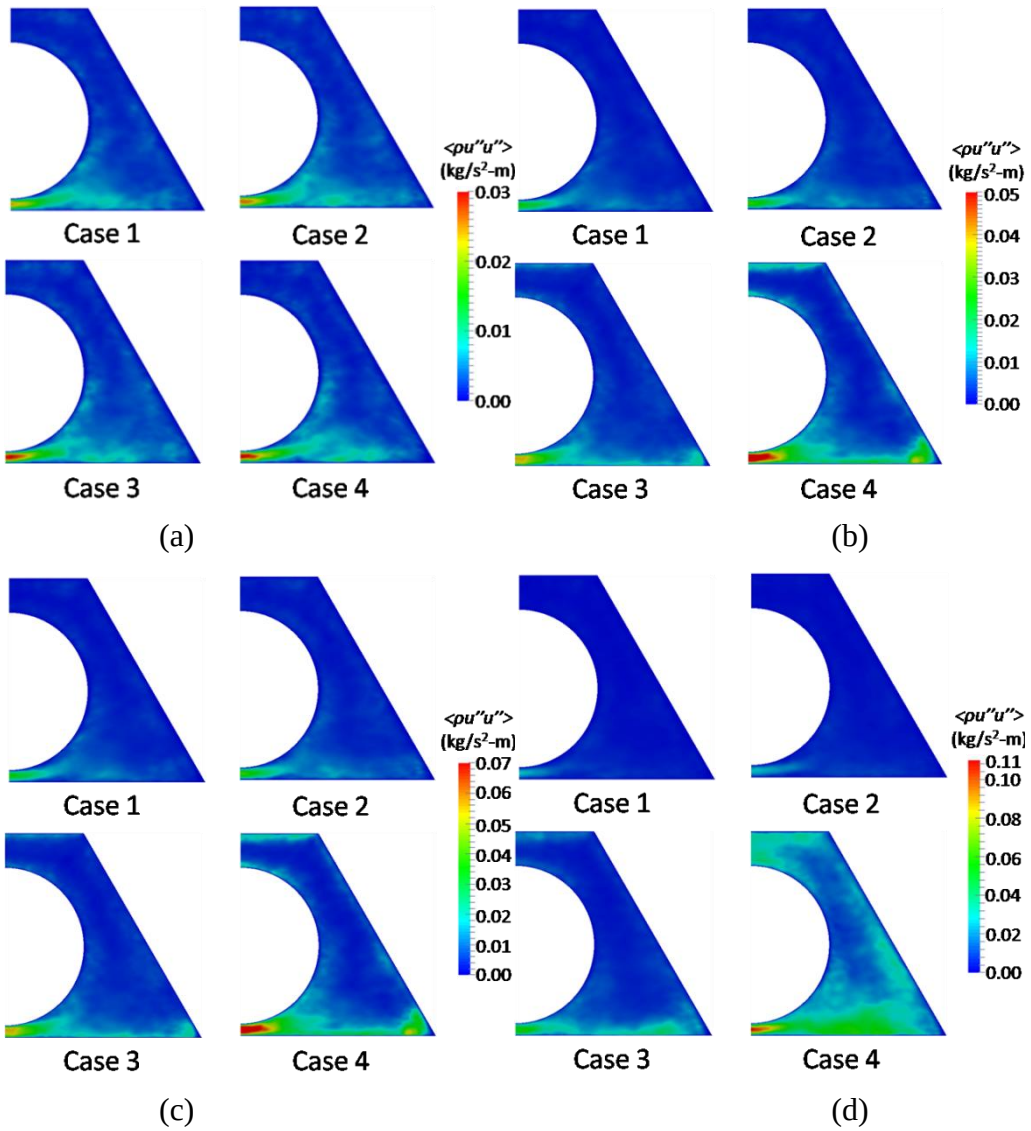

Fig.6.20 Distribution of $\langle \boldsymbol{\rho u'' u''} \rangle$ at (a) 0.157m; (b) 0.471m; (c) 0.785m; (d) 1.10m down the channel.

Distribution of the turbulent quantities on ‘P1’, ‘P3’, ‘P2’ and ‘ML’

Fig. 6.21, Fig. 6.22, Fig. 6.23 and Fig. 6.24show the profiles of $0.5 * \langle \rho u_i'' u_i'' \rangle$, $\langle \rho w'' w'' \rangle$ & $\langle \rho u'' u'' \rangle$, respectively, along the same lines as those used for the mean velocity. Considering the narrow gap first, it is interesting that $0.5 * \langle \rho u_i'' u_i'' \rangle$ is actually very high in the narrow gap even though the velocity profile appears to imply a laminar flow there. This is evidence of the large coherent structures especially the swinging flow. The shapes of $\langle \rho w'' w'' \rangle$ & $\langle \rho u'' u'' \rangle$ are different.The peaks of the former are located near the walls, showing $\langle \rho w'' w'' \rangle$ is related to the wall shears even though the profile is every different from that of a typical flow. The $\langle \rho u'' u'' \rangle$ profile peaks in the centre of the gap and is clearly strongly related to the swinging flow. The profiles of the turbulence kinetic energy $0.5 * \langle \rho u_i'' u_i'' \rangle$ and $\langle \rho u'' u'' \rangle$ are very much the same in Case 2 as in the isothermal flow (Case 1).The values of $\langle \rho w'' w'' \rangle$ seems, however, to reduce somewhat in the centre of the gap in the heated section. This implies that the third component $\langle \rho v'' v'' \rangle$, not shown, must increase to keep $0.5 * \langle \rho u_i'' u_i'' \rangle$ unchanged as shown above.

The values of $0.5 * \langle \rho u_i'' u_i'' \rangle$ in Cases 3 increase slightly at z = 0.471m & 0.785m, and is about double that of Case 1 and z = 1.10m. In contrast to this, $\langle \rho w'' w'' \rangle$ reduces at z =0.471 & 0.785m over most central region of the gap, but increases near the wall. It increases slightly in the centre at z =1.10m. The $\langle \rho u'' u'' \rangle$ increases strongly at all locations, though the increase is relatively small at the middle height z = 0.785m. These changes suggest that the swinging flow is strengthened, which is consistent with the results presented earlier. The overall trends of variation of $0.5 * \langle \rho u_i'' u_i'' \rangle$, $\langle \rho w'' w'' \rangle$ and $\langle \rho u'' u'' \rangle$ in Case 4 is same as that in Cases 3 but the changes are much larger. In addition, $\langle \rho w'' w'' \rangle$ is only reduced at z = 0.471m slightly, but is increased strongly at z = 0.785 & 1.10m. This is again consistent with the observations presented earlier that the flow in the narrow gap becomes more turbulent in the strongly heated flow (Case 4), but the more organised large flow structures, however, actually reduced (See Fig. 6.9).

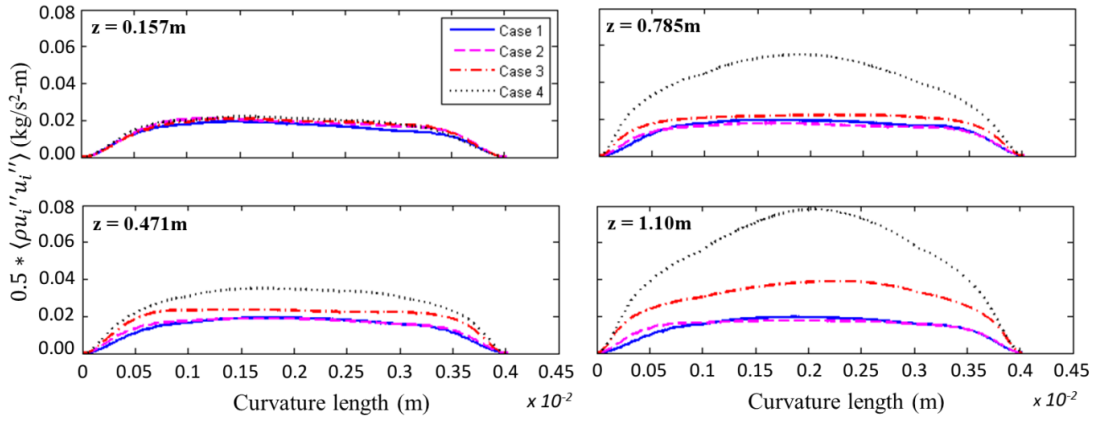

(a)

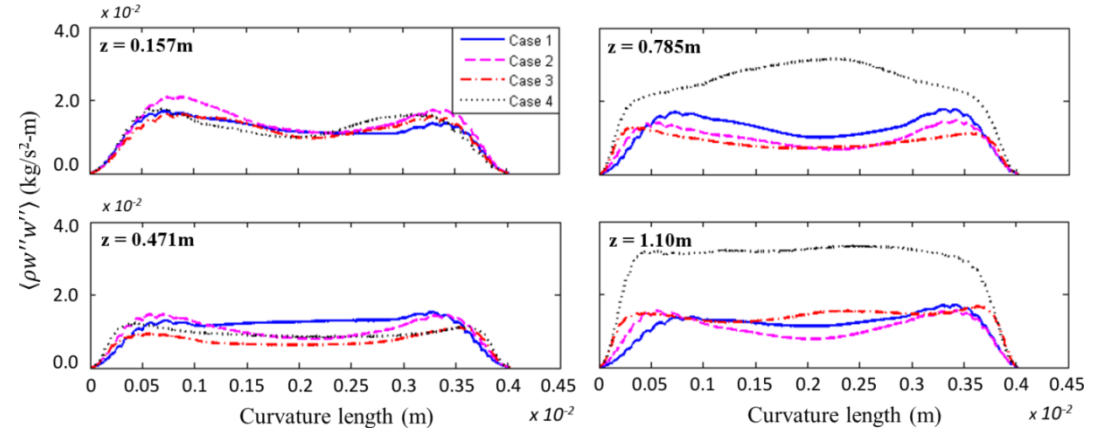

(b)

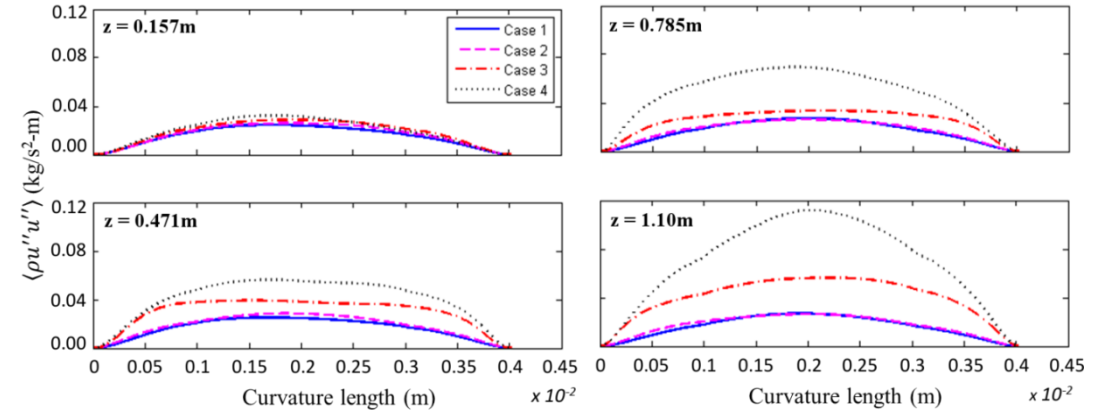

(c)

Fig.6.21 Different turbulent quantities on 'P1' (a) $0.5 * \langle \rho u_i^{''} u_i'' \rangle$; (b) $\langle \rho w'' w'' \rangle$; (c) $\langle \rho u'' u'' \rangle$.

The distributions of the three turbulent quantities ($0.5 * \langle \rho u_i^{''} u_i'' \rangle$, $\langle \rho w'' w'' \rangle$ and $\langle \rho u'' u'' \rangle$) in the wider gap in Case 1 overall show characteristics of a wall turbulent flow as illustrated in Fig. 6.22 (a). The turbulence in Case 2 in the wider gap is hardly changed by the heating as can be seen in Fig. 6.22 (b). $\langle \rho w'' w'' \rangle$ in the wider

gap is largely reduced in Case 3, with the peaks near the wall nearly completely disappeared. This shows that the flow is largely laminarised in the sense of the conventional wall shear flow. In strong contrast, $\langle \rho u'' u'' \rangle$ increases strongly, particularly near the wall, resulting into two peaks. The increase is larger with increasing distance down the channel. This appears to suggest that there is now a strong cross flow across the wider gap, which results in a wall shear layer on the walls. It is very interesting that the strong changes in $\langle \rho w'' w'' \rangle$ and $\langle \rho u'' u'' \rangle$ components seem to largely cancel each other (at z = 0.475 and 0.785m) and the total turbulent kinetic energy remains largely unchanged from those of the isothermal flow (Case 1).Towards the bottom of the channel, the increase in $\langle \rho u'' u'' \rangle$ is clearly stronger than the reduction in $\langle \rho w'' w'' \rangle$ and, hence, the overall turbulence ($0.5 * \langle \rho u_i^{''} u_i'' \rangle$) increases. $\langle \rho w'' w'' \rangle$ in the wider gap in Case 4 first also reduces strongly (z = 0.471m) but it recovers at 0.785m. And by z=1.10m, it becomes much stronger than that in the isothermal flow (Case 1). In addition, the distribution is uniform across the region (rather than peaking close to the wall). The behaviour of $\langle \rho u'' u'' \rangle$ in Case 4 is similar to that in Case 3, but the increase in latter is about double of that in the former. The total $0.5 * \langle \rho u_i^{''} u_i'' \rangle$ only increases slightly near the outer wall at z = 0.471m, but it increases strongly further down the channel because of the stronger increase of $\langle \rho u'' u'' \rangle$ near the outer wall.

The distributions of three turbulence quantities mentioned above in the main channel ('P2') largely show characteristics of a wall shear flow in Case 1, see Fig. 6.23 (a). The effect of heating in the various cases on turbulence in the main channel appears to be very much the same as that in the wider gap. $\langle \rho w'' w'' \rangle$ is reduced in most cases/locations, though recovery is seen towards the lower part of the channel in Case 4, as shown in Fig. 6.23 (b). The $\langle \rho u'' u'' \rangle$ is always enhanced by the heating, which is stronger with increasing heat flux, as presented in Fig. 6.23 (b).

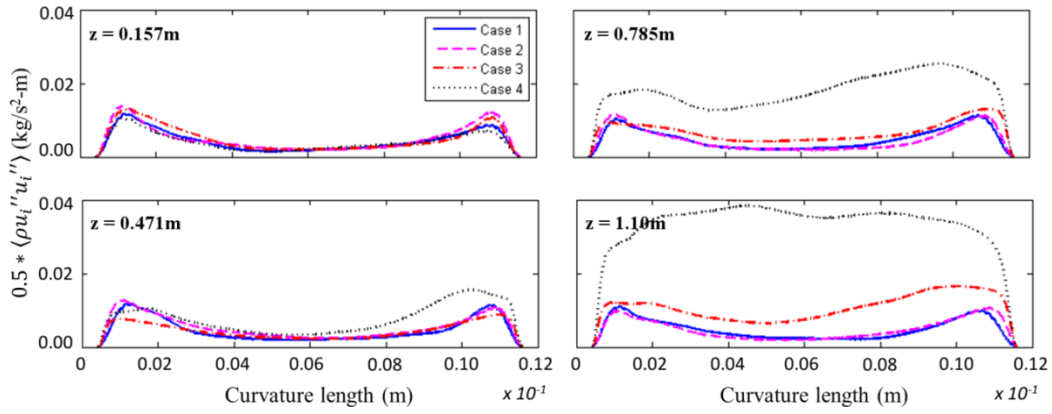

(a)

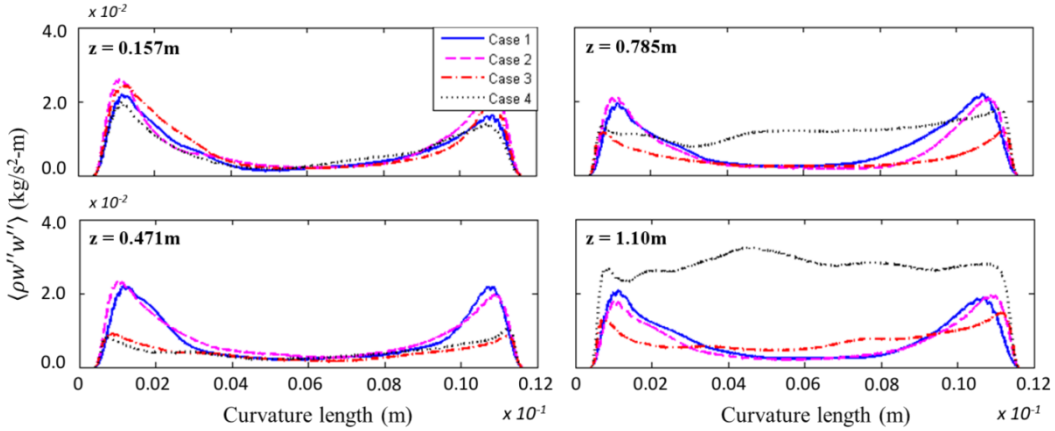

(b)

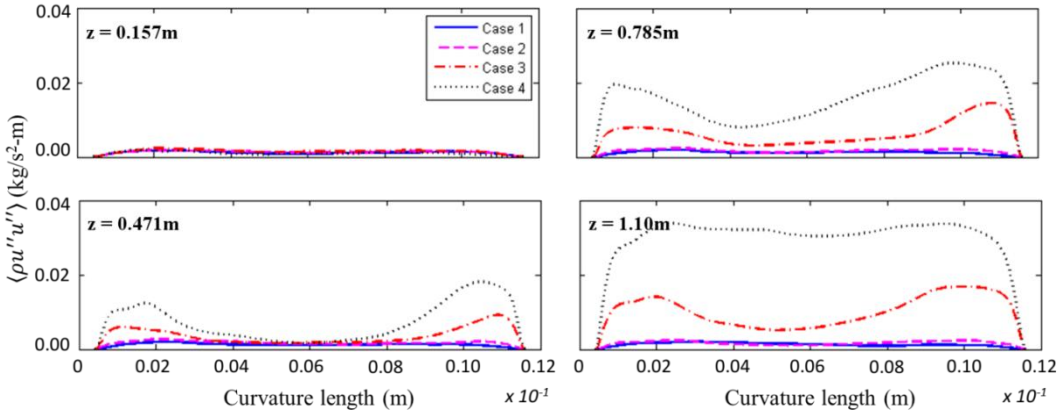

(c)

Fig.6.22 Different turbulent quantities on 'P3' (a) $0.5 * \langle \rho u_i^{''} u_i'' \rangle$; (b) $\langle \rho w'' w'' \rangle$; (c) $\langle \rho u'' u'' \rangle$.

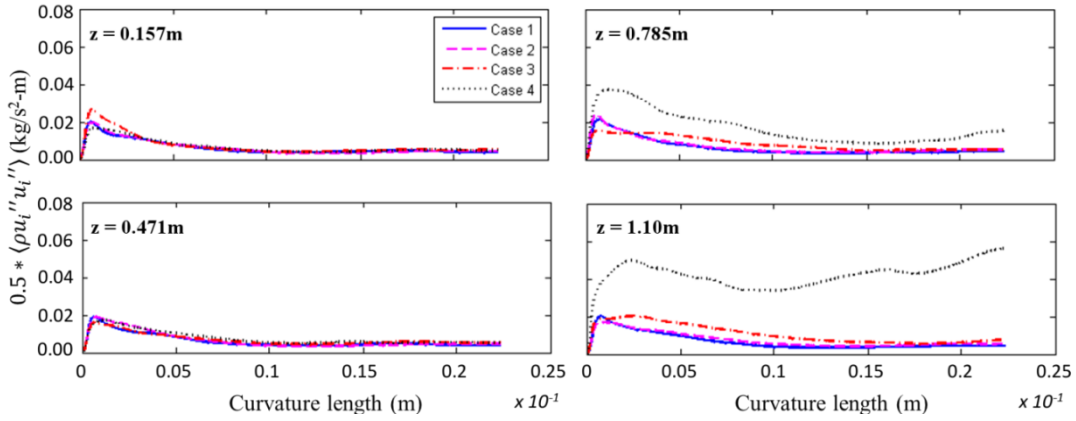

(a)

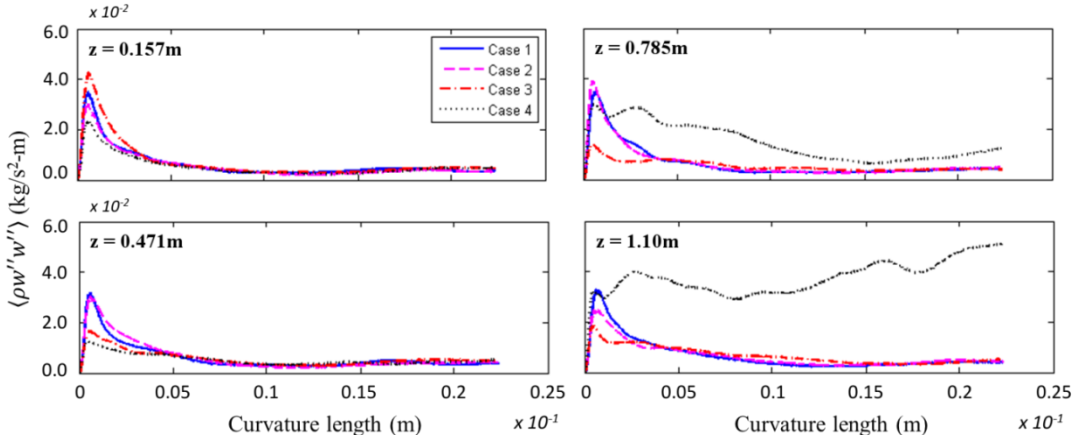

(b)

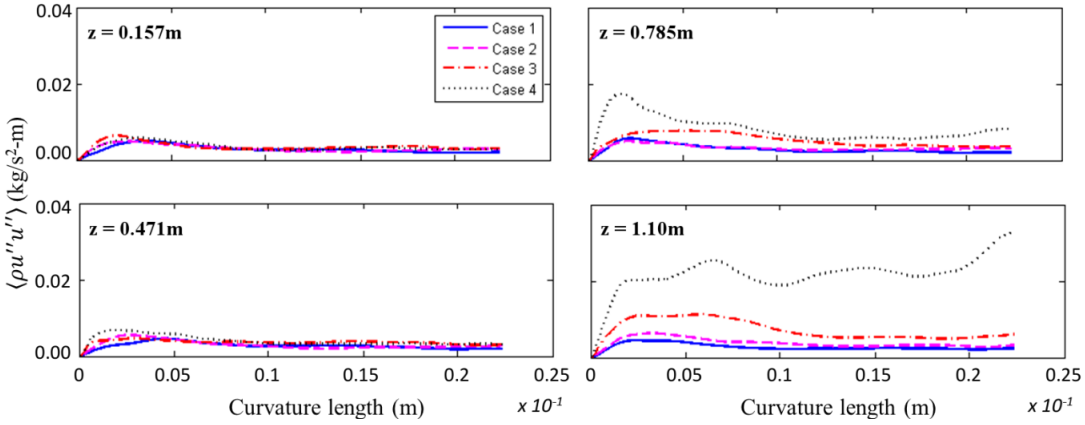

(c)

Fig.6.23Different turbulent quantities on 'P2' (a) $0.5 * \langle \rho u_i^{''} u_i'' \rangle$; (b) $\langle \rho w'' w'' \rangle$; (c)$\langle \rho u'' u'' \rangle$.

Fig. 6.24 shows the transition of the turbulence in the narrow gap to the main channel along 'ML'. (i. e. the equal-distance line). The distribution along 'ML' in Fig. 6.24 (a) shows that $0.5 * \langle \rho u_i^{''} u_i{}'' \rangle$ peaks at the centre of the narrow gap and reduces monotonically with the distance away from the centre. The magnitude of $0.5 * \langle \rho u_i^{''} u_i{}'' \rangle$ of the Case 2 remains more or less unchanged at the different levels, like in Case 1, demonstrating a negligible influence by the heating. In contrast, $0.5 * \langle \rho u_i^{''} u_i{}'' \rangle$ increases significantly down the channel in cases 3 & 4. The increase firstly occurs in the small gap region, then spreading to the main channel. A very similar trend can be observed in Fig. 6.24 (c) for $\langle \rho u'' u'' \rangle$, while the behaviour of $\langle \rho w'' w'' \rangle$ is a little bit different. It can be seen in Fig. 6.24 (b) that $\langle \rho w'' w'' \rangle$ in Cases 2 & 3 remain largely unchanged from that in Case 1 for all locations, whereas it is significantly increased at z = 0.785m & 1.10m in Case 4, as illustrated in Fig. 6.24 (b). Generally, $\langle \rho w'' w'' \rangle$ is higher in the narrower gap, increases away from the centre of the gap and reduces towards the centre of the main channel. At z = 1.10m in Case 4, however, the value is lower in the gap, and is higher in the main channel.

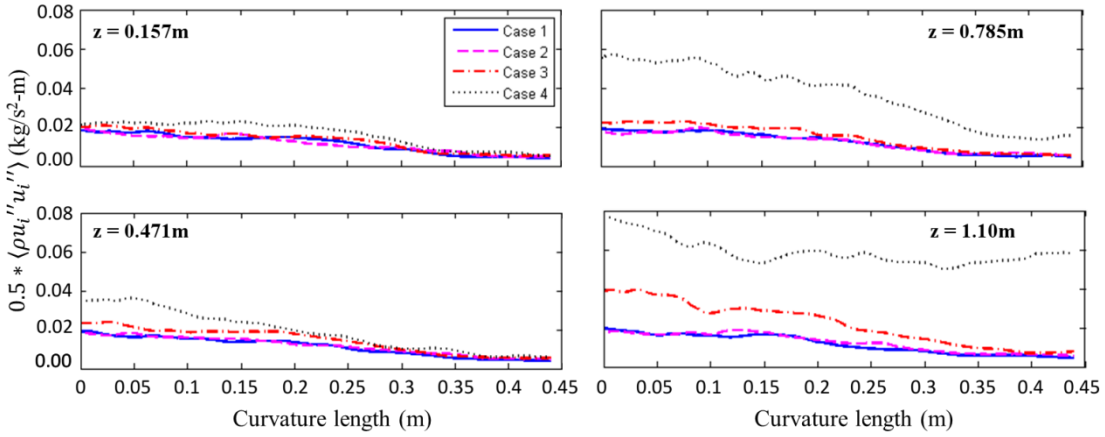

(a)

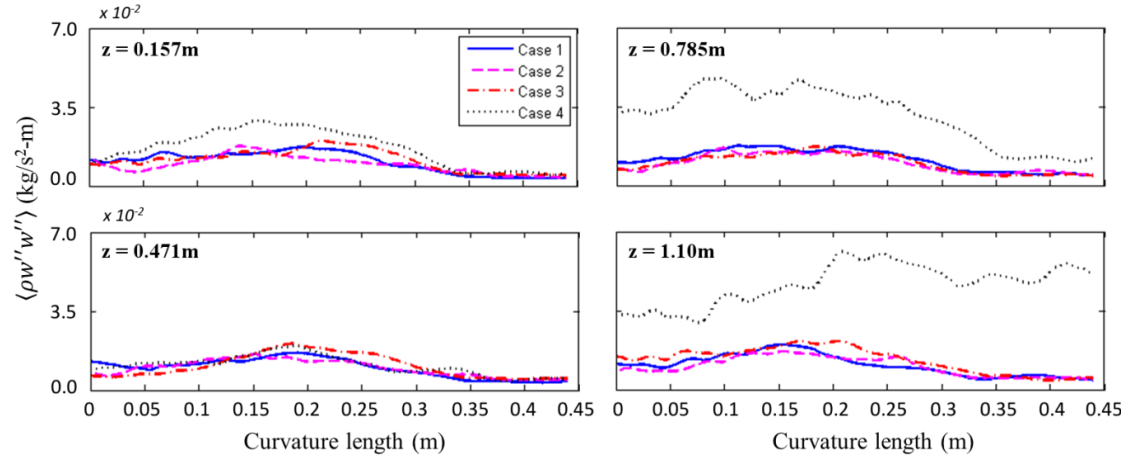

(b)

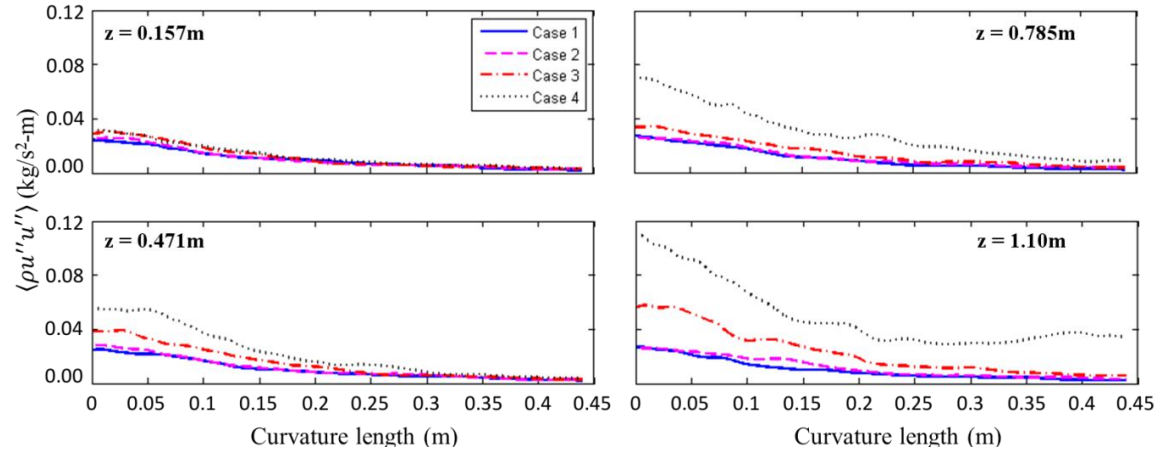

(c)

Fig.6.24 Different turbulent quantities on 'ML' (a) $0.5 * \langle \rho u_i^{''} u_i{}'' \rangle$; (b) $\langle \rho w'' w'' \rangle$; (c) $\langle \rho u'' u'' \rangle$.

6.3 Conclusions

The simulation of a forced convection supercritical water flow with a Reynolds number of incoming flow of 10540 in a non-uniform flow passage with various heat fluxes imposed on the wall has been carried out by using Code_Saturne. The effect of the thermal expansion on the flow structures in the channel has been revealed. And some interesting turbulence behaviour has been also observed in the case for the condition of $T_b < T_{pc} < T_{wall}$. The main conclusions are summarised below.

The thermal expansion due to heating does not change the general form of the swinging flow structure in the narrow gap. The dominant frequency of the flow structures in the narrow gap does not change with increase in heat flux and hence the changes in properties of the fluid in the heat section in the domain. As a result, the St^{-1}evaluated by using the incoming bulk velocity remains the same in all the cases considered here. The value is very close to that obtained in the forced convection as discussed in Chapter 5. The main change due to thermal expansion is that the structure in the narrow gap can be elongated as a result of the increase of the bulk velocity in the downstream part of the channel due to the high fluid temperature, and hence a lower density. There are also large flow structures existing in the big gap. Different from the findings in Chapter 5, the dominant flow structures have a dominant frequency similar to that of the flow structures in the narrow gap. These structures in the two gaps are highly correlated with each other. But it should be pointed out that the flow structure in the big gap is potentially Reynolds number- and property-dependent. In particular, the phase of the flow structures in the big gap can change as the temperature is sufficiently high.

The quantities of $0.5 * \langle \rho u_i^{''} u_i{}'' \rangle$ and $\langle \rho u'' u'' \rangle$ peak at the centre of the narrow gap. Since the flow in the narrow gap is very much laminar, it can be caused by the strong swing flow structure in the region. Moreover, both quantities generally increase as the heat flux and fluid temperature increase. This again indicates that the flow structure in the narrow gap is strengthened. However, the behaviour of $\langle \rho w'' w'' \rangle$ is different. In both gaps, it decreases in the near wall region first as the temperature increases, but it recovers or even increases when the fluid temperature is sufficiently

high at the levels close to the outlet. It means the conventional wall stress becomes weak as the heat initially started but recovers or even enhances as the fluid temperature sufficiently high. In the meantime, the flow structures in the big gap are enhanced by the heat flux. The enhanced flow structures in the big gap can not only cause high $\langle \rho u'' u'' \rangle$ in the near wall region but also results in a flat distribution of $\langle \rho w'' w'' \rangle$.

Chapter 7

Conclusions and Future Work

7.1 Summary of work and findings

The aim of the present PhD project is to develop a better understanding of the complex thermal hydraulic phenomenon of nuclear reactors using advanced computational fluids dynamics (CFD). In particular, this PhD project investigates the horizontal flows in the AGRs and the large flow structure and flow instability in tightly packed fuel assemblies. The latter study is divided into two parts: (i) the effect of the buoyancy force; (ii) the effect of strong variation of thermal properties and thermal expansion on flow structures. The main conclusions are summarized in the following sections.

7.1.1 Horizontal flows in the AGR

CFD models have been developed to solve for the temperature and other thermal hydraulic parameters in a cluster of AGR bricks in the Hartlepool/Heysham I reactor. This has been done to investigate whether the lack of modelling of cross flow heat transfer is responsible for the over-prediction of brick temperatures by the system code PANTHER currently employed by the nuclear industry. Also, the effect of the axial variation of the moderator brick geometry and the horizontal inter-brick leakage (HIBL flow) on the cooling of the moderator brick is studied. The findings are summarized below.

The 'cross flow effect' referred to herein, which is calculated from the difference between the brick temperatures predicted using the no-cross-flow (NoCF) and the

cross-flow (CF) CFD models, is a measure of the over-prediction of the brick temperature by PANTHER due to not fully accounting for the ring-to-ring cross flow phenomena. By considering the difference in CFD simulations with and without cross flow, the magnitude of the 'cross flow effect' has been established. The cross flow causes a reduction of 20 ℃ to 35 ℃ in moderator brick temperature, due to the mechanisms listed below:

(i) There is a strong cross flow in the narrow gaps, which significantly increases heat transfer in this region;

(ii) The cross flow causes the peak of the axial velocity to shift away from the centre of the main arrowhead passage towards the cross-flow downstream side. As a result, the effectiveness of heat transfer on the surfaces next to the upstream of the cross flow is reduced, but that downstream is enhanced. More importantly, the downstream heat transfer enhancement penetrates into the narrow gap region causing the heat transfer coefficient there to increase significantly.

(iii) A further effect is that the cross flow tends to reduce the gas temperature in the narrow gap region thanks to the mixing with the main arrowhead down-flow which increases the brick cooling effect.

The cross flow effect is insensitive to the increase of the cross flow rate. As the cross flow rate is doubled, the cross flow effect is increased by only about 3 ℃.

The cooling effect of the cross flow varies within each bricklayer due to the axial variation of the geometry of moderator brick. The keys block the cross flow in the region of the key/keyways, which results in a significantly decrease in the cooling effect of the cross flow in the narrow gap region. However, the cut-out part can enhance the cooling effect at the bottom of the brick by allowing more coolant cross flow through it. The horizontal inter-brick leakage (HIBL) has a visible impact on the axial flow in the narrow gap when the cross flow is not strong. It can significantly reduce the axial velocity in the narrow gap region or even cause the flow to reverse, leading to some hot spots in the region. The effect is small in the main arrowhead passage.

Finally, it is also shown that the flow towards the bottom of the fuel channel is unstable when the cross flow is small. Its effect on the brick temperature is negligible. The cross flow between the fuel channels can significantly moderate or even stop such instability.

7.1.2 The effect of buoyancy-aid force on the flow and heat transfer in the non-uniform geometry.

Ascending air flow in a non-uniform geometric flow cross section is studied using the large eddy simulation (LES), while the buoyancy force is modelled by using the Boussinesq approximation. This study focuses on the behaviour of the large flow structures in the narrow gap of the rod-bundle-like geometry. In particular, the effect of the buoyancy on the flow and heat transfer is studied. The quality of the results is checked by using different criteria, which demonstrates the good resolution of the flow domains. The main conclusions are included below.

There are least two kinds of large flow structures in the channel in the forced convection case and in the case with sufficiently weak buoyancy force. Firstly, there is a strong swinging flow in the narrow gap of the flow passage. Secondly, there are another flow structures passing the big gap in the channel. In such cases, these two kinds of flow structures are weakly correlated with each other. As proposed by Krauss and Meyer (1998), the swinging flow is formed due to the mean flow and two streets of counter rotating turbulent vortices on either sides of the narrow gap. The turbulent vortices are caused by the high velocity gradient due to the non-uniformity of the geometry.

When the buoyancy force is strong, the mean velocity in the narrow gap can be higher than the velocity in the main channel, which makes the velocity gradient opposite to that in a forced convection case and is more like a jet flow. As a result, there are two sets of vortices locating on either side of the narrow gap. The boundary between these two set of vortices is not stable, so the vortex form one side can still propagate to the other side. These two flow structures are strongly correlated with

each other. Actually, the correlations between these two types of flow structures become gradually stronger, as the buoyancy force becomes great.

The value of the Strouhal number $St^{-1}$of the flow structures was suggested to be only dependent on the geometric configuration in some previous studies. In their discussion St^{-1} was evaluated using friction velocity. Some inconsistency can be found in different studies of the similar geometries. The present study demonstrates that the bulk velocity is a better choice. St^{-1} decreases with the increase of buoyancy force when $Bo^* < Bo_0^*$. The trend reverses when $Bo^* > Bo_0^*$.

The heat transfer data reveals a similar dependence of *Nu* in the buoyancy parameter Bo^* as shown in a tube. The overall Nusselt number (*Nu*) decreases with increase of buoyancy when $Bo^* < Bo_0^*$. But the heat transfer impairment is more moderate in the non-uniformly geometry in comparison with a tube flow. For example, the Nu/Nu_f at Bo_0^* is 50% higher than that of a tube flow. Furthermore the heat transfer recovery is more significant when $Bo^* > Bo_0^*$. The non-uniform distribution of the buoyancy force which induces the non-uniform buoyancy effect is the main reason.

7.1.3 Supercritical water flow in the heated non-uniform channel

Supercritical water flowing in a rod-bundle-like geometry is investigated using LES with WALE SGS model implemented in the Code_Saturne. The plan view of the geometry is the same as the study on the buoyancy-aided flow. A turbulence generator is created to generate a fully developed turbulent flow used as the inlet flow for the heat domain. It is further demonstrated that the bulk velocity is a better choice for the evaluation of St^{-1} to characterise the flow structures. Although the Reynolds number is doubled in this study but St^{-1} is about the same as that obtained in the previous section. Some preliminary understandings of the effects of thermal expansion on the large flow structures have been achieved, which are summarised below.

The general behaviour of the flow structures in the narrow gap does not change with the variation of the thermal properties of the fluids. The $St^{-1}$of the large flow

structures in the narrow gap remains the same all of the cases considered. And the valve agrees with the value obtained in the isothermal case considered in the Chapter 5. However, the flow structures in the narrow gap are elongated as a result of the accelerated flow due to the increased fluid temperature and hence lower fluid density at downstream part of the channel.

The large flow structures are also observed in the wider gap. The behaviour of these structures is different from those demonstrated in the Chapter 5. The dominant frequencies of them are quite similar to the swinging flow structures in the narrow gap. The study also indicates that these flow structures possibly are Reynolds number and property dependent. Particularly, the heat flux can change the phase of the flow structure.

The peaks of the $0.5 * \langle \rho u_i^{''} u_i{}'' \rangle$ and $\langle \rho u'' u'' \rangle$ can be observed at the middle of narrow gap at different levels down the channel. As the flow in the region is very much laminar, such high value is only because of the swinging flow structures. Furthermore, the values of these two quantities are generally increased with the increase of heat flux and fluid temperature. It demonstrates that the flow structure in the narrow gap is strengthened as a result of high fluid temperature. However, $\langle \rho w'' w'' \rangle$ decreases with the increase of the heat flux and fluid temperature first, before it recovers or even enhanced thanks to the further increased heat flux and fluid temperature. More interestingly, the $\langle \rho u'' u'' \rangle$ in the near wall region always increases with the increase of heat flux and fluid temperature, which indicates the strong secondary fluids motion in the region.

7.2 Suggestions for future work

Future research work is recommended to extend the current study of flow in the heated tightly packed rod bundles using LES methods.

First of all, to better understand the buoyancy effect on the flow behaviour in a heated non-uniform geometry, some other cases with different conditions are recommended. As mentioned in the literature review, most people focused on the

buoyancy effect in a heated pipe flow, while the investigation on the buoyancy effect in a flow in a heated tightly pack fuel assembly is very limited, especially for buoyancy opposite flow. In the current study, only the buoyancy-aid forced convection is considered. The behaviour of the large flow structures in the vicinity of the narrow gap under the buoyancy opposite condition is another field worth to study.

Secondly, the researchers are encouraged to apply stronger heat flux or to use a larger domain to improve the understanding of the thermal expansion effects on the flow structures in the non-uniform domain. Phenomena similar to those observed in the strongly heated buoyancy-aided flow are expected to occur.

Finally, the effect of thermal expansion on the flow in a heated non-uniform geometric configuration is separated from the buoyancy effect in the current study. These two effects are combined in the real world, such as in the SCWR/HPLWR. So mixed convection of the supercritical fluids flow in a heated non-uniform geometry should be investigated in the future. The understanding on topic is very limited. Some experiments have been done and heat transfer data have been published. But detailed flow fields have not been obtained. According to the present author's best knowledge, the numerical studies which have been carried out on this topic are based on RANS model, which are deemed inaccurate on predicting the flow field. Large eddy simulation can potentially produce new understanding. Expect the heat transfer data and the turbulence statistics, the large flow structures in the vicinity of the narrow gap will again be very interesting. In addition, the new correlations of mixing rate between the subchannels will be interesting to study.

Appendix 1

Mesh Independent Study of the CFD Investigation of the effect Horizontal Flows in the AGR reactor.

Description

Then objective of this appendix is to report the mesh independent study of the CFD investigation of the effect of the horizontal flows, which is discussed in the Chapter 4. All of the settings and the procedures in the study are the same as the original simulations, except a coarser mesh is adopted. To be simple, the cases based on the coarse mesh are named as '0.5MSH-NoCF' and '0.5MSH-CF' while two cases with 100% cross flow rate introduced in the Chapter 4 is named as 'ONG-NoCF' and 'ONG-CF' here.In the models studied here, the number of mesh elements in both the solid and flow domains are halved, which means that one block contains 0.9million cells. In the 0.5MSH-NoCF, the y^+ is from 20 to 475, while it is from 50 to 400 in 0.5MSH-CF. Again the lower y^+ values are located in the vicinity of the narrow gap, while the higher value of y^+ located at the wall facing the main arrowhead flow passage.

The vertical distribution of temperature and temperature differences (cross flow effect) at locations 'AHs' and 'NGs' on the outer surface are discussed here. The outer surface temperature from the output PANTHER AE and results mentioned in the Chapter 4 are plotted with the results obtained by using the coarse mesh here.

Results and discussions

The vertical temperature profiles at ‘AHs’ and ‘NGs’ in 0.5MSH-NoCF/NoCF case are presented in Figure A1.1, while the results in 0.5MSH-CF/CF case are shown in the Figure A1.2. The outer surface temperature obtained by PANTHER AE is only illustrated in Figure A1.1(a), with the temperature distribution at ‘AHs’ in 0.5MSH-NoCF case and ONG-NoCF Case. Since ‘AHs’ is close to the main channel, the temperature at these locations are more relevant to the prediction obtained by PANTHER AE. Finally, the cooling effects of cross flow (NoCF-CF) in both types of simulations (original and coarse mesh simulations) are illustrated in Figure A1.3. It should be mentioned here the location ‘AHs’ and ‘NGs’ were introduced in Chapter 5.

Generally, CFD simulations can capture the trend of the temperature distribution as PANTHER AE, while the up shift exists either in the ONG-NoCF case or 0.5MSH-NoCF case, as shown in Figure A1.1(a). As expected the results at different vertical levels in ONG-NoCF case are closer to the prediction by PANTHER AE, compared to the results in 0.5MSH-NoCF case. The over-prediction in ONG-NoCF case is <10 ℃, while in 0.5MSH-NoCF it can be up to 20 ℃. Although, the shapes of the temperature distributions within each brick layer are very similar in both cases, which can be seen from the temperature distribution at ‘NGs’ in Figure A1.1(b). It also can be seen that the temperature inconsistency between ONG-NoCF case and 0.5MSH-NoCF case starts from the very beginning of the fuel channel and the divergence becomes bigger as the level down the fuel channel at ‘AHs’ and ‘NGs’. The temperature, in the 0.5MSH-NoCF, is ~10 ℃ higher at top of the fuel channel and it rises to ~15 ℃ at bottom in comparison with the ONG-NoCF case, as seen in Figure A1.1. And over-prediction of the temperature is more significant at ‘AHs’ than it is at ‘NGs’.

The shapes of the temperature distribution predicted in ONG-CF case and 0.5MSH-CF case are also very similar to each other, seeing Figure A1.2. Comparing the results obtained in the 0.5MSH-CF case to ONG-CF case, the temperature is also higher in the simulation with coarse mesh, but the value of the difference is most significant at the level where the cross flow just starts, but lower at the bottom. Especially, the difference at ‘AH1’ ‘AH2’ and ‘NG1’ almost disappears at the last brick layer in the channel. Because of this controversial trend on the temperature

difference in 0.5MSH-NoCFand 0.5MSH-CF case, it is reasonable to expect the cooling effect of the cross flow at the lower level of the fuel channel can be over-predicted by using the coarse mesh.

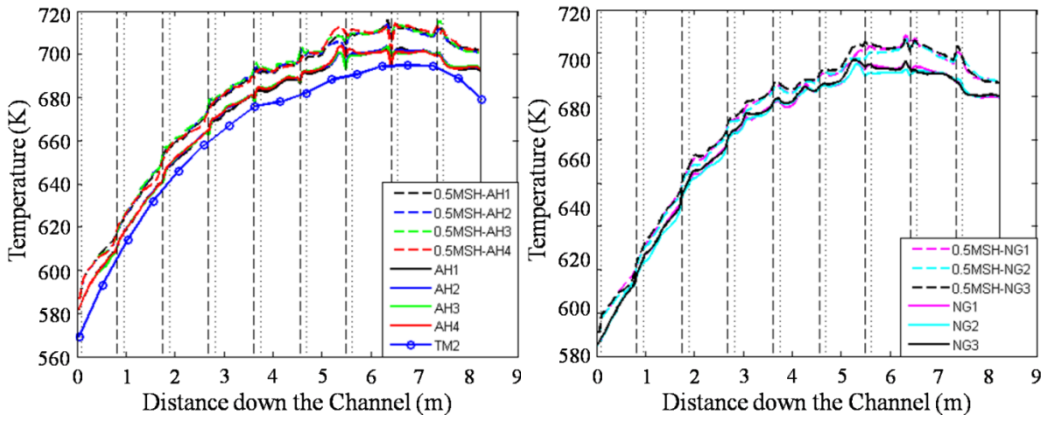

(a) (b)

Figure A1.1 The vertical distribution of temperature at (a) ‘AHs’ and (b) ‘NGs’ in the 0.5MSH-NoCF case and original NoCF case.

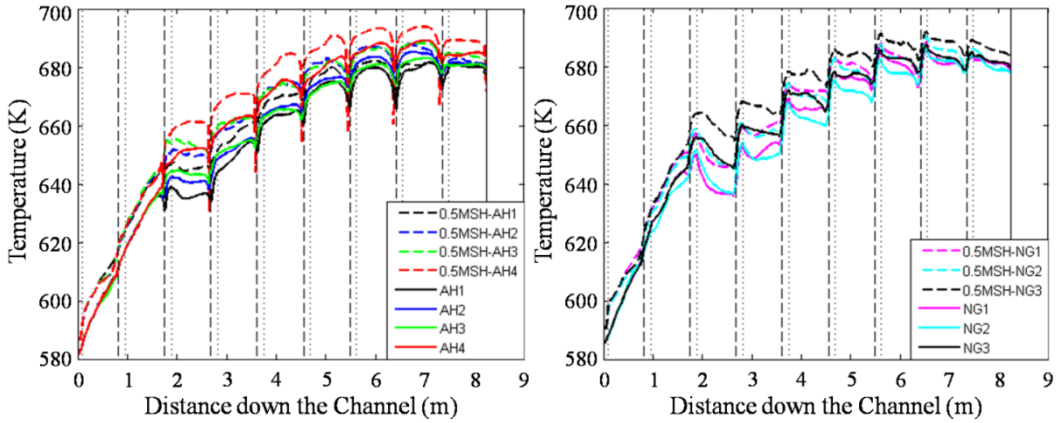

(a) (b)

Figure A1.2 The vertical distribution of temperature at (a) ‘AHs’ and (b) ‘NGs’ in the 0.5MSH-CF case and original CF case.

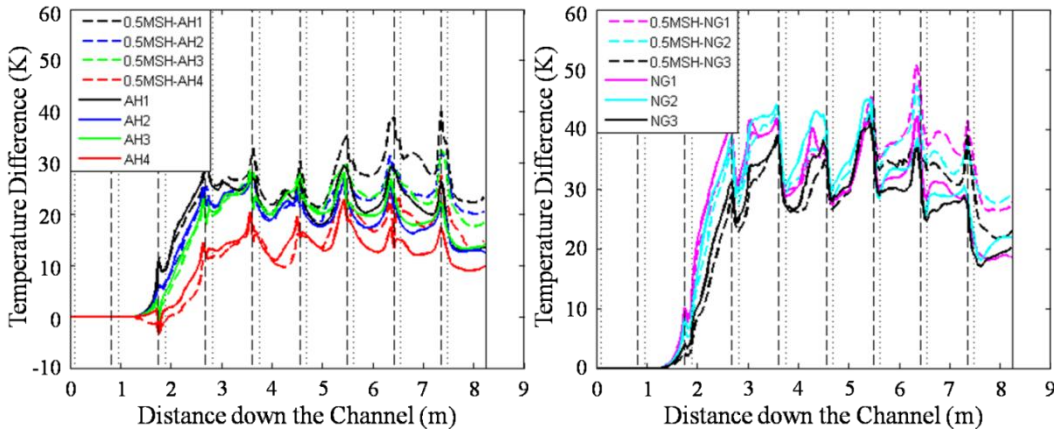

(a) (b)

Figure A1.3 The vertical distribution of temperature difference at (a) 'AHs' and (b) 'NGs' in the 0.5MSH-CF case and original CF case.

As illustrated the Figure A1.3, the cross flow cooling effect at brick layers 10, 9, 8 & 7, is almost the same in the both simulations, which indicates the coarse mesh can also predict the reasonable cross flow effect at these layers. However, the difference of the cross flow cooling effect can be as high as ~10 ℃ at the bottom three brick layers at 'AH1' 'AH2' and 'NG1' and ~5°C at 'AH4' and 'NG3', which makes the averaged deviation ~7 ℃.

Conclusion

The simulation with coarse mesh leads to the higher temperature prediction on the outer-surface of the brick in both types of simulations without/with momentum of cross flow. Such over-prediction is much more significant between the cases excluding the momentum of cross flow. And the difference between ONG-NoCF case and 0.5MSH-NoCF case becomes bigger with distance down the channel, while it is smaller in the lower level in the case which includes the momentum of the cross flow. In the meantime, mesh effect on evaluation of the cross flow cooling effect is dependent on the level of the brick layers. The inconsistency of the cross flow cooling effect predicted by using the coarse mesh and fine mesh is negligible at middle brick layers such as layer 10, 9, 8 and 7. However a visible divergence (~7 ℃) can be found at the bottom three layers.

All in all, the mesh applied in the original simulations is suitable for the study. Firstly, it can more accurately predict the temperature on the outer surface of the moderator brick in the NoCF. And also a finer mesh can reduce the numerical dissipation. The cross flow cooling effect obtained by using the coarse mesh is almost the same as it is obtained by using the finer mesh except bottom 3 layer. The difference in 3 layers can be ~7 ℃.It is deemed acceptable as cooling effect of cross flow is ~25 ℃.

Appendix 2

The Subroutine of the Turbulence Generator

Brief Introduction

The code listed below has been added into one of the standard subroutines of Code_Saturne 3.0.*, named as 'cs_user_boundary_conditions.f90', in order to produce the fully developed turbulence at the inlet of the simulation domain. The velocity field as internal face 'INLET1A' is copied to the inlet boundary after several time steps of the simulation. Moreover, the copied velocity field is corrected by using the targeted mass flow rate. This code is based on Fortran, and some of the predefined subfunctions in Code_Saturne 3.0.* are also used.

Main code

```
! Newly added variables
integer, allocatable, dimension(:) :: lstelt

! Added allocatable array
integer, allocatable, dimension(:) :: lsteltm
integer, allocatable, dimension(:) :: icnt
double precision, allocatable, dimension(:) :: xm, ym, xmg, ymg, rxmg, rymg
double precision, allocatable, dimension(:) :: uloc, vloc, wloc, tloc
double precision, allocatable, dimension(:) :: xtabfluxcyl, xtabfluxcyl2, xtabsurfl

double precision, allocatable, dimension(:) :: ulocg, vlocg, wlocg, tlocg
double precision, allocatable, dimension(:) :: xtabfluxcylg, xtabfluxcylg2, xtabsurflg
```

```
double precision, allocatable, dimension(:) :: rulocg, rvlocg, rwlocg, rtlocg
double precision, allocatable, dimension(:) :: rxtabfluxcylg, rxtabfluxcylg2,
rxtabsurflg

! Local variables
Integerifac, iel, ii, ivar, jj
Integerilelt, nlelt, ileltm

! added integer variables
integer       ielm1, ielm2
integernleltm, nleltg, nleltmg, inleltmg
integer       idx0, idx
integer       nlelt0, nleltm0
integeriflmas
integer       i1, i2

! added double precision variables
double precision rxi, ryi, rxj, ryj
double precision xeps
double precision surf, ipond
double precision surfin, mmflux, mmflux2
double precision ubulk
double precision uin, vin, win, xin, yin, zin

!===============================================================
=======
! Initialization
!===============================================================
=======

allocate(lstelt(nfabor))  ! temporary array for boundary faces selection
allocate(lsteltm(nfac))  ! temporary array for boundary faces selection
```

```
! INSERT_ADDITIONAL_INITIALIZATION_CODE_HERE
! Get the coordinates of the face centres at the mapped face.
callgetfbr("INLET1", nlelt, lstelt)

if (.true.) then! test whether the recycling need to be turned on.
callgetfac('INLET1A', nleltm, lsteltm)  ! select internal faces of 'INLET1A'.
deallocate(lsteltm)

 nleltm0=nleltm
 nlelt0 =nlelt
allocate(lsteltm(nleltm0))  ! temporary array for boundary faces selection
callgetfac('INLET1A', nleltm, lsteltm)  ! select internal faces of 'INLET2A'.

 ! (parallel action)global sum
if (irangp.ge.0) then
callparcpt(nleltm0)
callparcpt(nlelt0)
endif

nleltmg = nleltm0
nleltg = nlelt0

allocate(xm(nleltm))                ! temporary array for x-cor of the face centres of
mapped faces selection on the local node.
allocate(ym(nleltm))                ! temporary array for y-cor of the face centres of
mapped faces selection on the local node.

! Transfer the x and y coordinate on the node to the user defined array xm() and ym().
The
!length of the arraies is 'nlelm'

doileltm = 1, nleltm
```

```
ifac = lsteltm(ileltm)
xm(ileltm) = cdgfac(1,ifac)
ym(ileltm) = cdgfac(2,ifac)
enddo

! (parallel action) send coordinate to global arrays
allocate(xmg(nleltmg))
allocate(ymg(nleltmg))
if (irangp.ge.0) then
callparagv(nleltm,nleltmg, xm, xmg)
callparagv(nleltm,nleltmg, ym, ymg)
endif

allocate(uloc(nleltm))
allocate(vloc(nleltm))
allocate(wloc(nleltm))

allocate(tloc(nleltm))

allocate(xtabfluxcyl(nleltm))
allocate(xtabfluxcyl2(nleltm))
allocate(xtabsurfl(nleltm))

iflmas = ipprof(ifluma(iw)) !Rank i in propfa(.,i) of the properties defined at the internal faces.

doileltm = 1, nleltm
ifac = lsteltm(ileltm)
   i1 = ifacel(1,ifac)      ! Index-numbers of the 1st neighboring cells for each internal face.
   i2 = ifacel(2,ifac)      ! Index-numbers of the 1st neighboring cells for each internal face.
```

```
ipond = pond(ifac)
uloc(ileltm) = ipond*rtpa(i1,iu)+(1.d0-ipond)*rtpa(i2,iu)
vloc(ileltm) = ipond*rtpa(i1,iv)+(1.d0-ipond)*rtpa(i2,iv)
wloc(ileltm) = ipond*rtpa(i1,iw)+(1.d0-ipond)*rtpa(i2,iw)
tloc(ileltm) = ipond*rtpa(i1,isca(1))+(1.d0-ipond)*rtpa(i2,isca(1))

xtabfluxcyl(ileltm) = propfa(ifac,iflmas)*surfac(3,ifac)/abs(surfac(3,ifac))    ! mass flow rate crossing the each selected internal face
    surf = sqrt(surfac(1,ifac)**2+surfac(2,ifac)**2+surfac(3,ifac)**2)          ! area of the internal surface.
xtabfluxcyl2(ileltm) = ro0*wloc(ileltm)*surf  ! mass flow rate calculated by formula rho*w*A.
xtabsurfl(ileltm) = surf           ! array of area of each elements on the internal surface on local nodes.
enddo

! (parallel action) send velocity, mass flow rate and aera of each faces to global arrays
allocate(ulocg(nleltmg))
allocate(vlocg(nleltmg))
allocate(wlocg(nleltmg))
allocate(tlocg(nleltmg))

! (parallel action) mark the dupicated faces
xeps = 1.0d-12
do ii = 1, nleltmg-1
rxi=xmg(ii)
ryi=ymg(ii)
dojj = ii+1, nleltmg
rxj = xmg(jj)
ryj = ymg(jj)
if (abs(rxi-rxj) .lt. xeps .and. abs(ryi-ryj) .lt. xeps) then
```

```
xmg(jj)=1.0d12
ymg(jj)=1.0d12
endif
enddo
enddo
allocate(xtabfluxcylg(nleltmg))
allocate(xtabfluxcylg2(nleltmg))
allocate(xtabsurflg(nleltmg))

if (irangp.ge.0) then
callparagv(nleltm,nleltmg, uloc, ulocg)
callparagv(nleltm,nleltmg, vloc, vlocg)
callparagv(nleltm,nleltmg, wloc, wlocg)
callparagv(nleltm,nleltmg, tloc, tlocg)
callparagv(nleltm,nleltmg, xtabfluxcyl, xtabfluxcylg)
callparagv(nleltm,nleltmg, xtabfluxcyl2, xtabfluxcylg2)
callparagv(nleltm,nleltmg, xtabsurfl, xtabsurflg)
endif

! (parallel action) find the number of the faces (avoid the deplicated faces)
inleltmg = 0
do ii = 1, nleltmg
if (xmg(ii) .lt. 1.0d10 .and. ymg(ii) .lt. 1.0d10)then
inleltmg = inleltmg+1
endif
enddo

! (parallel action) set the un-duplicated coordinates information to 'rxmg' and 'rymg'
allocate(rxmg(inleltmg))
allocate(rymg(inleltmg))
allocate(rulocg(inleltmg))
allocate(rvlocg(inleltmg))
```

```
allocate(rwlocg(inleltmg))
allocate(rtlocg(inleltmg))
allocate(rxtabfluxcylg(inleltmg))
allocate(rxtabfluxcylg2(inleltmg))
allocate(rxtabsurflg(inleltmg))

 idx0 = 0
do ii = 1, nleltmg
if (xmg(ii) .lt. 1.0d10 .and. ymg(ii) .lt. 1.0d10)then
      idx0 = idx0+1
rxmg(idx0)=xmg(ii)
rymg(idx0)=ymg(ii)
rulocg(idx0)=ulocg(ii)
rvlocg(idx0)=vlocg(ii)
rwlocg(idx0)=wlocg(ii)
rtlocg(idx0)=tlocg(ii)
rxtabfluxcylg(idx0)=xtabfluxcylg(ii)
rxtabfluxcylg2(idx0)=xtabfluxcylg2(ii)
rxtabsurflg(idx0)=xtabsurflg(ii)
endif
enddo

! Find the index number of mapped faces.
allocate(icnt(nlelt)) ! The size of array icnt = number of inlet faces on the node
idx = 0
doilelt = 1, nlelt
ifac = lstelt(ilelt)
xin = cdgfbo (1,ifac)
yin = cdgfbo (2,ifac)
zin = cdgfbo (3,ifac)
doileltm = 1, inleltmg
if(abs(xin-rxmg(ileltm)) .le. xeps .and. abs(yin-rymg(ileltm)) .le. xeps) then
```

```
idx = idx + 1
icnt(idx) = ileltm    ! Transfer the index number of the mapped face to the array 'icnt'
endif
enddo
enddo
endif !test of whether need to turning on recycling ended.

ubulk = -1.94d-2
!initial running steps of the simulation
if (ntcabs .le. 800) then
doilelt = 1, nlelt
ifac = lstelt(ilelt)
iel = ifabor(ifac)
itypfb(ifac)=ientre
icodcl(ifac,iu)     = 1
rcodcl(ifac, iu, 1) = 0.00d0
icodcl(ifac,iu)     = 1
rcodcl(ifac, iv, 1) = 0.00d0
icodcl(ifac,iu)     = 1
rcodcl(ifac, iw, 1) = ubulk*2.0d0
icodcl(ifac, isca(1))    = 1
rcodcl(ifac, isca(1), 1) = 633.0d0
enddo
! Copy the velocities and temperature at internal from face 'INLET1A' to the inlet of
the channel.
! Using the targeted mass flow rate to correct the mapped velocity field.
elseif (ntcabs .gt. 800 .and. ntcabs .le. 6400) then
doilelt = 1, nlelt
ifac = lstelt(ilelt)
iel = ifabor(ifac)
itypfb(ifac)=ientre
icodcl(ifac,iu)     = 1
```

```
rcodcl(ifac, iu, 1) = rulocg(icnt(ilelt))*ubulk*2.0d0*ro0*surfin/mmflux
icodcl(ifac,iu)     = 1
rcodcl(ifac, iv, 1) = rvlocg(icnt(ilelt))*ubulk*2.0d0*ro0*surfin/mmflux
icodcl(ifac,iu)     = 1
rcodcl(ifac, iw, 1) = rwlocg(icnt(ilelt))*ubulk*2.0d0*ro0*surfin/mmflux
icodcl(ifac, isca(1))    = 1
rcodcl(ifac, isca(1), 1) = rtlocg(icnt(ilelt))
enddo
endif
```

List of published/submitted paper

Duan, Y., He, S., Ganesan, P., & Gotts, J. (2013). Modelling of the cooling of the moderator brick in the advanced gas-cooled reactor. In :*The 15th International Topical Meeting on Nuclear Reactor Thermal Hydraulics, NURETH-15, Pisa, Italy, May 12-17*.

Duan, Y., He, S., Ganesan, P., & Gotts, J. (2014). Analysis of the horizontal flow in the advanced gas-cooled reactor. *Nuclear Engineering and Design*, *272*, 53–64.

Duan, Y.& He, S. (2015). Numerical investigation of buoyancy-aided flow in the rod-to-wall gap regions. In: *The 16th International Topical Meeting on Nuclear Reactor Thermal Hydraulics, NURETH-16, Chicago, USA, August 30 - September 4*. (Accepted)

References:

Abbasian, F., Yu, S. D., & Cao, J. (2010). Large Eddy Simulation of Turbulent Axial Flow Along an Array of Rods. Journal of Fluids Engineering, 132(2), 021105.

Abe, K., Kondoh, T., & Nagano, Y. (1994). A new turbulence model for predicting fluid flow and heat transfer in separating and reattaching flows—I. Flow field calculations. International Journal of Heat and Mass Transfer, 37(1), 139–151.

Achenbach, E. (1989). Heat transfer from a staggered tube bundle in cross-flow at high Reynolds numbers. *International Journal of Heat and Mass Transfer*, *32*(2), 271–280.

Achenbach, E. (1991). Heat transfer from smooth and rough in-line tube banks at high Reynolds number. *International Journal of Heat and Mass Transfer*, *34*(1), 199–207.

Aiba, S. (1990). Heat transfer Around a Tube in In-Line tube Banks Near a Plane Wall. *Journal of Heat Transfer*, *112*.

Aiba, S., Tsuchida, H., Shoji, H., & Sasaki, A. (1985). Heat transfer around a circular cylinder near a plane boundary. *Transactions of the Japan Society of Mechanical Engineers Series B*, *51*, 866–873.

Aiba;, S., Tsuchida, H., & Terukazu, O. (1982). Heat Transfer around Tubes in Staggered Tube Banks. *JSME*, *25*(204).

Bae, J. H., Yoo, J. Y., & Choi, H. (2005). Direct numerical simulation of turbulent supercritical flows with heat transfer. *Physics of Fluids*, *17*(10), 105104.

Bae, J. H., Yoo, J. Y., & McEligot, D. M. (2008). Direct numerical simulation of heated CO2 flows at supercritical pressure in a vertical annulus at Re=8900. *Physics of Fluids*, *20*(5), 055108.

Baglietto, E., & Ninokata, H. (2005). A turbulence model study for simulating flow inside tight lattice rod bundles. *Nuclear Engineering and Design*, *235*(7), 773–784.

Baglietto, E., Ninokata, H., & Misawa, T. (2006). CFD and DNS methodologies development for fuel bundle simulations. *Nuclear Engineering and Design*, *236*(14-16), 1503–1510.

Baratto, F., Bailey, S. C. C., & Tavoularis, S. (2006). Measurements of frequencies and spatial correlations of coherent structures in rod bundle flows. *Nuclear Engineering and Design*, *236*(17), 1830–1837.

Behnia, M., Parneix, S., & Durbin, P. A. (1998). Prediction of heat transfer in an axisymmetric turbulent jet impinging on a flat plate. *International Journal of Heat and Mass Transfer*, *41*(12), 1845–1855.

Behzadmehr, A., Galanis, N., & Laneville, A. (2003). Low Reynolds number mixed convection in vertical tubes with uniform wall heat flux. *International Journal of Heat and Mass Transfer*, *46*(25), 4823–4833.

Biemüller, M., Meyer, L., & Rehme, K. (1996). Large eddy simulation and measurement of the structure of turbulence in two rectangular channels connected by a gap. *Engineering Turbulence Modeling and Experiments*, *3*, 249–258.

Bishop, A.A., Sandberg, R.O., Tong, L.S. (1964). High temperature supercritical pressure water loop: Part IV. Forced convection heat transfer to water at near-critical temperatures and super-critical pressures. Westinghouse Electric Corporation, Pittsburgh, PA.

Bouhairie, S., & Chu, V. H. (2007). Two-dimensional simulation of unsteady heat transfer from a circular cylinder in crossflow. *Journal of Fluid Mechanics*, 570.

Brunner, G. (2010). Applications of supercritical fluids. *Annual Review of Chemical and Biomolecular Engineering*, *1*, 321–42.

Carr, a. D., Connor, M. a., & Buhr, H. O. (1973). Velocity, Temperature, and Turbulence Measurements in Air for Pipe Flow With Combined Free and Forced Convection. *Journal of Heat Transfer*, *95*(4), 445.

Celik, I. B., Cehreli, Z. N., & Yavuz, I. (2005). Index of Resolution Quality for Large Eddy Simulations. *Journal of Fluids Engineering*, *127*(5), 949.

Celik, I., Klein, M., & Janicka, J. (2009). Assessment Measures for Engineering LES Applications. *Journal of Fluids Engineering*, *131*(3), 031102.

Chang, D., & Tavoularis, S. (2005). Unsteady Numerical Simulations of Turbulence and Coherent Structures in Axial Flow Near a Narrow Gap. *Journal of Fluids Engineering*, *127*(3), 458.

Chang, D., & Tavoularis, S. (2006). Convective Heat Transfer in Turbulent Flow Near a Gap. *Journal of Heat Transfer*, *128*(7), 701.

Chang, D., & Tavoularis, S. (2007). Numerical simulation of turbulent flow in a 37-rod bundle. *Nuclear Engineering and Design*, *237*(6), 575–590.

Chang, D., & Tavoularis, S. (2008). Simulations of turbulence, heat transfer and mixing across narrow gaps between rod-bundle subchannels. *Nuclear Engineering and Design*, *238*(1), 109–123.

Chang, D., & Tavoularis, S. (2012). Numerical simulations of developing flow and vortex street in a rectangular channel with a cylindrical core. *Nuclear Engineering and Design*, *243*, 176–199.

Cheng, X., Kuang, B., & Yang, Y. H. (2007). Numerical analysis of heat transfer in supercritical water cooled flow channels. *Nuclear Engineering and Design*, *237*(3), 240–252.

Cheng, X., & Schulenberg, T. (2001). *Heat Transfer at Supercritical Pressures - Literature Review and Application to an HPLWR*.

Chien, K. Y. (1982) Predictions of channel and boundary-layer flows with a low-Reynolds number turbulence model. *Am. Inst. Aeronaut. Astronaut. J.*, 20, 33–38.

Choueiri, G. H., & Tavoularis, S. (2014). Experimental investigation of flow development and gap vortex street in an eccentric annular channel. Part 1. Overview of the flow structure. *Journal of Fluid Mechanics*, *752*, 521–542.

Chaunhan, A.K., Prasad, B.V.S.S.S., & Pantnaik, B.S.V. (2014) Numerical simulation of flow through an eccentric annulus with heat transfer. *International Journal of Numerical Methods for Heat & Fluid Flow*, 24(8), 1864-1887.

Cotton, M. A., & Jackson, J. D. (1990). Vertical tube air flow in the turbulent mixed convection regime calculated using a low-Reynold-number k~epsilon. *International Journal of Heat and Mass Transfer*, *33*(2).

Cotton,M.A., Theoretical studies of mixed convection in vertical tubes, Ph.D. Thesis, The University of Manchester, 1987.

Cotton, M. A., & Kirwin, P. J. (1995). A variant of the low-Reynolds-number two-equation turbulence model applied to variable property mixed convection flows. *International Journal of Heat and Fluid Flow*, *16*(6), 486–492.

Dang, C., & Hihara, E. (2004a). In-tube cooling heat transfer of supercritical carbon dioxide. Part 1. Experimental measurement. *International Journal of Refrigeration*, *27*(7), 736–747.

Dang, C., & Hihara, E. (2004b). In-tube cooling heat transfer of supercritical carbon dioxide. Part 2. Comparison of numerical calculation with different turbulence models. *International Journal of Refrigeration*, *27*(7), 748–760.

Deissler (1950): R.G. Deissler, NACA, Technical Note 2138.

Dittus FW, Boelter LMK. Heat transfer in automobile radiators of the tubular type, 3rd ed. University of California, Berkeley: Publications in Engineering; 1930. p. 443.

Du, Z., Lin, W., & Gu, A. (2010). Numerical investigation of cooling heat transfer to supercritical CO2 in a horizontal circular tube. *The Journal of Supercritical Fluids*, *55*(1), 116–121.

Dyadyakin, B.V., Popov, A.S.(1977). Heat transfer and thermal resis- tance of tight seven-rod bundle, cooled with water flow at super- critical pressures. Trans. VTI (11), 244–253 (in Russian).

Easby, J. P. (1978). The effect of buoyancy on flow and heat transfer for a gas passing down a vertical pipe at low turbulent reynolds numbers. *International Journal of Heat and Mass Transfer*, *21*(6), 791–801.

Fischer, P., Lottes, J., Siegel, A., & Palmiotti, G. (2007). LARGE EDDY SIMULATION OF WIRE-WRAPPED FUEL PINS I : Hydrodynamics in a Periodic Array.

Forooghi, P., Abdi, I. A., Dahari, M., & Hooman, K. (2015). Buoyancy induced heat transfer deterioration in vertical concentric and eccentric annuli. *International Journal of Heat and Mass Transfer*, *81*, 222–233.

Ganesan, P., He, S., Hamad, F., Gotts, J.(2013). Effect of horizontal cross flow on the heat transfer form the moderator bricks in the Advanced Gas-cooled Reactor: A CFD study.*Nucl. Eng. Des.*, 263, 151-163.

Geurts, B. J., & Fröhlich, J. (2002). A framework for predicting accuracy limitations in large-eddy simulation. *Physics of Fluids*, *14*(6), L41.

Gorban, L., Pomet'ko, O., Khryaschev, O.(1990). Modeling of water heat transfer with Freon of supercritical pressure. Institute of Physics and Power Engineering, Obninsk, Russia (in Russian).

Gosset, a., & Tavoularis, S. (2006). Laminar flow instability in a rectangular channel with a cylindrical core. *Physics of Fluids*, *18*(4), 044108.

Gu, H. Y., Cheng, X., & Yang, Y. H. (2008). CFD analysis of thermal–hydraulic behavior in SCWR typical flow channels. *Nuclear Engineering and Design*, *238*(12), 3348–3359.

Gu, H. Y., Cheng, X., & Yang, Y. H. (2010). CFD analysis of thermal–hydraulic behavior of supercritical water in sub-channels. *Nuclear Engineering and Design*, *240*(2), 364–374.

Guellouz, M. S., & Tavoularis, S. (1992). Heat transfer in rod bundle subchannels with varying rod-wall proximity. *Nuclear Engineering and Design*, *132*, 351–366.

Guellouz, M. S., & Tavoularis, S. (2000a). The structure of turbulent flow in a rectangular channel containing a cylindrical rod - Part 1 : Reynolds-averaged measurements. *Experimental Thermal and Fluid Science*, *23*(1-2), 59–73.

Guellouz, M. S., & Tavoularis, S. (2000b). The structure of turbulent flow in a rectangular channel containing a cylindrical rod - Part 2 : phase-averaged measurements. *Experimental Thermal and Fluid Science*, *23*(1-2), 75–91.

Gupta, S., Mokry, S., Farah, A., King, K., Pioro, I.(2010). Developing a new heat transfer correlation for supercritical water flow in vertical bare tubes. In: International Conference on Nuclear Engineering (ICONE-18), Xi'an

Haghshenas Fard, M. (2010). CFD modeling of heat transfer of CO2 at supercritical pressures flowing vertically in porous tubes. *International Communications in Heat and Mass Transfer*, *37*(1), 98–102.

Hall, W. B., Jackson, J. D., & Watson, A. (1967). Proceedings of the Institution of Mechanical Engineers , Conference.

He, S., Kim, W. S., Jiang, P. X., & Jackson, J. D. (2004). Simulation of mixed convection heat transfer to carbon dioxide at supercritical pressure. *Proceedings of the Institution of Mechanical Engineers, Part C: Journal of Mechanical Engineering Science*, *218*(11), 1281–1296.

He, S., Jiang, P.-X., Xu, Y.-J., Shi, R.-F., Kim, W. S., & Jackson, J. D. (2005). A computational study of convection heat transfer to CO2 at supercritical pressures in a vertical mini tube. *International Journal of Thermal Sciences*, *44*(6), 521–530.

He, S., Gotts, J., 2005. A computational study of the effect of distortions of the moderator cooling channel of the Advanced Gas-Cooled Reactor. *Nucl. Eng. Des.*, 235, 965-982.

He, S., Kim, W. S., & Bae, J. H. (2008). Assessment of performance of turbulence models in predicting supercritical pressure heat transfer in a vertical tube. *International Journal of Heat and Mass Transfer*, *51*(19-20), 4659–4675.

He, S., Kim, W. S., & Jackson, J. D. (2008). A computational study of convective heat transfer to carbon dioxide at a pressure just above the critical value. *Applied Thermal Engineering*, *28*(13), 1662–1675.

Head, J.L., Kinkead, A.N., 1972. Graphite fuel element structures for high temperature gas-cooled reactors. *Nucl. Eng. Des.* 18, 115-144.

Hiroaki, T., Ayao, T., Masaru, H., & Nuchi, N. (1973). Effects of buoyancy and of acceleration owing to thermal expansion on forced turbulent convection in vertical circular tubes—criteria of the effects, velocity and temperature profiles, and reverse transition from turbulent to laminar flow. *International Journal of Heat and Mass Transfer*, *16*(6), 1267–1288.

Home, D., Arvanitis, G., Lightstone, M. F., & Hamed, M. S. (2009). Simulation of flow pulsations in a twin rectangular sub-channel geometry using unsteady Reynolds Averaged Navier–Stokes modelling. *Nuclear Engineering and Design*, *239*(12), 2964–2980.

Hooper, J. D., & Rehme, K. (1984). Large-scale structural effects in developed turbulent flow through closely-spaced rod arrays. *Journal of Fluid Mechanics*, *145*, 305–337.

Hsu, Y.-Y., & Smith, J. M. (1961). The Effect of Density Variation on Heat Transfer in the Critical Region. *Journal of Heat Transfer*, *83*, 176.

Hua, Y.-X., Wang, Y.-Z., & Meng, H. (2010). A numerical study of supercritical forced convective heat transfer of n-heptane inside a horizontal miniature tube. *The Journal of Supercritical Fluids*, *52*(1), 36–46.

Hutt, P.K., Gaines, N., Halsall, M.J., McEllin, M., and White, R.J,. 1991. The UK core performance code package. Nuclear Energy, 30, 291-298

Hwang,C.B., Lin, C.A. (1998), Low-Reynolds number modelling of tran- spired flows, in: 2nd EF Conference in Turbulent Heat Transfer, Manchester, UK.

IAEA, (2014). Heat Transfer Behaviour and Thermohydraulics Code Testing for Supercritical Water Cooled Reactors (SCWRs), IAEA TECDOC 1746, (ISBN:978-92-0-107614-4).

Ikeno, T., & Kajishima, T. (2010). Analysis of dynamical flow structure in a square arrayed rod bundle. *Nuclear Engineering and Design*, *240*(2), 305–312.

In, W.-K., Shin, C.-H., Oh, D.-S., & Chun, T.-H. (2004). Numerical Analysis of the Turbulent Flow and Heat Transfer in a Heated Rod Bundle. *Journal of the Korean Nuclear Society*, *36*, 153–164.

Jackson and Hall (1979): Jackson, J. D. and Hall, W. B. Influences of buoyancy on heat transfer to fluids flowing in vertical tubes under turbulent conditions. Turbulent Forced Convection in Channels and Bundles Theory and Applications to Heat Exchangers and Nuclear Reactors, 2, Advanced Study Institute Book (eds. Kakac, S. and Spalding, D. B.), 1979, 613-640

Jackson, J. D., Cotton, M. a., & Axcell, B. P. (1989). Studies of mixed convection in vertical tubes. *International Journal of Heat and Fluid Flow*, *10*(1), 2–15.

Jackson, J.D. (2002), Consideration of the heat transfer properties of supercritical pres- sure water in connection with the cooling of advanced nuclear reactors. In: Proc. 13th Pacific Basin Nuclear Conference, Shenzhen City, China,21–25.

Jackson, J.D., (2006). Studies of buoyancy-influenced turbulent flow and heat transfer in vertical passages. In: Invited Keynote Lecture Given at the 13th International Heat Transfer Conference, Sydney, Australia.

Jaromin, M., & Anglart, H. (2013). A numerical study of heat transfer to supercritical water flowing upward in vertical tubes under normal and deteriorated conditions. *Nuclear Engineering and Design*, *264*, 61–70.

Jones, W. P., Launder,B.E.(1972), The prediction of laminarization with a two-equation model of turbulence, *Int. J. Heat Mass Transfer*, 15 301–314.

Jones, W. P., & Launder, B. E. (1973). The calculation of low-Reynolds-number phenomena with a two-equation model of turbulence. *International Journal of Heat and Mass Transfer*, *16*(6), 1119–1130.

Kao, M.-T., Lee, M., Ferng, Y.-M., & Chieng, C.-C. (2010). Heat transfer deterioration in a supercritical water channel. *Nuclear Engineering and Design*, *240*(10), 3321–3328.

Kasagi, N., & Nishimura, M. (1997). Direct numerical simulation of combined forced and natural turbulent convection in a vertical plane channel. *International Journal of Heat and Fluid Flow*, *18*(1), 88–99.

Keshmiri, A., Cotton, M. a., Addad, Y., & Laurence, D. (2012). Turbulence Models and Large Eddy Simulations Applied to Ascending Mixed Convection Flows. *Flow, Turbulence and Combustion*, *89*(3), 407–434.

Kim, W. S., He, S., & Jackson, J. D. (2008). Assessment by comparison with DNS data of turbulence models used in simulations of mixed convection. *International Journal of Heat and Mass Transfer*, *51*(5-6), 1293–1312.

Kolmogorov, A.N. (1941b). The local structure of turbulence in incompressible viscous fluids for very large Reynolds numbers. Dokl. Akad. Nauk SSSR 30. 299-303 [in Russian].

Koshizuka, S., Tankano, N., & Oka, Y. (1995). Numerical analysis of deterioration phenomena in heat transfer to supercritical water. *International Journal of Heat and Mass Transfer*, *38*(16), 1–8.

Krauss, T., & Meyer, L. (1996). Characteristics of Turbulent Velocity and Temperature in a Wall Channel of a Heated Rod Bundle. *Experimental Thermal and Fluid Science*, *1777*(95), 75–86.

Krauss, T., & Meyer, L. (1998). Experimental investigation of turbulent transport of momentum and energy in a heated rod bundle. *Nuclear Engineering and Design*, *180*(3), 185–206.

Kunik, C., Otic, I., & Schulenberg, T. (2011). Large Eddy Simulation Turbulent Flows at Supercritical Pressure. Toronto.

Kurganov, V. A., Zeigarnik, Y. A., & Maslakova, I. V. (2012). Heat transfer and hydraulic resistance of supercritical-pressure coolants. Part I: Specifics of thermophysical properties of supercritical pressure fluids and turbulent heat

transfer under heating conditions in round tubes (state of the art). *International Journal of Heat and Mass Transfer*, *55*(11-12), 3061–3075.

Kurganov, V. A., Zeigarnik, Y. A., & Maslakova, I. V. (2013). Heat transfer and hydraulic resistance of supercritical-pressure coolants. Part II: Experimental data on hydraulic resistance and averaged turbulent flow structure of supercritical pressure fluids during heating in round tubes under normal and deteriorate. *International Journal of Heat and Mass Transfer*, *58*(1-2), 152–167.

Lam,C.K.G., Bremhorst,K. (1981) A modified form of the k–e model for predicting wall turbulence, Trans. ASME 103 456–460.

Launder, B. E., & Sharma, B. I. (1974). Application of the energy-dissipation model of turbulence to the calculation of flow near a spinning disc. *Letters in Heat and Mass Transfer*, *1*(2), 131–137.

Launder, B. E., & Spalding, D. B. (1974). The numerical computation of turbulent flows. *Computer Methods in Applied Mechanics and Engineering*, *3*(2), 269–289.

Lee, J. I., Hejzlar, P., Saha, P., Kazimi, M. S., & Mceligot, D. M. (2008). Deteriorated turbulent heat transfer (DTHT) of gas up-flow in a circular tube : Heat transfer correlations. *International Journal of Heat and Mass Transfer*, *51*, 5318–5326.

Lee, J. S., Xu, X., & Pletcher, R. H. (2004). Large eddy simulation of heated vertical annular pipe flow in fully developed turbulent mixed convection. *International Journal of Heat and Mass Transfer*, *47*(3), 437–446.

Lee, S. H. (2010). Numerical study of convective heat transfer to supercritical water in rectangular ducts. *International Communications in Heat and Mass Transfer*, *37*(10), 1465–1470.

Lei, X., Li, H., Yu, S., & Chen, T. (2012). Numerical investigation on the mixed convection and heat transfer of supercritical water in horizontal tubes in the large specific heat region. *Computers & Fluids*, *64*, 127–140.

Li, H., Wang, H., Luo, Y., Gu, H., Shi, X., Chen, T., … Zhu, Y. (2009). Experimental investigation on heat transfer from a heated rod with a helically wrapped wire inside a square vertical channel to water at supercritical pressures. *Nuclear Engineering and Design*, *239*(10), 2004–2012.

Li, X., Wu, X., & He, S. (2014). Numerical investigation of the turbulent cross flow and heat transfer in a wall bounded tube bundle. *International Journal of Thermal Sciences*, *75*, 127–139.

Liu, M., & Ishiwatari, Y. (2011). Unsteady numerical simulations of the single-phase turbulent mixing between two channels connected by a narrow gap. *Nuclear Engineering and Design*, *241*(10), 4194–4205.

Liu, M., & Ishiwatari, Y. (2013). Unsteady numerical simulations of single-phase turbulent mixing in tight lattice geometries. *Nuclear Engineering and Design*, *256*, 28–37.

Lowery, G. W., & Vachon, R. I. (1975). The effect of turbulence on heat transfer from heated cylinders. *International Journal of Heat and Mass Transfer*, *18*(11), 1229–1242.

Merzari, E., & Ninokata, H. (2008). Anisotropic Turbulence and Coherent Structures in Eccentric Annular Channels. *Flow, Turbulence and Combustion*, *82*(1), 93–120.

Merzari, E., & Ninokata, H. (2009). Development of an LES Methodology for Complex Geometries. *Nuclear Engineering and Technology*, *41*(7), 893–906.

Merzari, E., Wang, S., Ninokata, H., & Theofilis, V. (2008). Biglobal linear stability analysis for the flow in eccentric annular channels and a related geometry. *Physics of Fluids*, *20*(11), 114104.

Meyer, L. (1994). Measurement of turbulent velocity and temperature in axial flow through a heated rod bundle. *Nuclear Engineering and Design*, *146*, 71–82.

Meyer, L., & Rehme, K. (1994). Large-Scale Turbulence Phenomena Compound Rectangular Channels. *Experimental Thermal and Fluid Science*, *8*, 286–304.

Meyer, Leonhard, & Rehmen, K. (1995). PERIODIC VORTICES IN FLOW THROUGH CHANNELS WITH LONGITUDINAL SLOTS OR FINS. In *Tenth Symposioum on Turbulent shear flows* (p. 6).

Moller, S. V. (1991). On Phenomena of Turbulent Flow Through Rod Bundles. *Experimental Thermal and Fluid Science*, *4*(1), 25–35.

Moller, S. V. (1992). Single-Phase Turbulent Mixing in Rod Bundles. *Experimental Thermal and Fluid Science*, *5*, 26–33.

Mokry, S., Gospodinov, Y., Pioro, I., Kirillov, P(2009). Supercritical water heat-transfer correlation for vertical bare tubes. In: ICONE-17, Brussels.

Murray, D. B. (1993). A comparison of heat transfer in staggered and inline tube banks with a gas-particle crossflow. *Experimental Thermal and Fluid Science*, *6*(2), 177–185.

Myoung,H.K., Kasagi,N. (1990). A new approach to the improvement of k– e turbulence model for wall bounded shear flows, JSME Int. J. 33 63–72.

Ničeno, B., & Sharabi, M. (2013). Large eddy simulation of turbulent heat transfer at supercritical pressures. *Nuclear Engineering and Design*, *261*, 44–55.

Nicoud, F., & Ducros, F. (1999). Subgrid-Scale Stress Modelling Based on the Square of the Velocity Gradient Tensor, 183–200.

Ninokata, H., Merzari, E., & Khakim, a. (2009). Analysis of low Reynolds number turbulent flow phenomena in nuclear fuel pin subassemblies of tight lattice configuration. *Nuclear Engineering and Design*, *239*(5), 855–866.

O'Connor, T.J., 2009. Gas reactors-A review of the past, an overview of the present and a view of the future. Paper presented at the GIF Symposium, Paris (France).

Ornatsky, A.P., Glushchenko, L.P., Siomin, E.T.(1970). The research of temperature conditions of small diameter parallel tubes cooled by water under supercritical pressures. In: Proceedings of the 4th International Heat Transfer Conference, Paris-Versailles, France. Elsevier, Amsterdam.

Orszag,S.A., Yakhot,V., Flannery,W.S., Boysan,F., Choudhury,D., Maruzewski,J., and Patel, B. (1993). Renormalization Group Modeling and Turbulence Simulations. In International Conference on Near-Wall Turbulent Flows, Tempe, Arizona.

Ouma, B. H., & Tavoularis, S. (1991). Flow measurements in rod bundle subchannels with varying rod-wall proximity. *Nuclear Engineering and Design*, *131*, 193–208.

Paul, S. S., Ormiston, S. J., & Tachie, M. F. (2008). Experimental and numerical investigation of turbulent cross-flow in a staggered tube bundle. *International Journal of Heat and Fluid Flow*, *29*(2), 387–414.

Perkins, H. C., & Leppert, G. (1964). Local heat-transfer coefficients on a uniformly heated cylinder. *International Journal of Heat and Mass Transfer*, *7*(2), 143–158.

Petukhov and Polyakov (1988): B.S. Petukhov, A.F. Polyakov, Heat transfer in turbulent mixed convection, Hemisphere Publishing Corporation, New York, 1988.

Petukhov, B. S. and Polyakov, A. F. (1988). Heat Transfer in Turbulent Mixed Convection, B.E. Launder (ed.), Hemisphere, Bristol, PA, USA

Pioro, I. L., Duffey, R. B., & Dumouchel, T. J. (2004). Hydraulic resistance of fluids flowing in channels at supercritical pressures (survey). *Nuclear Engineering and Design*, *231*(2), 187–197.

Pioro, I. L., Khartabil, H. F., & Duffey, R. B. (2004). Heat transfer to supercritical fluids flowing in channels—empirical correlations (survey). *Nuclear Engineering and Design*, *230*(1-3), 69–91.

Pioro, I. L., & Duffey, R. B. (2005). Experimental heat transfer in supercritical water flowing inside channels (survey). *Nuclear Engineering and Design*, *235*(22), 2407–2430.

Pioro, I., & Duffey, R.,(2007) Heat Transfer & Hydraulic Resistance at Supercritical Pressures in Power Engineering Applications. ASME, ISBN: 0791802523.

Piot, E., & Tavoularis, S. (2011). Gap instability of laminar flows in eccentric annular channels. Nuclear Engineering and Design, 241(11), 4615–4620.

Podila, K., & Rao, Y. F. (2014). Assessment of CFD for the Canadian SCWR bundle with wire wraps. *Progress in Nuclear Energy*, *77*, 373–380.

Podila, K., & Rao, Y. F. (2015). CFD analysis of flow and heat transfer in Canadian supercritical water reactor bundle. *Annals of Nuclear Energy*, *75*, 1–10.

Pope, S.B. (2000). Turbulent Flows. Cambridge University Press.

Richardson, L.F. (1922). Weather Prediction by Numerical Process. Cambridge: Cambridge University Press.

Richards, G., Harvel, G. D., Pioro, I. L., Shelegov, a. S., & Kirillov, P. L. (2013a). Heat transfer profiles of a vertical, bare, 7-element bundle cooled with supercritical Freon R-12. *Nuclear Engineering and Design*, *264*, 246–256.

Richards, G., Harvel, G. D., Pioro, I. L., Shelegov, A. S., & Kirillov, P. L. (2013b). Heat transfer profiles of a vertical, bare, 7-element bundle cooled with supercritical Freon R-12. *Nuclear Engineering and Design*, *264*, 246–256.

Rouai, N. M. Influences of buoyancy and imposed flow transients on turbulent convective heat transfer in a tube. Ph.D. Thesis, University of Manchester, 1987

Safwat Wilson, A., & Khalil Bassiouny, M. (2000). Modeling of heat transfer for flow across tube banks. *Chemical Engineering and Processing: Process Intensification*, *39*(1), 1–14.

Schulenberg, T. and Starflinger, J.(2007). Core sesign concepts for high performance light water reactors. Nucl. Eng. Technol., 39(04), 249-256.

Schulenberg, T. and Starflinger, J.(2012). High performance light water reactor: design and analyses. KIT Scientific Publishing, Karlsruhe, Germany.

Shahab Khushnood, Zaffar Muhammad Khan, Muhammad Afzaal Malik, Zafarullah Koreshi, Muhammad Akram Javaid, Mahmood Anwer Khan, Arshad Hussain Qureshi, Luqman Ahmad Nizam, Khawaja Sajid Bashir, Syed Zahid Hussain (2012). Cross-Flow-Induced-Vibrations in Heat Exchanger Tube Bundles: A Review, Nuclear Power Plants, Dr. Soon Heung Chang (Ed.), ISBN: 978-953-51-0408-7, InTech, Available from: http://www.intechopen.com/books/nuclear-power-plants/cross-flow-induced-vibrations-in-heat-exchanger-tube- bundle-a-review

Shang, Z. (2009). CFD investigation of vertical rod bundles of supercritical water-cooled nuclear reactor. *Nuclear Engineering and Design*, *239*(11), 2562–2572.

Shang, Z., & Chen, S. (2011). Numerical investigation of diameter effect on heat transfer of supercritical water flows in horizontal round tubes. *Applied Thermal Engineering*, *31*(4), 573–581.

Shang, Z. (2013). Performance analysis of large scale parallel CFD computing based on Code_Saturne. *Computer Physics Communications*, 184(2), 381–386.

Shang, Z., & Lo, S. (2010). Numerical investigation of supercritical water-cooled nuclear reactor in horizontal rod bundles. *Nuclear Engineering and Design*, *240*(4), 776–782.

Shang, Z., & Lo, S. (2011). CFD in supercritical water-cooled nuclear reactor (SCWR) with horizontal tube bundles. *Nuclear Engineering and Design*, *241*(11), 4427–4433.

Shang, Z., Yao, Y., & Chen, S. (2008). Numerical investigation of system pressure effect on heat transfer of supercritical water flows in a horizontal round tube. *Chemical Engineering Science*, *63*(16), 4150–4158.

Sharabi, M., & Ambrosini, W. (2009). Discussion of heat transfer phenomena in fluids at supercritical pressure with the aid of CFD models. *Annals of Nuclear Energy*, *36*(1), 60–71.

Sharabi, M., Ambrosini, W., He, S., & Jackson, J. D. (2008). Prediction of turbulent convective heat transfer to a fluid at supercritical pressure in square and triangular channels. *Annals of Nuclear Energy*, *35*(6), 993–1005.

Sharabi, M. B., Ambrosini, W., & He, S. (2008). Prediction of unstable behaviour in a heated channel with water at supercritical pressure by CFD models. *Annals of Nuclear Energy*, *35*(5), 767–782.

Silin, V. A., Voznesensky, V. A., & Afrov, A. M. (1993). The light water integral reactor with natural circulation of the coolant at supercritical pressure B-500 SKDI. *Nuclear Engineering and Design*, *144*(2), 327–336.

Smagorinsky, J. (1963). General Circulation Experiments with the Primitive Equations. I. The Basic Experiment. Monthly. Weather. Review., 91:99–164.

Steiner, A. (1971). On the reverse transition of a turbulent flow under the action of buoyancy forces. *Journal of Fluid Mechanics*, *47*(03), 503.

Swenson, H., Carver, J., Kakarala, C.(1965). Heat transfer to supercritical water in smooth-bore tubes. J. Heat Transfer 87 (4).

Tabor, G. R., & Baba-Ahmadi, M. H. (2010). Inlet conditions for large eddy simulation: A review. *Computers & Fluids*, *39*(4), 553–567.

Tennekes, H. and Lumley, J.L. (1972). A First Course in Turbulence, Cambridge MA: MIT Press.

Walklate P.L., A comparative study of theoretical models of turbulence for the numerical prediction of boundary layer flows, Ph.D. Thesis, UMIST, 1976.

Wang, H., Bi, Q., Wang, L., Lv, H., & Leung, L. K. H. (2014). Experimental investigation of heat transfer from a 2×2 rod bundle to supercritical pressure water. *Nuclear Engineering and Design*, *275*, 205–218.

Wang, J., Li, J., He, S., & Jackson, J. D. (2004). Computational simulations of buoyancy-influenced turbulent flow and heat transfer in a vertical plane passage. *Proceedings of the Institution of Mechanical Engineers, Part C: Journal of Mechanical Engineering Science*, *218*(11), 1385–1397.

Weaver, D. S. and Fitzpatrick, J. A.(1988). A review of cross-flow induced viberations in the heat exchanger tube arrays. J. Fluids Struct., 2, 73-93.

Welch, P. D. (1967). The use of fast fourier transform for the estimation of power spectra: a method based on time average over short, modified periodograms.

Wen, Q. L., & Gu, H. Y. (2010). Numerical simulation of heat transfer deterioration phenomenon in supercritical water through vertical tube. *Annals of Nuclear Energy*, *37*(10), 1272–1280.

Wen, Q. L., & Gu, H. Y. (2011). Numerical investigation of acceleration effect on heat transfer deterioration phenomenon in supercritical water. *Progress in Nuclear Energy*, *53*(5), 480–486.

Wilcox, D.C., Reassessment of the scale determining equation for advanced turbulence models, AIAA J. 26 (1988) 1299–1310.

Wu, X., & Trupp, a. C. (1993). Experimental study on the unusual turbulence intensity distributions in rod-to-wall gap regions. *Experimental Thermal and Fluid Science*, *6*(4), 360–370.

Yamagata, K., Nishmawa, K., & Hasegawa, S. (1972). FORCED CONVECTIVE HEAT TRANSFER TO Supercitical water flowing in tubes. *International Journal of Heat and Mass Transfer*, *15*, 29.

Yamaji, A., Kamer, K., Oka, Y., and Koshizuka, S.(2005). Improved core design of the high temperature supercritical-pressure light water reactor, Ann. Nucl. Energy, 32, 651-670.

Yang, J., Oka, Y., Ishiwatari, Y., Liu, J., & Yoo, J. (2007). Numerical investigation of heat transfer in upward flows of supercritical water in circular tubes and tight fuel rod bundles. *Nuclear Engineering and Design*, *237*(4), 420–430.

Yang, Z., Shih,T.H., (1993). New time scale based k–e model for near-wall turbulence, AIAA J. 31 1191–1198.

Yakhot, V., Orszag, S. A. (1986). Renormalization Group Analysis of Turbulence: I. Basic Theory. Journal of Scientific Computing, 1(1):1–51.

Yoo, J. Y. (2013). The Turbulent Flows of Supercritical Fluids with Heat Transfer. *Annual Review of Fluid Mechanics*, *45*(1), 495–525.

You, J., Yoo, J. Y., & Choi, H. (2003). Direct numerical simulation of heated vertical air flows in fully developed turbulent mixed convection. *International Journal of Heat and Mass Transfer*, *46*(9), 1613–1627.

Zdravistch, F., A. Fletcher, C., & Behnia, M. (1995). Numerical laminar and turbulent fluid flow and heat transfer predictions in tube banks. *International Journal of Numerical Methods for Heat & Fluid Flow*, *5*, 717–733.

Zhang, S., Gu, H., Xiong, Z., & Gong, S. (2014). Numerical investigation on heat transfer of supercritical fluid in a vertical 7-rod bundle. *The Journal of Supercritical Fluids*, *92*, 8–15.

Zhang, Y., Zhang, C., & Jiang, J. (2011). Numerical Simulation of Fluid Flow and Heat Transfer of Supercritical Fluids in Fuel Bundles. *Journal of Nuclear Science and Technology*, *48*(6), 929–935.

Zhang, Y., Zhang, C., & Jiang, J. I. N. (2012). Turbulent Mixing Coefficient for Supercritical fluids,*Nuclear Technology*,*177*, *98-106*.